# Amorphous solids from the glass transition to 1 Kelvin

Camille Scalliet

**THÈSE POUR OBTENIR LE GRADE DE DOCTEUR DE L'UNIVERSITE DE MONTPELLIER**

**En Physique**

**École doctorale : Information, Structures, Systèmes**

**Unité de recherche Laboratoire Charles Coulomb UMR 5221**

# Amorphous solids from the glass transition to 1 Kelvin


**Présentée par Camille Scalliet**


**Le 26 Septembre 2019**

**Sous la direction de Ludovic Berthier et Francesco Zamponi**

**Devant le jury composé de**

| | |
|---|---|
| Jean-Louis Barrat, Professeur, Université Grenoble Alpes | Rapporteur |
| Ludovic Berthier, Directeur de Recherche, Laboratoire Charles Coulomb | Directeur de thèse |
| Mark D. Ediger, Professor, University of Wisconsin-Madison | Président du Jury |
| Liesbeth M. C. Janssen, Assistant Professor, Eindhoven University of Technology | Examinatrice |
| David Rodney, Professeur, Université de Lyon | Rapporteur |
| Francesco Zamponi, Directeur de Recherche, Laboratoire de Physique de l'ENS | Directeur de thèse |

UNIVERSITÉ DE MONTPELLIER

**Solides amorphes de la transition vitreuse jusqu'à 1 Kelvin**

Comprendre la nature fondamentale de la transition vitreuse et des solides amorphes est au coeur d'un vaste effort de recherche. La description théorique des solides vitreux reste essentiellement phénoménologique. Ce travail explore l'hypothèse selon laquelle une nouvelle phase amorphe de la matière expliquerait naturellement leurs propriétés physiques. Nous analysons la thermodynamique des verres dans la limite de dimension infinie. Cette théorie exacte de champ moyen prédit deux phases vitreuses, une "simple" et une "marginalement stable", séparées par une transition de Gardner. Nous démontrons que les verres sont marginalement stables dans une grande variété de conditions physiques, couvrant des régimes pertinents pour décrire la matière granulaire, les mousses, les émulsions, les colloïdes durs et mous, ainsi que les verres moléculaires. Nous confrontons nos prédictions théoriques à des simulations numériques en trois dimensions. Nous développons un algorithme numérique efficace qui crée des verres très stables. Nous montrons que les verres colloïdaux et granulaires sont marginalement stables: ils évoluent dans un paysage hiérarchique et présentent des excitations délocalisées de basse énergie. Dans ce régime, des variations cycliques de la température donnent lieu à des effets de rajeunissement et de mémoire, précédemment observés dans les verres de spin. En revanche, le comportement des verres moléculaires est régi par des défauts localisés, dont les propriétés quantiques à basse température sont également analysées. Nous étudions le rôle de l'entropie configurationnelle dans le ralentissement dynamique qui accompagne la formation du verre. Nous mesurons l'entropie configurationnelle dans des liquides à très basse température, et analysons les théories thermodynamiques de la transition vitreuse.

**Mot-Clés** : Physique statistique des systèmes désordonnés, théorie de champ moyen, simulations numériques, transition vitreuse, transition de Gardner, dynamique hors d'équilibre, entropie configurationnelle.

**Amorphous solids from the glass transition to 1 Kelvin**

Understanding the fundamental nature of the glass transition and amorphous solids is at the core of a large research effort. The theoretical description of glassy solids remains mainly phenomenological. This work explores the hypothesis that a new amorphous phase of matter naturally explains their physical properties. We analyze the thermodynamics of glasses in the limit of large dimensions. This exact mean-field theory predicts two glassy phases, 'simple' and 'marginally stable', separated by a Gardner transition. We find that glasses are marginally stable in a wide range of physical conditions, covering regimes relevant to describe granular matter, foams, emulsions, hard and soft colloids, and molecular glasses. We confront our theoretical predictions to three-dimensional numerical simulations. We develop an efficient numerical scheme which creates well-relaxed glasses. Colloidal and granular glasses are found to be marginally stable: they evolve in a hierarchical landscape, and present delocalized low-lying excitations. Temperature cycles in this regime give rise to rejuvenation and memory effects, previously observed in spin glasses. In contrast, the behavior of molecular glasses is governed by localized two level systems, whose low-temperature tunneling properties are also analyzed. We investigate the role of the configurational entropy in the glassy dynamical slowdown accompanying glass formation. We measure the configurational entropy in extremely supercooled liquids, and assess thermodynamic theories of the glass transition.

**Keywords** : Statistical physics of disordered systems, mean field theory, computer simulations, glass transition, Gardner transition, out-of-equilibrium dynamics, configurational entropy.

# Acknowledgements

I thank the members of the jury, Jean-Louis Barrat, Mark Ediger, Liesbeth Janssen, and David Rodney for accepting my invitation to be present on this final, important day of my doctoral studies. I am grateful to my referees, Jean-Louis Barrat and David Rodney, for the time devoted to assessing my manuscript.

Francesco and Ludovic, it was both a pleasure and a great honour to perform my doctoral studies under your guidance. Thank you for accepting to supervise my work, and suggesting an exciting project which brought together the most recent analytical and computational advances in the field. Learning to master both aspects of the project was challenging, but your continuous support, insightful discussions and advice helped me in this endeavour. You gave me an incredible flexibility in terms of the projects and external collaborations that I wanted to pursue. You pushed me to give the best I could, never to rest on past successes, and aim higher. I really appreciated to have the opportunity to present and defend my work independently at conferences, workshops, and seminars.

Luckily, the start of my PhD coincided with the substantial funding of the Simons collaboration 'Cracking the glass problem', of which Ludovic and Francesco are principal investigators. Being part of this international network enriched my experience as a PhD student in an invaluable way. I thank Sidney Nagel, for directing this incredible team of researchers, and for the inspiring discussions on memory, rejuvenation, and other topics. I thank all the members of the collaboration for creating such a stimulating environment. I am grateful to Patrick Charbonneau for giving me the opportunity to give my first seminar, and Dave Reichman for hosting me at Columbia University during July 2018. I had the chance to attend two amazing summer schools, in Boulder (2017) and Beg Rohu (2018). Thanks to Giulio Biroli and Chiara Cammarota: I waited impatiently for the summer school, and it was beyond my expectations, both for the science and the sailing.

I would like to thank Ludovic for creating a stimulating work environment in the laboratoire Charles Coulomb. I had the chance to work closely with brilliant postdocs and PhD students. I thank Andrea Ninarello and Benjamin Guiselin, with who I had the pleasure to share the same office during my stay in Montpellier. Andrea, I really appreciated your help in the first months of the PhD. Brilliant, kind and gentle people are rare, so I was lucky to have Benjamin as a neighbor. Thanks to Misaki Ozawa for all the scientific discussions, and collaborations. It was a pleasure to learn from you. The LAMMPS project was made possible thanks to Elijah Flenner, Christopher Fullerton, and Murari Singh, and I appreciated working with you. I am grateful to the people in the physique statistique team in general. I was lucky to be introduced to computer simulations by

such an expert as Daniele Coslovich. I appreciated your pedagogical help in the beginning, and for being here for me when I needed.

The scientific advice which emerged during my annual comité de thèse were an important guidance to my work. I thank Giulio Biroli, Walter Kob, Gilles Tarjus, Matthieu Wyart, and Lucyna Firlej for this.

I acknowledge the Fondation L'Oréal for awarding me a l'Oréal-UNESCO For women in Science Fellowship. This allowed me to reach financial independence very early, to gain confidence, and to meet inspiring young female scientists.

I am deeply grateful to the members of the association 'Femmes et Sciences'. I had the chance to meet and exchange with successful and inspiring women scientists. The discussions during the monthly lunches helped me overcome and fight some of my fears, gain consciousness on my position as a women scientist, with its opportunities and constraints. I sincerely thank my mentor, Mireia Pelegrin, for all the discussions, and exchanges during the last two years. My greatest wish would be to be able, one day, to help and advise someone as well as you did.

# Table of contents

Chapter 1

# Introduction

What do a sandpile, a mayonnaise and a window glass have in common? They are 'amorphous' solids, characterized by a disordered organization of their constituent particles. At the microscopic scale, the presence of disorder generates excitations and defects much more complex to quantify than in crystalline solids. For example, the lifespan of the billions of screens of smartphones or computers marketed each year is limited. Why? Because of the slow relaxation of the amorphous layer contained in the organic light-emitting diodes. In the context of fundamental research, the resolution of interferometers built for gravitational wave detection, which was awarded the Nobel Prize in Physics in 2017, is mainly limited by the mechanical dissipation caused by defects present in the amorphous thin films covering their mirrors.

How can we characterize the excitations and microscopic defects of amorphous solids? What are the consequences for their macroscopic, mechanical, and thermal behavior? There is still no theory describing how the macroscopic properties of amorphous solids emerge from a microscopic description. This problem combines two theoretical challenges, as it tackles disordered systems, which evolve out of thermodynamic equilibrium. This area of research is known for its multitude of phenomenological approaches, none of which has allowed us to understand the profound nature of materials that we use daily.

This introduction presents the main aspects of amorphous solids relevant for the work presented below. Complete reviews on glass phenomenology and theories can be found in Refs. [1–3].

## 1.1 Supercooled liquids and glasses

We focus on a class of physical systems that we call 'glassy'. Let us give a general definition, and therefore quite vague. The term 'glassy' is used in a variety of contexts to describe systems characterized by an apparent lack of order in their degrees of freedom, and whose relaxation time becomes extremely large, eventually infinite, as a control parameter is changed [4]. If the divergence of the relaxation time is well localized in temperature, or density, one can talk about a 'glass transition'.

### 1.1.1 The experimental glass transition

Atomic and molecular liquids can transform into amorphous solids at low temperature. They are canonical examples of glassy systems. We describe the phenomenology of glass formation, starting from the high-temperature liquid. The liquid is characterized by a high degree of structural disorder. Relaxations occur on timescales of order $10^{-13}-10^{-11}$ s. In this regime, the liquid is easily thermalized during an experiment. The high-temperature liquid can be described with theoretical tools from thermodynamics and equilibrium statistical mechanics [5]. Its state is defined by few control parameters (pressure, temperature, volume, etc.), which are related by an equation of state. For example, at constant pressure, the volume of a liquid decreases with temperature, as illustrated in Fig. 1.1 [6].

If the liquid is cooled at an infinitely slow rate, thermodynamic equilibrium is reached at all temperatures. For most materials, the stable thermodynamic phase below the melting temperature, $T_m$, is the crystal. Slowly cooled liquids crystallize at $T_m$. This first-order phase transition is signaled by a discontinuous jump of the volume in Fig. 1.1 [7]. The presence of the crystal should be carefully considered when studying glass formation, either experimentally or numerically. The material's composition and the protocol should frustrate crystallization [2]. In experiments, mixtures of different atoms or large molecules are cooled at fast rates, typically $0.1 - 100$ K/min [8].

If the disordered liquid is robust against crystallization, it becomes supercooled below $T_m$ (shaded box in Fig. 1.1). In the supercooled region, the liquid is at thermal equilibrium, but is metastable with respect to the crystal. Most importantly, it remains structurally disordered. As temperature decreases, dynamical processes become increasingly slow. When relaxation processes become longer than the observation time, the liquid can no longer thermalize. This defines the experimental glass transition at $T_g$, at which an out-of-equilibrium amorphous solid is formed. Below $T_g$, the system does not follow the equilibrium equation of state, and its properties depend on time. The experimental glass transition is not a thermodynamic phase transition: its location depends explicitly on the operator [9]. Longer timescales, or slower cooling rates, allow to reach equilibrium down to lower temperatures, creating denser glasses (the glass 2 is denser than the glass 1 in Fig. 1.1).

The phenomenon described above is observed in a wide variety of materials: atomic and molecular liquids [8], but also polymer films [10, 11], metallic alloys [12, 13], suspensions of small colloidal particles [14–16], or driven granular matter [17–20]. In the last two cases, a glass transition is observed by compressing the system.

The phenomenology presented in Fig. 1.1 raises many fundamental questions. What is the origin of the dynamical slowdown in supercooled liquids? Is it a purely dynamical process, or is it driven by an underlying thermodynamic phase transition? Solving the glass problem amounts to identifying and obtaining direct experimental signatures about the fundamental nature and the mathematical description of this mechanism. Beyond its formation, the properties of the amorphous solid obtained at $T_g$ remain theoretically unexplained. Can we build a first-principles theory for amorphous solids? Are the properties of the solid the same from $T_g$ down to zero temperature? In this work, we provide new theoretical insights to these open questions using a combination of analytical and computational techniques. The approach explored in this work relies heavily on a thermodynamic description of glass formation and glasses.

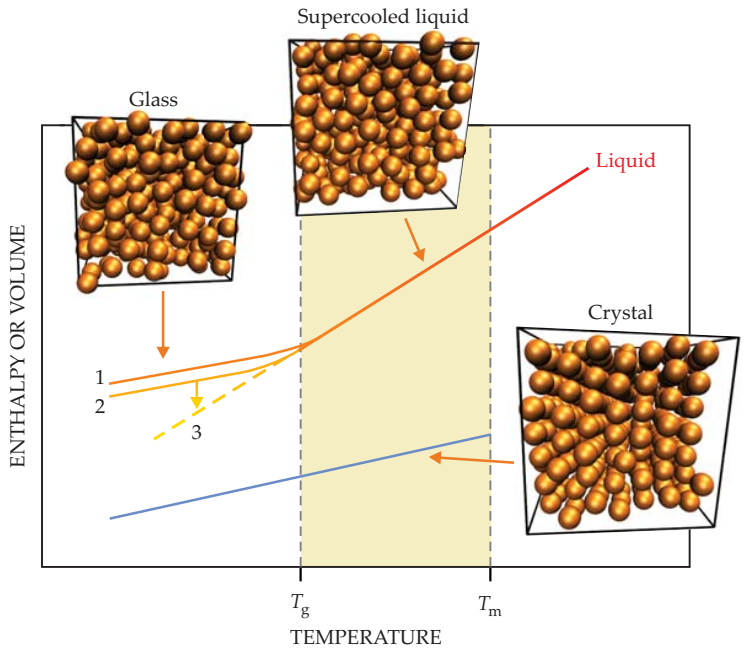


Figure 1.1 | **Schematic plot of the enthalpy, or volume, of a glass-forming liquid as a function of temperature.** Glass-forming liquids are robust against crystallization and remain disordered below the melting temperature $T_m$, in a supercooled region (shaded). The liquid becomes increasingly viscous upon cooling, and eventually falls out of equilibrium at $T_g$, defining the experimental glass transition. Glasses do not follow the equilibrium equation of state (line 1). Denser glasses are created by slower cooling protocols (glass 2), or isothermal aging (downward arrow). Particle configurations from computer simulations are shown for a supercooled liquid, a glass and a crystal. Reprinted from [6].

### 1.1.2 Stylized facts on supercooled liquids

The experimental glass transition observed at $T_g$ is not the phenomenon theoreticians are most interested in. Its definition is anthropocentric, and appears different from usual critical phenomena. The existence of universal features associated to glass formation is of theoretical interest [1]. It opens up the possibility of a unified theoretical description of glass formation. This universality contrasts with the microscopic diversity of materials considered. We describe two universal features of equilibrium liquids approaching the glass transition.

**Dynamical slowdown** – A dramatic dynamical slowdown is observed as supercooled liquids are cooled towards $T_g$ [8]. The growth of the microscopic relaxation time $t_r$ can be tracked experimentally by measuring macroscopic transport coefficients, such as the viscosity $\eta$. Both are linked by Maxwell's relation $\eta = G_\infty t_r$, where $G_\infty$ is the infinite-frequency shear modulus (whose temperature dependence is weak) [21]. The temperature dependence of the viscosity of several liquids is presented in Fig. 1.2. The representation of the data in terms of $\log(\eta)$ versus $T_g/T$ allows to appreciate the complexity of the relaxation processes in the liquid. For simple relaxation processes controlled by the thermally-activated crossing of energy barriers $\Delta$, the relaxation time obeys an

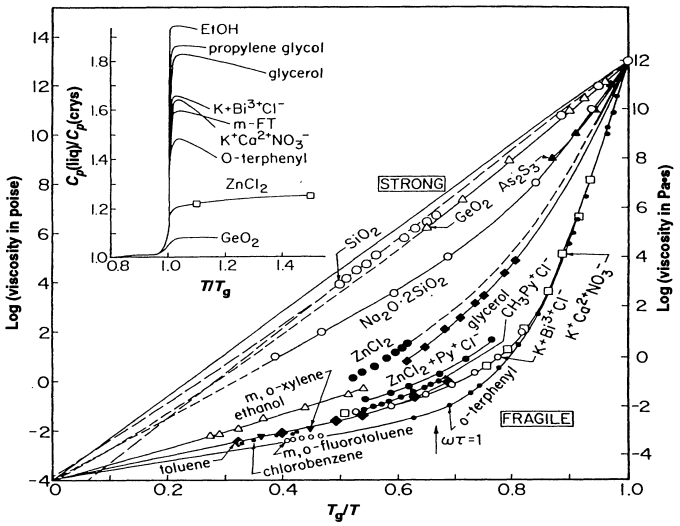


Figure 1.2 | **Rapid increase in the viscosity of various materials upon approaching the glass transition**, from Ref. [8]. Reducing the temperature by a factor of two results in an increase of more than 10 orders of magnitude in the viscosity. The temperature at which the viscosity reaches $10^{13}$ poise defines the experimental glass transition temperature $T_g$. For most materials, the increase in viscosity is super-Arrhenius, i.e. faster than exponential with temperature. The exact origin of this dramatic dynamical slowdown is still unclear.

Arrhenius law $t_r \propto \exp(\Delta/T)$. Simple processes correspond to straight lines in Fig. 1.2. This is the case for a few materials, such as silica and $GeO_2$, which have a strong tetrahedral order, labelled 'strong' glass-formers. Most materials are 'fragile': their viscosity increases in a super-Arrhenius way, suggesting instead $t_r \propto \exp(\Delta(T)/T)$, with $\Delta(T)$ an effective activation energy which increases upon cooling. This indicates that relaxations in supercooled liquids are increasingly collective as temperature decreases. The idea that a growing static lengthscale drives the glassy slowdown is explored in Sec. 1.4.1.

**Configurational entropy** – Liquids have a specific heat larger than crystals [23]. This implies that the liquid entropy $S_{liq}$ decreases faster than the crystal one $S_X$. This led Kauzmann to define an excess entropy for supercooled liquids $\Delta S = S_{liq} - S_X$ [22]. This quantity was interpreted as the (log of the) number of available states to the liquid. Kauzmann compiled the excess entropy of various glass-forming liquids, presented in Fig. 1.3. The excess entropy measured in equilibrium decreases sharply with temperature (full lines), until the liquid falls out of equilibrium (dashed lines), where a saturation of $\Delta S$ is observed. A reasonable extrapolation of the equilibrium excess entropy below $T_g$ gives a vanishing $\Delta S$ at a finite temperature. In Kauzmann's words: "Certainly it is unthinkable that the entropy of the liquid can ever be very much less than that of the solid." To avoid this unthinkable situation, called an 'entropy crisis', Kauzmann suggested the possibility of a thermodynamic glass transition well below $T_g$, at a positive temperature, $T_K$, called Kauzmann temperature. Although he indicated that crystallization may prevent an entropy crisis, Kauzmann's intuition of a thermodynamic transition remains very influential.

While the decrease of the excess entropy with temperature is an indisputable fact, its interpre-

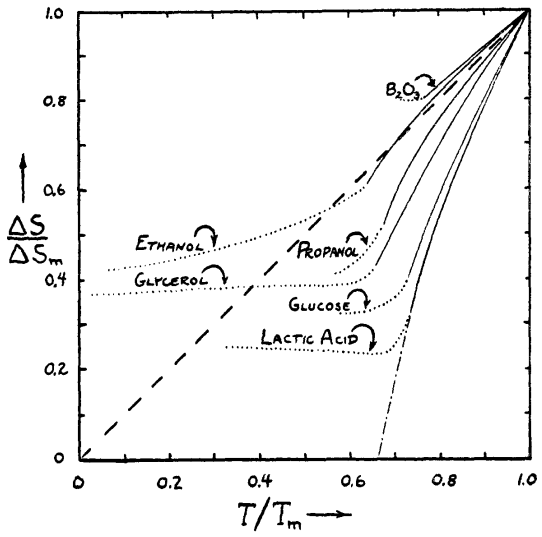


Figure 1.3 | **Kauzmann's insight of a finite-temperature thermodynamic transition.** Temperature dependence of the excess entropy $\Delta S = S_{liq} - S_X$ measured at equilibrium for various liquids (full lines). Both axis are normalized by their value at the melting temperature $T_m$. At low temperature, the data is measured out of equilibrium (dashed lines). Extrapolation of the liquid excess entropy (dashed-dotted line) suggests the existence of a thermodynamics transition at finite temperature. Reprint from [22].

tation is still debated, more than 70 years later. Two are two main theoretical positions. In one of them, thermodynamics plays no role in glass formation, and the decrease in $\Delta S$ is an irrelevant fact. The other position, explored in this work, interprets the dynamical slowdown as the consequence of an underlying thermodynamic transition.

The reason for which the glass problem remains unsolved lies in its nature. By definition, equilibrating liquids below $T_g$ is challenging. This makes it difficult to draw conclusive statements about the existence of an equilibrium thermodynamic transition below $T_g$. Getting closer to $T_K$ is an important research goal [24]. In the following, we describe two recent methods, one experimental (Sec. 1.1.5) and the other computational (Sec. 1.4.4), which succeed in getting closer to the Kauzmann transition.

### 1.1.3 Nonequilibrium dynamics in glassy systems

A liquid transforms into a glass when its slowest relaxation processes exceed the observation time. The dynamics of glasses takes place out of equilibrium. This does not imply that all dynamical processes are frozen below $T_g$, as they continue to take place on all timescales. Despite microscopic differences, many systems display similar 'glassy' dynamics: aging, hysteresis, rejuvenation and memory effects, violation of equilibrium properties, etc. [25, 26]. Contrary to equilibrium liquids, the properties of a glass depend on its complete history. In order to study the universality of nonequilibrium effects, one should clearly specify the protocol used.

**Aging** – A prototypical feature of glassy dynamics is aging [26–30]. The standard protocol consists in rapidly cooling an equilibrium liquid down to $T < T_g$. The age of the glass, also

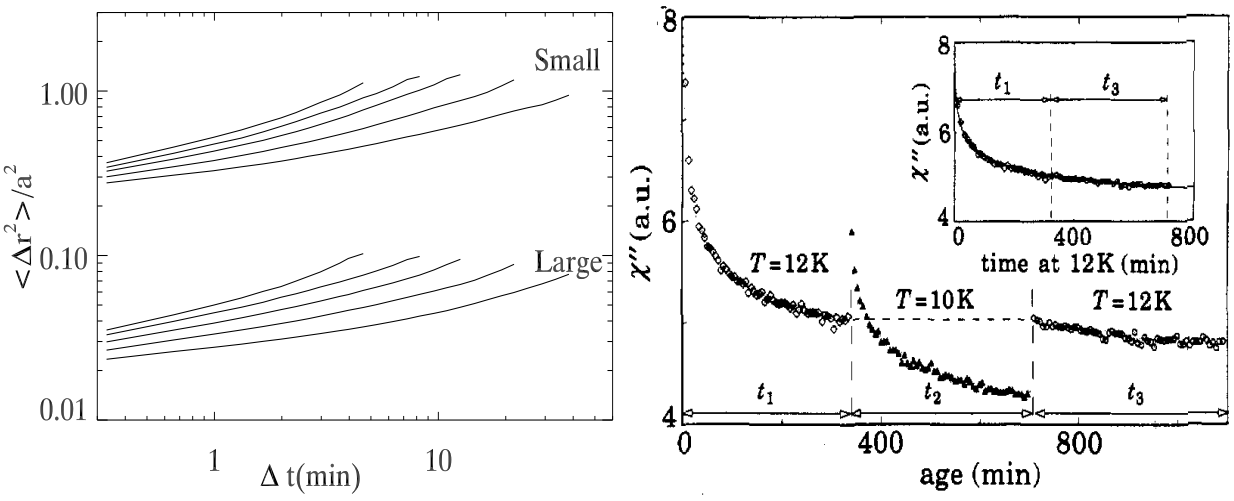


Figure 1.4 | **Nonequilibrium dynamics in glassy materials.** Left: Aging in the mean-squared displacement of large and small particles in a binary colloidal glass [34]. The age of the glass increases from top to bottom. Right: Aging, rejuvenation, and memory effects in the dynamic susceptibility of a disordered magnet subjected to a temperature cycle, from Ref. [35].

called waiting time $t_{\rm w}$, starts at the time of the quench. Glasses are said to age because their dynamics slows down with $t_{\rm w}$. A consequence of aging dynamics is that the relaxation time of a glass $t_r$ increases with $t_{\rm w}$. In a remarkable number of experiments, one finds that $t_r \propto t_{\rm w}$ [31–33]. This 'simple aging' behavior indicates that the age of the system $t_{\rm w}$ is the only relevant timescale in the system. Experimental results suggest that the relation $t_r \propto t_{\rm w}^{\mu}$ describes the data more accurately [31]. The cases $\mu > 1$ and $\mu < 1$ have been termed superaging and subaging, respectively. This point was discussed extensively in the spin glass literature [29].

The properties of glassy systems, which evolve out of equilibrium, depend explicitly on the time at which they are measured. The violation of time-translational invariance, evidenced by two-time quantities, allows to detect and quantify aging effects. Two-time observables $C(t, t_{\rm w})$ compare the state of the system at time $t_{\rm w}$ and $t_{\rm w} + t$, where $t$ the observation time ($t < t_{\rm w}$). Aging studies in structural glasses follow the evolution of density-density correlations. In colloidal experiments, the mean-squared displacement of particles can be computed, as shown in Fig. 1.4 (left). The age $t_{\rm w}$ of the glass increases from top to bottom curves. The abscissa corresponds to the measurement time $t$ in the above definition. The evolution of the dynamics with $t_{\rm w}$ is the hallmark of aging. The relaxation of the glass can be decomposed into two relaxation time scales. A fast '$\beta$-relaxation', identical at all temperatures, and a longer '$\alpha$-relaxation' at which correlation functions drop to zero (usually defined as $C(\tau_\alpha, t_{\rm w}) = e^{-1}$). The $\alpha$-relaxation time depends on the age of the system and corresponds to the time $t_r$ introduced above: $t_\alpha \simeq t_r \simeq t_{\rm w}$. For structural glasses, the $\beta$-relaxation can be interpreted as the fast exploration by particles of the 'cage' formed by their neighbors. The breaking of the cage requires cooperative rearrangements, which happen over long times, resulting in a plateau in $C(t, t_{\rm w})$ at intermediate times $t$. The relaxation of the cage takes place on timescales of order $\tau_\alpha$, for which $C(t > \tau_\alpha, t_{\rm w}) \sim 0$.

At the theoretical level, aging in glasses is a consequence of disorder in the system. Glasses are disordered, and thus characterized by a huge number of possible arrangements. This complexity is

captured by the concept of a rough free energy landscape [26, 36]. The roughness of the free energy landscape leads to slow relaxations, and eventually aging effects.

**Rejuvenation and memory** – More elaborate protocols were designed to investigate the nonequilibrium dynamics of glassy systems. Adequate thermo-mechanical histories can reveal unexpected effects, such as memory and rejuvenation effects (see [37] for a review). A glass 'rejuvenates' if it has aged for a long time at temperature $T_1$, and restarts to age as a young glass when cooled to $T_2 < T_1$. These effects were first evidenced in spin glass materials, see Fig. 1.4 (right) [29, 35, 38–42]. Such complex protocols were employed to probe the free energy landscape of a glass: how many minima there are, how they are organized, and by which type of barriers they are separated. Temperature cycles have been used in the past to classify and compare the behaviour of distinct classes of disordered materials. In particular, they reveal rejuvenation and memory effects in spin glasses. When similar protocols are applied to molecular glasses, such as glycerol, no rejuvenation is observed [43], although some memory can be found [44–46]. Both effects were however reported in gelatin gels [47].

In Chapter 3, we are able to identify in which physical conditions structural glasses are characterized by a complex landscape which should give rise to complex aging effects. We are successful in numerically observing memory and rejuvenation effects in a simple structural glass, for the first time.

### 1.1.4 Low-temperature anomalies of glasses

Experiments conducted on a wide variety of atomic and molecular materials reveal that glasses share a number of low-temperature 'anomalies' with respect to crystals. Again, the universality of these anomalies suggests that their origin lies in the disordered nature of glasses, and that microscopic details of materials may be irrelevant. The excitations and defects in glasses are still mostly explained by phenomenological arguments. An important research goal is to find a universal explanation for these anomalies, starting from first-principles.

The first careful measurements of the thermal conductivity and specific heat of silica and germania-based glasses was performed by Zeller and Pohl in the early 1970s [48]. They compared their results with available data (polystyrene, glycerol, PMMA) and concluded that with no exception, the specific heat of glasses departs from Debye's prediction $c_P \propto T^3$ below 1 K, where they find an anomalous scaling $c_P \propto T$ [49]. A similar anomaly is observed in the thermal conductivity which behaves as $\kappa \propto T^2$, instead of $T^3$. The deviation from Debye's prediction is revealed in Fig. 1.5 (right): the ratio $c_P/T^3$ of the 'conventional' liquid-cooled glass (top curve) departs from a plateau around $T \lesssim 1$ K, and diverges roughly as $1/T^2$.

These results are puzzling, since sound waves (longitudinal and transversal) are known to exist in glasses. One would expect only long-wavelength phonons to contribute to the specific heat at low temperature. The disorder, present at small lengthscales, should not be relevant to these phonons, and Debye theory should hold in amorphous solids [49]. This conclusion is invalidated by experiments: the paradigm of solid state physics, small harmonic vibrations around a reference equilibrium structure, does not apply to glasses. If, in addition to phonons, there is an excess of quasi-particles active at $T \lesssim 1$ K, one can rationalize the above scalings.

Shortly after Zeller and Pohl's paper was published, a phenomenological 'tunneling two-level system' (TLS) model was proposed independently by Phillips [50] and by Anderson, Halperin, and Varma [51]. The model postulates that because of the disordered nature of the system, some

entities in the glass (an atom, or groups of atoms) can take two almost degenerate configurations. These TLS are assumed to be randomly distributed in the glass. At low temperature, these entities can tunnel quantum mechanically between the two configurations. Assuming a plausible form for the distribution of TLS parameters (classical energy asymmetry, quantum splitting), the model accounts for the linear behavior of the specific heat.

Let us assume that there is a quantized excess excitation with two states, and that the energy of the excited state is $E$. The partition function of this TLS is $Z = (1 + e^{-\beta E})$. Its heat capacity is given by

$$C_p^{TLS} = \frac{1}{k_B T^2} \frac{E^2 e^{-\beta E}}{(1 + e^{-\beta E})^2}. \tag{1.1}$$

Assuming that there are many independent TLS, distributed with a constant $P(0 \leq E \leq \infty) = n_0$, the heat capacity of the system is equal to

$$C_p = \frac{\pi^2}{6} n_0 k_B^2 T, \tag{1.2}$$

which yields the correct linear behavior of the specific heat.

The original model has been improved, but its spirit remains the same [52]. The TLS model is still a prominent theoretical explanation for the low-temperature anomalies of glasses. Its weakness is that most ingredients are introduced by hand. Even if some arguments are given for the choice of the TLS distribution, the situation is unsatisfactory. Although some independent support for the existence of TLS comes from single-molecule spectroscopy experiments [53], the structural origins of the TLS are unclear. Some believe that they are made by small groups of atoms that can locally tunnel between two distinct mechanically stable states [50, 51]. Others suggested that collective effects are extremely important in determining TLS properties [54].

Ideally, one would like to identify the tunneling entities in a real glass, measure their properties (distribution, parameters), and check the validity of the model. In Chapter 3, we search for TLS in stable computer glasses, and analyze their classical and quantum properties.

### 1.1.5 An alternative to liquid cooling: vapor-deposited glasses

The fact that different protocols may create glasses with different properties opens exciting scenarios. Materials with desired physical properties could be obtained following a specific protocol. However, the liquid-cooling procedure described in Sec. 1.1.1 does not offer much flexibility. The very steep increase of the viscosity (Fig. 1.2) confines the glass transition temperature $T_g$ to a relatively narrow interval. Since liquid-cooled glasses are all prepared in similar conditions, their physical properties cannot be significantly modified.

Recently, experimental molecular glasses were synthesized by vapor deposition. Vapor deposition has been used to prepare organic glasses for several decades [55, 56]. The method is also widely used in the industry. For example, the active layer in the OLED display of mobile phones are vapor-deposited organic semiconductors. It was realized only in the last 10 years that some deposition conditions produce glasses with remarkable properties [57].

The vapor deposition technique contrasts with the canonical liquid-cooling protocol. Glasses are 'grown' layer after layer by vapor depositing molecules onto a substrate. The key is to hold the substrate at a temperature below the experimental glass transition temperature of the bulk material, typically $0.8 - 0.85\ T_g$. At such temperatures, the molecules in the top few nanometers of the sample are considerably more mobile than in the bulk [57, 58]. Recent work on molecular

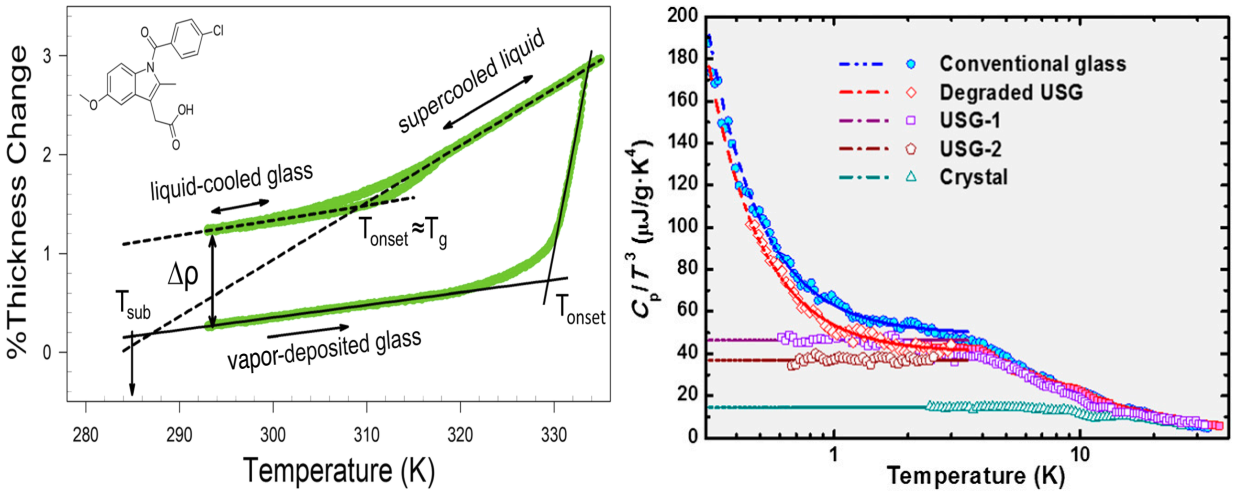


Figure 1.5 | **Enhanced kinetic stability and suppression of tunneling two-level systems in vapor-deposited glasses.** Left: Liquid indomethacin cooled at 1 K/min transforms into a glass at $T_g \simeq 310$ K (top curve, downwards). Heated at the same rate, the glass melts at $T_{onset} \simeq T_g$ (top curve, upwards). A glass vapor-deposited at 285 K, 0.2 nm/s is more kinetically stable: heated at the same rate than the liquid, it melts at a much higher temperature (bottom curve, upwards). Reprint from [67], original data from Ref. [68]. Right: the specific heat $C_p$ of conventional glasses departs from Debye's prediction $C_p \propto T^3$ below 1 K. The anomaly is not observed in vapor-deposited ultrastable glasses (USG). Reprint from Ref. [69].

glass formers has shown that surface diffusion can be up to $10^8$ times faster than bulk diffusion at $T_g$ [59–62]. At sufficiently low deposition rate, the molecules can sample many configurations before getting buried and immobilized by the next layers. This surface equilibration mechanism has been supported by computer simulations [63–65]. Each layer can almost reach thermalization at the substrate temperature, *i.e.* significantly below $T_g$. Vapor-deposited glasses synthesized within a few hours are more stable than 20-million-year-old glasses [66].

Vapor-deposited glasses bring new exciting challenges to glassy physics [67]. Below, we describe three of them which are related to our theoretical work.

**Dense and kinetically stable glasses** – For a given molecule, vapor-deposited glasses are denser than any liquid-cooled glass [68], as shown in Fig. 1.5 (left). While only few scientists master vapor-deposition, many people have already played at Tetris. The idea is the same: the particles at the surface are more mobile and can find an optimal position. This process naturally produces glasses denser than liquid cooling, in which rearrangements are costly, cooperative motion of particles.

In addition, vapor-deposited glasses exhibit greatly enhanced kinetic stability: they remain solid up to temperatures much higher than $T_g$, as shown in Fig. 1.5 (left). More precisely, the kinetic stability of a glass is defined by $\mathcal{S}(T) = t_{melt}(T)/\tau_\alpha(T)$, where $t_{melt}(T)$ is the time for the glass to melt after its sudden heating to temperature $T$, and $\tau_\alpha(T)$ the relaxation time of the equilibrium liquid at $T$. The values given below correspond to $\mathcal{S} = \max_T \mathcal{S}(T)$. Standard experimental glasses have a stability ratio $\mathcal{S} \lesssim 10^2$ [70], while values of $\mathcal{S} \sim 10^4 - 10^6$ are typically

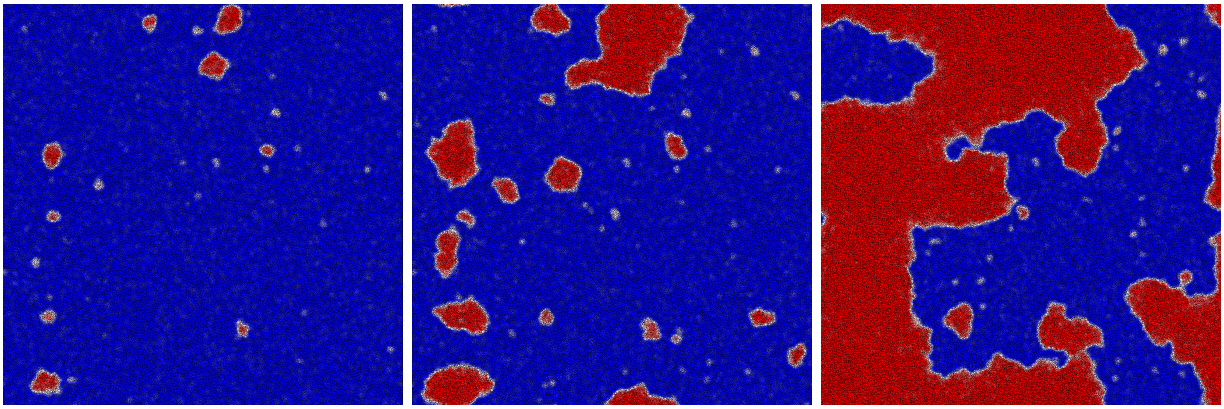

Figure 1.6 | **Bulk melting of ultrastable computer glass.** A two-dimensional *in silico* glass sample is synthesized in equilibrium conditions at 0.4 $T_g$ using the particle-swap algorithm (see Chapter 4). We study the dynamics of the sample after a constant-pressure heating into the liquid, around the Mode-Coupling temperature. During the melting process, we compare the neighbors of each particles between time $t = 0$ (initial sample) and $t$. For each particle, we compute the fraction of unchanged neighbors, and color it accordingly, from fraction equal to 1 (blue) to 0 (red). The red regions correspond to the liquid: the local structure has changed, and is much more mobile. Melting proceeds by nucleation of liquid bubbles (red) in the glass sample (blue), which grow over time and gradually transform the sample into a liquid. Left to right: $t = 4.10^5, 7.10^5, 10^6$ after the temperature jump.

measured in ultrastable glasses [71, 72]. Computer stable glasses prepared with the swap algorithm have an equivalent stability ratio $\mathcal{S} \simeq 10^5$ [73].

The melting mechanism of ultrastable glasses is of current interest [74, 75]. The melting of ultrastable films is mediated by a constant-velocity front initiated at the free surface. Such a melting process is reminiscent of crystal melting [76]. This analogy is difficult to rationalize theoretically because glass and liquid are not distinct thermodynamic phases [77, 78]. The heterogeneous melting of stable glasses is being studied by several experimental groups. I am currently performing a similar study on stable computer glasses. Preliminary results confirm the nucleation-and-growth melting mechanism of stable glasses proposed by Jack and Berthier [78]. We show in Fig. 1.6 a snapshot of a stable glass during melting. The particles in blue are in the dynamically arrested phase (glass), while the red particles are mobile (liquid). The liquid domains are much larger than observed in the melting of stable, randomly pinned, computer glasses [79]. In Fig. 1.6, the typical size $l$ of a liquid droplet is comparable with the linear system size $L \simeq 20$ nm. An accurate measurement of the average domain size requires the use of even larger samples. My work also aims at characterizing the speed at which the liquid droplets invade the glass, as a function of the glass preparation, and melting temperature. I am also investigating several aspects of the nucleation-and-growth picture. In particular, if we create a liquid droplet of radius $R$ inside the glass, do we find a critical radius $R_c$ above which melting proceeds?

**Suppression of TLS** – The results reported by Pérez-Castañeda and collaborators call into question the 'universality' of glassy anomalies at $T \sim 1$K [69, 80]. In Fig. 1.5 (right), the specific heat of vapor-deposited indomethacin is measured down to 0.6 K, and no deviation from Debye's

law is observed. Provided that TLS are the origin of the anomalous scaling, Fig. 1.5 suggests a suppression of TLS in ultrastable glasses, at least those active at $T > 0.6$ K. While the data does not exclude a $C_p \propto T$ scaling at $T < 0.6$ K, the behavior of ultrastable glasses contrasts with conventional glasses. The low-$T$ anomalies would not be a hallmark of amorphous materials, but rather specific to liquid-cooled glasses. Two arguments were put forward to explain the heat capacity of USG. Whether the observed depletion of TLS in vapor-deposited USG is due to the fact that they lie deep much deeper in the energy landscape than conventional liquid-cooled glasses [81], or to the anisotropy induced by vapor-deposition [68, 82, 83], is debated [84].

We bring new insight to this question by means of computer simulations. We perform a numerical search for TLS in glasses prepared with cooling rates which differ by 10 orders of magnitude, presented in Chapter 3. Using the same glass-forming model and protocols, we determined that the density of TLS depends dramatically on the cooling rate, and is therefore not an inherent property of disordered materials. This conclusion opens the way to the design and synthesis of new materials with low density of two-level systems, needed to meet new technological applications, in particular quantum computing [85].

**Revisiting the entropy crisis** – Getting closer to the equilibrium entropy crisis is an important research goal. By definition, liquid cooling will not get us there. Vapor-deposited glasses provide new insights into the entropy crisis. The excess entropy of vapor-deposited glasses can be estimated, and support the occurence of a finite-temperature entropy crisis [66]. Vapor-deposited glasses have the density expected from extrapolating the supercooled liquid data to lower temperature [86]. Vapor-deposited glasses bring experiments closer to the Kauzmann transition. A similar achievement in computer studies is presented in Chapter 5.

## 1.2 Glass and jamming transitions

### 1.2.1 The jamming transition of athermal systems

In the last decades, the study of glasses at low temperature has attracted significant interest, both from a theoretical and an experimental point of view [87–89]. This is motivated by the fact that a different solidity transition, the jamming transition, can be observed in a large class of systems: suspensions of large colloids, foams, emulsions, granular matter, and powders. These systems are 'athermal': the constituent particles are so large that the typical energy scales are orders of magnitude larger than $k_B T$. Contrary to the glass transition, thermal fluctuations play no role in the jamming transition, which is a purely geometrical transition [90, 91].

**A $T = 0$ geometric transition** – The basic jamming scenario takes place in models of frictionless spheres interacting via finite-range repulsive forces. Temperature plays no role: one considers $T = 0$. Suppose that a low-density assembly of particles is gradually compressed. At low density, the particles do not interact and the system is not mechanically stable. The jamming transition is defined as the density at which a mechanically stable network of particle contacts emerges [87, 92]. If the interaction between particles is 'hard' (they cannot overlap), the pressure of the packing diverges at jamming, and the system cannot be compressed further. This is the case for large PMMA colloidal particles, metallic beads or disks. If particles are 'soft' (they can deform), the solid can be compressed beyond the jamming transition. The network of contact forces sustains the

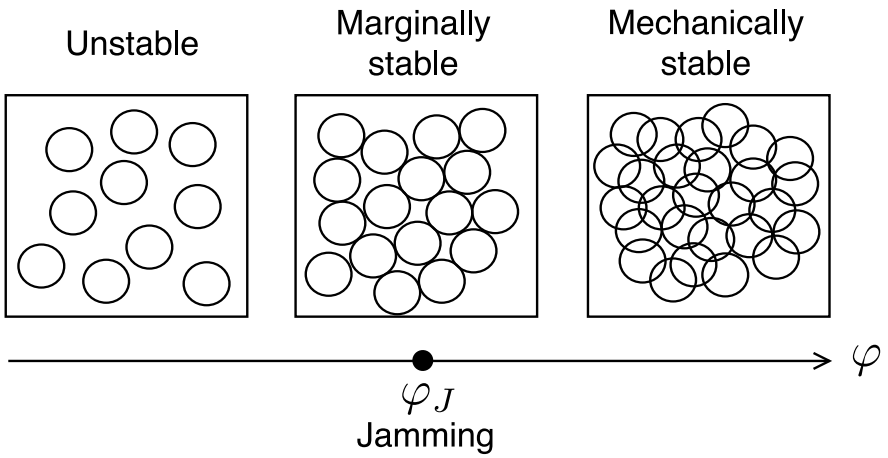


Figure 1.7 | **The jamming transition of soft frictionless spheres.** At low packing fraction $\varphi$, the system is mechanically unstable, and describes non-Brownian suspensions. Jamming takes place at $\varphi_J$, where a mechanically stable force network emerges. Frictionless granular solids sit at the jamming transition. At densities above jamming, the particles overlap and the system is jammed. The region $\varphi > \varphi_J$ describes foams and emulsions of large droplets.

rigidity of the system. Foams and emulsions are examples of 'soft' solids. This basic phenomenology is illustrated in Fig. 1.7.

**Models and protocols for jamming** – Numerical and theoretical studies of jamming led to the development of canonical models, soft frictionless repulsive spheres, as well as protocols to create jammed packings. The interaction potential between two particles $i$ and $j$ is given by

$$V(r_{ij}) = \frac{\epsilon}{\alpha}\left(1 - \frac{r_{ij}}{\sigma_{ij}}\right)^{\alpha} \Theta\left(1 - \frac{r_{ij}}{\sigma_{ij}}\right), \tag{1.3}$$

where $r_{ij}$ is the distance between the centers of the two particles, $\sigma_{ij}$ the average of both diameters, and $\epsilon$ the typical interaction energy. The particles do not interact if they do not overlap, hence the $\Theta$ Heaviside step function in Eq. 1.3. The exponent $\alpha$ can be varied to tune the softness of the interaction repulsion. Values of $\alpha = 5/2$ (Hertzian model) and $\alpha = 2$ (Harmonic model) are mostly employed. The harmonic sphere model was first devised to study the jamming rheology of wet foams [93, 94]. Hard sphere interactions are modeled in the limit $\epsilon \to \infty$.

Numerical protocols have been developed to create jammed states. Note that these are nonequilibrium protocols. A popular algorithm consists in starting from a dilute system, and 'inflating' the particles at a fixed rate during a molecular dynamics run [95]. Alternatively, one may start by assigning random positions to $N$ particles in a box of volume $V$ (this is an equilibrium configuration at $T = \infty$, $\rho = N/V$). The algorithm proceeds as a succession of minimization and compression steps [92]. During a minimization step, the potential energy of the system is minimized using, for example, conjugate gradient [96]. The system is then slightly compressed, before being minimized again, and so on. At $\varphi_J$, the potential energy of the minimized packing becomes non-zero.

The jamming transition is determined by measuring the reduced pressure $Z = \beta P/\rho$ or potential energy $e$ of the system, where $\beta = 1/T$, $P$ is the pressure, and $\rho = N/V$ the number density.

As $\varphi$ approaches $\varphi_J$ from above, $e(\varphi) \propto (\varphi - \varphi_J)^\alpha$ [92]. Approaching jamming from below, $Z(\varphi) \propto (\varphi_J - \varphi)^{-1}$, where $\alpha$ is defined in Eq. 1.3 [97, 98].

The jamming transition can be located unambiguously within one realization of a protocol. It is now understood that various protocols may lead to different values $\varphi_J$ [99]. This is particularly striking when the algorithm described above is initialized with packings deeply thermalized in the fluid phase of polydisperse hard spheres. In this three-dimensional model, $\varphi_J$ can be varied from 0.655 to 0.71 [100].

**Jamming criticality** – While the location of the jamming transition is system and protocol-dependent, there are a number of universal features associated to jamming. The transition bears similarities with ordinary second-order phase transitions, for which the scaling theory of critical phenomena applies. The observables are expressed in terms of the distance to jamming, $\varphi - \varphi_J$. Contrary to glass criticality, which is elusive, jamming criticality is easily observed.

At $\varphi_J$, all frictionless packings are 'isostatic' [101, 102]: the average number of force-bearing contacts is $z_{\text{iso}} = 2d$, the minimal value to ensure mechanical stability [103]. The coordination number $z$ jumps discontinuously from 0 to $2d$ as $\varphi_J$ is approached from below, recalling a first-order phase transition. The excess contact number follows a scaling $z - z_{\text{iso}} \propto (\varphi - \varphi_J)^{\nu_z}$, where $\nu_z = 1/2$ [92, 104](for isostatic jamming) is independent of the interaction potential.

There are three non-trivial critical exponents related to the isostatic jamming transition. The distribution of contact forces has a pseudo-gap, as it scales as $P(f) \propto f^\theta$ for $f \to 0^+$. The mechanic stability of packings at $\varphi_J$ is ensured by contacts carrying extremely small forces [105]. The distribution of gaps $h$ between particles at jamming scales as $g(h) \propto h^{-\gamma}$ as $h \to 0^+$ [97]. Finally, the plateau value of the mean-squared displacement $\Delta$, or Debye-Waller factor, vanishes as $\Delta \propto p^{-\kappa}$ when jamming is approached from below [106, 107].

The critical exponents $\theta, \gamma$, and $\kappa$ can be accurately measured numerically and experimentally. The exponent $\theta$ depends on the physical dimensions $d$, but numerical results indicate $\theta \in [0.41, 0.44]$ [108, 109]. The dimensional dependence is caused by the presence of rattlers, *i.e.* particles sustained by $d+1$ contacts, that can move in and out of the plane formed by these neighbors at almost no cost, creating an abundance of small forces. The critical exponent $\theta$ and $\gamma$ computed by removing rattling particles does not depend on $d$. The exponent $\kappa$ measured numerically does not vary with $d$ [97, 107, 108]. This suggests that the transition has universal properties, and that a theoretical derivation of the critical exponents is possible [108–110].

**Marginal stability and scaling relations** – The network of contact forces formed at $\varphi_J$ is the minimal to ensure mechanical stability [91]. The opening of one contact may destabilize the entire system. Jammed packings are marginally stable [111] (in a mechanical sense), and possess many soft vibrational modes [104]. Wyart and coworkers derived scaling relations for the exponents $\theta, \gamma$, and $\kappa$ by assuming marginal stability [105, 112, 113]. They considered that the system is close to a mechanical instability, and identified its elementary excitations. They selected low-lying excitations, perturbed the system along them, and looked for stabilisation mechanisms. The derived scaling relations are consistent with numerical results.

### 1.2.2 Glass and jamming phase diagram

Over the last few years, a remarkable unification of concepts has helped clarify the respective roles of geometry and thermal fluctuations in systems as diverse as molecular glasses, colloidal systems

and granular matter. The glass transition is responsible for the emergence of amorphous solids at finite temperature, whereas the jamming transition is responsible for the emergence of mechanical rigidity in athermal systems. The glass and jamming transitions are distinct phenomena, with different origins [114–116].

The physics of both transitions can be captured with models of thermal soft repulsive spheres, defined in Eq. 1.3. This strategy naturally follows Liu and Nagel's initial attempt to propose a unique phase diagram for amorphous solids, and to connect various rigidity transitions [87]. The two control parameters for the model are the packing fraction $\varphi$ and the ratio $T/\epsilon$ (noted $T$ for simplicity). Sufficiently dense packings of thermal soft spheres transform into glasses when cooled. In this model, there is a line separating the liquid at high temperature, from the glass at low temperature [106]. A numerical phase diagram for $3d$ harmonic spheres is given in Fig. 1.8 (left). Mode-Coupling Theory (MCT) [117] and Vogel-Fulcher-Tammann (VFT) fits to the equilibrium relaxation time $\tau_\alpha(T)$ provide an estimate for the 'glass transition' temperature of harmonic spheres (dashed lines). The MCT law underestimates the experimental glass transition temperature. It however gives an estimate of the computer glass transition: state points below $T_{MCT}$ cannot be equilibrated (open symbols) with standard algorithms. The zero-temperature jamming transition of random packings is indicated by a dashed arrow in the phase diagram.

The Weeks-Chandler-Andersen (WCA) model was employed in this context [118, 119]. It is a variant of the Lennard-Jones potential, cut at its minimum, and shifted:

$$V(r_{ij}) = 4\epsilon \left[ \left( \frac{\sigma_{ij}}{r_{ij}} \right)^{12} - \left( \frac{\sigma_{ij}}{r_{ij}} \right)^{6} \right] + \epsilon \quad \text{if } r_{ij} < 2^{1/6}\sigma_{ij}, \tag{1.4}$$

and $V(r_{ij}) = 0$ for $r_{ij} > 2^{1/6}\sigma_{ij}$. By construction, the potential is harmonic around the cutoff $r_{ij}/\sigma_{ij} = 2^{1/6}$: the harmonic model is recovered for intermediate densities. Hard sphere behavior is recovered in the limit $T/\epsilon = 0$, obtained for $\epsilon \to \infty$ at constant temperature. Contrary to the harmonic model which has a trivial large-density limit, the WCA potential models an atomic-like repulsion $1/r^{12}$ at large densities. A wide diversity of materials can be described by continuously varying the packing fraction of WCA glasses [119]. This approach is employed analytically and numerically in Chapters 2 and 3.

We presented glass formation and jamming transition through different protocols. However, a class of jammed packings can be identified with the infinite-pressure limit of thermal repulsive glasses [98, 106, 120]. In Fig. 1.8 (right), the equations of state for the reduced pressure $Z(\varphi)$ of hard spheres fluids and glasses are shown. Equilibrium fluids are rapidly compressed and depart from the equilibrium equation of state (full line). The pressure of the glasses increases sharply upon compression, and eventually form a jammed packing in the limit $Z \to \infty$. The identification of jammed packings as the infinite-pressure limit of glasses, opens up the possibility to build a common theoretical framework for glassy and jammed states [98, 121–123]. This program was achieved in the mean field theory of glasses introduced in Sec. 1.3.

### 1.2.3 Critical region of the jamming transition

An important theoretical effort was devoted to elucidate where glass and jamming physics are at play in the $T - \varphi$ phase diagram [124–126]. Numerical exploration of the region around the jamming transition $(\varphi_J, T = 0)$ was undertaken at finite temperature. Evidence was given for a

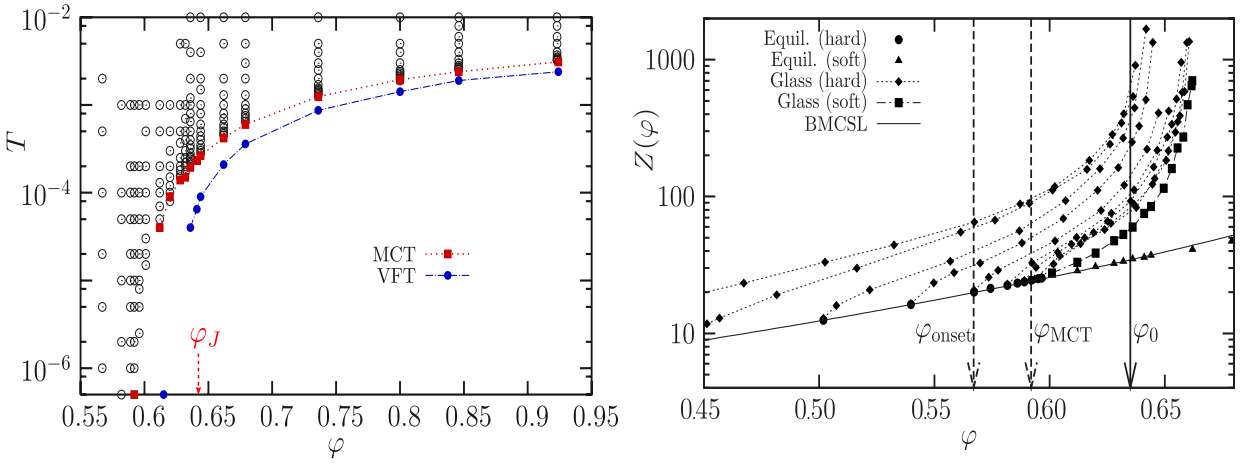


Figure 1.8 | **Glass and jamming transitions of hard and harmonic spheres** in $3d$, data from Ref. [106]. (Left) Harmonic spheres are studied in equilibrium (open symbols). Estimates for the glass transition obtained by fitting the relaxation time $\tau_\alpha(T)$ to known functional forms (dashed lines). The jamming transition occurs around $\varphi_J$ (dashed arrow, more in Fig. 1.9). Right: Reduced pressure $Z$ of fluids (solid line) and glasses (dashed lines). Rapidly compressed fluids transform into glasses, before jamming in the limit $Z \to \infty$. The jamming location $\varphi_J$ depends on glass preparation.

critical region in which critical signatures of the $T = 0$ transition are found [126]. More precisely, single particle dynamics reveal the divergence of a time and length scale as jamming is approached. The jamming critical region, shown in Fig. 1.9, is narrow in the $T - \varphi$ diagram and does not extent beyond $T \sim 10^{-7} - 10^{-6}$. This narrowness makes its experimental investigation intricate [127–129]. No experimental study was able to probe this region yet. In the vicinity of the critical point, the theory predicts three critical scalings, depending on the location with respect to jamming (colored regions) [126].

A comparison of the temperature and packing fraction scales of the phase diagrams in Fig.1.8 (left) and Fig.1.9 indicate that the critical region of jamming is found deep in the glassy phase, in a region much narrower than the glassy one. Jamming criticality is felt at temperatures lower than those in Fig. 1.8. Figure 1.9 shows that a third protocol can be used to reach jamming. Glasses of thermal soft repulsive spheres can be cooled down to $T = 0$, and gradually compressed or decompressed until a jamming transition is found. This corresponds to entering the critical region from above in the diagram Fig. 1.9. This protocol is employed in the numerical work of Chapter 3.

The phase diagram in Fig. 1.8 organizes the physics of a variety of materials by describing how fluids loose their ability to flow. It however suggests that the solid phase has similar properties across a broad range of physical conditions. We describe below recent analytical results revealing the existence of two distinct glassy phases, separated by a sharp 'Gardner' transition. Both phases should be located in the phase diagram Fig. 1.8 (left) in order to describe correctly amorphous solids. This theoretical and numerical effort is at the centre of this work. Theoretical predictions are presented in Chapter 2, and confronted with $3d$ numerical simulations of various glass formers in Chapter 3.

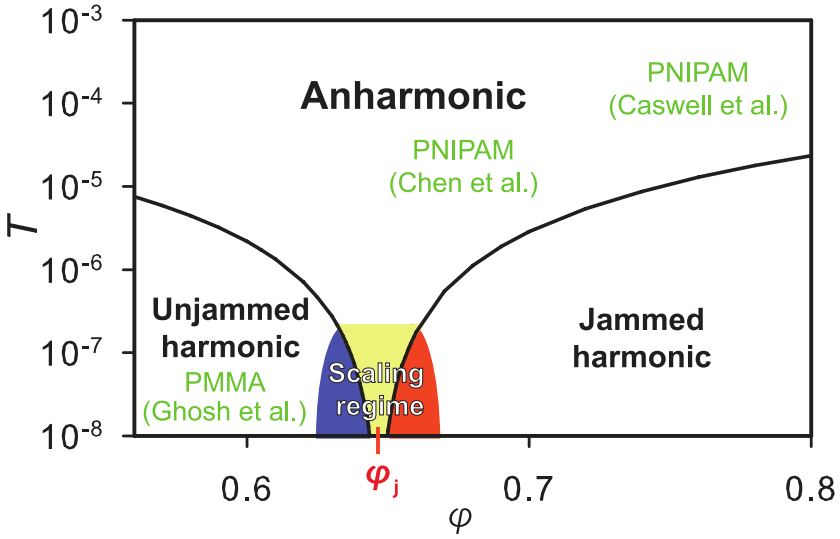


Figure 1.9 | **Dynamic criticality at the jamming transition**, from Ref. [126]. The criticality of the jamming transition ($T = 0$, $\varphi = \varphi_J$) survives a small amount of temperature and packing fraction variation (colored region), where power law divergences and 'anomalous' vibrational motion obey various scaling relations. No experimental study (green labels) has been able to detect the jamming dynamic criticality. Note the small range of parameters for which the effect of the $T = 0$ jamming critical point is felt, which can directly be compared with the temperature range of Fig. 1.8 (left).

## 1.3 Thermodynamics of liquids and glasses in large dimensions

Building a first-principles theory for glasses is both a tremendous challenge and a major research goal. Theoretically dealing with disordered, out-of-equilibrium systems requires the development of new tools and concepts which fall outside the scope of standard statistical mechanics.

Building a statistical mechanics framework of simple equilibrium liquids, which are also characterized by a high degree of structural disorder, already required a large theoretical effort. Starting from the 1950s, this effort lead to the development of a liquid-state theory [5]. It allows to compute the thermodynamic and structural quantities of liquids from the knowledge of the microscopic interactions [5]. Quantitative results are obtained using closure relations, such as Hypernetted Chain [130] or Percus-Yevick [131] closures, which neglect three-body correlations. The results are therefore approximate, but compare well with experiments and simulations [5, 132].

Contrary to standard condensed matter systems, glasses cannot be described using a perturbative treatment around a reference frame: there is no small parameter in the glass problem. The theoretical description of amorphous solids is more complex than crystalline solids, which are described by harmonic vibrations around an ideal periodic lattice [133]. Statistical physicists compensate the absence of a small parameter by studying the problem in a hypothetical space of dimension $d = \infty$. The problem simplifies in this limit, and an exact solution can be derived. Once the infinite-dimensional problem is solved, $1/d$ can be treated as a small parameter, with the hope of recovering the behavior of the physical system in $d = 2, 3$. The idea of using $1/d$ as a small parameter led to significant progress in the fields of strongly coupled electrons [134], atomic

physics [135], and gauge field theory [136].

In the 1980s, Frisch, Rivier and Wyler laid the foundation for a theory of liquids in large dimensions. They computed the free energy of $d \to \infty$ hard-sphere fluids in the high-temperature regime, from which they derived the fluid equation of state [137–142].

Shortly afterwards, Kirkpatrick and Wolynes suggested to extend the high-dimensional expansion to the low-temperature glassy regime [143]. They established a connection between hard sphere systems and a class of exactly solvable frustrated spin systems. They also pointed out that while disorder is put by hand (quenched) in spin models, it is self-generated in structural glasses. Replica methods needed to compute the free energy of systems without explicit disorder were only developed in the following decade [144–150].

It was realized recently that the theoretical tools needed to construct an exact theory of $d \to \infty$ liquids and glasses in all regimes were available. This observation triggered an important research effort, leading to the extensive analysis of the hard-sphere phase diagram in $d \to \infty$ [98, 121–123, 151, 152]. In this work, we contribute to this theoretical effort, explore and test its predictions.

### 1.3.1 Exact mean field theory

We are interested in the statistical mechanics treatment of a system made of $N$ monodisperse particles with short-ranged interactions, embedded in a space of $d$ dimensions, in the thermodynamic limit. A reasonable strategy to this statistical physics problem is to study its mean field formulation. This strategy was undertaken in virtually all domains in physics. In the dense regime, the particles have on average $2d$ neighbors. As $d \to \infty$, the force due to neighboring particles can be treated as a mean force, hence the mean-field nature of the limit.

The starting point of the treatment is a density-functional formulation of the problem. The virial expansion, a low-density expansion commonly used in liquid theory, allows to write a diagrammatic expansion of the partition function (entropy, or free energy) [5]. In the finite-dimensional case, the truncation of the virial expansion at any order is an approximation. In $d \to \infty$, the truncation of the virial expansion to second order is exact, up to densities relevant to describe the glassy phase [98].

The reason for this simplification is geometric: consider three particles A, B and C, with AB and BC interacting. The probability that A and C interact themselves is vanishingly small in large dimensions: all terms in the virial expansion above the second one can be neglected. The network of interactions is tree-like in the high-dimensional limit, as in mean field approximations [137, 140, 142].

### 1.3.2 Glasses as metastable states

The concept of metastable states is central to the theory of liquids and glasses in $d \to \infty$. The system is defined by a density profile $\rho(\mathbf{x}) = \sum_{i=1}^{N} \delta(\mathbf{x} - \mathbf{x}_i)$, where $\mathbf{x}_i$ is the $d$-dimensional vector position of particle $i$. The free energy of the system is a functional of the density profile $F[\rho(\mathbf{x})]$. The thermodynamic phases of the system can be identified with the minima of the free energy functional.

At each temperature, the stable thermodynamic state is the global minimum of $F[\rho(\mathbf{x})]$. At high temperature, it is the liquid state with uniform density $\rho(\mathbf{x}) = \rho$, and the crystal with a periodically modulated density profile at low temperature. In the limit $d \to \infty$, the two situations are clearly distinguishable: the crystal can be eliminated from the theoretical analysis by imposing uniformity of $\rho$.

The amorphous density profiles $\rho(\mathbf{x})$ may give rise to a complex free energy landscape, with an exponentially large number of minima. In the thermodynamic limit and $d \to \infty$, the free energy barriers between local minima are infinite, because the system is fully connected. The minima of the free energy have an infinite lifetime in the thermodynamic limit: they are relevant thermodynamic 'metastable states'.

The free energy of a state $\alpha$, sampled at equilibrium at $T = 1/\beta$ is obtained by summing over configurations $X$ belonging to this state

$$\mathrm{f}_\alpha(T) = -\frac{1}{\beta N} \log \int_{X \in \alpha} dX e^{-\beta U(X)}, \tag{1.5}$$

where $U(X)$ is the total potential energy of the configuration $X$.

### 1.3.3 The Random First Order Transition theory

The state of the system is encoded in the free energy functional $F[\rho(\mathbf{x})]$, which contains the information of all particles in the system, but is potentially highly complex. Instead, one can study a reduced free energy, which already contains interesting information. This approach, known as the potential method, was introduced by Franz and Parisi in the context of spin glass models, and later applied to mean field structural glasses [148].

In the mean field theory of glasses, the order parameter of the glass transition is the overlap (a measure of similarity), or equivalently the distance, between two equilibrium configurations. We consider a typical equilibrium configuration $Y$, selected with the Gibbs-Boltzmann distribution at temperature $T = 1/\beta$. The configuration selects one of the metastable states, noted $\alpha$, whose free energy is computed by averaging over the configurations $X$ that are close (in distance) to $Y$ [121–123, 151, 152]

$$\mathrm{f}(T, Y, \mathsf{D}_r) = -\frac{1}{\beta N} \log \int dX e^{-\beta U(X)} \delta[\mathsf{D}_r - \mathsf{D}(X, Y)], \tag{1.6}$$

where

$$\mathsf{D}(X, Y) = \frac{d}{N} \sum_{i=1}^{N} (\mathbf{x}_i - \mathbf{y}_i)^2. \tag{1.7}$$

This is the free energy of the state selected by an equilibrium amorphous configuration $Y$. Its explicit dependence on $Y$, which is a priori unknown, prevents its practical computation. It is an extensive quantity and should not fluctuate in the thermodynamic limit, unless some phase transition happens. The free energy is 'self-averaging' [153], its average over $Y$, distributed with the canonical distribution at $T = 1/\beta$, is representative of its typical value in the thermodynamic limit

$$V(\mathsf{D}_r) = \int \frac{\mathrm{d}Y}{Z[\beta]} e^{-\beta U(Y)} f(T, Y, \mathsf{D}_r), \tag{1.8}$$

where $Z[\beta]$ is the standard configurational integral at temperature $1/\beta$. The free energy cost of maintaining a configuration at an average distance $\mathsf{D}_r$ of a reference equilibrium configuration at $T$ is equal to $V(\mathsf{D}_r)$. It is also called the Franz-Parisi (FP) potential, and noted $V(\mathsf{D}_r)$, by analogy with spin glasses [148]. The FP potential $V(\mathsf{D}_r)$ is also a large deviation function for the order parameter $\mathsf{D}_r$.

Let us comment the form of Eqs. 1.6 and 1.8. The amorphous configuration $Y$ acts as an external disordered potential for $X$ in Eq. 1.6. The average over the disorder $Y$ is then taken

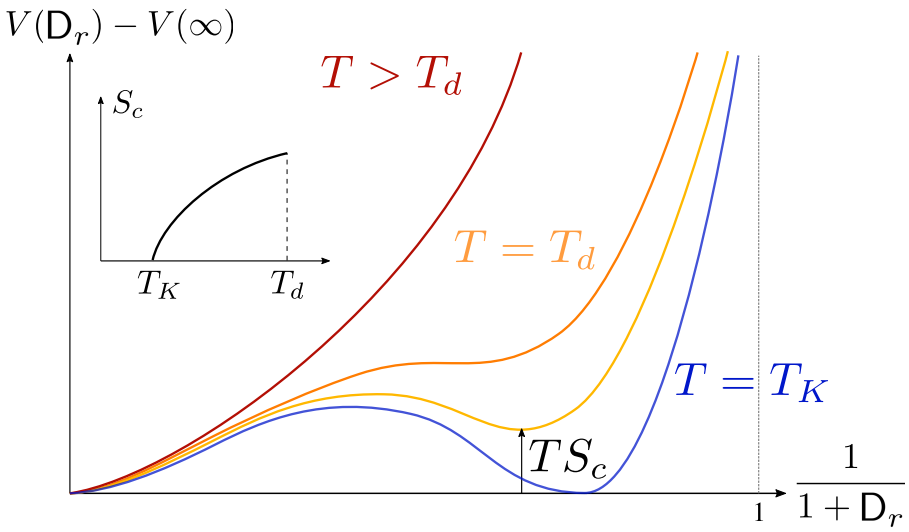


Figure 1.10 | **Sketch of the Franz-Parisi potential as a function of temperature.** At $T > T_d$, the potential has a unique minimum in $\mathsf{D}_r = \infty$, corresponding to the ergodic liquid. At $T_d$, a second minimum appears at a finite $\mathsf{D}_r$, signaling the apparition of exponentially many metastable glassy states, giving rise to an extensive configurational entropy $S_c$. The free energy cost of constraining two configurations in the same state, *i.e.* at a distance $\mathsf{D}_r$, is $TS_c$. A thermodynamic transition take place at $T_K$, where the order parameter $\mathsf{D}_r$ jumps discontinuously to a finite value, and $S_c \to 0$ continuously. Inset: Configurational entropy as a function of temperature.

in Eq. 1.8. The configuration $Y$ acts as a quenched disorder for $X$, which breaks translational invariance and prevents the use of standard statistical mechanics methods. The replica method was developed to compute $V(\mathsf{D}_r)$ [148]. This derivation is presented in Chapter 2.

The equilibrium value of $\mathsf{D}_r$ minimizes the free energy $V(\mathsf{D}_r)$ at temperature $T$. The knowledge of which minima of the free energy functional $F[\rho(\mathbf{x})]$ are relevant to the thermodynamics is reduced to the knowledge of the minima of $V(\mathsf{D}_r)$.

We describe the behavior of $V(\mathsf{D}_r)$ with $\mathsf{D}_r$ and temperature. Whatever the temperature, the probability that two equilibrium configurations are equal is zero: $V(\mathsf{D}_r = 0) = \infty$. In the limit $\mathsf{D}_r = \infty$, the free energy is that of the liquid. For convenience, we sketch the FP potential with respect to the liquid free energy $V(\mathsf{D}_r) - V(\infty)$ as a function of $1/(\mathsf{D}_r + 1) \in [0 : 1]$ in Fig. 1.10.

At high temperature, the Gibbs distribution is effectively uniform, and larger $\mathsf{D}_r$ consists in a larger region in configurational space: the FP potential increases monotonically with $1/(\mathsf{D}_r + 1)$, as shown in Fig. 1.10.

At the dynamical transition temperature $T_d$, a local minimum appears at finite $\mathsf{D}_r$ in the FP potential. The free energy difference $V(\mathsf{D}_r) - V(\infty)$ between constraining the system close to a glass state, and the liquid free energy has an entropic origin. Indeed, in equilibrium, the liquid and glass energies are equal. We can therefore define a configurational entropy $S_c = -\beta(V(\infty) - V(\mathsf{D}_r))$. Alternatively, one can write $s_{liq} = s_{glass} + S_c$. The entropy of a liquid is that of a typical glass, plus a contribution accounting for the many possible glasses, selected by distinct equilibrium liquid configurations. We conclude that below $T_d$, the partition function becomes dominated by an

exponentially large number $\mathcal{N}$ of metastable states, with

$$S_c = \lim_{N\to\infty} \frac{1}{N} \log \mathcal{N}. \tag{1.9}$$

The configurational entropy $S_c$ decreases with temperature, as shown in the inset of Fig. 1.10. At $T = T_K$, a thermodynamic transition takes place, the configurational entropy vanishes continuously, and the free energy of the liquid and glass become equal. In mean field, the entropy crisis envisioned by Kauzmann (Fig. 1.3) is exactly realized, hence the notation $T_K$.

The reduced free energy $V(\mathsf{D}_r)$ captures the nature of the glass transition in mean field theory. The theory goes under the name of Random First Order Transition (RFOT) theory, and predicts the existence of two temperatures $T_d$ and $T_K$ [154]. The first temperature $T_d$ corresponds to the appearance of exponentially many metastable glassy states, but the thermodynamic transition takes place at a lower temperature $T_K$. The shape of the Franz-Parisi potential in Fig. 1.10 illustrates the first-order character of this transition as the order parameter $\mathsf{D}_r$ jumps discontinuously at $T_K$. This transition is however second order in the usual thermodynamic sense, since there is no a latent heat associated to it. The mixed nature of the transition at $T_K$ is at the origin of the name 'random first order' transition.

### 1.3.4 Thermodynamics of glasses: state-following construction

The Franz-Parisi method allows to compute the free energy of an equilibrium liquid at temperature $T$. It gives important information on the nature of the equilibrium glass transition in mean field. Interestingly, the method can be extended to study the properties of glasses out of thermal equilibrium.

In order to motivate this statistical mechanics treatment, let us think about how the properties of a glass are measured in an experiment. One should first create a glass. Various protocols can be used, in order to shift the temperature $T_g$ at which the system falls out of equilibrium. This glass can then be subjected to an adiabatic perturbation, may it be a temperature change, compression, shear, etc. While the perturbation is applied, the glass is thermalized inside an amorphous structure selected at $T_g$.

The Franz-Parisi construction is therefore adapted to describe glasses in a statistical mechanics framework. The only modification to be done to the equilibrium construction is to consider that the configuration $X$ probing the amorphous state is thermalized at a temperature $T \neq T_g$. In this case, the computation is called 'state-following'. It was developed in the context of spin glass models [155–158].

The method was applied only recently to the simplest structural glass former, hard spheres, in $d \to \infty$ [121–123, 151, 152]. In Chapter 2, we study more realistic models and compute their phase diagram. The phase diagram depends in general on two control parameters, temperature $T$ and packing fraction $\varphi$.

The free energy $\mathrm{f}_g$ of a glass prepared at temperature $(\varphi_g, T_g)$, and adiabatically brought to $(T, \varphi)$ can be written as

$$\mathrm{f}_g(\varphi, T|\varphi_g, T_g, \mathsf{D}_r) = -\frac{T}{N} \int \frac{\mathrm{d}Y}{Z\left[\varphi_g, \beta_g\right]} e^{-\beta_g V[Y]} \log Z\left[\varphi, \beta | Y, \mathsf{D}_r\right], \tag{1.10}$$

where $Z\left[\varphi_g, \beta_g\right]$ is the standard configurational integral at $(\varphi_g, T_g)$. The free energy has to be computed for the parameter $\mathsf{D}_r$ verifying $\partial_{\mathsf{D}_r} \mathrm{f}_g = 0$.

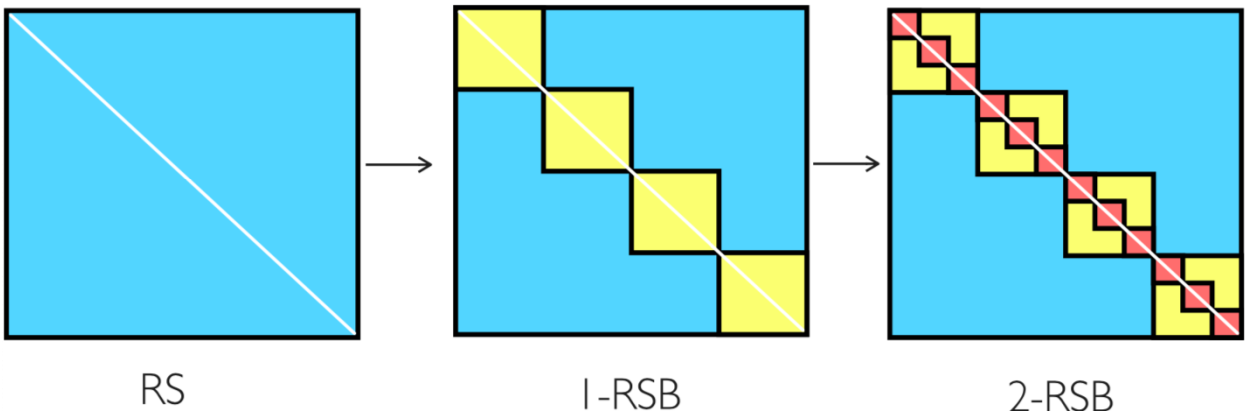


Figure 1.11 | **Schematic representation of the Parisi Replica Symmetry Breaking scheme,** in the matrix $\hat{\Delta}$ of mean square displacement between $n$ replicas. In the replica symmetric (RS) case, all replicas are at the same distance $\mathsf{D}_0$ (left). At a 1-RSB transition, the $n$ replicas are divided into $n/m$ groups of $m$ replicas. Two replicas in the same group are at a distance $\mathsf{D}_1$, and $\mathsf{D}_0$ if they belong to different groups (center). This step can be reproduced to obtain a 2-RSB solution (right). In the full RSB phase, $k \to \infty$, the number of symmetry breaking goes to infinity. From [159].

The replica method used to compute explicitly the glass free energy Eq. 1.10 is based on the mathematical identity [150]

$$\log[Z] = \lim_{s \to 0} Z^s. \tag{1.11}$$

The initial atomic liquid made of $N$ particles, is replicated $s$ times. One ends up with a 'molecular liquid', in which each of the $N$ molecules is made of $s+1$ atoms. The computation of the glass free energy Eq. 1.10 is replaced by the computation of the free energy of a molecular liquid [98, 122, 123]. The derivation is presented in Sec. 2.1. The replica method allows to rewrite the original problem, with broken translational invariance, into the translationally-invariant problem of a molecular liquid. Once translational and rotational invariance are restored, standard statistical mechanics techniques can be employed.

Translational and rotational invariances imply that free energy of a molecular liquid is function of the mean-squared distance between atoms, $\mathsf{D}_{ab}$, defining a $s \times s$ MSD matrix $\hat{\mathsf{D}}$. Finding explicitly the matrix for which the replicated free energy is stationary is in general not possible. However, symmetries are very helpful to guess its form. The replicas of the liquid are introduced as a mathematical trick, and should a priori be equivalent. The replica symmetric (RS) ansatz for the matrix $\hat{\mathsf{D}}$ is $\mathsf{D}_{ab} = \mathsf{D}$ for all $a \neq b$ [153]. The RS assumption implies that a glass state is a restricted portion of phase space, in which typical configurations are at the same distance $\mathsf{D}$, *i.e.* the glass is a simple free energy basin. The glass free energy can be expressed explicitly in terms of $\mathsf{D}$. Its thermodynamic value is taken at $\mathsf{D}$ minimizing $\mathrm{f}_g$.

This structure for the glass, remains however an assumption. One should check a posteriori the stability of the ansatz, by computing the stability matrix of the free energy, and verifying that Gaussian fluctuations around the RS solution are stable. In $d \to \infty$ hard spheres, glasses are simple basins at small compression. At a certain point, however, the replica symmetric solution destabilizes, signaling the emergence of a complex structure for the glass basin.

### 1.3.5 A new amorphous phase of matter: the Gardner phase

**Replica symmetry breaking** – Replica symmetry can be broken in many ways. The simplest one can think of is a one-step replica symmetry breaking (1-RSB) [153, 159]. In this case, a glass state is no longer a simple basin. It becomes a 'metabasin', containing two sub-basins. The structure of the glass is then parametrized by two values $\mathsf{D}_0 < \mathsf{D}_1$: two typical configurations within the metabasin are at a distance $\mathsf{D}_0$ or $\mathsf{D}_1$, whether they belong to the same sub-basin or not. See Fig. 1.11 (center) for an illustration of a 1-RSB matrix $\hat{\mathsf{D}}$ (different colors represent different values).

One can iterate this construction by going to higher number $k$ of replica symmetry breaking steps, as pictured in Fig. 1.11. The glass metabasin is split into sub-basins, each containing other sub-basins, and so on. This hierarchy goes on up to the point where, at the end, one finds the individual metastable states, which correspond to dynamically connected groups of configurations in configurational space.

A generic $(k-1)$-RSB matrix is parametrized by a set of MSDs $\mathsf{D}_0, \mathsf{D}_1, ..., \mathsf{D}_k$, and a set of blocks $s_0 = s, s_1, s_2, ..., s_{k-1}, s_k = 1$. The knowledge of this set of parameters defines entirely a $k$-RSB matrix $\hat{\mathsf{D}}$. One can then define a piece-wise function $\mathsf{D}(x)$, with $1 < x < s$, such that $\mathsf{D}(x) = \mathsf{D}_k$ for $x \in ]s_{k-1}, s_k]$. This function basically describes the profile of the first row of the matrices $\hat{\mathsf{D}}$ presented in Fig. 1.11. While the limit $s \to 0$ of a $s \times s$ matrix $\hat{\mathsf{D}}$ makes little sense, its interpretation in terms of a piece-wise function $\mathsf{D}(x)$ defined on the domain $[0:1]$ is physical [160]. The infinite number of replica symmetry breakings (full RSB) is parameterized by a continuous function $\mathsf{D}(x)$ [153].

**Gardner phase in $d \to \infty$ hard spheres** – In hard spheres, replica symmetry is broken at a full RSB transition, where the glass metabasin splits into am ultrametric fractal structure of sub-basins [123]. The most important property of the full RSB individual states is that they are marginally stable [161]: the Hessian has an eigenvalue which is identically zero in this phase.

Full RSB transitions were already discussed in the context of spin glasses. Elizabeth Gardner first discovered (concomitantly with Gross and coworkers, who studied Potts models [162]) a full RSB transition in Ising spin glasses at low temperature [163]. The full RSB transition in hard spheres, discovered for the first time in the context of structural glasses, was called 'Gardner transition' in tribute to E. Gardner. The Gardner transition in $d \to \infty$ hard spheres is equivalent to the spin-glass transition found in the Sherrington-Kirkpatrick model, a mean field spin glass model [164]

We show in Fig. 1.12 the phase diagram of the equilibrium liquid (black line) and glasses (colored lines) of hard spheres in $d \to \infty$ [152]. Metastable states exist at densities larger than $\varphi_d$. Glasses are prepared in equilibrium conditions (on the liquid equation of state) at some $\varphi_g > \varphi_d$, and compressed or decompressed adiabatically. Below the Gardner transition $\varphi < \varphi_G$ (bullets), the glass is in a stable state. Above the Gardner transition $\varphi > \varphi_G$, the glass enters a new amorphous phase of matter. The solid fractures in a hierarchical collection of marginally stable states [107]. The Gardner transition happens deep in the glass phase, and its location depends on the glass preparation $\varphi_g$.

**Jamming criticality** – One of the successes of the infinite dimensional theory for hard spheres is to identify jammed packings with the endpoints of metastable glassy states at infinite pressure (see Fig. 1.12). This approach to the jamming transition, first reviewed in Ref. [98], allows the

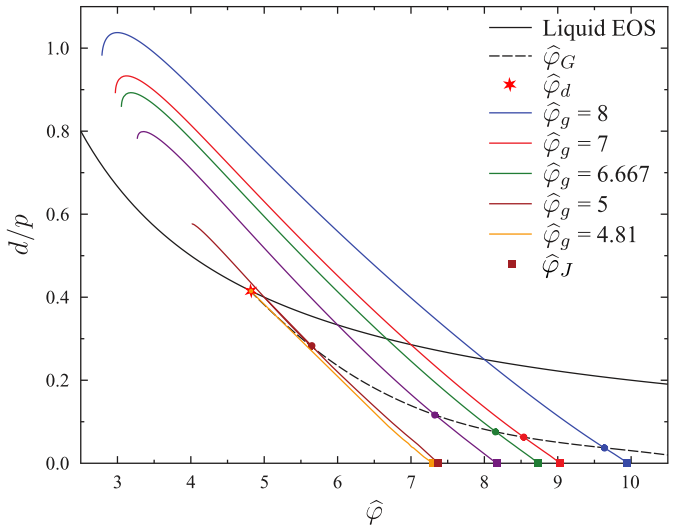


Figure 1.12 | **Phase diagram of infinite dimensional hard spheres: rescaled inverse pressure versus packing fraction.** The liquid equation of state $d/p = 1/\varphi$ is shown, along with the equation of state of glasses prepared at various $\varphi_g$ below the dynamical transition $\varphi_d$. Upon compression, the glasses transform from simple metastable states to hierarchical structures of marginal states at the Gardner transition $\varphi_G$ (bullets). The infinite pressure limit of glassy states correspond to jamming packing (squares). From [152].

treatment of jammed packings in a purely static way, and an exact computation of the critical exponent of jamming in $d \to \infty$. As seen in Fig. 1.12, jamming takes place inside the Gardner phase. Taking into account the marginality of the glass is crucial to predict correctly jamming criticality. It was shown that the marginality condition of the full RSB solution directly implies the isostaticity of jammed packings, which manifests as a critical mode [123]. This corroborates the picture of jamming as a critical phenomenon, anticipated in Sec. 1.2.1. More than this, the full RSB solution yields the correct critical exponents at jamming. While a replica symmetric predicts for example $\kappa = 1$, which is incoherent with the observations in $d = 2, 3$, the full RSB solution predicts $\kappa = 1.41574$, $\theta = 0.42311$ and $\gamma = 0.41269$, which are consistent with numerical and experimental observations. These exact results, obtained from first principles, represent one of the greatest accomplishment of the infinite dimensional theory for glasses. They prove the relevance of the infinite-$d$ Gardner phase to predict accurately the properties of glasses at high pressure, even down to $d = 2$.

**Consequences of a Gardner phase** – The hierarchical structure of the marginally stable glass has profound implications on its physical properties. In particular, the picture of the glass being a simple solid, with phonon-like vibrations of the particles around well-defined disordered positions, and density fluctuations with very fast relaxation timescale, breaks in the Gardner marginal phase.

Beyond the Gardner point, the hierarchical nature of the free energy landscape is expected to give rise to complex dynamical effects. The aging dynamics of spin glasses characterized by a complex landscape was explored theoretically and experimentally. It is extremely rich and as of now still not fully understood [26, 35, 36, 38–42]. Similar aging effects should be observed in the

Gardner phase of structural glasses. This aging phenomenology should be much more complicated than the standard aging presented in Sec. 1.1.3, commonly observed in structural glasses. The existence of a hierarchy of timescales implies that equilibration inside the glass metabasin becomes extremely slow (yet shorter than the relaxation time $\tau_\alpha$). In Chapter 3, we present results for the off-equilibrium dynamics of $3d$ marginally stable glasses. We find that it is similar to the aging phenomenology of spin glasses.

Solids are characterized by their elastic response to small strains. The elastic properties of glasses are affected by the Gardner phase, where theory predicts complex elastic responses, similarly to what is observed in spin glasses [153]. More specifically, elastic modulii are strongly dependent on the protocol used to measure them [165–167]: compressing a glass, then applying a strain is not equivalent to applying the strain before compression. Some non-linear elastic moduli are predicted to be divergent in the Gardner phase, implying that standard elasticity breaks down in this phase.

Marginally stable glasses are characterized by soft modes, and low-energy barriers separating the glassy minima [111]. This picture, obtained from first principles, seems to explain naturally the anomalies observed in amorphous solids. In this work, we explore the hypothesis that the Gardner phase provides a paradigm to explain the anomalies of amorphous solids. In particular, we focus on more realistic model glass formers, which interact with Lennard-Jones type pair potentials. In these models, the jamming transition plays no role. Their study is relevant to determine whether a Gardner phase is found at low temperature, in the absence of jamming. We present mean field results in the limit $d \to \infty$ in Chapter 2, and by computer simulations in $d = 3$ in Chapter 3.

## 1.4 Towards finite dimensions

The $d \to \infty$ theory of glasses brings the dynamical, time-based description of the glass transition down to a thermodynamic transition at a well-defined temperature, which is appealing to physicists. It correctly predicts the jamming critical exponents measured in $d = 2, 3$, which is quite a success. The theory predicts an entropy crisis at a finite temperature $T_K$, in agreement with Kauzmann's observations in Fig. 1.3.

Mean field theory, however, relies heavily on the concept of metastability. As a consequence, it does not capture finite-dimensional fluctuations and activation mechanisms. This is problematic since the glassy slowdown is dominated by activated relaxations at low temperature. One can wonder whether metastability in $d \to \infty$ is an artifact, or if some of its features remain in finite-$d$ glasses. To settle this question, one should analyze the effect of finite-$d$ fluctuations on the mean-field description. The renormalization group is a method of choice to treat fluctuations beyond mean-field theory [168]. The problem is that the spatial fluctuations relevant to the glassy phenomenology in finite dimensions are still unknown.

Without a proper renormalization scheme at hand, theoreticians have focused on a class of 'Kac' models in which the interaction range can be tuned [169–171], in order to continuously connect the mean-field limit with the finite-dimensional one. Scaling arguments were proposed to take into account activation within the mean field picture [3, 172–174].

### 1.4.1 Metastability and configurational entropy

The concept of long-lived metastable state does not make sense in finite dimensions. The interaction range between particles in a real glasses is short. As a consequence, free-energy barriers remain

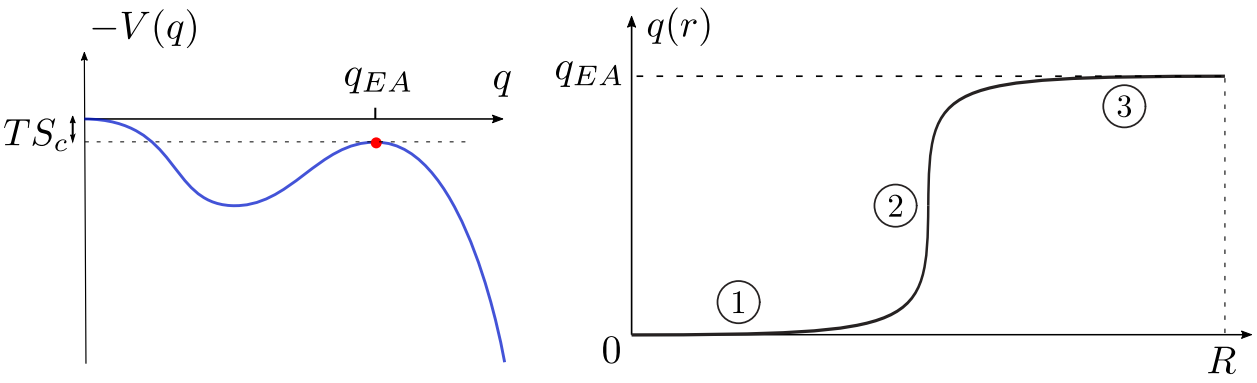


Figure 1.13 | **Overlap profile in a cavity of radius R.** (Left) Finding the overlap profile $q(r)$ is equivalent to solving Newton's equation for a $1d$ particle in the potential $-V(q)$, starting at $q = q_{EA}$ (red point). (Right) One possible trajectory goes from $q_{EA}$ to 0, with a sharp interface in between.

finite in the thermodynamic limit. We prove below that the mean field picture of an exponential number of states breaks down in finite dimensions.

**Nucleation destroys metastable states** – Let us assume that there exists an exponential number of metastable states. We pick a configuration which belongs to a metastable state, say $\alpha$, and follow its dynamics using a stochastic rule. Since $\alpha$ is a metastable state, there is at least one other state, $\beta$, with a lower free energy $f_\beta < f_\alpha$. The nucleation of a bubble of radius $R$ of the state $\beta$ in $\alpha$ can occur with finite probability. Its free energy cost is the sum of a free energy gain, and the cost of creating an interface ($\Upsilon$ is the surface tension): $\Delta F = -(f_\alpha - f_\beta)R^d + \Upsilon R^{d-1}$. If $R > \Upsilon/(f_\alpha - f_\beta)$, the state $\beta$ will invade the system. In the thermodynamic limit, $\alpha$ will disappear within a finite time: it is not a thermodynamic state. Metastable states are destroyed by finite-dimensional fluctuations.

The definition of metastable states is blurred in finite dimensions. So is the configurational entropy, which counts the number of 'states'. There can be no clear definition of the configurational entropy in finite dimensions. In Chapter 5, we review several definitions for the configurational entropy, along with numerical techniques to measure it, and discuss their relative merits [175].

**A lengthscale for amorphous order** – As a first step to go beyond mean field theory, let us consider a spatially-fluctuating order parameter [170]. The order parameter for the glass transition is the overlap $q(\mathbb{C}, \mathbb{C}_{eq})$ between an equilibrium configuration $\mathbb{C}$ and a reference one $\mathbb{C}_{eq}$. We consider an inhomogeneous order parameter, $q(\mathbb{C}, \mathbb{C}_{eq}, \vec{x})$. Where $\vec{x}$ denotes a point in $Nd$-dimensional space.

The partition function can be expressed in terms of the order parameter

$$Z = \int \mathcal{D}q(\vec{x}) e^{-\beta F[q(\vec{x})]}, \tag{1.12}$$

where the free energy functional is

$$F[q(\vec{x})] = -\frac{1}{\beta} \log \left\{ \sum_{\mathbb{C}} e^{-\beta H(\mathbb{C})} \delta \left[ q(\mathbb{C}, \mathbb{C}_{eq}, \vec{x}) - q(\vec{x}) \right] \right\}. \tag{1.13}$$

In mean field, $F[q(\vec{x})]$ is the Franz-Parisi potential $V(q)$ shown in Fig. 1.10 (its shape is similar by replacing $1/(1+\mathsf{D}_r)$ with $q$). As a first approximation, we assume that

$$F[q(\vec{x})] = \int \mathrm{d}^d x \left\{ \frac{c}{2} (\nabla q)^2 + V(q) \right\}. \tag{1.14}$$

While $V(q)$ is a priori different from position to position, we neglect these fluctuations. As a consequence, this construction will yield results with trivial mean-field exponents.

We force the configuration $\mathbb{C}$ to be equal to $\mathbb{C}_{eq}$ outside a spherical cavity of radius $R \gg 1$, and free inside the cavity [176]. We study whether $\mathbb{C}$ remains close to $\mathbb{C}_{eq}$ inside the cavity or not. The boundary condition imposed is $q(R) = q_{EA}$, where $q_{EA}$ is the value of the overlap in the secondary minimum of the FP potential. If there is long-range amorphous order, one should find $q(\vec{x}) = q_{EA}$ inside the cavity. The most probable profile $q(\vec{x})$ is found by minimizing $F[q(\vec{x})]$ in the presence of the boundary condition. Assuming spherical symmetry, $R \gg 1$, $r \gg 1$ (the computation is easier and remains general), the overlap profile in the radial direction $q(r)$ verifies

$$c\partial_r^2 q(r) = -V'(q). \tag{1.15}$$

This is the Newton equation for a $1d$ particle evolving in the inverted potential $-V(q)$, with $q \leftrightarrow x$, $r \leftrightarrow t$, $c \leftrightarrow m$. See Fig. 1.13 (left) for a schematic representation of the problem. The total energy of the system is conserved. Starting from the position $q = q_{EA}$, what is the 'dynamics' (or spatial dependence) of $q$? The solution depends on the initial kinetic energy $c/2\ \partial_r^2 q - V(q)$. There are two relevant 'trajectories'.

The first one is a constant profile $q(r) = q_{EA}$. In this case, $F_{const} = 4/3\pi R^3 V(q_{EA})$. The other solution consists in starting from $q_{EA}$ with kinetic energy $V(q_{EA}) = TS_c$, in order to reach the point $q = 0$ with zero kinetic energy. The solution for the profile $q(r)$ is shown in Fig. 1.13 (left). Its free energy is the sum of three parts. In region ①, $F_1 = 0$. The region ②, where $q$ varies from 0 to $q_{EA}$, adds a contributions $F_2 = \Upsilon 4\pi R^{d-1}$. This is an interfacial term. The interface tension $\Upsilon$ is a function of the function $V(q)$. In ③, $q(r) = q_{EA}$ and $F_3 = V(q_{EA})$. In the limit $T \sim T_K$, $V(q_{EA}) \sim 0$ and the free energy of the fluctuating profile reduces to $F_{fluct} = \Upsilon 4\pi R^{d-1}$.

Depending on the radius $R$ of the cavity, the overlap profile will be flat, equal to $q_{EA}$, or non-homogeneous. For large $R$, $q(r=0) = 0$: the amorphous boundary condition is not felt at the center of the cavity. For small $R$, the effect of amorphous boundary condition propagates to the center, where $q = q_{EA}$. The crossover defines the 'point-to-set' length

$$\xi_{PTS} \sim \frac{\Upsilon}{V(q_{EA})} \sim \frac{\Upsilon}{TS_c} \underset{T \to T_K}{\sim} \frac{\Upsilon}{T - T_K} \tag{1.16}$$

which quantifies the scale on which amorphous order propagates. $\xi_{PTS}$ can also be interpreted as the lengthscale on which metastable states can be defined The configurational entropy vanishes near $T_K$ as $S_c \sim (T - T_K)$. The amorphous lengthscale $\xi_{PTS}$ diverges at the thermodynamic glass transition $T_K$. The point-to-set length can be computed in numerical simulations [177–180], as described in Chapter 5.

In disordered systems, the interfacial free energy cost is written as $\Upsilon R^\theta$, where $\Upsilon$ is a generalized surface tension, and a non-trivial exponent $\theta \leq d-1$ is introduced to account for fluctuations of the interface [181]. Physically, the interface can take advantage of the weakest spots by moving in transverse directions. The relation between the point-to-set length and the configurational entropy becomes

$$\xi_{PTS} \sim \frac{1}{S_c^{1/(d-\theta)}} \tag{1.17}$$

There are several predictions for the value of $\theta$. Kirkpatrick and coworkers argue for the value $\theta = d/2$ [173]. The value $\theta = d - 1$, as obtained above, was put forward by Franz [170]. Note that in $d = 2$, both theoretical predictions give the same exponent $\theta = 1$. The difference between the two predictions increases with $d$. In Chapter 5 we present new numerical simulations aiming at the measurement of these non-trivial exponents in realistic model glass-formers.

**Connecting statics and dynamics** – A static description of glass formation should explain the dynamical slowdown of supercooled liquids approaching the glass transition. The point-to-set length provides an upper bound for the relaxation time $\tau_\alpha < e^{b\xi_{PTS}^d/T}$ (with b constant) [182, 183]. A diverging $\xi_{PTS}$ at $T_K$ also implies a diverging relaxation time.

At low temperature, the relaxation of the supercooled liquid is expected to be thermally activated $\tau \sim \tau_0 \exp[\Delta E/T]$ with an energy barrier growing with the point-to-set length $\Delta E \sim \Delta_0 \xi^\psi$, where we introduce a dynamical exponent $\psi \leq d$. $\tau_0$ is a microscopic timescale. By replacing the point-to-set length with configurational entropy Eq. 1.17 in the relaxation time, one finds

$$\log(\tau/\tau_0) \sim \frac{1}{TS_c^\alpha} \quad \text{, with} \quad \alpha = \frac{\psi}{d-\theta}. \tag{1.18}$$

The consequence of a mean-field like entropy crisis is a super-Arrhenius increase of the relaxation time, which diverges at the Kauzmann transition. Depending on the relative values of the two independent exponents $\psi$ and $\theta$, this expression may or may not be equivalent to the Adam-Gibbs relation ($\alpha = 1$), which was derived as a first attempt to connect the statics and dynamics of glasses [184]. The Adam-Gibbs relation has been tested in many experimental and numerical setups, and has been often synonymous with testing the thermodynamic nature of glass formation [175]. The generalized Adam Gibbs relation should also be confronted with experimental and numerical results. Measuring the non-trivial exponents $\theta$ and $\psi$ in numerical simulations of finite-dimensional glass formers is crucial to guide and test theoretical predictions beyond mean field [154]. In Chapter 5, we provide a critical numerical test of the standard and generalized Adam Gibbs relation, as well as estimates for $\psi$ and $\theta$.

### 1.4.2 The Gardner transition in finite dimensions

The mean-field Gardner transition is a critical phenomenon associated with the existence of soft, long-range excitations. A full understanding of its criticality in finite dimensions should be accessible from a renormalization group (RG) approach.

While the Gardner transition was discovered recently in $d \to \infty$ structural glasses, its mean field description is similar to the de Almeida-Thouless (dAT) transition for Ising spin-glasses in an external magnetic field [186]. This transition, discovered in 1978, marks the transition from a paramagnetic phase at high temperature to a full RSB phase at low temperature. The model is described by the Hamiltonian

$$H = \sum_{1 \leq i_1 < \ldots \leq N} J_{i_1,\ldots,i_p} S_{i_1} S_{i_2} \ldots S_{i_p} - h \sum_i S_i, \tag{1.19}$$

where the $S_i$ are Ising spins, and the $J_{i_1,\ldots,i_p}$ are independent random gaussian variables. Since both transitions display the same kind of order parameter and instability, they share the same field theory of critical fluctuations. When the Gardner transition was discovered in $d \to \infty$ hard spheres in 2013, the problem of its finite-$d$ features already benefited from forty years of research. Over the

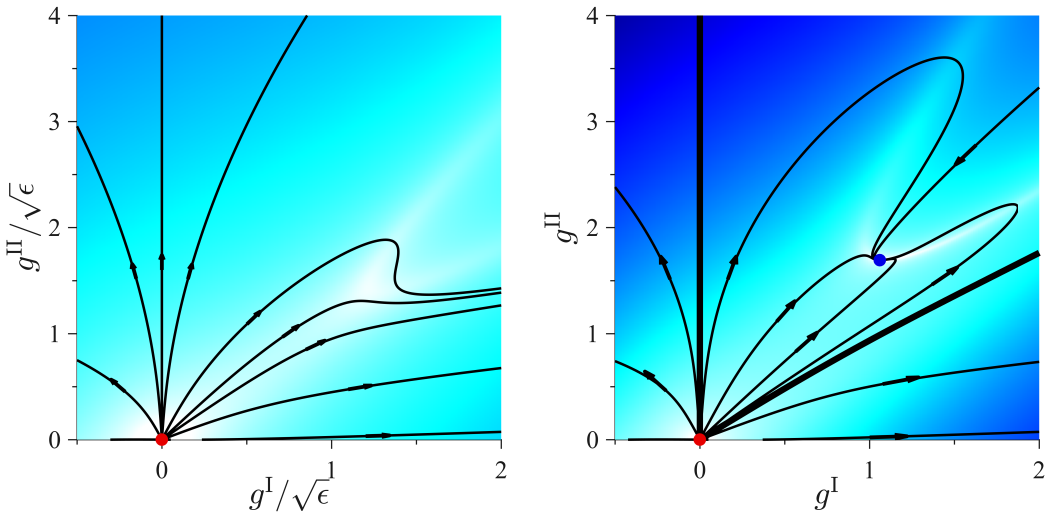


Figure 1.14 | **RG flow in the space of couplings for the dAT and Gardner universality class in** $d = 3$ for (a) a one-loop order RG expansion and (b) a two-loop expansion. The Gaussian FP (red point) is unstable in both cases. In the two-loop expansion, a stable non-perturbative FP (blue point) appears. Its basin of attraction is delimited by the two thick black lines. From [185].

last few years, the activity on the Gardner transition triggered several new RG approaches to the problem.

In their recent work, Moore and coworkers [187] confirmed and detailed the original result of Bray and Roberts, obtained in 1980 [188]. They explored the existence of a Gaussian fixed point (FP) associated with mean-field theory. They showed that its bassin of attraction shrinks to zero when the dimension approaches from above the upper critical dimension $d_u = 6$. For many decades, the conclusion was that a Gardner/dAT critical transition could not exist in $d < 6$. The possibility of a non-perturbative FP was not explored until recently. Several approaches were developed: non-perturbative renormalization group [185], high-order resummations [189], and real space RG [190–192]. They all predict that a non-perturbative FP can exist in relatively low $d < 6$.

Yet, the presence of a non-perturbative FP in finite dimensions does not ensure the existence of a critical transition in a given physical system. Its existence depends on whether the initial condition of the RG flow (encoded in the microscopic details of the system) lies within the basin of attraction of the FP. For example, in $d = 3$, the transition could be present for some glass-forming models, but not in others, as shown in Fig. 1.14 (right). Since no mapping exists between a microscopic model and the RG flow parameters, probing numerically the relationship between time and length scales in a model is a way to ascertain to which basin of attraction, or scenario, it belongs to [193]. This is the aim of Chapter 3.

The lower critical dimension of the transition, if present, is not known. One can elaborate on spin glasses without a field, for which a consensus $d_l \simeq 2.5$ was found [190]. Assuming that adding an external field weakens the transition, the lower critical dimension of the dAT/Gardner transition should be equal or higher than 2.5. This assumption is not fully motivated, but suggests that the transition may be observed in $3d$ structural glass-formers. In short, a Gardner transition could take place in three dimensions and be related to a non-perturbative FP. Further investigations using

more refined RG treatments, combined with new numerical simulations, are necessary to solve this long and intricate problem.

Our works are motivated by a recent study of $3d$ hard sphere glasses, in which growing time scales and lengthscales reminiscent of a Gardner transition were found [193]. This was a direct confirmation that the RG predictions were correct and that a transition could be found in three dimensional glasses. Employing relevant observables, first defined in Ref. [194], they detected extremely slow, cooperative and heterogeneous vibrational dynamics within the glass at high packing fraction.

The Gardner transition had been discussed only for the hard sphere model. It is a good model for colloidal or granular glasses, but its relevance to describe atomic or molecular glasses can be questioned. The works presented in Chapter 3 aim at a numerical exploration of the Gardner phase in several glass-forming models which describe amorphous solids at large: atomic and molecular glasses, soft colloidal glasses, emulsions, granular glasses. We are able to predict in which type of materials and physical conditions Gardner physics is relevant. In the last article of Chapter 3 'Rejuvenation and memory effects in a structural glass', we use this knowledge to explore the nonequilibrium dynamics of structural glasses, which is expected to take place in a 'hierarchical' landscape, and exhibit novel features. We are successful in observing rejuvenation and memory effects in a realistic model for structural glasses in $3d$.

Analyzing the nature of the Gardner 'transition' observed in finite dimensional numerical simulations is intricate. In particular, it is not known whether a critical transition takes place in $3d$ hard spheres. The same debate has been going on for several decades in the spin-glass community about the dAT transition. Here, we take a pragmatic view on this problem and explore whether new Gardner physics emerges in real glasses. We confirm in Chapter 3 that glasses exhibit a rich new phenomenology.

### 1.4.3 Numerical simulations of glass-forming models

Computer simulations can be defined as the entire process of choosing a model, computing observables, and analyzing the resulting data [132, 195]. They have become essential to the study of supercooled liquids and glasses [196, 197]. All 'ingredients' in a simulation are known. The influence of each parameter can be analyzed independently in order to identify the relevant ones. In the works presented below, we take advantage of the great flexibility offered by computer simulations to investigate the nature of supercooled liquids and glasses.

In the present context, a model is a set of $N$ classical particles with some properties (size, mass, or even shape), which interact via a pairwise interaction potential. The aim is to find the simplest model which reproduces qualitatively some experimental features. For example, computer studies of model glass-formers should reproduce the glassy slowdown in Fig. 1.2. Because glass formation shares universal features amongst a variety of materials, one can focus on the simplest numerical models, which are efficiently simulated and exhibit the desired phenomenology. They do not, for example, capture the complexity of molecular glass-formers. In the context of the Gardner transition, we study various simple models to understand in which conditions the transition is found.

**Numerical algorithms** – Once a model for the particles is set up, one should choose a dynamical rule to follow its evolution. Two important schemes are used in this context: molecular dynamics (MD) [132], and Monte Carlo (MC) simulations [195].

The physical dynamics of a system may be studied with MD simulations. They consist in solving numerically the equations of motion of the $N$ interacting particles. The differential equations are discretized in time and solved numerically step by step. Given an initial position and velocity, the trajectories of particles are computed. By construction, the trajectories take place in the $NVE$ ensemble. Additional fluctuating variables that mimic the effect of an external bath may be added to simulate the $NVT$ or $NPT$ ensembles [198]. During the preparation of a sample, before any measurement, cruder techniques such as velocity rescaling or a Berendsen thermostat may be used. They both rescale instantaneously and smoothly, respectively, the velocities to attain the desired kinetic temperature.

Another important scheme is the Monte Carlo method. It is a stochastic algorithm built to sample efficiently configurational space. The particles' trajectories are a priori not physical, but the configurations are sampled with a probability proportional to the Boltzmann distribution (canonical distribution). The evolution takes place in a series of 'trial move', and acceptance or rejection of it. In a standard move, a particle is chosen at random, and displaced in a random direction. The most common algorithm is the Metropolis MC, which uses the ratio of the Boltzmann weights of the old and new configurations to accept or reject the move [199]. In the limit of small displacements, the method is equivalent to Brownian dynamics. The method was however not developed to simulate physical trajectories for particles.

A number of usual tricks are employed to simulate the bulk behavior of a system. Computer simulations typically study system sizes $N \sim 1000 - 10000$, orders of magnitude smaller than in experiments. To remove strong boundary effects, periodic boundary conditions are systematically implemented. The system is an 'infinite', repetition of the original cell of size $L^d$. The counterpart is that lengthscales larger than $L$ cannot be probed [200]. The idea behind finite size scaling, is to use this 'limitation' as a way to extract values for critical exponents.

**Complex observables** – Experiments have always played a crucial role in understanding glass formation. However, there is a gap between the observables identified as relevant by mean field theories, and what can be technically achieved in experiments.

In mean field theory, the glass and Gardner transition are revealed by the similarity between equilibrium configurations for the former, and identical copies of a configuration, for the latter. This is obviously impossible in experiments, but can be realized with computers. The exact knowledge of the positions of the particles enables the computation of almost any observable [5]. Elaborate setups, such as the cavity construction presented in Sec. 1.4.1 can be implemented to measure the point-to-set lengthscale in realistic models [177–180].

In the mean field theory of glasses, we discussed their free energy landscape (FEL), which acquires an exponential number of minima at $T_d$, and may becomes fractal at a Gardner transition. It is not possible to 'measure' the FEL in simulations. Yet, one has access to the potential energy landscape (PEL) of a system [201]. It corresponds to the $3N$-dimensional potential energy surface, composed of many minima separated by energy barriers. Contrary to the FEL, the PEL does not depend on temperature. What is temperature dependent is the way the system explores it. In the PEL framework, an inherent structure (IS) is defined as the minimum of the basin of attraction of many equilibrium configurations. Starting from an equilibrium configuration, one minimizes its potential energy (*e.g.* using the conjugate gradient method), to find its inherent structure [96]. One can compute its potential energy $e_{IS}$, and its properties, for example vibrational modes. One can also study the barriers separating two nearby IS. Techniques such as the Nudged Elastic Band (NEB) provide the mean energy path between two minima, and give an estimate for the

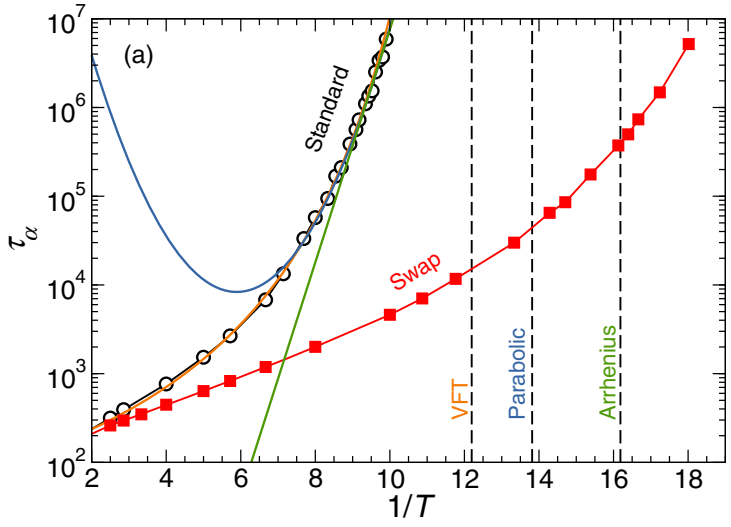


Figure 1.15 | **The swap algorithm breaks the glass ceiling.** Relaxation time of a continuously polydisperse model measured with the standard MC algorithm (open points), fitted to three common functions (lines). The experimental glass transition is defined from each fit as $\tau_\alpha/\tau_0 = 10^{12}$ (vertical dashed lines). The SWAP algorithm (squares) achieves thermalization at temperatures well below the extrapolated glass transition. From Ref. [204].

corresponding energy barrier [202]. This method will be employed in Chapter 3 to explore the complexity of the PEL of stable computer glasses.

**Dynamical arrest in simulations** – The two main numerical methods present advantages over experiments, presented above. They however suffer from a serious timescale limitation. In an experimental liquid, the onset of glassy dynamics (departure from Arrhenius behavior) occurs when $\tau_\alpha \sim 10^{-10}$ s, and the experimental glass transition is reached for $\tau_\alpha \sim 100$ s. Experiments can follow glassy slowdown at equilibrium over a time window of 12 orders of magnitude. By comparison, the numerical methods described above, run with the best hardware available (graphic cards or large-scale parallelization) can access around $4-5$ orders of magnitude of glassy slowdown [203]. This is more than seven orders of magnitude smaller than in experiments.

Computer supercooled liquids fall out of equilibrium at temperatures much higher than the experimental glass transition. Glasses created by standard annealing procedure are much less stable than their experimental counterparts (kinetic stability, but also mechanic stability). This is a serious limitation to model supercooled liquids approaching the glass transition, and the properties of glasses. Below, we describe a novel simulation method which allow to study supercooled liquids down to temperatures below the extrapolated experimental glass transition.

### 1.4.4 Computer supercooled liquids below the experimental glass transition

The search for algorithms that speed up the thermalization of supercooled liquids led to the development of new numerical schemes. Methods such as the Event-Chain Monte Carlo algorithm [205, 206] and Parallel Tempering [207] were introduced. Despite years of research, the best dynamical gain obtained with these techniques is at most a couple of orders of magnitude.

This is unsatisfactory considering that computer simulations lag seven orders of magnitude behind experiments.

The SWAP algorithm [208–210] was recently pushed to its maximal efficiency, allowing to generate supercooled liquids configurations below the experimental glass transition [204, 211]. The standard MC displacement moves are complemented with particle-swap moves, in which two particles are randomly selected and their sizes are exchanged. The moves are accepted or rejected following the Metropolis criterion, ensuring an equilibrium sampling of the canonical distribution [199]. The algorithm is designed to simulate poly-disperse systems (at least bidisperse), which englobe virtually all glass-forming models. The algorithm is so efficient at sampling configurational space that the crystal of bidisperse systems is found very easily [204, 212]. The development of this method required the design of new glass-forming models, more robust against crystallization. In this effort, non-additive continuously polydisperse systems were identified as very good glass-formers [204, 211].

The small difference between the standard and SWAP MC methods contrasts with their thermalization efficiency. In Fig. 1.15, we show the relaxation time of a continuously polydisperse system measured with standard and SWAP algorithms. While the standard method fails to reach equilibrium at temperatures below $T = 0.1$ (about two weeks of CPU time), the SWAP algorithm achieves thermalization down to $T \simeq 0.055$. This value lies below several estimates for the experimental glass transition $T_g \in [0.063 - 0.083]$, obtained by fitting the standard dynamics to known fitting functions and identifying the temperature at which $\tau_\alpha = 10^{15}$ (12 orders of magnitude of glassy slowdown).

The development of the SWAP algorithm, combined to the design of new computer models suddenly closed the gap with experimental studies. Temperatures even below the experimental glass transition are now numerically accessible in equilibrium conditions. The SWAP algorithm places computer simulations at the centre of supercooled liquid and glass studies.

Deeply equilibrated configurations are crucial to test correctly mean field predictions. The theory addresses supercooled liquids in the regime $T_K < T < T_d$. However, standard algorithms can access temperatures $T > T_d$ at equilibrium, where $T_d$ is a 'Mode Coupling' crossover temperature [117] ($T_d \simeq 0.1$ in Fig. 1.15). In particular, the concept of metastable state applies far better to supercooled liquids thermalized at $T < T_d$. At these temperatures, numerical estimates for the configurational entropy become more meaningful, as detailed in Chapter 5. The numerical detection of the Gardner transition, presented in Chapter 3, necessitates well-thermalized samples, in which diffusion is completely arrested. The SWAP algorithm allows to access the relevant temperature regime, and test accurately the theoretical predictions detailed in Sec. 1.3.

In Chapter 4, we explore an alternative to SWAP MC, in which particle-swap MC is combined with standard molecular dynamics [213]. This Hybrid algorithm is implemented in the LAMMPS simulation package. We optimize and compare the efficiency of the Hybrid method with the SWAP MC. The Hybrid algorithm is employed to generate most of the stable configurations used in the numerical studies presented below.

## 1.5 Structure of the manuscript

This work addresses the two main research directions in glassy physics. The first one aims at revealing the fundamental mechanism at the origin of the dynamical slowdown of supercooled liquids upon approaching the glass transition temperature $T_g$. The other research direction aims at understanding the physical properties of glasses from their formation around $T_g$ down to cryogenic temperatures, around 1 Kelvin. Compared to the first direction, the second one is much less developed theoretically and is known for its multitude of phenomenological approaches. This unsatisfactory situation is due to the fact that describing out-of-equilibrium and disordered solids is a theoretical challenge.

The works presented in Chapters 2 to 6 addresses both research directions, covering the entire temperature range, from the glass transition to very low temperatures. The manuscript is organized as follows:

- Chapters 2 and 3 address the nature and properties of glassy solids below the glass transition temperature. Chapter 2 presents a mean field study of the glass free energy landscape. Chapter 3 presents numerical studies of the energy landscape of three dimensional glasses.
- Chapter 4 presents the computational method employed in all the computer studies presented in this manuscript. This method allows to tune the stability of *in silico* glasses over an unprecedented range, paving the way to the novel computer studies presented in this manuscript (Chapters 3 and 5).
- Chapter 5 addresses the fundamental nature of the equilibrium glass transition. It explores the thermodynamic theory of glass formation, in which the dynamical slowdown of liquids is driven by a reduction of the number of available amorphous configurations, quantified by the configurational entropy.

Chapter 2

# Phase diagram of glasses in large dimensions

In this Chapter, we derive and solve the thermodynamics of realistic model glass-formers, in the limit where the number of spatial dimensions is large, $d \to \infty$. We describe the state following construction and obtain the main formulae describing the thermodynamics restricted to a glass. We then derive the phase diagram of realistic model glass formers. While it was previously accepted that glasses are stable from formation down to very low temperature, I identify and locate two glassy phases. One is the stable, common, glassy phase, and the other is a marginally stable phase, also called Gardner phase. The latter phase, whose mathematical description is extremely complex, could explain a range of observations in amorphous solids, which remain unaccounted by microscopic theory.

In Sec. 2.1, we provide an analytical derivation of the glass thermodynamics. The derivation is valid for a large class of interaction potentials and is simpler than previously published ones [107, 121–123, 151], which were restricted to the hard sphere model. The glass free energy is computed within the state-following formalism, using the replica method. We show that the problem is equivalent to computing the free energy of a molecular liquid. The atoms forming a molecule correspond to replicas of the original system. Assuming that the atoms are equivalent (replica symmetric ansatz), and that the shape of the molecule is Gaussian, we compute the glass free energy. In the limit $d \to \infty$, the approximations made in the derivation become exact. We obtain an exact expression for the glass free energy in the limit of large dimensions. Thermodynamic observables, such as the glass potential energy, are computed from the free energy. The limit of stability of the replica symmetric solution is analyzed to detect replica symmetry breaking transitions.

The equilibrium and state-following phase diagrams obtained for realistic glass-formers in large dimensions are presented in the article 'Marginally stable phases in mean-field structural glasses' [214]. We study the thermodynamics of Weeks-Chandler-Andersen glasses, as well as glasses interacting via a harmonic repulsion, and an inverse power-law. These models allow to cover physical regimes relevant to granular matter, foams, emulsions, hard and soft colloids, and molecular glasses. We investigate how glass preparation and physical conditions influence the location and extent of the Gardner phase. We follow the evolution of glasses prepared at various packing fractions and temperatures, corresponding to different physical regimes and stabilities, respectively. Our main result is that a Gardner phase is found in glasses prepared in all physical conditions. A

Gardner phase is always present around the jamming transition of glasses, and takes the form of a 'dome' in temperature and packing fraction. A Gardner phase is also found in the limit of large compressions. The extent of the Gardner phase decreases with increasing glass stability.

This work presents in a unified framework the liquid phase, the simple and marginal glass phases, as well as the jamming transition. We identify the location of the two distinct glassy phases, and therefore complete the phase diagram for amorphous solids presented in Fig. 1.8. The mean field results provide a solid starting point for the numerical investigation of the glass phase in $3d$ models, presented in Chapter 3.

## 2.1 Thermodynamics of liquids and glasses in the large-dimensional limit

The idea of using a thermodynamic formalism to describe dynamical arrest in liquids dates back to the work of Kirkpatrick, Thirumalai, and Wolynes [143, 215–217], and is at the root of the Random First Order Transition approach to the glass transition [1, 2, 173]. The state following construction, introduced in Sec. 1.3.4, is based on this idea [148, 155]. The method was adapted to particles in $d \to \infty$ in Refs. [151, 218], and is based on the following idea. In equilibrium statistical physics, the long time limit of dynamical observables can be computed, in the thermodynamic limit, using a probabilistic approach that relies on the use of appropriate statistical ensembles [219, 220]. For example, in equilibrium, entropy is maximized under the constraint of constant total energy, which leads to the Gibbs-Boltzmann distribution of the canonical ensemble [220]. By analogy, the state following construction aims at describing metastable glass states by a probability distribution that maximises the entropy under a minimal set of constraints.

### 2.1.1 Definition of the model

We consider a system of $N$ identical atoms, modeled as point particles, enclosed in a volume $V \subset \mathbb{R}^d$, with number density $\rho = N/V$. A configuration, noted $\underline{X}$, is specified by a set of $d$-dimensional vectors $\underline{X} = \{\mathbf{x}_i\}_{i=1,\dots,N}$, each $\mathbf{x}_i$ having components $x_{i\mu}$ for $\mu = 1, \dots, d$. We consider pairwise interactions between the atoms, which can only depend on their distance. The total interaction energy is

$$V(\underline{X}) = \sum_{i<j} v(|\mathbf{x}_i - \mathbf{y}_i|). \tag{2.1}$$

The derivation is valid for a large class of interaction potentials $v(r)$. In the article 'Marginally stable phases in mean-field structural glasses', we show the results for three specific pair potentials. The state of the system is a priori controlled by two parameters: its temperature $T/\epsilon$, and packing fraction $\varphi = \rho V_d \sigma^d / 2^d$, where $\sigma$ is the interaction range, $\epsilon$ the interaction energy, and $V_d$ the volume of a $d$-dimensional ball of unit radius. In practice, we tune the interaction range $\sigma$ to induce a change of the packing fraction $\varphi$, at constant $\rho$.

### 2.1.2 The glass free energy

As introduced in Sec. 1.3.4, we are interested in computing the free energy of a typical glass state $\underline{Y}$ prepared at the state point $(\varphi_g, T_g)$, and followed to $(\varphi, T)$, for a given choice of $\mathsf{D}_r$,

$$\mathrm{f}_g(\varphi, T|\varphi_g, T_g, \mathsf{D}_r) = -\frac{T}{N} \int \frac{\mathrm{d}\underline{Y}}{Z\left[\varphi_g, \beta_g\right]} e^{-\beta_g V[\underline{Y}]} \log Z\left[\varphi, \beta|\underline{Y}, \mathsf{D}_r\right], \tag{2.2}$$

where the $Z\left[\varphi_g, \beta_g\right] = \int \mathrm{d}\underline{Y} e^{-\beta_g V[\underline{Y}]}$, is the standard configurational integral at $(\varphi_g, \beta_g)$, and $Z\left[\varphi, \beta|\underline{Y}, \mathsf{D}_r\right]$ is a restricted configurational integral defined by

$$Z\left[\varphi, \beta|\underline{Y}, \mathsf{D}_r\right] = \int \mathrm{d}\underline{X} e^{-\beta V[\underline{X}]} \delta(\mathsf{D}(\underline{X}, \underline{Y}) - \mathsf{D}_r). \tag{2.3}$$

The presence of the disordered space-dependent external potential, $\underline{Y}$, in Eq. 2.2 prevents the use of a virial expansion. This problem is solved by the replica method. Applying Eq. 1.11 to the

glass free energy Eq. 2.2, we get

$$\mathrm{f}_g(\varphi, T|\varphi_g, T_g, \mathsf{D}_r) = -\lim_{s\to 0} \frac{T}{N}\partial_s \int \frac{\mathrm{d}\underline{Y}}{Z\left[\varphi_g, \beta_g\right]} e^{-\beta_g V[\underline{Y}]} Z\left[\varphi, \beta|\underline{Y}, \mathsf{D}_r\right]^s , \tag{2.4}$$

which allows to continue the computation if $s$ is an integer. In this case, one can introduce $s+1$ replicas of the original system, labelled by $a = 1, \ldots, s+1$, with $\underline{X}^1 = \underline{Y}$, $\beta_1 = \beta_g$, $\varphi_1 = \varphi_g$, $\beta_{a\geq 2} = \beta$, and $\varphi_{a\geq 2} = \varphi$. The glass free energy can be written as

$$\mathrm{f}_g(\varphi, T|\varphi_g, T_g, \mathsf{D}_r) = -\frac{T}{N}\lim_{s\to 0} \frac{1}{Z\left[\varphi_g, \beta_g\right]} \partial_s Z_{s+1}\left[\varphi_a, \beta_a, \mathsf{D}_r\right], \tag{2.5}$$

with

$$Z_{s+1}\left[\varphi_a, \beta_a, \mathsf{D}_r\right] = \int \left(\prod_{a=1}^{s+1} \int \mathrm{d}\underline{X}^a e^{-\beta_a V[\underline{X}^a]}\right) \left(\prod_{a=2}^{s+1} \int \mathrm{d}\underline{X}^a \delta(\mathsf{D}(\underline{X}^a, \underline{X}^1) - \mathsf{D}_r)\right). \tag{2.6}$$

The mean-squared displacement constraint imposes that the $s+1$ atoms $\mathbf{x}_i^a$ are close to one another, and thus form a 'molecule'. The replicated system is therefore a 'molecular liquid', and $Z_{s+1}$ is the configurational integral of this molecular liquid.

The replica method allows to rephrase the problem in order to restore translational and rotational invariance, and apply standard statistical mechanics treatments. The configurational integral of the molecular liquid is indeed invariant by global translation $\mathbf{x}_i^a \to \mathbf{x}_i^a + \mathbf{X}$, or global rotation. Assuming that an analytical continuation to real $s$ can be performed, the glass free energy Eq. 2.2 can be computed using the replicated free energy, $\mathrm{f}_{s+1}(\varphi_a, \beta_a, \mathsf{D}_r) = -\beta \log Z_{s+1}\left[\varphi_a, \beta_a, \mathsf{D}_r\right]/N$. An expansion of the replicated free energy in powers of $s$, indeed gives

$$\mathrm{f}_g(\varphi, T|\varphi_g, T_g, \mathsf{D}_r) = \lim_{s\to 0} \partial_s \mathrm{f}_{s+1}(\varphi_a, \beta_a, \mathsf{D}_r). \tag{2.7}$$

### 2.1.3 The replicated free energy

We now consider a molecular liquid, made by $N$ molecules labelled $\underline{\mathbf{x}}_i = \{\mathbf{x}_i^1, \ldots, \mathbf{x}_i^{s+1}\}$, where $\mathbf{x}_i^a$ is the position of atom $a = 1, \ldots, s+1$ in the molecule $i = 1, \ldots, N$. A molecular liquid configuration is noted $\underline{\mathbf{X}} = \{\underline{\mathbf{x}}_i\}_{i=1,\ldots,N}$. We define the local molecular density $\rho(\underline{\mathbf{x}})$, normalized by $\int \mathrm{d}\underline{\mathbf{x}}\rho(\underline{\mathbf{x}}) = N$. In the molecule, the atom 1 corresponds to the 'master' replica at state point $(\varphi_g, T_g)$, while the $a = 2, \ldots, s+1$ others atomes correspond to 'slave' replicas which evolve at $(\varphi, T)$.

We consider the virial expansion of the molecular liquid to second order, which becomes exact in the limit $d \to \infty$ [121]

$$-\beta N \mathrm{f}_{s+1} = \int \mathrm{d}\underline{\mathbf{x}}\ \rho(\underline{\mathbf{x}})\left(1 - \log \rho(\underline{\mathbf{x}})\right) + \frac{1}{2}\int \mathrm{d}\underline{\mathbf{x}}\mathrm{d}\underline{\mathbf{y}}\ \rho(\underline{\mathbf{x}})\rho(\underline{\mathbf{y}})\underline{f}(\underline{\mathbf{x}} - \underline{\mathbf{y}}). \tag{2.8}$$

The free energy is the sum of an ideal (molecular) gas part (first term in Eq. 2.8), and interaction part (second term). The molecular Mayer function $\underline{f}(\underline{\mathbf{x}} - \underline{\mathbf{y}})$ is defined by

$$\underline{f}(\underline{\mathbf{x}} - \underline{\mathbf{y}}) = e^{-\beta_g v(\mathbf{x}^1 - \mathbf{y}^1)} \prod_{a=2}^{s+1} e^{-\beta v(\mathbf{x}^a - \mathbf{y}^a)} - 1 \quad . \tag{2.9}$$

The translational invariance of the molecular liquid implies that the probability of finding a molecule in $\underline{\mathbf{x}} = \{\mathbf{x}^1, \ldots, \mathbf{x}^{s+1}\}$ is the same as finding the molecule in a translated configuration

$\underline{\mathbf{x}} - \mathbf{X} \equiv \{\mathbf{x}^1 - \mathbf{X}, \ldots, \mathbf{x}^{s+1} - \mathbf{X}\}$, *i.e.* $\rho(\underline{\mathbf{x}}) = \rho(\underline{\mathbf{x}} - \mathbf{X})$. By convenience, we make a change of variables taking atom 1 as reference ($\mathbf{X} = \mathbf{x}^1$), defining $\mathbf{u}^a = \mathbf{x}^a - \mathbf{x}^1$, for $a = 1, \ldots, s+1$. In the new variables, $\mathrm{d}\underline{\mathbf{x}} = \mathrm{d}\mathbf{X}\mathrm{d}\underline{\mathbf{u}}$, with $\mathrm{d}\underline{\mathbf{u}} = \prod_{a=2}^{s+1} \mathrm{d}\mathbf{u}^a$. The displacements of atoms in a molecule, relative to the first atom, are $\underline{\mathbf{u}} = \{\mathbf{0}, \mathbf{u}^2, \ldots, \mathbf{u}^{s+1}\}$. We define $\Pi(\underline{\mathbf{u}}) = \rho(\underline{\mathbf{u}})/\rho$ the normalized probability distribution of atom displacements $\int \Pi(\underline{\mathbf{u}})\mathrm{d}\underline{\mathbf{u}} = 1$. With this change of variables, the ideal gas term in the replicated free energy becomes

$$-\beta \mathrm{f}_{s+1}^{id} = 1 - \log\rho - \int \mathrm{d}\underline{\mathbf{u}}\ \Pi(\underline{\mathbf{u}}) \log \Pi(\underline{\mathbf{u}}), \tag{2.10}$$

and the interaction term

$$-\beta \mathrm{f}_{s+1}^{int} = \frac{\rho}{2} \int \mathrm{d}\mathbf{R}\mathrm{d}\underline{\mathbf{u}}\mathrm{d}\underline{\mathbf{v}}\ \Pi(\underline{\mathbf{u}})\Pi(\underline{\mathbf{v}}) f(\underline{\mathbf{u}} - \underline{\mathbf{v}} + \mathbf{R}) \quad , \tag{2.11}$$

where $\mathbf{R} = \mathbf{x}^1 - \mathbf{y}^1$.

Rotational invariance of the molecular liquid implies that the probability distribution function of displacements $\Pi(\underline{\mathbf{u}})$ is invariant under a global rotation of all vectors $\mathbf{u}^a$, and is therefore only function of the scalar products $\mathbf{u}^a \cdot \mathbf{u}^b$. The derivation is simpler if one considers a Gaussian ansatz for the molecular density $\rho(\underline{\mathbf{u}})$. We use this assumption, which is a priori unjustified, since it becomes exact in the limit $d \to \infty$ [121, 123]. We introduce a $s \times s$ matrix $\hat{A}$ of scalar products, with $A_{ab} = \langle u_\mu^a u_\mu^b \rangle$, where $\langle \cdot \rangle$ is the average over the probability distribution $\Pi(\underline{\mathbf{u}})$. The probability distribution $\Pi(\underline{\mathbf{u}})$ is a $d$-dimensional Gaussian, parametrized by $\hat{A}$

$$\Pi_{\hat{A}}(\underline{\mathbf{u}}) = \frac{1}{\left[(2\pi)^s \det \hat{A}\right]^{d/2}} \exp\left\{ -\frac{1}{2} \sum_{\mu=1}^{d} \sum_{a,b=2}^{s+1} u_\mu^a A_{ab}^{-1} u_\mu^b \right\}. \tag{2.12}$$

The gaussian parametrization allows to write the ideal gas term in the free energy as

$$-\beta \mathrm{f}_{s+1}^{id} = 1 - \log\rho + \frac{d}{2} s[1 + \log(2\pi)] + \frac{d}{2} \log\det \hat{A}. \tag{2.13}$$

The variables $\underline{\mathbf{u}}$ and $\underline{\mathbf{v}}$ in the interaction term (Eq. 2.11) are independently and identically distributed according to the Gaussian distribution $\Pi_{\hat{A}}(\underline{\mathbf{u}})$. The difference $\underline{\mathbf{u}} - \underline{\mathbf{v}}$ is thus Gaussian, with covariance $2\hat{A}$. Making the change of variables $\underline{\mathbf{w}} = \underline{\mathbf{u}} - \underline{\mathbf{v}}$,

$$-\beta \mathrm{f}_{s+1}^{int} = \frac{\rho}{2} \int \mathrm{d}\mathbf{R}\mathrm{d}\underline{\mathbf{w}} \Pi_{2\hat{A}}(\underline{\mathbf{w}}) f(\underline{\mathbf{w}} + \mathbf{R}) \tag{2.14}$$

It is more convenient to use the mean-squared displacement (MSD) matrix $\hat{\mathsf{D}}$, which encodes the MSDs between atoms in a molecule. The matrix $\hat{\mathsf{D}}$ has a simpler physical interpretation, and is equivalent to the matrix $\hat{A}$. The atoms $a = 2, \ldots, s+1$ are fixed at a distance $\mathsf{D}_r$ from atom 1, therefore $\langle (u_\mu^a)^2 \rangle = \mathsf{D}_r$. The MSD between replicas $a \geq 2$ is given by the MSD matrix, $\langle (u_\mu^a - u_\mu^b)^2 \rangle = \mathsf{D}_{ab}$ (for $a \neq b$, $a, b \geq 2$), with $\mathsf{D}_{aa} = 0$. The matrix $\hat{A}$ can be written in terms of $\hat{\mathsf{D}}$

$$A_{ab} = \mathsf{D}_r\, \delta_{ab} + \left( \mathsf{D}_r - \frac{\mathsf{D}_{ab}}{2} \right) (1 - \delta_{ab}) \tag{2.15}$$

### 2.1.4 The replica symmetric glass free energy

Once optimized over $\hat{\mathsf{D}}$, the sum of Eqs. 2.10 and 2.11 yields the entropy of the replicated system. If its analytic continuation to real $s$ can be performed, the linear order in $s$ gives the glass free energy $\mathrm{f}_g$. To perform this computation, we have to make an ansatz for the matrix $\hat{\mathsf{D}}$, which encodes the structure of the molecular liquid. In the simplest replica symmetric (RS) assumption, all replicas $a \geq 2$ are equivalent, thus $\mathsf{D}_{ab} = \mathsf{D}$ for $a, b \geq 2$, $a \neq b$. The matrix $\hat{A}$ can be written as

$$\hat{A} = \left(\mathsf{D}_r - \frac{\mathsf{D}}{2}\right)\hat{\mathbb{1}}_s + \frac{\mathsf{D}}{2} I_s, \qquad \det \hat{A} = \left[\left(\frac{\mathsf{D}}{2} + s\left(\mathsf{D}_r - \frac{\mathsf{D}}{2}\right)\right)\left(\frac{\mathsf{D}}{2}\right)^{s-1}\right] \tag{2.16}$$

where $\hat{\mathbb{1}}_s$ is a $s \times s$ matrix with elements equal to 1, and $I_s$ is the $s \times s$ identity matrix. The eigenvalues of $\hat{A}$ are $\{\mathsf{D}/2 + s(\mathsf{D}_r - \mathsf{D}/2)\}$ and $\{\mathsf{D}/2\}$ with multiplicity 1 and $(s-1)$, respectively. By plugging the determinant Eq. 2.16 in the ideal gas part of the replicated free energy Eq. 2.13, then taking the linear order in $s$, we obtain the ideal gas part of the replica-symmetric glass free energy

$$-\beta \mathrm{f}_g^{id} = \frac{d}{2}\left\{1 + \log(\pi\,\mathsf{D}) + \frac{2\,\mathsf{D}_r - \mathsf{D}}{\mathsf{D}}\right\} \tag{2.17}$$

Regarding the interaction term, the replica symmetric ansatz and the Gaussian approximation allow to write the local molecular density as

$$\rho(\underline{\mathbf{x}}) = \rho \int \mathrm{d}\mathbf{X} \gamma_{A_1}(\mathbf{x}^1 - \mathbf{X}) \prod_{a=2}^{s+1} \gamma_{A_2}(\mathbf{x}^a - \mathbf{X}), \tag{2.18}$$

where

$$\gamma_A(\mathbf{x}) = \frac{e^{-\sum_\mu \frac{x^{\mu 2}}{2A}}}{(2\pi A)^{d/2}} \tag{2.19}$$

is a $d$-dimensional centered Gaussian of variance $A$. The first atom is constrained in a cage of size $A_1$, while the $s$ others are constrained by $A_2$. They are related to the MSDs between replicas: $A_1 = \mathsf{D}_r - \mathsf{D}/2$ and $A_2 = \mathsf{D}/2$. By plugging the expression of Eq. 2.18 for the local molecular density in the interaction term Eq. 2.8, then performing adequate changes of variables (see Eq. C2 in Ref. [98]), the interaction term of the replicated free energy is equal to

$$-\beta \mathrm{f}_{s+1}^{int} = \frac{\rho}{2} \int \mathrm{d}\mathbf{R} \left[\left(\gamma_{2\,\mathsf{D}_r - \mathsf{D}} \otimes e^{-\beta_g v}\right)(\mathbf{R}) \left\{\left(\gamma_{\mathsf{D}} \otimes e^{-\beta v}\right)(\mathbf{R})\right\}^s - 1\right], \tag{2.20}$$

where $\otimes$ denotes a $d$-dimensional convolution. In practice, the $d$-dimensional convolutions present in Eq. 2.20 are hard to compute. Using bipolar coordinates (Eqs. C9-C16 in Ref. [98] ), a $d$-dimensional convolution reduces to a one-dimensional integral, using the modified Bessel functions $I_n(x)$. We introduce the following function:

$$q\left(\mathsf{D}, r, d, \beta\right) \equiv \left(\gamma_{\mathsf{D}} \otimes e^{-\beta v}\right)(r) = \int_0^\infty \mathrm{d}u e^{-\beta v(u)} \left(\frac{u}{r}\right)^{\frac{d-1}{2}} \frac{e^{-\frac{(r-u)^2}{2\,\mathsf{D}}}}{\sqrt{2\pi\,\mathsf{D}}} \left[e^{-\frac{ru}{\mathsf{D}}} \sqrt{2\pi \frac{ru}{\mathsf{D}}} I_{\frac{d-1}{2}}\left(\frac{ru}{\mathsf{D}}\right)\right] \tag{2.21}$$

By expressing the replicated free energy Eq. 2.20 in terms of a one-dimensional integral, then taking the linear order in $s$, we obtain the interaction term of the glass free energy

$$-\beta \mathrm{f}_g^{int} = \frac{\rho}{2} dV_d \int r^{d-1} \mathrm{d}r \; q(2\,\mathsf{D}_r - \mathsf{D}, r, d, \beta_g) \log q(\mathsf{D}, r, d, \beta), \tag{2.22}$$

where $V_d = \pi^{d/2}/\Gamma(1+d/2)$ is the volume of a $d$-dimensional sphere of radius unity. Putting together Eqs. 2.17 and 2.22, we obtain the replica symmetric glass free energy

$$-\beta \mathrm{f}_g = \frac{d}{2}\left(1+\log(\pi\,\mathsf{D}) + \frac{2\,\mathsf{D}_r - \mathsf{D}}{\mathsf{D}}\right) + \frac{\rho}{2} dV_d \int r^{d-1}\mathrm{d}r\; q(2\,\mathsf{D}_r - \mathsf{D}, r, d, \beta_g)\log q(\mathsf{D}, r, d, \beta) \quad (2.23)$$

### 2.1.5 Replica symmetric glass free energy in the large-dimensional limit

We are interested in the large dimensional limit of the problem. The glass free energy can be obtained by taking $d \to \infty$ in Eq. 2.23, since the virial expansion to second order and the Gaussian approximation are exact in this limit. We define rescaled variables in order to have a well-defined large-dimensional limit. The relevant interactions correspond to particles at a distance $r \sim \sigma$, with $\mathcal{O}(1/d)$ fluctuations. We make the change of variables $r = \sigma(1+h/d)$. This defines 'gaps' $h$ which remain finite when $d \to \infty$.

The large dimensional limit of the function $q$ defined in Eq. 2.21 can be computed (see Eqs. C27-C32 of Ref. [98]). The rescaled MSD $\Delta = d^2\,\mathsf{D}\,/\sigma^2$, which has a finite value when $d \to \infty$, appears naturally, and

$$q\,(\mathsf{D}, r, d, \beta) \xrightarrow[d\to\infty]{} q(\Delta, \beta; h) = \int_{-\infty}^{\infty} dy\, e^{-\beta v(y)} \frac{e^{-\frac{(y-h-\Delta/2)^2}{2\Delta}}}{\sqrt{2\pi\Delta}}\ . \quad (2.24)$$

We make the change of variables from distances $r$ to gaps $h$ in Eq. 2.22. In particular, in the limit $d \to \infty$,

$$r^{d-1}\mathrm{d}r \sim r^d \mathrm{d}r = \sigma^d\left(1+\frac{h}{d}\right)^d \frac{\sigma}{d}\mathrm{d}h = \frac{\sigma^{d+1}}{d} e^{d\log(1+h/d)}\mathrm{d}h \sim \frac{\sigma^d}{d} e^h \mathrm{d}h. \quad (2.25)$$

In the limit $d \to \infty$, the glass free energy Eq. 2.23 is equal to

$$-\beta f_g = \frac{d}{2}\left\{1 + \frac{2\Delta_r - \Delta}{\Delta} + \log(\pi\sigma^2\Delta/d^2) + \widehat{\varphi}_g \int_{-\infty}^{\infty} \mathrm{d}h\, e^h q(2\Delta_r - \Delta, \beta_g; h)\log q(\Delta, \beta; h-\eta)\right\}\ , \quad (2.26)$$

where we identified the rescaled packing fraction $\hat{\varphi} = 2^d\varphi/d$, using the definition of $\varphi = \rho V_d \sigma^d/2^d$. The last term $\eta = \log(\widehat{\varphi}/\widehat{\varphi}_g)$ comes from the change of packing fraction from $\varphi_g$ to $\varphi$. It is done by modifying the interaction range of the constrained particles. If $\sigma_g$ is the interaction range of the particles in the reference system (at $\beta_g$), we use $\sigma = \sigma_g(1+\eta/d)$ for the constrained replicas at $\beta$. The packing fraction of the constrained replicas is therefore $\widehat{\varphi} = \widehat{\varphi}_g(\sigma/\sigma_g)^d \sim \widehat{\varphi}_g e^\eta$ in the large dimensional limit.

The thermodynamic values of $\Delta$ and $\Delta_r$ correspond to a saddle point of Eq. 2.26, and are thus solution of the set of equations

$$\begin{aligned} 2\Delta_r &= \Delta + \widehat{\varphi}_g\Delta^2 \int_{-\infty}^{\infty} \mathrm{d}h\, e^h \frac{\partial}{\partial\Delta}\left[q(2\Delta_r - \Delta, \beta_g; h)\log q(\Delta, \beta; h-\eta)\right], \\ \frac{2}{\Delta} &= -\widehat{\varphi}_g \int_{-\infty}^{\infty} \mathrm{d}h\, e^h \left[\frac{\partial}{\partial\Delta_r} q(2\Delta_r - \Delta, \beta_g; h)\right]\log q(\Delta, \beta; h-\eta). \end{aligned} \quad (2.27)$$

In practice, Eqs. 2.27 are solved by iteration. Starting from a guess for $\Delta$ and $\Delta_r$ (a good one is $\Delta = \Delta_r = \Delta_g$ solution of Eq. 2.29), one computes numerically the right hand side to obtain new estimates. Upon iteration, the new estimates get closer to the previous ones, and the procedure converges.

By taking derivatives of the free energy Eq. 2.26 with respect to $T, \widehat{\varphi}$, one obtains the average of thermodynamic observables. For example, the average glass energy is the derivative of the free energy with respect to the inverse temperature,

$$e_g = \frac{\partial(\beta f_g)}{\partial\beta} = -\frac{d\widehat{\varphi}_g}{2}\int_{-\infty}^{\infty} \mathrm{d}h\, e^h q_\gamma(2\Delta_r - \Delta, \beta_g; h)\frac{\partial}{\partial\beta}\log q(\Delta, \beta; h-\eta). \tag{2.28}$$

### 2.1.6 The dynamical transition

We focus on the case where the glass is prepared and studied at the same state point $(\widehat{\varphi}, T) = (\widehat{\varphi}_g, T_g)$. In this case, all $s+1$ replicas are equivalent: $\Delta = \Delta_r \equiv \Delta_g$, and Eqs. 2.27 are conveniently written as

$$\frac{1}{\widehat{\varphi}_g} = \mathcal{F}_\beta(\Delta_g) = -\Delta_g \int_{-\infty}^{\infty} dy\, e^y \log[q(\Delta_g, \beta_g; y)]\frac{\partial q(\Delta_g, \beta_g; y)}{\partial \Delta_g}\ . \tag{2.29}$$

In practice, this equation is used to compute the dynamical transition. One can show that at all temperatures, the function $\mathcal{F}_\beta(\Delta)$ generally vanishes both for $\Delta \to 0$ and $\Delta \to \infty$, and has a unique maximum in between. No solution can be found if $\widehat{\varphi}_g < \widehat{\varphi}_d$, where $\widehat{\varphi}_d$ is the dynamical transition at temperature $\beta_g$, defined by

$$\frac{1}{\widehat{\varphi}_d(\beta_g)} = \max_{\Delta} \mathcal{F}_{\beta_g}(\Delta) \tag{2.30}$$

The absence of a solution means that the Franz-Parisi potential has no local minimum at finite $\Delta_r$. No stable glass phase then exists, and the system is therefore a liquid.

### 2.1.7 The Gardner transition

One can follow a glass prepared at $(\widehat{\varphi}_g, T_g)$ to different state points $(\widehat{\varphi}, T)$ using the replica symmetric matrix $\hat{\Delta}^{RS}$. However, the replica symmetric form of the matrix $\hat{\Delta}$ is an assumption, and we need to check that it is a stable local minimum of the replicated free energy. To perform this check, we need to compute the stability operator, or Hessian $\mathcal{H}$, of the replicated free energy on the RS solution at the saddle point

$$\mathcal{H}_{a>b;c>d} = \left.\frac{\partial^2 \mathrm{f}_{s+1}}{\partial\Delta_{ab}\partial\Delta_{cd}}\right|_{\hat{\Delta}=\hat{\Delta}^{RS}}. \tag{2.31}$$

The replica symmetric solution is locally stable if all the eigenvalues of $\mathcal{H}$ are positive. Replica symmetry strongly constrains the form of the Hessian. Its eigenvalues can be computed explicitly, as done in Refs. [153, 186]. Most importantly, the Hessian computed on the RS solution has three independent eigenvalues, $\lambda_R, \lambda_L, \lambda_A$ called replicon, longitudinal, and anomalous modes, respectively. The replicon mode is the one linked to instabilities towards replica symmetry breaking.

A practical way to compute the limit of stability of the RS solution is to derive the fullRSB solution for the replicated free energy. We do not wish to report the complete derivation here, which can be found in Refs. [123, 221]. In the fullRSB case, the solution is parametrized by a continuous function $\Delta(x)$ for $x \in [0:1]$, which is strictly decreasing: $\dot{\Delta}(x) < 0$. Similarly to Eqs. 2.27, the thermodynamic solution for $\Delta(x)$ verifies an integro-differential equation. By taking the derivative

of this equation, one obtains an expression which is proportional to the replicon eigenvalue $\lambda_R$. Evaluating this expression on the RS solution, one gets

$$\lambda_R \propto -1 + \frac{\widehat{\varphi}_g}{2}\Delta^2 \int_{-\infty}^{\infty} \mathrm{d}h\, e^h q_\gamma(2\Delta_r - \Delta, \beta_g; h) \left( \frac{\partial^2}{\partial h^2} \log q(\Delta, \beta; h - \eta) \right)^2 . \tag{2.32}$$

The Gardner transition is the point where the replicon $\lambda_R$ vanishes.

In the following article, we present the phase diagrams obtained by solving numerically Eqs. 2.27, 2.28, and 2.32 for three different pair potentials.

Article

# Marginally stable phases in mean-field structural glasses

C. Scalliet, L. Berthier and F. Zamponi, Physical Review E E 99 (1), 012107 (2019).

**A novel form of amorphous matter characterized by marginal stability was recently discovered in the mean-field theory of structural glasses. Using this approach, we provide complete phase diagrams delimiting the location of the marginally stable glass phase for a large variety of pair interactions and physical conditions, extensively exploring physical regimes relevant to granular matter, foams, emulsions, hard and soft colloids, and molecular glasses. We find that all types of glasses may become marginally stable, but the extent of the marginally stable phase highly depends on the preparation protocol. Our results suggest that marginal phases should be observable for colloidal and non-Brownian particles near jamming, and poorly annealed glasses. For well-annealed glasses, two distinct marginal phases are predicted. Our study unifies previous results on marginal stability in mean-field models, and will be useful to guide numerical simulations and experiments aimed at detecting marginal stability in finite dimensional amorphous materials.**

## I Introduction

Twenty years ago, a unified phase diagram for amorphous matter [1] motivated the search for similarities and differences between the properties of a broad range of materials, from granular materials to molecular glasses [2]. It is now well-established that in the presence of thermal fluctuations, dense assemblies of atoms, molecules, polymers, colloidal particles undergo a glass transition [3, 4] as the temperature is decreased or the density increased. In the absence of thermal fluctuations, solidity instead emerges by compressing particles across the jamming transition [5, 6], relevant for foams, non-Brownian emulsions, and granular materials. These two transitions have qualitatively distinct features.

Models of soft repulsive spheres faithfully capture this diversity [7, 8], as shown in Fig. 1. The relevant adimensional control parameters are the packing fraction, $\varphi$, and the ratio of thermal agitation,

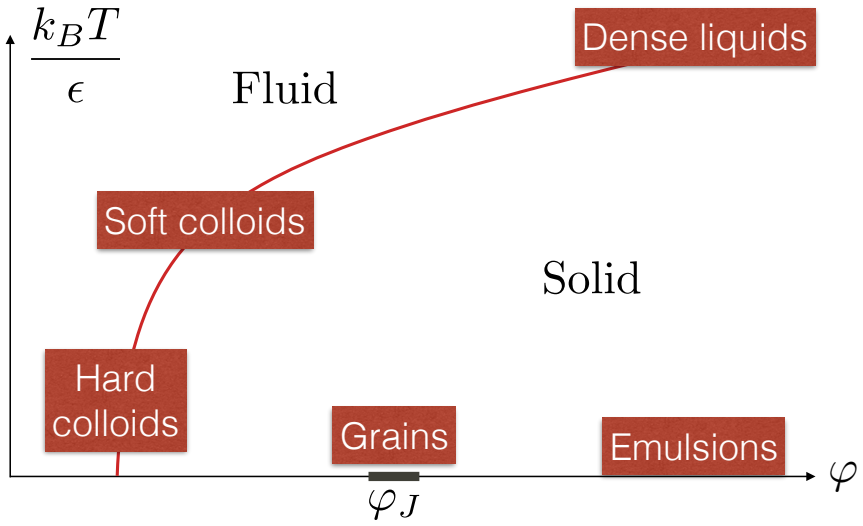


Figure 1: Schematic (temperature, packing fraction) phase diagram for soft repulsive spheres and its experimental relevance. The dynamic glass transition is represented by the red line. Jamming transitions are observed in the athermal limit over a protocol-dependent range of packing fractions (grey line). Different regions of the phase diagram are relevant for a variety of amorphous materials, indicated in boxes. In this work, we explore in which conditions these amorphous materials become marginally stable.

$k_BT$, to the interaction strength between particles, $\epsilon$. A dense assembly of soft particles transforms into a glass when thermal fluctuations decrease. Glasses can also be obtained by compression at constant temperature, and in particular the limit $\epsilon \to \infty$ at constant $T$ corresponds to compression of colloidal hard spheres. At large density and temperature, the particles constantly overlap and the system behaves identically to glass-forming liquids. Intermediate densities and temperatures describe the glass transition of soft colloids. Jamming transitions are observed in the athermal regime $k_BT/\epsilon \to 0$ relevant for granular materials, foams and non-Brownian emulsions. Because this occurs deep inside the glassy phase at $T = 0$, jamming transitions are protocol-dependent and occur over a continuous range of packing fractions $\varphi_J$ [9, 10, 11, 12].

The phase diagram in Fig. 1 organizes the physics of a broad variety of materials by describing how fluids lose their ability to flow, but incorrectly suggests that the solid phase has similar properties across a broad range of physical conditions. In fact, while ordinary glasses formed by cooling dense liquids behave roughly as crystalline solids with a high density of defects [13, 14], glasses formed by compressing granular materials or non-Brownian emulsions across their jamming transition display unique properties distinct from ordinary solids [6, 5]. For example, they may respond to weak stresses with very large deformations, and their low-frequency excitations are very different from phonons [15, 16, 17]. These properties were theoretically explained by invoking *marginal stability* [18, 19]: because these glasses are formed by zero-temperature compression across a rigidity transition, they have barely enough contacts to be mechanically stable. From this observation, several anomalous properties of athermal glasses in the vicinity of jamming can be understood [20].

Theoretical calculations in the framework of the mean-field theory of the glass transition [21, 22, 23, 11, 24] have confirmed these ideas, and suggested in addition the existence of two distinct types of amorphous solids separated by a sharp phase transition [25, 26]. One phase is the normal

glass, and corresponds to a free energy basin that responds essentially elastically to perturbations, as any regular solid. The second is a *Gardner glass* [27, 28]. The Gardner glass is marginally stable due to full replica symmetry breaking, as in mean-field spin glasses [29]. Physically, marginal stability implies the existence of long-ranged correlations in the vibrational dynamics [30, 31], an excess of low-frequency modes [32, 33], unusual rheological properties [34, 35, 36], and system-spanning responses to weak, localized perturbations, manifested for instance by diverging mechanical susceptibilities [37, 34, 38]. The Gardner phase may thus provide an elegant route to understand the nature of a multitude of experimental observations of glassy excitations [25, 26]. Explicit mean-field calculations for the location of marginally stable glasses were carried out for hard [25, 26] and soft [34, 39, 40] potentials, providing some insight about mean-field phase diagrams. Furthermore, a way to take into account fluctuations around the mean field limit, within the nucleation theory associated to the Random First Order Transition approach, has been proposed in [41].

Numerical simulations and experiments in finite dimensional systems were performed to explore these theoretical ideas, yielding contrasting results. Numerical studies of three dimensional hard sphere glasses [30, 36, 42, 43], and numerical and experimental study of two dimensional hard disks [30, 44, 45], have revealed a rich vibrational dynamics, with diverging lengthscales, suggestive of a Gardner phase. On the other hand, numerically cooling soft glass-formers has only revealed sparse, localized defects [40, 46], whereas experimental studies remain inconclusive [47]. It has also been suggested that in low dimensions localized defects could induce an apparent Gardner-like phenomenology, without an underlying sharp phase transition [40, 48]. Overall, this recent flurry of results suggests that distinct glassy materials may have distinct properties, depending on both their preparation and location in the phase diagram of Fig. 1, thus calling for a systematic microscopic investigation of marginally stable glassy phases. This is the central goal of the present work.

We use a microscopic mean-field theory to study thermal soft repulsive spheres in the limit of infinite spatial dimensions to systematically investigate the physical properties and marginal stability of glasses prepared in a wide range of physical conditions, covering all regimes illustrated in Fig. 1. For a glass prepared at any given location in Fig. 1, we investigate how its properties evolve under further compression and cooling, thus providing complete phase diagrams locating simple and marginally stable glasses. We find that all glasses may become marginally stable, but Gardner phases are more easily accessible for systems close to jamming (such as grains, foams, hard and soft colloids), and for poorly annealed glasses obtained by a fast quench. The extent of the marginally stable phase depends, in all cases, on the preparation protocol. For well-annealed glasses at intermediate packing fractions, two distinct Gardner phases are predicted. Our study extends and unifies previous analytical studies [26, 39, 40] and will serve as a useful theoretical guide for systematic investigations of marginal stability in finite dimensional glasses, via numerical simulations or experiments. In particular, we are currently completing a three dimensional numerical study that parallels the calculations presented here [49].

The article is organized as follows. In Sec. II, we introduce the models studied in this work. In Sec. III, we present the theoretical methods we use. In Sec. IV, we present the results for the phase diagrams obtained for a variety of physical conditions. In Sec. V, we discuss our results and provide some perspectives.

## II Models for glassy materials

While we are ultimately interested in the phase diagram of dense particle systems for which the spatial dimension is $d = 2$ or $d = 3$, we focus on assemblies of particles embedded in an abstract,

but analytically tractable, space of $d \to \infty$ dimensions. In this limit, an exact solution for the thermodynamic properties of the liquid and glass phases can be obtained [21, 26].

We study several conventional interaction potentials for glass-forming materials, that allow us to interpolate between the various physically relevant limits shown in Fig. 1. In particular, it is useful to consider the following harmonic sphere model:

$$v_{\rm HARM}(r) = \frac{\epsilon}{2}\left(1-\frac{r}{\sigma}\right)^2 \theta\left(\sigma - r\right) \ , \tag{1}$$

where $r$ is the inter-particle distance, $\sigma$ the diameter of particles, $\epsilon$ the repulsion strength and $\theta(r)$ the Heaviside function. The harmonic sphere model was first introduced to study the jamming transition [50], and later studied extensively at finite temperature [7]. Harmonic spheres become equivalent to hard spheres when $\epsilon \to \infty$.

To study the large density limit relevant for dense liquids, harmonic spheres are not useful, as their extreme softness gives rise to exotic phenomena that we do not wish to discuss here. Instead, it is more relevant to analyze the Weeks-Chandler-Andersen (WCA) potential,

$$v_{\rm WCA}(r) = \epsilon\left[1+\left(\frac{\sigma}{r}\right)^{4d} - 2\left(\frac{\sigma}{r}\right)^{2d}\right]\theta(\sigma-r) \ , \tag{2}$$

because it resembles the harmonic potential around the cutoff $r \sim \sigma$, but behaves as a Lennard-Jones potential at smaller inter-particle distance. Our analysis shows that the WCA model yields results qualitatively similar to the harmonic model at moderate densities, and behaves as the inverse power law (IPL) potential

$$v_{\rm IPL}(r) = \epsilon(\sigma/r)^{4d} \ , \tag{3}$$

in the large density limit. Therefore we decided to concentrate on the two models in Eqs. (1, 3) to report our results. Technically, the harmonic potential is easier to handle, as one can go one step further analytically than for WCA, which simplifies the numerical resolution of the equations presented below. The WCA model, on the other hand, is numerically very convenient for finite-$d$ studies, which justifies our effort to study it as well. While the expression of the harmonic potential is the same regardless of spatial dimension, we have extended the standard definitions of the WCA and IPL models in $d = 3$ to arbitrary dimension $d$. This is done because thermodynamic stability and the existence of the thermodynamic limit, a prerequisite for performing the theoretical development described below, require the potential to decay faster than $r^{-d}$ in dimension $d$ [51].

We consider the thermodynamic limit for $N$ particles in a volume $V$, both going to infinity at fixed number density $\rho = N/V$. When $d = \infty$, we can consider monodisperse particles, as crystallization is no longer the worrying issue it is in finite dimensions [52, 53]. Our adimensional control parameters are the packing fraction $\varphi = NV_d(\sigma/2)^d/V$, defined as the fraction of volume covered by particles of diameter $\sigma$ ($V_d$ is the volume of a $d$-dimensional unit sphere), and the scaled temperature $T/\epsilon$ (in the following, we will take $k_B = 1$). To obtain a non-trivial phase diagram in the limit $d \to \infty$, the packing fraction has to be rescaled as $\widehat{\varphi} = 2^d\varphi/d$. Note that in the case of the IPL model, the form of the interaction potential leads to a unique control parameter $\Gamma = \widehat{\varphi}/T^{1/4}$. We also define rescaled gaps between particles $h = d(r/\sigma - 1)$, and rescaled potentials $\bar{v}(h)$ such that $\lim_{d\to\infty} v(r) = \bar{v}(h)$:

$$\begin{aligned} \bar{v}_{\rm HARM}(h) &= \frac{\epsilon}{2}h^2\theta(-h) \ , \\ \bar{v}_{\rm IPL}(h) &= e^{-4h} \ . \end{aligned} \tag{4}$$

We will be particularly interested in mean-squared displacements (MSD) between configurations. In finite dimensions, they are usually defined as $\mathsf{D}(X,Y) = 1/N \sum_i |\mathbf{x}_i - \mathbf{y}_i|^2$, where $X$ and $Y$ represent two configurations. Finite values for the MSD in infinite dimensions are obtained by defining $\Delta(X,Y) = d^2\,\mathsf{D}(X,Y)/\sigma^2$.

In the following section, we summarize the formalism that allows us to compute the thermodynamic properties and the phase diagram for the above models.

# III Theoretical methods

The general strategy of our work is devised to mimic the following experimental protocol. During the gradual cooling or compression of a glass-forming liquid, the equilibrium relaxation time $\tau_\alpha$ of the system increases very sharply. For a given protocol, there comes a moment where the system falls out of equilibrium; this represents the experimental glass transition, at state point $(T_g, \widehat{\varphi}_g)$. After this moment, the system follows a 'restricted' equilibrium, where the amorphous structure frozen at the glass transition is adiabatically followed at different temperature and density, $(T, \widehat{\varphi})$. Our analytical strategy follows this protocol closely. We draw an equilibrium but dynamically arrested configuration at $(T_g, \widehat{\varphi}_g)$, and follow its thermodynamics when brought adiabatically to another state point $(T, \widehat{\varphi})$ within the same glass basin.

## III.1 Glass free energy

The state-following protocol described above is possible if the relaxation time of the initial state is extremely large [54, 55, 56, 57, 26]. In infinite dimensions, the equilibrium relaxation time diverges at the dynamic glass transition $T_d(\widehat{\varphi})$, which is of the mode-coupling type [58, 59, 26]. Our construction, which is briefly summarized in the following, is thus devised to follow glasses created below the dynamical transition [57, 34].

Let us consider an equilibrium configuration $Y$, extracted from the Boltzmann distribution at $(T_g, \widehat{\varphi}_g)$, which falls into the dynamically arrested region $T_g < T_d(\widehat{\varphi}_g)$. To construct the thermodynamics restricted to the glass state $Y$, we consider a sub-region of phase space probed by configurations $X$ constrained to remain close to $Y$. The configuration $X$ can be at a different state point $(T, \widehat{\varphi})$, but its mean-squared distance to $Y$ is fixed to a finite value $\Delta(X,Y) = \Delta_r$. The free energy $f_Y$ of the glass state selected by $Y$ and brought to $(T, \widehat{\varphi})$ can be expressed in terms of a restricted configuration integral [57]

$$\begin{aligned} Z\left[T, \widehat{\varphi} | Y, \Delta_r\right] &= \int \mathrm{d}X e^{-\beta V[X]} \delta(\Delta_r - \Delta(X,Y)) \quad , \\ f_Y(T, \widehat{\varphi} | Y, \Delta_r) &= -\frac{T}{N} \log Z\left[T, \widehat{\varphi} | Y, \Delta_r\right] \quad , \end{aligned} \tag{5}$$

where $V(X)$ is the total potential energy of the glass $X$. The glass free energy $f_Y$ in Eq. (5) depends explicitly on the initial glass $Y$. In the thermodynamic limit, its typical value $f_g$ is given by averaging over all equilibrium states $Y$

$$\begin{aligned} f_g(T, \widehat{\varphi} | T_g, \widehat{\varphi}_g, \Delta_r) = -\frac{T}{N} \int \frac{\mathrm{d}Y}{Z\left[T_g, \widehat{\varphi}_g\right]} e^{-\beta_g V[Y]} \\ \times \log Z\left[T, \widehat{\varphi} | Y, \Delta_r\right] \end{aligned} \tag{6}$$

where $Z[T_g, \widehat{\varphi}_g]$ is the standard configurational integral at $(T_g, \widehat{\varphi}_g)$. The free energy has to be computed for the parameter $\Delta_r$ verifying $\partial_{\Delta_r} f_g = 0$ [57]. Note that the density dependence of the free energy is encoded by the interaction length scale $\sigma$ of the potential, which can be changed to induce a change in packing fraction.

Performing the disorder average in Eq. (6) is challenging. Translational invariance, necessary to use saddle-point and perturbative methods, is broken by the presence of disorder. To compute the glass free-energy in Eq. (6) we use the replica method, and introduce $(s+1)$ identical replicas of the original atomic system to undertake the computation [54, 57, 26]. The 'master' replica represents the initial glass at $(T_g, \widehat{\varphi}_g)$, while the $s$ others 'slave' replicas represent the glass at $(T, \widehat{\varphi})$. The glass free-energy can then be expressed in terms of the MSD between the different replicas. The MSD between any slave replica and the master replica are parametrized by $\Delta_r$. We make the simplest assumption, called replica symmetric, and consider that all slave replicas are equivalent [57], at a distance $\Delta$ from each other. At the end of the computation, we take the analytic continuation $s \to 0$ and obtain the replica symmetric glass free energy

$$-\frac{2}{d}\beta f_g = \frac{2\Delta_r}{\Delta} + \log(\pi\Delta/d^2) + \widehat{\varphi}_g \int_{-\infty}^{\infty} dh\, P(h) f(h) \ , \tag{7}$$

defining for simplicity $\eta = \log(\widehat{\varphi}/\widehat{\varphi}_g)$,

$$q(\Delta, \beta; h) = \int_{-\infty}^{\infty} dy\, e^{-\beta \bar{v}(y)} \frac{e^{-\frac{(y-h-\Delta/2)^2}{2\Delta}}}{\sqrt{2\pi\Delta}} \ , \tag{8}$$

and

$$\begin{aligned} P(h) &= e^h\, q(2\Delta_r - \Delta, \beta_g; h) \ , \\ f(h) &= \log q(\Delta, \beta; h - \eta) \ . \end{aligned} \tag{9}$$

Compressing and decompressing a glass corresponds to $\eta > 0$ and $\eta < 0$, respectively. The glass free energy should be computed with the thermodynamic values for $\Delta$ and $\Delta_r$, determined by setting to zero the derivatives of $f_g$ with respect to these parameters, which provides two implicit equations for $\Delta$ and $\Delta_r$:

$$\begin{aligned} 2\Delta_r &= \Delta + \widehat{\varphi}_g \Delta^2 \int_{-\infty}^{\infty} dh\, \frac{\partial}{\partial \Delta} \left[ P(h) f(h) \right] \ , \\ \frac{2}{\Delta} &= -\widehat{\varphi}_g \int_{-\infty}^{\infty} dh\, f(h) \frac{\partial}{\partial \Delta_r} P(h) \ . \end{aligned} \tag{10}$$

### III.2 Dynamic glass transition

Our method focuses on glasses prepared at $(T_g, \widehat{\varphi}_g)$, below the dynamical transition. Our first task is thus to compute the dynamical transition line, $T_d = T_d(\widehat{\varphi})$ for the models presented in Sec. II. To do so, let us consider the special case $(T_g, \widehat{\varphi}_g) = (T, \widehat{\varphi})$ in the above construction. In that case, $\Delta = \Delta_r \equiv \Delta_g$ is solution of $f_g$ in Eq. (10) if the glass MSD $\Delta_g$ verifies

$$\begin{aligned} \frac{1}{\widehat{\varphi}} &= -\Delta_g \int_{-\infty}^{\infty} dh\, e^h \log q(\Delta_g, \beta; h) \frac{\partial q(\Delta_g, \beta; h)}{\partial \Delta_g} \\ &\equiv \mathcal{F}_\beta(\Delta_g) \ . \end{aligned} \tag{11}$$

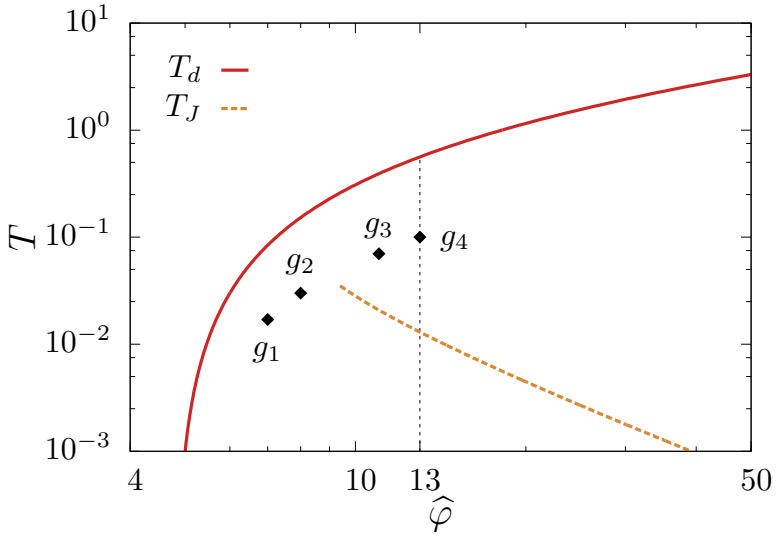


Figure 2: Equilibrium mean-field phase diagram for harmonic spheres. The dynamical transition $T_d$ (red line) separates liquids that flow (above) from dynamically arrested ones (below). We select equilibrium glasses in the dynamically arrested region, for example $g_1, ..., g_4$, and follow each glass adiabatically in temperature and packing fraction. The corresponding state-following phase diagrams are presented Fig. 5(a-d). Glasses equilibrated above the line $T_J$ (dashed line) are jammed once minimized to $T = 0$, while glasses selected below the line are unjammed at $T = 0$. The state-following phase diagrams of glasses prepared at $\widehat{\varphi}_g = 13$ (vertical dashed line) are presented in Figs. 3-4.

For the models considered here, the function $\mathcal{F}_\beta(\Delta)$ is positive, vanishes both for $\Delta \to 0$ and $\Delta \to \infty$ and has an absolute maximum in between. This means that Eq. (11) has a solution at temperature $1/\beta$ only if $1/\widehat{\varphi}$ is smaller or equal to the maximum of $\mathcal{F}_\beta$ with respect to $\Delta$. Glassy states at $T$ thus exist only at packing fractions higher than $\widehat{\varphi}_d$, defined by

$$1/\widehat{\varphi}_d = \max_{\Delta} \mathcal{F}_\beta(\Delta) \ . \tag{12}$$

We numerically solve Eq. (12) for all temperatures and find the dynamical transition line $\widehat{\varphi}_d(T)$, or equivalently $T_d(\widehat{\varphi})$. The result is represented for the harmonic potential in Fig. 2. The line separates liquids that flow from dynamically arrested ones. The qualitative behavior of $T_d(\widehat{\varphi})$ in the WCA model is similar to that of harmonic spheres presented in Fig. 2. In both cases, the dynamical transition temperature is an increasing function of $\widehat{\varphi}$, and is defined for $\widehat{\varphi} > 4.8067$, which corresponds to the dynamical transition for hard spheres [11]. In the large density limit, the WCA model behaves as the inverse power law potential, and the dynamical transition scales as $T_d \sim \widehat{\varphi}^4$. The coefficient of proportionality is $1/\Gamma_d^4$, where $\Gamma_d = 4.304$ is given by the dynamical transition of IPL glasses.

### III.3 Adiabatically following the glass properties

We focus on glasses prepared at $(T_g, \widehat{\varphi}_g)$ in the dynamically arrested phase. We study their thermodynamic properties when adiabatically brought to temperature and packing fraction $(T, \widehat{\varphi})$. In

particular, we compute the average potential energy per particle $\widehat{e}_g$, given by the derivative of $f_g$ in Eq. (7) with respect to the inverse temperature

$$\widehat{e}_g = \frac{1}{d}\frac{\partial(\beta f_g)}{\partial\beta} = -\frac{\widehat{\varphi}_g}{2}\int_{-\infty}^{\infty} dh\, P(h)\frac{\partial}{\partial\beta}f(h)\ . \tag{13}$$

The energy is to be computed using the thermodynamic values for $\Delta, \Delta_r$, which solve Eqs. (10).

We employ the following strategy to numerically solve the equations, find the values of $\Delta$ and $\Delta_r$ at each state point, and consequently compute the glass potential energy. First, we compute the MSD $\Delta_g$ of the glass at $(T_g, \widehat{\varphi}_g)$, by numerically solving Eq. (11). Starting at $(T_g, \widehat{\varphi}_g)$ with the initial condition $\Delta = \Delta_r = \Delta_g$, we gradually change the temperature and/or packing fraction by small steps towards $(T, \widehat{\varphi})$. At the beginning of each step, we use the values $\Delta, \Delta_r$ of the previous step as initial guesses. We then solve iteratively Eqs. (10) by computing the right hand side of the equations to obtain new estimates of $\Delta$ and $\Delta_r$ until convergence is reached. We repeat this procedure until the final state $(T, \widehat{\varphi})$ is reached.

### III.4 Gardner transition

The glass free energy $f_g$ defined in Eq. (7) is derived assuming that the symmetry under permutations of replicas remains unbroken. At each state point, we must check the validity of this assumption. In practice, we check that the replica symmetric solution is a stable local minimum of the free energy. The replica symmetric solution becomes locally unstable against replica symmetry breaking when one of the eigenvalues of the stability operator of the free energy changes sign [29]. This so-called replicon eigenvalue can be expressed in terms of $\Delta, \Delta_r$ as follows [60]

$$\lambda_R = 1 - \frac{\widehat{\varphi}_g}{2}\Delta^2\int_{-\infty}^{\infty} dh\, P(h) f''(h)^2\ . \tag{14}$$

At each state point, the converged values for $\Delta, \Delta_r$ are used to compute the replicon eigenvalue. In the replica symmetric, or simple glass phase, the replicon is positive. The replicon might become negative upon cooling or compressing a glass, signaling its transformation to a replica-symmetry broken glass. We show that in most cases, the simple glass transforms into a marginally stable glass, characterized by full replica symmetry breaking (fullRSB). This is a Gardner transition, in analogy to a similar phase transition found at low temperature in some spin glasses [28, 27].

In the marginally stable phase a complex, full replica symmetry breaking, solution should be used to derive accurately the thermodynamics of the glass [60]. Such solution is parametrized by a function $\Delta(x)$, for $x \in [0, 1]$, associated to the distribution of mean-squared distances between states. While computing the full function $\Delta(x)$ requires a rather heavy numerical procedure [60], one can estimate its shape close to the transition where $\lambda_R = 0$, by a perturbative calculation [61, 62]. One gets

$$\Delta(x) \sim \begin{cases} \Delta(\lambda) - \epsilon\dot{\Delta}(\lambda) & x < \lambda - \epsilon\ , \\ \Delta(\lambda) + \dot{\Delta}(\lambda)(x-\lambda) & \lambda - \epsilon < x < \lambda + \epsilon\ , \\ \Delta(\lambda) + \epsilon\dot{\Delta}(\lambda) & x > \lambda + \epsilon\ . \end{cases} \tag{15}$$

Here, $\lambda$ is called the *breaking point* or *MCT parameter*. It is related to the mean field dynamical critical exponents of the transition [63, 64, 25, 65] and, presumably, to the universality class of the transition beyond mean field theory [66]. At the transition point, $\epsilon \to 0$, and the constant RS solution $\Delta(x) = \Delta(\lambda) = \Delta$ is recovered. Because $\Delta(x)$ must be monotonically decreasing

for $x \in [0,1]$, a consistent fullRSB solution requires $\lambda \in [0,1]$ and $\dot{\Delta}(\lambda) < 0$. The perturbative calculation gives [61, 62],

$$\begin{aligned}
\lambda &= \frac{\widehat{\varphi}_g \int_{-\infty}^{\infty} dh\, P(h) f'''(h)^2}{\frac{4}{\Delta^3} + 2\widehat{\varphi}_g \int_{-\infty}^{\infty} dh\, P(h) f''(h)^3} \ , \\
\dot{\Delta}(\lambda) &= \frac{\frac{4}{\Delta^3} + 2\int_{-\infty}^{\infty} dh P(h) f''(h)^3}{\frac{12\lambda^2}{\Delta^4} - \int_{-\infty}^{\infty} dh P(h) A(h)} \ , \\
&\text{with} \\
A(h) &= f''''(h)^2 - 12\lambda f''(h) f'''(h)^2 + 6\lambda^2 f''(h)^4 \ ,
\end{aligned} \tag{16}$$

which should be evaluated at the transition point. We systematically compute the value of the breaking point $\lambda$ and slope $\dot{\Delta}(\lambda)$ at the point where $\lambda_R = 0$ in order to characterize the type of symmetry breaking transition. If $\lambda \in [0,1]$ and $\dot{\Delta}(\lambda) < 0$ it is a Gardner transition. If instead $\lambda \in [0,1]$ but $\dot{\Delta}(\lambda) > 0$, the transition is likely to be continuous towards a non-marginal 1RSB phase [62].

In the following, we will show results for the boundary between simple and replica-symmetry broken phases (1RSB and fullRSB), without further solving the thermodynamics of the glass inside the replica-symmetry broken phase. Note that here we are mostly interested in the location of the marginally stable fullRSB glass phase.

### III.5 Spinodal transition

A glass prepared at $(T_g, \widehat{\varphi}_g)$ can also be followed upon heating ($T > T_g$), or in decompression ($\widehat{\varphi} < \widehat{\varphi}_g$, equivalently $\eta < 0$). In that case, the glass energy becomes lower than the one of the liquid, until a spinodal transition is reached at $(T_{sp}, \widehat{\varphi}_{sp})$. In practice, the spinodal transition is found when the solution for $\Delta, \Delta_r$ disappears through a bifurcation. This spinodal transition physically corresponds to the melting of the glass into the liquid. At the spinodal transition thermodynamic quantities display a square-root singularity, for instance $\widehat{e}_g \sim \sqrt{T_{sp} - T}$.

Note that the replica symmetric solution also displays an unphysical spinodal transition in the region where it is unstable against fullRSB [57, 40]. This spinodal is unphysical because, for example, one finds that a glass might become unstable and melt upon cooling, which is physically inconsistent. The correct computation of the stability limit in the region where the replica symmetric solution is unstable should be done by solving the fullRSB equations, which goes beyond the scope of this work. In the phase diagrams we will show in the following, we will not draw the replica symmetric spinodal in the region where the replica solution is unstable.

### III.6 Jamming transition

The harmonic and WCA potentials Eqs. (1, 2) define a physical size for the particles. Dense assemblies of particles interacting via these two potentials will therefore have a jamming transition at $T = 0$ and some packing fraction. For each studied glass, we find the location of its corresponding jamming transition point at the replica-symmetric level. To do so, we monitor the potential energy $\widehat{e}_g$ of the glass, Eq. (13), down to $T = 0$. Depending on its value at $T = 0$, we either compress (if $\widehat{e}_g(T = 0) = 0$) or decompress (if $\widehat{e}_g(T = 0) > 0$) the zero-temperature packing until we reach the packing fraction $\widehat{\varphi}_J$ at which the energy changes from a finite value to zero. The jamming transition of the initial glass occurs at $(T = 0, \widehat{\varphi}_J)$, or equivalently at $(T = 0, \eta_J)$.

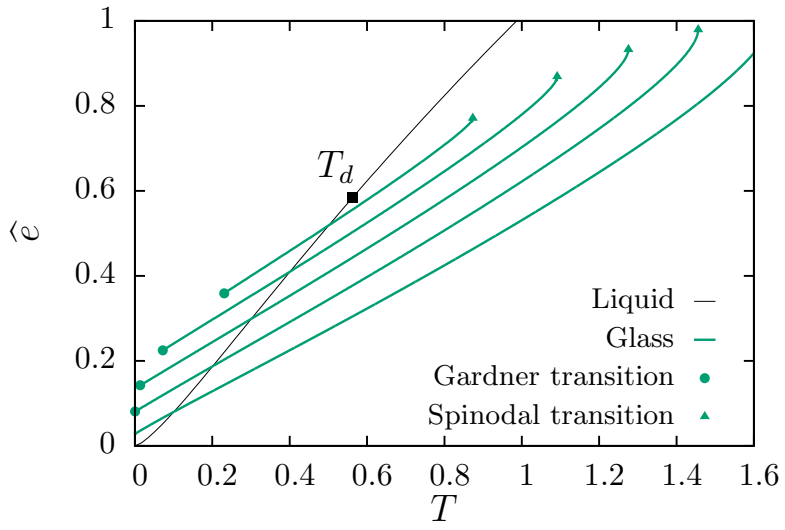


Figure 3: Energy per particle $\widehat{e}$ of the equilibrium liquid and several glasses selected at $\widehat{\varphi}_g = 13$ (vertical dashed line in Fig. 2), as a function of temperature $T$ for constant $\widehat{\varphi} = \widehat{\varphi}_g$. The energy of the liquid is given by the thin black line, on which lies the dynamical transition at $T_d = 0.562$ (black square). The energy of simple glasses created at $T_g < T_d$ ($T_g = 0.5$, 0.4, 0.3, 0.2, 0.1, from top to bottom) are represented by green lines. Upon cooling, these glasses may undergo a Gardner transition (bullets) to a marginally stable glassy phase, in which the equation of state must be computed solving the fullRSB equations (not shown). When heated, the glasses remain stable up to a temperature $T_{sp}$ (triangles) at which the glass melts into the liquid.

We stress that the location of the jamming transition depends on the specific choice of the state point $(T_g, \widehat{\varphi}_g)$ at which the glass was prepared in the phase diagram of Fig. 2. It is useful to define an additional line $T_J(\widehat{\varphi}_g)$ in the phase diagram to rationalize the results in Sec. IV. This line separates glasses into two classes: if $T_g > T_J(\widehat{\varphi}_g)$, the state is jammed at $T = 0$ and $\widehat{e}_g(T = 0) > 0$, while if $T_g < T_J(\widehat{\varphi}_g)$, the state is unjammed at $T = 0$ and $\widehat{e}_g(T = 0) = 0$. We compute this line by taking analytically the zero-temperature limit of Eqs. (10-13), and solving them numerically for all initial equilibrium glasses.

The resulting line $T_J(\widehat{\varphi}_g)$ for harmonic glasses is represented in Fig. 2. This line is qualitatively similar for WCA glasses. In both models, $T_J$ is a decreasing function of $\widehat{\varphi}$: starting from better annealed glasses (lower $T_g$) shifts the jamming transition of the glass to higher packing fractions. This feature is also observed in the phase diagram of infinite dimensional hard sphere glasses. The line $T_J$ should in principle extend to lower packing fractions and reach $T_d$. This is not the case in Fig. 2, as glasses prepared in this region present an extended marginal phase at finite temperature (for example, see Fig. 3), and the replica symmetric solution is lost before reaching $T = 0$. Using a fullRSB solution, we would find that this line extends smoothly at lower densities until hitting the dynamical transition line.

## IV State-following phase diagrams

We now present how glasses prepared in a wide range of conditions evolve when subject to cooling/heating or compression/decompression, or a combination of both. We are particularly interested

in finding the boundaries of the marginally stable phase. In Secs. IV.1 to IV.3, we present results for the harmonic sphere model. Equilibrium glasses at $(T_g, \widehat{\varphi}_g)$ are chosen in the region delimited by the dynamical transition in Fig. 2. For each initial glass, we construct a two-dimensional state-following phase diagram, presented in terms of $T$ and $\eta$. Results for the inverse power law are presented in Sec. IV.4: in this case, the representation is easier because there is a single control parameter $\Gamma = \widehat{\varphi}/T^{1/4}$. As stated above, the WCA potential would yield results similar to harmonic spheres for densities close to jamming, but similar to the inverse power law potential at large densities. We will present selected state-following results that highlight the main features of these phase diagrams, and propose a representation which summarizes the most important findings (see Fig. 6).

## IV.1 Cooling and heating glasses

We first focus on heating and cooling glasses prepared at an intermediate packing fraction, $\widehat{\varphi}_g = 13$, and several temperatures $T_g$. These equilibrium initial states are selected along the vertical dashed line displayed in the phase diagram in Fig. 2.

We present the results in terms of potential energy per particle $\widehat{e}$ as a function of temperature in Fig. 3, with the density being kept constant at its original value, $\widehat{\varphi} = \widehat{\varphi}_g$. The energy of the equilibrium liquid is computed, along with the dynamical transition at temperature $T_d = 0.562$. We select glasses within a large range of glass stabilities, prepared at $T_g = 0.5$, 0.4, 0.3, 0.2, 0.1. We then follow their energy as a function of temperature, and report the corresponding glass equations of state in Fig. 3 (colored lines). Note that all the glasses presented in Fig. 3 have a strictly positive potential energy at zero temperature. Indeed, they have all been prepared at temperatures $T_g$ higher than $T_J(\widehat{\varphi}_g = 13) = 0.013$.

Upon cooling, the simple glass may destabilize when the replicon vanishes. The slope $\dot{\Delta}(\lambda)$ is formally positive for $T_g > T_g^\dagger \simeq 0.524$, indicating that glasses prepared near the dynamical transition $T_g^\dagger < T_g < T_d$ undergo a continuous one step replica-symmetry breaking (1RSB) transition towards a non-marginal phase. We find instead that for glasses prepared at $T_g < T_g^\dagger$, such as those presented in Fig. 3, the slope $\dot{\Delta}(\lambda)$ is negative at the transition. The simple glass thus transforms into a marginally stable glass at a Gardner transition, reported with bullets in Fig. 3. The breaking point $\lambda$ computed with Eq. (16) at the Gardner transition equals $\lambda = 0.315$, 0.159, 0.068, 0.01 for $T_g = 0.5$, 0.4, 0.3, 0.2, respectively. Note that $\lambda \to 0$ when the Gardner transition temperature $T_G \to 0$, while $\dot{\Delta}(\lambda) \to -\infty$ when $T_g \to T_g^\dagger$ from below. We observe that the glass is marginally stable over a large temperature range when prepared at higher $T_g$. The extent of the marginally stable region diminishes for better annealed glasses (decreasing $T_g$). The Gardner transition temperature $T_G$ of a given glass decreases with decreasing $T_g$, so that better annealed glasses remain stable down to lower temperatures. For the most stable glass reported in Fig. 3, prepared at $T_g = 0.1$, the glass remains stable down to zero temperature, and no marginally stable phase is observed when cooling. When glasses are instead heated, their energy follows the glass equation of state and remains smaller than the energy of the liquid up to the spinodal transition $T_{sp}$ at which the glass melts into the liquid. The temperature range over which the glass remains stable increases when the glass transition temperature $T_g$ decreases, which is the experimental hallmark of increasing glass stability [67, 68, 69].

Overall, increasing the degree of annealing of the glass extends the region of stability of the simple glass phase, pushing the marginal phase to lower (possibly vanishing) temperatures and the spinodal transition to higher temperatures.

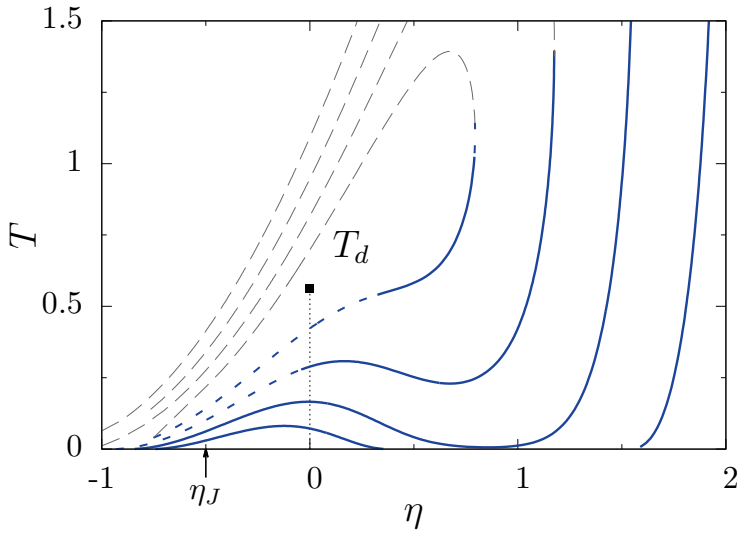


Figure 4: Glasses prepared at $\widehat{\varphi}_g = 13$, $T_g = 0.55$, 0.52, 0.47, 0.4 (top to bottom) are followed in temperature $T$ and packing fraction $\widehat{\varphi}$, expressed as $\eta = \log(\widehat{\varphi}/\widehat{\varphi}_g)$. The dynamical transition is indicated with a square. For each glass, we show the limits of stability of the simple glass. The simple glass loses it stability and melts at the glass spinodal (dashed grey). The simple glass also destabilizes at the Gardner transition (solid blue), or at a continuous transition towards a 1RSB phase (dashed blue). Below the Gardner transition line, the glass is marginally stable.

### IV.2 Temperature-density glass phase diagram

The results of thermal quenches shown in Fig. 3 give only a partial view of the state-following phase diagrams, because density is not varied. We now study how the marginally stable phase extends both in temperature and packing fraction. Specifically, we present how glass stability modifies the extent and nature of the marginally stable phase. We compute state-following phase diagrams for glasses prepared at $\widehat{\varphi}_g = 13$ and different annealing, $T_g = 0.55$, 0.52, 0.47, 0.4. For each glass, we compute the Gardner transition line $T_G(\eta)$ at which the glass becomes marginally stable, and we report it as a blue line in Fig. 4. As in Fig. 3, less annealed glasses first transform to a 1RSB glass, which we indicate with a blue dashed line. We expect the 1RSB glass to transform to a marginally stable fullRSB glass at lower temperature. For each $T_g$, we can also compute the replica symmetric spinodal where the glass melts into the liquid, also reported in Fig. 4 as a grey dashed line. For a given $T_g$, the region delimited by the solid and dashed lines defines the simple (replica symmetric) glass region. At temperatures below the blue line, the marginal (fullRSB) glass phase exists. This phase is delimited by the blue line, and by fullRSB spinodal lines that continue the grey line at lower temperatures; unfortunately, these lines can only be computed by solving the fullRSB equations, which goes beyond the scope of this work. We thus interrupt the spinodal grey line when it crosses the Gardner line, but the reader should keep in mind that this line should be continued at lower temperature to properly delimit the marginal glass phase. Glasses prepared exactly at the dynamical transition, $T_g = T_d$, are unstable towards RSB everywhere in the glassy phase. We see in Fig. 4 that the unstable phase of glasses prepared slightly below $T_d$ (top curve corresponding to $T_g = 0.55$) still extends over a large region of the state-following phase diagram. As the glass preparation temperature decreases, the unstable phase becomes everywhere marginally stable, and its extension diminishes. This observation is consistent with the results of the previous subsection,

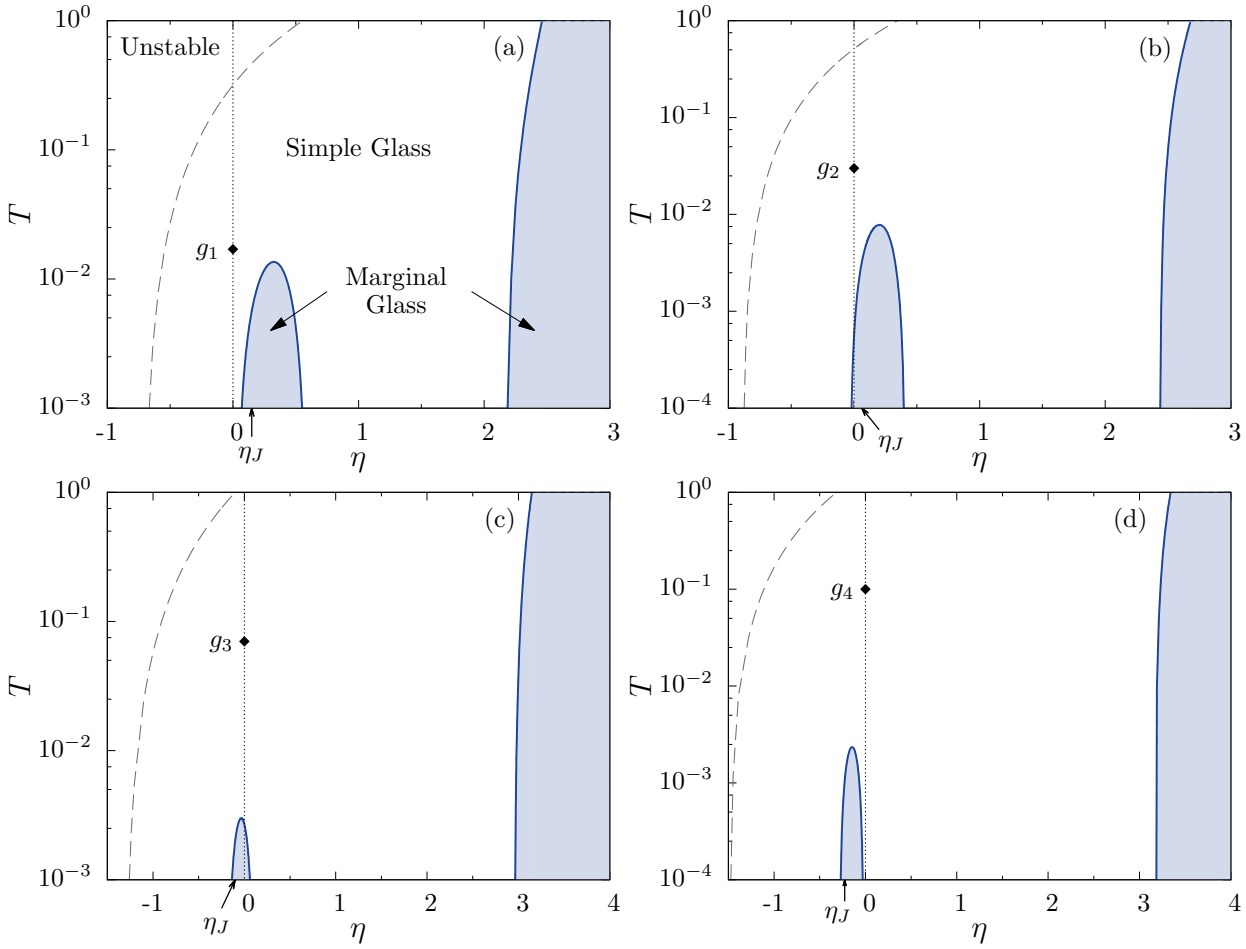


Figure 5: Mean-field state-following phase diagrams for four different starting harmonic glasses: (a) $g_1$, (b) $g_2$, (c) $g_3$, (d) $g_4$, whose location in the equilibrium phase diagram is shown Fig. 1. The region of stability of the simple glass phase is delimited by the spinodal (dashed grey line) and Gardner transition line (full blue line). Above the spinodal, the glass melts into the liquid. Below the Gardner transition line, the glass is marginally stable (shaded blue region). The jamming transition of the glasses takes place at $T = 0$, and $\eta_J$ indicated by an arrow.

but Fig. 4 reveals a new, more subtle, phenomenon. The shape of the Gardner transition line evolves qualitatively as $T_g$ decreases. While the Gardner transition line $T_G(\eta)$ of the less stable glasses (top curves in Fig. 4) increases monotonically with $\eta$, it becomes non-monotonic for lower $T_g$. For very well annealed glasses, such as $T_g = 0.4$, the line even forms two disconnected regions. The marginal phase then comprises a 'dome' around the jamming transition occurring at $\eta_J = \log(\widehat{\varphi}_J/\widehat{\varphi}_g)$, and a second region located at high compression $\eta$, as also observed in [39]. The Gardner transition line which defines the latter region is qualitatively similar to the one found for the less stable glasses, but it is shifted to much higher packing fractions.

We argue that these two distinct marginally stable phases have a different character. The Gardner phase surrounding the jamming transition is similar to the one found by compressing hard sphere glasses. The presence of a Gardner phase is crucial for an accurate mean-field description of jamming. The marginally stable phase at high compression appears as a remanent of the marginality which exists near the dynamical transition. It is always present, and increasing the glass stability only shifts that phase to higher density. Finally, these two distinct phases would also be present for the WCA pair potential over a range of intermediate densities, because WCA particles and harmonic spheres have the same behavior in this regime. However, WCA particles behave qualitatively differently at large densities, as described below in Sec. IV.4 where the inverse power law potential is analyzed.

### IV.3 Interplay between jamming and Gardner phase

We have studied the state-following phase diagrams of many initial glasses prepared in a variety of conditions $(T_g, \widehat{\varphi}_g)$. We find that the phenomenon described in the previous subsection is generically observed for glasses prepared in all regions of the glass phase. For well-annealed glasses, the marginally stable phase always splits into two distinct regions. We focus on four representative well-annealed glasses $g_1, ..., g_4$, prepared at state points marked by black squares in Fig. 2. These glasses are stable enough that the Gardner phase is separated into two distinct regions.

We present in Fig. 5(a-d) the state-following phase diagram for each initial glass $g_1, ..., g_4$. We first determine the location of the jamming transition $(T = 0, \widehat{\varphi}_J)$ for each initial glass. The value $\eta_J = \log(\widehat{\varphi}_J/\widehat{\varphi}_g)$ is indicated in Fig. 5(a-d). We then focus on the limit of stability of the simple glass phase. For all four glasses, we draw the corresponding Gardner transition lines separating the two types of glasses, which separates into a dome around jamming and a marginal phase at high compression. We have checked that the simple glass always destabilizes to a marginally stable (fullRSB) glass, as the slope $\dot{\Delta}(\lambda)$ is always negative. The parameter $\lambda$ is finite at the left end of the dome (corresponding to the hard sphere Gardner transition [60]), and decreases along the dome to reach $\lambda = 0$ at its right end, corresponding to a zero-temperature soft sphere Gardner transition. It then increases again from $\lambda = 0$ at zero temperature, along the higher-density Gardner transition line. The difference between the four diagrams is the relative location of all these elements.

The glasses $g_1$ and $g_2$ are prepared below the line $T_J$. Their jamming transition is therefore found by compressing the glass ($\eta_J > 0$) at $T = 0$. In addition, $|\eta_J^{g_2}| < |\eta_J^{g_1}|$ because $g_2$ is prepared closer to the line $T_J$ in Fig. 2. Glasses $g_3$ and $g_4$ are prepared above $T_J$, and their jamming transition takes place when decompressing them ($\eta_J < 0$) at $T = 0$. Moreover, $|\eta_J^{g_4}| > |\eta_J^{g_3}|$ because $g_3$ is prepared closer to $T_J$ in Fig. 2.

For the glass $g_1$, the dome surrounding jamming only appears for $\eta > 0$, and this glass does not undergo a Gardner transition as it is cooled down to zero temperature at constant density. By contrast, the denser glass $g_2$ is located above the dome of marginality, and that glass can

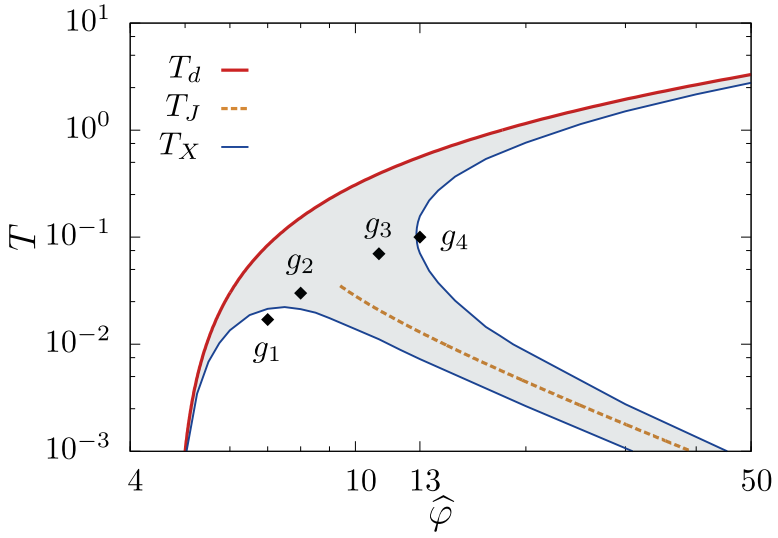


Figure 6: Equilibrium mean-field phase diagram of harmonic spheres, as in Fig. 2. We add the transition lines $T_X$ (thin lines) which delimit the glasses that become unstable upon cooling (shaded region), such as $g_2$, and $g_3$, or not, as for $g_1$ and $g_4$.

undergo a Gardner transition simply by cooling. A similar qualitative difference is observed for the glasses $g_3$ and $g_4$, both prepared above the $T_J$. The glass $g_3$ will become marginal if cooled at constant packing fraction, while the glass $g_4$ will remain stable down to its ground state. Despite these differences, all these glasses can nevertheless become marginal by a combination of cooling and compression/decompression over a broad range of state points. Finally, all these glasses also become marginal when compressed to large packing fractions far above jamming.

The phase diagrams found in Fig. 5 suggest the existence of two types of behaviors. Some glasses undergo a Gardner transition as they are cooled, while some glasses do not. This distinction depends both on the initial temperature $T_g$ of the glass, and on its initial density $\widehat{\varphi}_g$. To distinguish between these two types of glasses, we define a line $T_X(\widehat{\varphi}_g)$ which delimits in the $(T_g, \widehat{\varphi}_g)$ phase diagram. Our results for $T_X$ are reported in Fig. 6. Glasses prepared in the shaded part of this phase diagram, like $g_2$ and $g_3$ undergo a Gardner transition to a marginally stable phase upon cooling at constant density. The other glasses, like $g_1$ and $g_4$ do not and remain stable glasses down to $T = 0$. The corresponding phase diagram presented in Fig. 6 is rather complex, exhibiting non-monotonic re-entrant lines $T_X$. The mean-field phase diagram of soft repulsive spheres is therefore not a trivial extension of the one of hard spheres. Figure 6 shows that a Gardner phase is relevant for hard sphere glasses, for soft particles prepared not too far from either the dynamical transition $T_d$ and the temperature $T_J$, which suggests two distinct possible physical origins for the Gardner phase.

### IV.4 Dense liquid regime

We now focus on the dense liquid regime modeled by the IPL potential. This also corresponds to the large density limit of the WCA model, where only the repulsive part of the Lennard-Jones interaction is physically relevant. We follow the strategy and representation adopted in Sec. IV.2 for the harmonic spheres.

The thermodynamic state of IPL glasses only depends on the combination $\Gamma = \widehat{\varphi}/T^{1/4}$. The

complete phase diagram for the IPL model can therefore be completely understood by fixing for instance the packing fraction and changing the temperature of the glass. For convenience, we choose $\widehat{\varphi}_g = 4.304$, for which the dynamical transition takes place at $T_d = 1$. We consider glasses with different stabilities, prepared at $T_g < T_d$. Despite the one-dimensional nature of the phase diagram, we show results for IPL glasses using the same representation as for harmonic spheres, using both $T$ and $\eta$, to allow for a more direct comparison of the two types of models. By definition, all lines in this diagram exactly obey the relation $T \propto e^{4\eta}$.

We find that glasses prepared at $T_g < T_g^\dagger \simeq 0.92$ transforms into a marginally stable glass when cooled. Instead, glasses prepared in the range $T_g^\dagger < T_g < T_d$ first transform into a 1RSB glass. As for harmonic spheres, the slope $\dot{\Delta}(\lambda)$ is negative for $T_g < T_g^\dagger$, diverges upon approaching $T_g^\dagger$ from below, and is formally positive above it. The Gardner transition lines for glasses prepared at $T_g = 0.9$, 0.8, 0.7, and 0.6 are presented in Fig. 7. They have the form $T_G(\eta) = T_G(\eta = 0)e^{4\eta}$, where $T_G(\eta = 0)$ is the Gardner transition temperature obtained for a simple cooling of the glass. The breaking point $\lambda$ at the Gardner transition is equal to $\lambda = 0.407$, 0.283, 0.168, 0.042 for $T_g = 0.9$, 0.8, 0.7, and 0.6 respectively. As for harmonic spheres, $\lambda \to 0$ when $T_G$ vanishes. The marginally stable phase is pushed to larger densities and lower temperatures (in fact, to larger $\Gamma$) as the glass stability increases. In this model, however, particles do not possess a physical size (the potential has no cutoff at a finite distance), and hence the jamming transition cannot be observed. As a consequence, the 'domes' of marginal stability found around the jamming transition in Figs. 4-5 for harmonic spheres are absent for the IPL model. The behavior of the Gardner transition lines at high $\eta$ with decreasing $T_g$ is similar in the IPL and WCA models. The WCA potential instead behaves as harmonic spheres near jamming and is thus characterized by domes around jamming.

In this dense liquid regime, glasses prepared at $T_g < 0.567$ remain stable down to their ground state at $T = 0$, as reported before [40]. The most stable glass for which we report the Gardner transition line in Fig. 7 is $T_g = 0.6$. Below this value, glasses remain stable in the entire phase diagram and never undergo a transition to a marginally stable phase, even at arbitrarily large compressions. This is consistent with the high density/temperature limit found in the harmonic phase diagram Fig. 6, where only glasses prepared in the vicinity of the dynamical transition become marginally stable upon cooling (shaded region). However, harmonic spheres are qualitatively distinct from both WCA and IPL potential regarding compression of very stable glasses: whereas harmonic spheres always reach marginal states upon compression at constant temperature, very stable WCA and IPL glasses do not. Note also that for harmonic spheres, the Gardner and spinodal lines meet at high density, so that the glass always melts upon large enough compression, which is not the case of the WCA and IPL models.

# V Discussion and perspectives

In this work, we have obtained the complete mean-field phase diagrams of several glass-forming models. In particular, we provided detailed information regarding the location of the marginally stable glass phases for a variety of pair interactions and physical conditions, extensively exploring physical regimes relevant to granular materials, foams, emulsions, hard and soft colloids, and molecular glasses. We find that all types of glasses may become marginally stable upon cooling or compression, but the extent of marginal phases strongly depends on the preparation protocol and the chosen model. We find that increasing the glass stability systematically reduces the extent of marginality. For well-annealed glasses, we find that marginality emerges in two distinct regions, either around the jamming transition or at high compression. Our results suggest that marginal

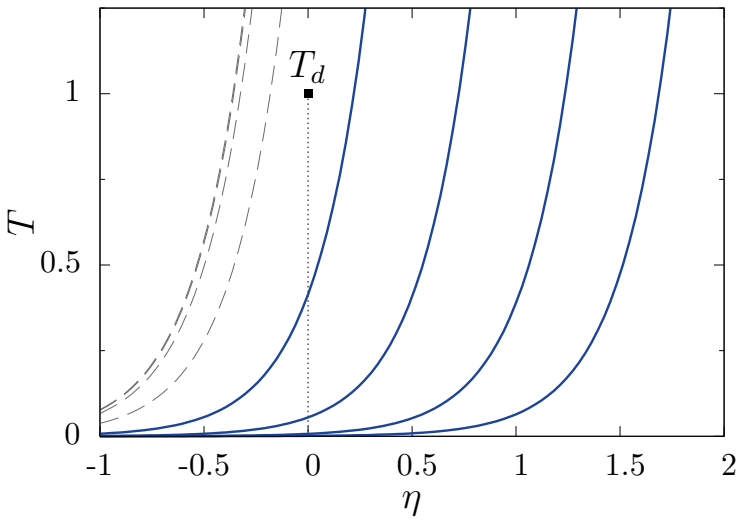


Figure 7: Dense liquid regime analyzed using the IPL potential. Glasses prepared at $\widehat{\varphi}_g = 4.304$ ($T_d = 1$), for various $T_g = 0.9$, 0.8, 0.7, 0.6 are followed in the $(T, \eta)$ plane. For each glass, we represent the state-following Gardner transition line $T_G(\eta)$ (full lines) and the spinodal (dashed lines). All lines obey $T \sim e^{4\eta}$. The marginal phase shifts to large density and lower temperatures as $T_g$ decreases, and disappears altogether for $T_g < 0.567$.

phases should be easily observable for colloidal and non-Brownian particles near jamming, or poorly annealed glasses.

Our study unifies previous results on marginal stability in mean-field models [25, 26, 39, 40]. Already in mean-field theory, marginal stability emerges under distinct physical conditions in different microscopic models. This provides a way to reconcile apparently contradictory numerical and experimental studies aimed at detecting Gardner phases in finite dimensional glasses, where its existence is still debated [70, 71]. In particular, the evidence for marginally stable phases reported for $2d$ and $3d$ hard spheres glasses under compression contrasts with its absence in $2d$ and $3d$ numerical models of dense liquids upon cooling. Our analysis shows that already at the mean-field level these two types of systems behave differently. In addition, while the critical properties around the jamming transition remain unchanged from $d = \infty$ down to $d = 2$ [72, 73], the nature of the mean-field dynamical transition is highly altered by finite dimensional fluctuations [74]. For instance, our results predict that highly compressed dense liquids should be marginally stable (see also [41]), a protocol that was never tested in finite dimensional studies.

Our results will be useful to guide future numerical simulations and experiments aimed at detecting marginally stable phases in finite dimensional glasses. We find that mean-field Gardner phases are not restricted to exist in the immediate vicinity of jamming, and could be more broadly relevant to a wide class of materials. We are currently numerically investigating, along the lines of this theoretical work, the evolution of the Gardner transition while continuously interpolating between regimes relevant to dense hard sphere glasses and dense liquids, using a WCA potential [49].

Our results open a number of additional perspectives for future work. One finding is that soft sphere glasses can undergo a zero-temperature Gardner transition, as reported in Fig. 5. A convenient protocol to observe this transition is suggested in Fig. 5d for the glass $g_4$. It can be quenched at $T = 0$, where it is jammed and in the simple glass phase. It is therefore a stable harmonic energy

minimum. Under decompression at $T = 0$, this state undergoes a Gardner transition before unjamming. The signature of this zero-temperature Gardner transition, if it exists in $2d$ or $3d$, would be particularly dramatic: the Hessian would develop delocalized soft modes [32], and the system would start responding by intermittent avalanches [35] to an applied strain. A divergent correlation length would also develop in the contact network [75]. The absence of thermal fluctuations should make the study of this transition much easier than in the thermal case.

While the nature of the mean-field Gardner transition is certainly affected in finite dimensions [70], the existence of extended marginally stable phases should give rise to interesting new physics in structural glasses. As happens in spin glasses, even if the Gardner phase transition is avoided in physical dimensions [48], it may still be the case that interesting physical phenomena, such as aging and non-linear dynamics, remain relevant to describe the behavior of structural glasses.

**Acknowledgments** – We thank G. Biroli and P. Urbani for useful exchanges. This work was supported by a grant from the Simons Foundation (#454933, L. Berthier, #454955, F. Zamponi). This project has received funding from the European Research Council (ERC) under the European Union's Horizon 2020 research and innovation program (grant agreement 723955 - GlassUniversality).

## Bibliography

[1] Andrea J. Liu and Sidney R. Nagel. *Nature*, 396(6706):21–22, 1998.

[2] Andrea J. Liu and Sidney R. Nagel. *Jamming and Rheology: Constrained Dynamics on Microscopic and Macroscopic Scales*. Taylor & Francis, 2001.

[3] Andrea Cavagna. *Phys. Rep.*, 476(4-6):51–124, 2009.

[4] Ludovic Berthier and Giulio Biroli. *Rev. Mod. Phys.*, 83:587–645, 2011.

[5] Andrea J. Liu and Sidney R. Nagel. *Annu. Rev. Condens. Matter Phys.*, 1(1):347–369, 2010.

[6] Andrea J. Liu, Sidney R. Nagel, Wim Van Saarloos, and Matthieu Wyart. In L. Berthier, G. Biroli, J-P Bouchaud, L. Cipelletti, and W. van Saarloos, editors, *Dynamical Heterogeneities and Glasses*. Oxford University Press, 2011.

[7] Ludovic Berthier and Thomas A. Witten. *Phys. Rev. E*, 80(2):021502, 2009.

[8] Atsushi Ikeda, Ludovic Berthier, and Peter Sollich. *Phys. Rev. Lett.*, 109:018301, 2012.

[9] Romain Mari, Florent Krzakala, and Jorge Kurchan. *Phys. Rev. Lett.*, 103(2):025701, 2009.

[10] Pinaki Chaudhuri, Ludovic Berthier, and Srikanth Sastry. *Phys. Rev. Lett.*, 104(16):165701, 2010.

[11] Giorgio Parisi and Francesco Zamponi. *Rev. Mod. Phys.*, 82(1):789–845, 2010.

[12] M. Ozawa, T. Kuroiwa, A. Ikeda, and K. Miyazaki. *Phys. Rev. Lett.*, 109:205701, 2012.

[13] R. C. Zeller and R. O. Pohl. *Phys. Rev. B*, 4(6):2029, 1971.

[14] David G Cahill and R. O. Pohl. *Annual review of physical chemistry*, 39(1):93–121, 1988.

[15] Leonardo E. Silbert, Andrea J. Liu, and Sidney R. Nagel. *Phys. Rev. Lett.*, 95(9):098301, 2005.

[16] E. Lerner, E. DeGiuli, G. Düring, and M. Wyart. *Soft Matter*, 10(28):5085–5092, 2014.

[17] Patrick Charbonneau, Eric I. Corwin, Giorgio Parisi, Alexis Poncet, and Francesco Zamponi. *Phys. Rev. Lett.*, 117:045503, 2016.

[18] Matthieu Wyart, Sidney R. Nagel, and Thomas A. Witten. *Europhysics Letters*, 72(3):486–492, 2005.

[19] Matthieu Wyart, Leonardo E. Silbert, Sidney R. Nagel, and Thomas A. Witten. *Phys. Rev. E*, 72(5):051306, 2005.

[20] Markus Müller and Matthieu Wyart. *Annu. Rev. Condens. Matter Phys.*, 6(1):177–200, 2015.

[21] T. R. Kirkpatrick and P. G. Wolynes. *Phys. Rev. A*, 35(7):3072–3080, 1987.

[22] Theodore R. Kirkpatrick and Devarajan Thirumalai. *Phys. Rev. Lett.*, 58(20):2091–2094, 1987.

[23] Marc Mezard and Giorgio Parisi. Glasses and replicas. In Peter G. Wolynes and Vassiliy Lubchenko, editors, *Structural Glasses and Supercooled Liquids: Theory, Experiment and Applications*. Wiley & Sons, 2012.

[24] Vassiliy Lubchenko and Peter G. Wolynes, editors. *Structural Glasses and Supercooled Liquids: Theory, Experiment, and Applications*. Wiley, 2012.

[25] Jorge Kurchan, Giorgio Parisi, Pierfrancesco Urbani, and Francesco Zamponi. *J. Phys. Chem. B*, 117:12979–12994, 2013.

[26] Patrick Charbonneau, Jorge Kurchan, Giorgio Parisi, Pierfrancesco Urbani, and Francesco Zamponi. *Annu. Rev. Condens. Matter Phys.*, 8:265–288, 2017.

[27] David J. Gross, Ido Kanter, and Haim Sompolinsky. *Phys. Rev. Lett.*, 55:304–307, 1985.

[28] Elisabeth Gardner. *Nucl. Phys. B*, 257:747–765, 1985.

[29] Marc Mézard, Giorgio Parisi, and Miguel A Virasoro. *Spin glass theory and beyond*. World Scientific, Singapore, 1987.

[30] Ludovic Berthier, Patrick Charbonneau, Yuliang Jin, Giorgio Parisi, Beatriz Seoane, and Francesco Zamponi. *Proc. Natl. Acad. Sci. U.S.A.*, 113(30):8397–8401, 2016.

[31] Atsushi Ikeda, Ludovic Berthier, and Giulio Biroli. *J. Chem. Phys.*, 138:12A507, 2013.

[32] Silvio Franz, Giorgio Parisi, Pierfrancesco Urbani, and Francesco Zamponi. *Proc. Natl. Acad. Sci. U.S.A.*, 112(47):14539–14544, 2015.

[33] Silvio Franz, Thibaud Maimbourg, Giorgio Parisi, and Antonello Scardicchio. Low-temperature anomalies in structural glasses: impact of jamming criticality. `arXiv:1811.11719`, 2018.

[34] Giulio Biroli and Pierfrancesco Urbani. *Nature Physics*, 12:1130–1133, 2016.

[35] Silvio Franz and Stefano Spigler. *Phys. Rev. E*, 95(2):022139, 2017.

[36] Yuliang Jin and Hajime Yoshino. *Nature Communications*, 8:14935, 2017.

[37] H. George. E. Hentschel, Smarajit Karmakar, Edan Lerner, and Itamar Procaccia. *Phys. Rev. E*, 83(6):061101, 2011.

[38] Itamar Procaccia, Corrado Rainone, Carmel A. B. Z. Shor, and Murari Singh. *Phys. Rev. E*, 93:063003, 2016.

[39] Giulio Biroli and Pierfrancesco Urbani. *SciPost Phys.*, 4:20, 2018.

[40] Camille Scalliet, Ludovic Berthier, and Francesco Zamponi. *Phys. Rev. Lett.*, 119:205501, 2017.

[41] Vassiliy Lubchenko and Peter G Wolynes. *The Journal of Physical Chemistry B*, 122(13): 3280–3295, 2017.

[42] Patrick Charbonneau, Eric I. Corwin, Lin Fu, Georgios Tsekenis, and Michael van der Naald. *Phys. Rev. E*, 99:020901, 2019.

[43] Beatriz Seoane and Francesco Zamponi. *Soft Matter*, 14:5222–5234, 2018.

[44] Antoine Seguin and Olivier Dauchot. *Phys. Rev. Lett.*, 117:228001, 2016.

[45] Qinyi Liao and Ludovic Berthier. *Phys. Rev. X*, 9:011049, 2019.

[46] Beatriz Seoane, Daniel R. Reid, Juan J. de Pablo, and Francesco Zamponi. *Phys. Rev. Mate-*

*rials*, 2:015602, 2018.

[47] Korbinian Geirhos, Peter Lunkenheimer, and Alois Loidl. *Phys. Rev. Lett.*, 120:085705, 2018.

[48] C. L. Hicks, Michael J. Wheatley, Michael J. Godfrey, and Micheal A. Moore. *Phys. Rev. Lett.*, 120:225501, 2018.

[49] Camille Scalliet, Ludovic Berthier, and Francesco Zamponi. In preparation (2019).

[50] Douglas J Durian. *Phys. Rev. Lett.*, 75:4780–4783, 1995.

[51] David Ruelle. *Statistical mechanics: Rigorous results*. World Scientific, 1999.

[52] Monica Skoge, Aleksandar Donev, Frank H. Stillinger, and Salvatore Torquato. *Phys. Rev. E*, 74(4):041127, 2006.

[53] Jacobus A. van Meel, Benoit Charbonneau, Andrea Fortini, and Patrick Charbonneau. *Phys. Rev. E*, 80(6):061110, 2009.

[54] Silvio Franz and Giorgio Parisi. *J. Phys. I France*, 5(11):1401–1415, 1995.

[55] Lenka Zdeborová and Florent Krzakala. *Phys. Rev. B*, 81:224205, 2010.

[56] Florent Krzakala and Lenka Zdeborová. *EPL (Europhysics Letters)*, 90(6):66002, 2010.

[57] Corrado Rainone, Pierfrancesco Urbani, Hajime Yoshino, and Francesco Zamponi. *Phys. Rev. Lett.*, 114(1):015701, 2015.

[58] Wolfgang Götze. *Complex dynamics of glass-forming liquids: A mode-coupling theory*, volume 143. OUP, USA, 2009.

[59] Thibaud Maimbourg, Jorge Kurchan, and Francesco Zamponi. *Phys. Rev. Lett.*, 116(1):015902, 2016.

[60] Corrado Rainone and Pierfrancesco Urbani. *J. Stat Mech.*, 2016(5):P053302, 2016.

[61] H-J Sommers. *Journal de Physique Lettres*, 46(17):779–785, 1985.

[62] S. Franz, G. Parisi, M. Sevelev, P. Urbani, F. Zamponi, and M. Sevelev. *SciPost Physics*, 2(3): 019, 2017.

[63] F. Caltagirone, U. Ferrari, L. Leuzzi, G. Parisi, F. Ricci-Tersenghi, and T. Rizzo. *Phys. Rev. Lett.*, 108:085702, 2012.

[64] Silvio Franz, Hugo Jacquin, Giorgio Parisi, Pierfrancesco Urbani, and Francesco Zamponi. *Proceedings of the National Academy of Sciences*, 109(46):18725–18730, 2012.

[65] Giorgio Parisi and Tommaso Rizzo. *Physical Review E*, 87:012101, 2013.

[66] Giorgio Parisi, Federico Ricci-Tersenghi, and Tommaso Rizzo. *Journal of Statistical Mechanics: Theory and Experiment*, 2014(4):P04013, 2014.

[67] Shakeel S. Dalal and Mark D. Ediger. *The Journal of Physical Chemistry Letters*, 3(10):1229–1233, 2012.

[68] Mark D. Ediger. *The Journal of Chemical Physics*, 147(21):210901, 2017.

[69] Christopher J. Fullerton and Ludovic Berthier. *EPL (Europhysics Letters)*, 119(3):36003, 2017.

[70] Pierfrancesco Urbani and Giulio Biroli. *Phys. Rev. B*, 91:100202, 2015.

[71] Patrick Charbonneau and Sho Yaida. *Phys. Rev. Lett.*, 118:215701, 2017.

[72] Carl P Goodrich, Andrea J Liu, and Sidney R Nagel. *Phys. Rev. Lett.*, 109(9):095704, 2012.

[73] P. Charbonneau, E. Corwin, G. Parisi, and F. Zamponi. *Phys. Rev. Lett.*, 114:125504, 2015.

[74] Theodore R. Kirkpatrick, Devarajan Thirumalai, and Peter G. Wolynes. *Phys. Rev. A*, 40(2): 1045–1054, 1989.

[75] Daniel Hexner, Andrea J. Liu, and Sidney R. Nagel. *Phys. Rev. Lett.*, 121:115501, 2018.

Chapter 3

# Numerical exploration of the glass phase in three-dimensional models

The mean field theory predicts that glasses prepared in various physical conditions are become marginally stable at low temperature or high compression. This opens the possibility for a unified study of low-temperature glassy anomalies. The theory predicts in particular that glasses characterized by long-ranged interactions, which model dense atomic glasses, are marginally stable at low temperature. The excess of low-lying excitations associated to a Gardner phase could provide a new explanation, based on first-principles, for the violation of Debye theory in atomic glasses.

The investigation of Gardner phases in $3d$ glasses is motivated by numerical evidence for a Gardner phase in three-dimensional hard sphere glasses [193]. These encouraging results suggest that mean field predictions may survive down in $3d$. In this Chapter, we provide an extensive exploration of the glass phase in $3d$ models. The aim is to determine whether or not a Gardner phase is found, as universally as in mean field, in $3d$ glasses.

In the first article, 'Absence of marginal stability in a structural glass' [222], we compare mean field and numerical results for a glass-forming model with soft, long-ranged repulsive interactions $V(r) \propto 1/r^{12}$. This study is the first numerical investigation of a Gardner transition upon cooling in a model which does not possess a jamming transition. The aim was to determine whether a Gardner transition can take place far from jamming in $3d$ glasses.

The mean field phase diagram of the model is first discussed. It is obtained by solving the equations derived in Chapter 2. At the mean field level, soft glasses become marginally stable upon cooling even in the absence of a jamming transition. We find that the presence of a Gardner phase is not universal: only glasses prepared in the range $0.5\ T_d \lesssim T_g \leq T_d$ enter a Gardner phase at low temperature. More stable glasses, prepared at lower $T_g$ remain stable down to $T = 0$. The physical relevance of glasses prepared in equilibrium at $T_g \lesssim 0.5\ T_d$, remains questionable. Thermalization at such temperatures is challenging both in computer simulations and experiments.

We study the same model in $3d$ by means of molecular dynamics simulations. Stable glasses are produced with the swap algorithm in the range $0.62\ T_d \leq T_g < T_d$. In order to probe the landscape of glasses, we create 'clones' of them (same initial positions, different velocities). The clones are quenched independently to a lower temperature $T$. We measure the mean-squared distance (MSD) between the particles in different clones, $\Delta_{AB}$, and the standard mean-squared displacement of particles within a clone $\Delta$. We focus in particular on their long-time limit as a

function of temperature. We find that for all glasses there exists a crossover temperature $T^\star$, such that $\Delta_{AB} = \Delta$ for $T > T^\star$, and $\Delta_{AB} > \Delta$ for $T < T^\star$, at long times. Ergodicity is lost in the glass at low temperature: the clones fall into dynamically inaccessible minima at $T < T^\star$. This loss of ergodicity inside a glass is consistent with the mean field picture of a Gardner transition.

However, the loss of ergodicity is not accompanied by further evidence for a Gardner transition. No slowing down in vibrational dynamics is detected as $T^\star$ is approached. We measure a spin-glass susceptibility $\chi_{AB}$, which quantifies the number of correlated particles in the vibrational dynamics. The susceptibility is of order one at all times and temperatures, signaling uncorrelated dynamics. The absence of growing timescale and lengthscale around $T^\star$ is observed for all the glasses studied $0.62\ T_d \leq T_g < T_d$. This is the largest glass preparation range currently accessible. Above $T_d$, activated events destabilize the glass, making the search for a Gardner transition intricate. The lower bound for $T_g$ is set by the efficiency of the swap algorithm.

We investigate at the particle level the origin of the loss of ergodicity, and find that it is due to localized defects. A small fraction of particles can take at least two nearby positions. At $T \lesssim T_g$, the particles can explore all available minima, but become trapped in one of them at lower temperature. The crossover temperature $T^\star$ is related to the energy barrier between the nearby minima. The localized nature of the defects explains the absence of a growing lengthscale: only a few particles are more mobile ; and timescale: the MSD $\Delta$ is dominated by the behavior of the majority of particles, which is featureless. As a conclusion, $3d$ soft repulsive glasses do not undergo a Gardner transition to a marginally stable phase at low temperature. An important effort is being devoted to identifying the consequences of localized, or 'quasi-localized' defects for the dynamics, vibrational density of states, and rheology of glasses.

The results of this study are in stark contrast with those of $3d$ hard sphere glasses [222]. This discrepancy was confirmed by subsequent studies on hard spheres [223, 224] and soft particles [225]. The same glass preparation protocol, and similar observables were employed in all studies. The existence of a Gardner phase in finite-dimensional glasses is not universal. As predicted by non perturbative RG studies, glass-forming models may or may not possess a Gardner transition in $3d$. This work points out the need for a systematic exploration of the glassy phase in $3d$, in order to reconcile the existence, and absence, of marginal stability in glasses with hard, respectively soft interactions.

The results of such a systematic exploration are presented in the second article, 'Nature of defects and excitations in structural glasses' [226]. We explore the glassy phase of the $3d$ Weeks-Chandler-Andersen model. This study parallels the work of the article 'Marginally stable phases in mean-field structural glasses' of Chapter 2. The WCA model allows to continuously interpolate between the hard-sphere regime, recovered in the limit $T = 0$, and the dense liquid regime, found at high packing fraction $\varphi$ and temperature. We study glasses prepared at various state points $(\varphi_g, T_g)$, corresponding to different physical regimes and glass stabilities.

The loss of ergodicity at low temperature is found in all glasses. This suggests that all glasses are characterized by a rough energy landscape, composed by many minima. This loss of ergodicity may or may not be accompanied by a growing lengthscale, dynamic heterogeneity and aging effects, depending on the density regime. Our main finding is that the nature of the energy landscape depends strongly on the density regime and evolves continuously from the jamming regime (hard-sphere behavior), to larger densities and temperatures (soft potential behavior).

At high densities, in the regime relevant for molecular and atomic glasses, the landscape is relatively simple, and characterized by few minima. The dynamical behavior of the glass is dictated by

highly localized defects, which correspond to a few particles hopping between nearby configurations. By contrast, at lower densities corresponding to the vicinity of the zero-temperature jamming transition, relevant for granular materials, the landscape is very rough and has a hierarchical structure. We find barriers with a broad range of energy scales, and a degree of localization that spans very localized to highly extended defects. This confirms the two previous numerical studies.

Most interestingly, in the intermediate regime of densities, relevant for soft colloidal particles and emulsions, the landscape is characterized by both features. We find localized defects associated to high energy barriers, and are responsible for ergodicity breaking inside the glass. The freezing of these defects, which involve a few particles, defines a small number of sub-basins. Each sub-basin, however, possesses a complex structure at lower energy scales, with extended defects associated to low barriers that appear similar to the ones found in the vicinity of jamming.

We provide the first numerical evidence for a Gardner transition in thermal soft glasses in $3d$, which extends the hard-sphere results to thermal systems. When present, the Gardner phase forms a 'dome' in temperature and packing fraction around the jamming transition. While the Gardner and jamming critical regions (see Sec. 1.2.3, Fig. 1.9) have a similar shape, the marginally stable region is much more extended than that of jamming criticality, and contains the latter.

We are successful in finding in which physical conditions $3d$ glasses are marginally stable. This opens the possibility to explore the low-temperature physics and dynamics of structural glasses characterized by complex landscapes.

In the third article, 'Rejuvenation and Memory Effects in a Structural Glass' [227], we take advantage of our systematic exploration of the glassy phase to study the nonequilibrium dynamics of glasses evolving in a hierarchical landscape. We perform a temperature cycle protocol, similarly to spin-glass studies. We study WCA glasses prepared at intermediate density, for which a Gardner phase was found at low temperature. The high-temperature fluid is suddenly cooled to $T_1$ in the glass phase, where it ages for a long time $t_1$. The glass is then cooled to a lower temperature $T_2 < T_1$. For sufficiently low $T_2$, aging dynamics restarts. This nontrivial 'rejuvenation' effect is due to the hierarchical structure of the glass landscape. The glass is aged for $t_2 = t_1$ at $T_2$, before being heated back to $T_1$. At $T_1$, the glass has kept a 'memory' of its state, and aging dynamics proceeds as if nothing had happened at $T_2$.

Rejuvenation and memory effects were used in the past to compare and classify different classes of glasses. We demonstrate that in some conditions, structural glasses such as colloidal and granular glasses, behave like spin-glasses rather than molecular glasses. Our three numerical studies rationalize the absence of memory and rejuvenation effects in atomic and molecular glasses. Their behavior is dominated by the presence of a few localized defects, and not a hierarchical distribution of energy barriers corresponding to extended defects.

In the last article of this Chapter, 'Reduction of tunneling two-level systems in ultrastable computer glasses' [228], we investigate the classical and quantum tunneling properties of the localized defects identified in the work 'Absence of marginal stability in a structural glass'.

Since the 70s, it is known that glasses universally present anomalous transport properties at low temperatures, typically around 1 $K$. While Debye's theory for crystalline solids predicts that the specific heat scales as $T^3$, it is found to scale as $T$ in many glasses [48]. This implies that phonons are not the only type of excitations in glasses at very low temperature. Shortly after the publication of these experimental observations, a phenomenological model was put forward to rationalise them [51]. Since then, it is broadly accepted that due to disorder, there exists

some localized defects, or two-level systems (TLS), which can tunnel quantum mechanically at low temperature. One cannot 'observe' TLS in glasses, which makes our understanding of these excitations very poor. Our study is motivated by the fact that glasses prepared via physical vapor deposition at temperature 0.85 $T_g$, do not show the so-called 'universal' anomalies [69]. There is evidence that these vapor deposited (VD) glasses lie very deep in the energy landscape [229]. There is additional evidence that VD glasses are anisotropic. The current debate among experimentalists is whether the suppression of TLS is due to the anisotropy of the glasses, or them having very low enthalpy.

We provide fresh insight into these old and new problems. We use the method presented in Chapter 4 to prepare *in silico* glasses in an unprecedentedly wide range of stabilities. This amounts to tuning the quench rate used during glass preparation. We focus in particular on three glass stabilities, referred to as hyper-quenched, liquid-cooled, and ultrastable.

We develop a method to identify nearby minima in the potential energy landscape, or 'double-well potentials' (DWP). We study the classical parameters of the DWPs, in particular the energy barrier, the asymmetry, the number of particles involved in the barrier crossing. We then analyze the quantum properties of the DWP, by solving the $1d$ Schrödinger equation for the minimum energy path connecting two minima. We compute the quantum splitting $\delta E$ of the DWPs, its probability distribution, and identify those active below 1 K, which are two-level systems (TLS). We show that the density of TLS decreases with glass stability, as found experimentally. Since the computer glasses are isotropic, we conclude that the density of TLS is directly connected to how deep the glass lies in the energy landscape. The 'universality' of glassy anomalies would stem from the similarity of liquid cooling protocols, and would therefore not be a universal feature of disordered solids.

Article

# Absence of marginal stability in a structural glass

C. Scalliet, L. Berthier and F. Zamponi, Physical Review Letters 119 (20), 205501 (2017).

**Marginally stable solids have peculiar physical properties that were first analyzed in the context of the jamming transition. We theoretically investigate the existence of marginal stability in a prototypical model for structural glass-formers, combining analytical calculations in infinite dimensions to computer simulations in three dimensions. While mean-field theory predicts the existence of a Gardner phase transition towards a marginally stable glass phase at low temperatures, simulations show no hint of diverging timescales or lengthscales, but reveal instead the presence of sparse localized defects. Our results suggest that the Gardner transition is deeply affected by finite dimensional fluctuations, and raise issues about the relevance of marginal stability in structural glasses far away from jamming.**

**Introduction** – Many types of fluids (molecular, colloidal, metallic) transform into amorphous glasses [1, 2]. In the glass phase, they present thermodynamic [3], transport [4], vibrational [5] and mechanical [6] properties that are not observed in crystals. These "low-temperature anomalies" are observed in a wide range of systems with very different particle types or interactions, and several theoretical approaches were developed to understand them [7, 4, 8, 9, 10], making specific assumptions about the nature of the excitations responsible for the anomalies.

A different proposal recently emerged from the convergence of two lines of research, based on the idea that collective excitations associated to marginal stability could be the key concept underlying these properties. First, it was realized that systems close to a jamming transition are marginally stable, in the sense that the number of mechanical interactions in the system is precisely tuned [11]. It was later proposed that marginal stability persists away from jamming [12, 13, 14]. Second, an extension of the random first order transition theory [15, 16, 17] to amorphous hard spheres in large dimensions was obtained [18]. It predicts a Gardner phase transition [19, 20] between a normal glass phase and a marginally stable one characterized by an excess of low-frequency modes [21] and unusual rheological properties [22, 23, 24]. The marginal stability of the Gardner phase could provide a universal explanation for glass anomalies [25, 18]. Marginal stability implies

that the system responds in a strong and system-spanning way to a weak, localized perturbation [12], implying the existence of delocalized soft modes [21], and diverging susceptibilities [26, 22].

These recent results provide new opportunities to explain the properties of amorphous materials, motivating ongoing efforts to understand whether marginal stability holds generally in these materials. Hard [27, 28, 29] and soft [14] spheres very close to the jamming transition have been analyzed, showing that marginal stability and the Gardner transition may be relevant in colloidal and granular glasses. However, molecular and metallic glasses are usually modeled by longer-ranged, continuous pair interactions for which no jamming transition takes place [1, 2]. In this context, much less is known about the role of marginal stability [30], and the existence of a Gardner phase has not been established. Therefore, it is not known whether marginal stability can be used to understand the low-temperature anomalies in generic structural glasses.

To address this important question, we combined theoretical and numerical analysis of the low-temperature vibrational properties of a standard model for atomic glasses. At the mean-field level, a marginally stable Gardner phase is predicted, which is then conceptually unrelated to jamming. However, our numerical simulations of the same model in three dimensions contrast with these predictions. We find no sign of a phase transition within the entire glass phase. We detect instead sparse localized defects at low temperature, but they do not give rise to growing timescales and lengthscales that would accompany the emergence of marginal stability at a Gardner phase transition.

**Mean-field theory** – We consider a monodisperse system of $d$-dimensional particles interacting through a continuous pair potential $v(r) = \epsilon(\sigma/r)^{4d}$. This is the repulsive part of the Lennard-Jones potential, generalized to an arbitrary dimension $d$. The exponent for the inverse power law is larger than $d$ to ensure that the virial coefficients remain finite in any dimension. We use $\sigma$ and $\epsilon$ as our unit length and energy, respectively. The state of the system is uniquely controlled by $\Gamma = \widehat{\varphi}/T^{1/4}$, where $T$ is the temperature and $\widehat{\varphi} = \rho V_d 2^d/d$ is the rescaled packing fraction ($\rho$ is the number density, and $V_d$ the volume of a $d$-dimensional sphere of diameter unity). We fix the packing fraction $\widehat{\varphi} = 1$ and vary the temperature, thus exploring the entire phase diagram.

In the limit $d \to \infty$, the thermodynamic properties of the liquid and glass can be computed exactly [15, 18]. In this limit, the system exhibits a sharp dynamical transition of the mode-coupling type [31, 18] at a temperature $T_d$ at which the relaxation time of the liquid diverges. Below $T_d$, the system is trapped in one of the exponentially-many minima of the free-energy landscape. We compute the properties of a typical equilibrium liquid at a temperature $T_g \leq T_d$. As temperature decreases, the glass is confined near the state selected at $T_g$ in a "restricted" equilibrium, and thus follows an equation of state different from the liquid. We compute exactly the free energy of this glass $f_g(T, T_g; \Delta, \Delta_r)$ at the replica symmetric level [32] thanks to a state-following construction [33, 32, 18]. It depends on two parameters: $\Delta$ is the long-time limit of the mean-squared displacement within the followed glass state, and $\Delta_r$ is the relative mean-squared displacement between the original equilibrium configuration at $T_g$ and the one followed to $T$. The free energy $f_g$ is stationary with respect to $\Delta$ and $\Delta_r$. The average pressure and energy of glasses are obtained by taking derivatives of $f_g$ with respect to density and temperature, respectively.

We solve the resulting set of coupled integro-differential equations given in Ref. [32] to obtain the phase diagram in Fig. 1a. First, we compute the potential energy $E$ of the equilibrium liquid and the dynamical transition temperature, $T_d = 0.002914$. We then compute the energy of glasses prepared at different $T_g \leq T_d$ as a function of temperature. A Gardner transition is detected when the replica symmetric solution becomes unstable [32], signaling the transformation of the simple

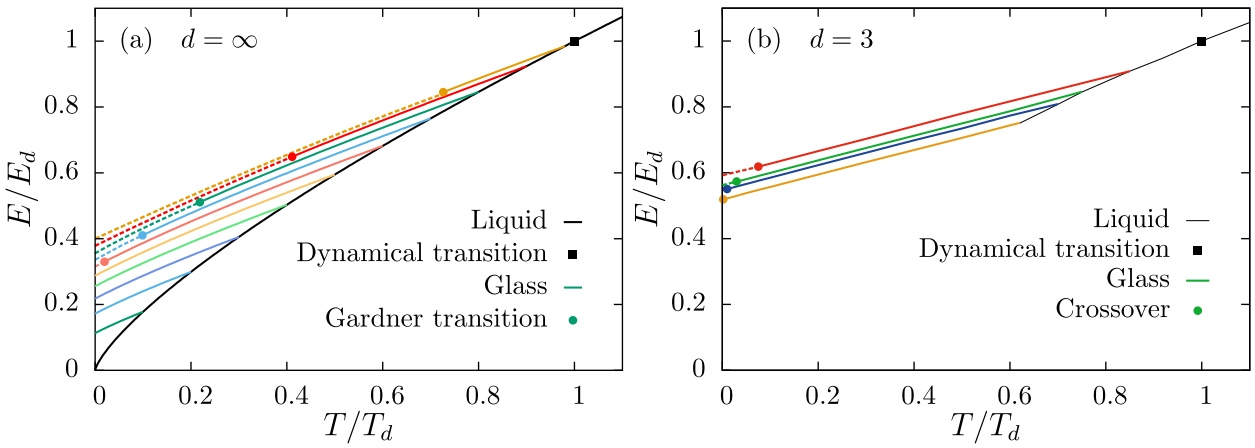


Figure 1: (a) Mean-field phase diagram. Energy of the equilibrium liquid (black line), and dynamical transition temperature $T_d$ (black square). Various glasses prepared at $T_g < T_d$ are followed out of equilibrium (full lines). When $T_g \gtrsim 0.5T_d$, these glasses undergo a Gardner transition (bullets) into marginally stable glasses (dashed lines). (b) Numerical phase diagram with equivalent representations of the liquid, dynamic transition and glass lines. Bullets locate the temperature crossover below which localized excitations appear, but do not correspond to a Gardner transition. In both panels, axes are rescaled by the value at $T_d$: $E_d = E(T_d)$.

glass into a marginally stable one. The low-temperature Gardner phase is described by breaking the replica symmetry [20, 34], and the transition belongs to the same universality class of the spin-glass transition in a magnetic field [35, 36]. The presence of a Gardner transition is in general not a universal result [35, 37]. In our model, over a large temperature window $0.5 \lesssim T_g/T_d < 1$, a marginally stable Gardner phase exists, while for $T_g \lesssim 0.5T_d$ no Gardner transition is found. Because our model does not possess a jamming transition, our results show that mean-field theory predicts that marginal stability is not restricted to the vicinity of jamming, but should be broadly relevant for generic structural glasses with continuous interactions.

**Numerical simulations** – There is no clear consensus on the influence of finite dimensional fluctuations on the Gardner transition [38, 39, 40, 36, 41, 42]. Contradictory results were reported in numerical works. The existence of a transition was suggested in $d = 4$ [39], but opposite claims were also made [38, 41]. A renormalization group approach [42] found a fixed point in all dimensions $d \geq 3$, while other works found different results [43, 36]. Thus, we must confront our theoretical predictions to a direct numerical investigation of the $3d$ version of the above model. Because the putative transition occurs deep inside the glass phase, it is crucial to prepare well-thermalized glasses, such that the structural relaxation time is larger than the duration of the simulation. This is now possible thanks to the development of an efficient swap Monte Carlo technique [44, 45, 46].

We simulate a continuously-polydisperse system composed of $N = 1500$ particles at number density $\rho = 1$. We perform selected simulations with $N = 12000$ to analyze finite size effects. Particles interact via the repulsive pair potential $v(r_{ij}) = \epsilon(\sigma_{ij}/r_{ij})^{12} + F(r_{ij})$, where $F(r_{ij})$ guarantees the continuity of the potential up to the second derivative at the numerical cutoff distance $r_{cut} = 1.25\ \sigma_{ij}$, beyond which $v = 0$ [46]. The particle diameters are drawn from the normalized continuous distribution $P(\sigma_m \leq \sigma \leq \sigma_M) \sim 1/\sigma^3$. The size ratio of $\sigma_m/\sigma_M = 0.45$ was optimized

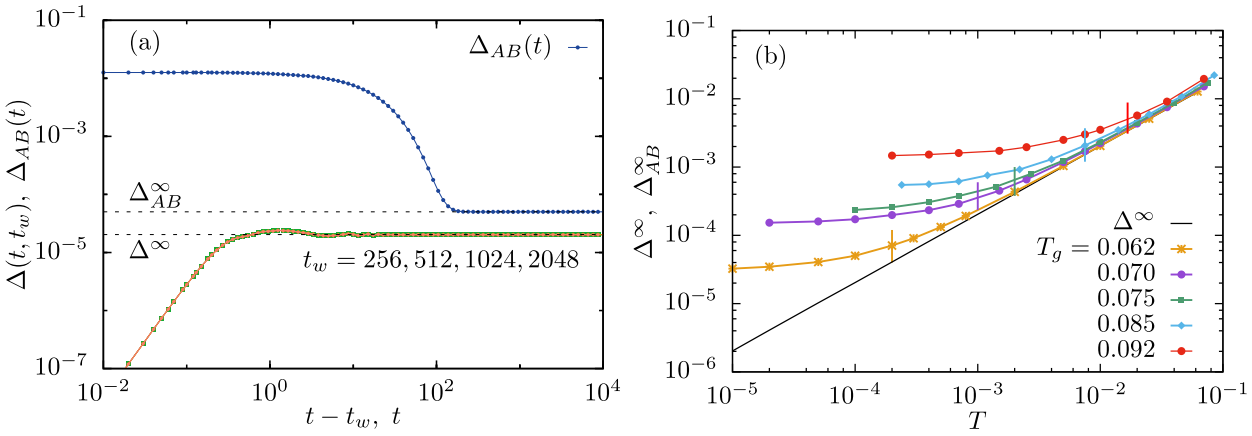


Figure 2: (a) Mean-squared displacement $\Delta(t, t_w)$ and mean-squared distance $\Delta_{AB}(t)$ as a function of $t - t_w$ and $t$ for $T_g = 0.062$ and $T = 10^{-4}$ rapidly converge to their long-time limits (dashed lines). (b) Long-time limits of $\Delta^\infty$ and $\Delta^\infty_{AB}$ as a function of temperature, for different $T_g$. Both quantities differ below $T^*(T_g)$, indicated by vertical segments.

to provide an excellent glass-forming ability. Similarly, we use a non-additive interaction rule for the cross diameters $\sigma_{ij} = \frac{\sigma_i+\sigma_j}{2}(1 - \eta|\sigma_i - \sigma_j|)$, with $\eta = 0.2$. Length, time and energy are respectively expressed in units of $\overline{\sigma} = \int \sigma P(\sigma) d\sigma$, $\sqrt{\epsilon/m\overline{\sigma}^2}$ and $\epsilon$. The mode-coupling crossover temperature $T_d \approx 0.1$ is determined by fitting the relaxation time $\tau$ measured with standard dynamics to $\tau \sim (T - T_d)^{-\gamma}$ [46]. Using swap Monte Carlo, equilibrium can be ensured (using standard criteria [46]) down to $T \approx 0.6T_d$.

To numerically mimic the state following scheme, swap Monte Carlo is used to produce $N_s = 50$ independent equilibrium configurations at each $T_g$ (0.062, 0.07, 0.075, 0.082, 0.092). We then generate $N_{\rm th} = 10$ copies of each configuration, that differ only by the initial velocities of particles (two such copies are referred to as $A$ and $B$). Each of the $N_s \times N_{\rm th}$ samples is simulated at $T_g$ in the $NVE$ ensemble during a time $t_q$, depending on $T_g$ ($t_q = 1000$ for $T_g = 0.062, 0.07$; $t_q = 100$ for $T_g = 0.075$; $t_q = 0$ for $T_g = 0.085$). The time $t_q$ is chosen such that particles in different copies have time to explore their cages without diffusing. After $t_q$, the glass is instantaneously cooled to a temperature $T < T_g$ with a Berendsen thermostat (coupling parameter $\tau_T = 10$) [47]. Waiting times $t_w$ are measured since the quench. We find that after $t_w \approx 100$, the temperature stabilizes to the desired value. For the highest $T_g = 0.092$ studied, diffusion is not totally suppressed at equilibrium. Glasses were first cooled down to $T = 0.07$ with a cooling rate $\gamma = 10^{-7}$ before making copies. We then used the same protocol as for $T_g = 0.07$ to obtain the data.

The Gardner transition is a second-order phase transition accompanied by diverging timescales and lengthscales characterizing vibrational dynamics. The transition signals profound changes in the structure of the landscape and the emergence of marginal stability. Mean-squared displacements (MSD) represent therefore the central observables for such investigation [48, 27]:

$$\begin{aligned} \Delta(t, t_w) &= \frac{1}{N'} \sum_{i=1}^{N'} \langle |\boldsymbol{r}_i(t + t_w) - \boldsymbol{r}_i(t_w)|^2 \rangle \ , \\ \Delta_{AB}(t) &= \frac{1}{N'} \sum_{i=1}^{N'} \langle |\boldsymbol{r}_i^A(t) - \boldsymbol{r}_i^B(t)|^2 \rangle \ , \end{aligned} \tag{1}$$

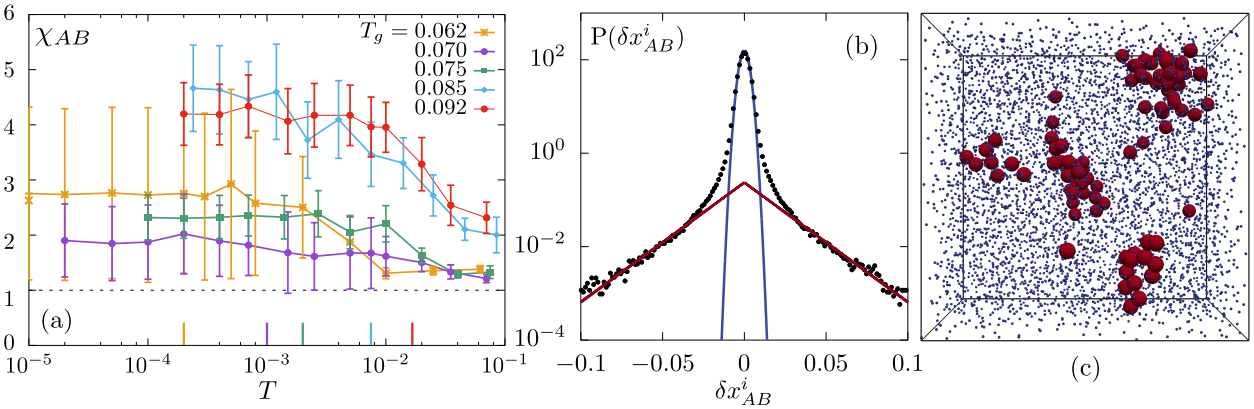


Figure 3: (a): The susceptibility $\chi_{AB}$ for different $T_g$ raises mildly above the floor level (dashed line) across $T^*$ (vertical segments). The error bars are computed using the jackknife method. (b): The van-Hove function of relative displacements has a narrow Gaussian core of width given by $\Delta^\infty$ (solid blue), and exponential tails (solid red) at $T_g = 0.062$ and $T = 10^{-4}$. (c) Corresponding snapshot with $N = 12000$ showing the few particles having displacements outside the Gaussian range (red spheres) among a majority of particles undergoing small amplitude Gaussian vibrations (blue dots).

where the brackets indicate averages over thermal fluctuations and disorder. They respectively represent the standard MSD and the relative MSD between two copies of the same glass. Since smaller particles may escape their cage more easily, we concentrate on the $N' = N/2$ larger particles.

The typical behavior of the MSDs after a quench is shown in Fig. 2a. Both quantities converge to their long-time limits, $\Delta^\infty_{AB}$, $\Delta^\infty$ after a time of order 100 (set by the thermostat). No sign of slower relaxation or aging behavior is detected at any state point, which indicates that the time dependence of the observables is not pertinent. The absence of slow relaxation contrasts dramatically with hard sphere simulations [27], and directly reveals the absence of marginal stability throughout the glass phase.

We gather the results for $\Delta^\infty_{AB}$ and $\Delta^\infty$ in Fig. 2b. The standard MSD changes linearly with $T$, as expected. The behavior of the relative distance is qualitatively the same for all $T_g$. The equality $\Delta^\infty_{AB} \approx \Delta^\infty$ holds at high enough $T$, meaning that the structure of the basin is relatively simple. There is a crossover temperature $T^*(T_g)$ (vertical segments), below which $\Delta^\infty_{AB} > \Delta^\infty$. The distance between two copies is then much larger than the vibrations they can perform individually, suggesting that the copies get quenched in distinct minima. This splitting of MSDs was observed in hard spheres [27, 28] and identified as a Gardner transition. We report in Fig. 1b the crossover temperatures and the glass energy. The similarity between the two phase diagrams in Fig. 1 is obvious.

The absence of slow relaxation in Fig. 2b reveals the lack of a growing timescale. To address lengthscales, we study the global fluctuations of the relative MSD. The variance of these fluctuations defines the susceptibility $\chi_{AB} = N[\langle\tilde{\Delta}^2_{AB}\rangle - \langle\tilde{\Delta}_{AB}\rangle^2]/[\langle{\Delta^i_{AB}}^2\rangle - \langle\Delta^i_{AB}\rangle^2]$, where $\tilde{\Delta}_{AB}$ is the plateau value of the relative MSD for a given pair $AB$, and $\Delta^i_{AB}$ its single particle version. The normalization in $\chi_{AB}$ ensures that $\chi_{AB} = 1$ for spatially uncorrelated motion and that $\chi_{AB}$ is a direct measure of the correlation volume. If the crossover at $T^*$ corresponded to a Gardner transition, the susceptibility would diverge near $T^*$. The results in Fig. 3a are very similar for all $T_g$ values: the susceptibility increases very weakly as temperature decreases. Within our error bars, there is actually very little global fluctuations above the floor level. This directly demonstrates that spatial

correlations between particle motion remain microscopic across the crossover $T^*$, which is thus not accompanied by a growing correlation length. This is consistent with the absence of slow dynamics in Fig. 2a. A similar value of $\chi_{AB}$ was observed in larger systems of $N = 12000$ particles at specific state points. We studied the spatial correlation function for the relative MSD [27], of which the volume integral is $\chi_{AB}$, and did not find hints of a growing length scale at any temperature. We conclude that $T^*$ does not coincide with the emergence of a marginally stable phase.

To understand the origin of the crossover observed in Fig. 2b, we resolve the vibrational dynamics at the particle scale. We measure the distribution of relative particle displacements, $P(\delta x^i_{AB})$, where $\delta x^i_{AB} = x^i_A - x^i_B$ is the relative motion of particle $i$ between copies $A$ and $B$ along the $x$-direction. We average over the three directions of space. The van-Hove function is nearly Gaussian when $T^* < T < T_g$ with a width controlled by $\Delta^\infty$. Close to $T^*$ and below, the distribution remains Gaussian in its core, but exhibits tails that are well-fitted by an exponential, as shown in Fig. 3b. We evaluate the statistical weight of the particles contributing to the tails by integrating the exponential fit. It varies between 1% and 3% for all state points and typically increases with $T_g$. This corresponds to a small subset of particles that get frozen in slightly distinct positions below $T^*$ in two copies. The error bars for $\chi_{AB}$ are large because the number of particles in the tails is small, and fluctuates significantly from one pair $AB$ to another. We have checked that these mobile particles encompass all particles, not only small ones that are more mobile. To gather spatial information on these few mobile particles, we select particles with a relative displacement $\delta x^i_{AB}$ outside of the Gaussian core of the distribution, and visualize them in snapshots. A typical snapshot obtained for $N = 12000$ is shown in Fig. 3c. We represent the vast majority of particles with Gaussian displacements as small points and highlight particles contributing to the tails with larger red spheres. Strikingly, these mobile particles are clustered into sparse localized defects. When $T_g$ increases, the number of mobile particles as well as their characteristic displacement $\Delta^i_{AB}$ increase weakly. This directly accounts for the shift of $T^*$ with $T_g$. These few localized clusters thus dominate the behavior of the relative displacement $\Delta^\infty_{AB}$ which is averaged over particles, and are responsible for its separation from $\Delta^\infty$ in Fig. 2b. Our key conclusion is that the emergence of these localized clusters at $T^*$ does not correspond to a Gardner phase transition, and glasses below $T^*$ are not marginally stable.

**Discussion** – In our system, the marginal stability described within mean-field approaches is strongly suppressed by finite-dimensional fluctuations. Our results differ dramatically from previous work on hard sphere systems [27, 28]. This surprising lack of universality contrasts with the universality of glass formation [2]. One possible explanation for this difference is that structural glasses may generically become marginal only when pushed towards specific "critical" transitions, such as jamming [49]. The jamming transition appears robust down to $2d$, with the same critical properties as in $d = \infty$ [50]. This could explain why a Gardner transition is observed in finite-dimensional hard sphere glasses near jamming, whereas glass-formers with continuous interactions reach non-marginal inherent structures at zero temperature. After this work was completed, two other works appeared reporting consistent findings [51, 52].

Our results raise two types of questions. First, the presence of a marginally stable glass phase seems highly dependent on the details of the particle interactions and on dimensionality. To better understand the nature of the Gardner transition, one should investigate better the crossover between continuous and discontinuous interactions, using for instance well-chosen particle interactions [53, 54]. One should also investigate the crossover towards non-mean-field behavior by using either

dimensionality [18] or the interaction range [55, 48] as tuning parameters. Second, it would be interesting to connect the present results with other observations of localized defects [10], such as soft localized modes controlling the low-frequency part of the vibrational spectrum in amorphous solids [56, 57], localized defects controlling relaxation in supercooled liquids [58, 59, 60, 61], or the shear-transformation-zones [62, 63, 64, 65] controlling the mechanical behavior of amorphous solids.

**Acknowledgments** – We thank G. Biroli, D. Coslovich, B. Seoane, P. Urbani for useful exchanges about this work, and A. Ninarello for providing initial configurations. The research leading to these results has received funding from the European Research Council under the European Unions Seventh Framework Programme (FP7/2007-2013)/ERC Grant Agreement No. 306845. This work was supported by a grant from the Simons Foundation (#454933, Ludovic Berthier; #454955, Francesco Zamponi).

## Bibliography

[1] A. Cavagna. *Phys. Rep.*, 476(4-6):51–124, 2009.

[2] Ludovic Berthier and Giulio Biroli. *Rev. Mod. Phys.*, 83:587–645, 2011.

[3] RC Zeller and RO Pohl. *Phys. Rev. B*, 4(6):2029, 1971.

[4] W A Phillips. *Rep. Prog. Phys.*, 50(12):1657, 1987.

[5] V K Malinovsky and A P Sokolov. *Solid State Commun.*, 57(9):757–761, 1986.

[6] Dennis L. Malandro and Daniel J. Lacks. *J. Chem. Phys.*, 110(9):4593–4601, 1999.

[7] P. W. Anderson, B. I. Halperin, and C. M. Varma. *Philos. Mag.*, 25(1):1–9, 1972.

[8] Walter Schirmacher, Gregor Diezemann, and Carl Ganter. *Phys. Rev. Lett.*, 81:136–139, 1998.

[9] Vassiliy Lubchenko and Peter G. Wolynes. *Phys. Rev. Lett.*, 87:195901, 2001.

[10] Vassiliy Lubchenko and Peter G. Wolynes. *Annu. Rev. Phys. Chem.*, 58(1):235–266, 2007. PMID: 17067282.

[11] A.J. Liu, S.R. Nagel, W. Van Saarloos, and M. Wyart. The jamming scenario – an introduction and outlook. In L. Berthier, G. Biroli, J-P Bouchaud, L. Cipelletti, and W. van Saarloos, editors, *Dynamical Heterogeneities and Glasses*. Oxford University Press, 2011.

[12] M. Wyart, L.E. Silbert, S.R. Nagel, and T.A. Witten. *Phys. Rev. E*, 72(5):051306, 2005.

[13] Ning Xu, Matthieu Wyart, Andrea J. Liu, and Sidney R. Nagel. *Phys. Rev. Lett.*, 98:175502, 2007.

[14] Eric DeGiuli, Adrien Laversanne-Finot, Gustavo Düring, Edan Lerner, and Matthieu Wyart. *Soft Matter*, 10(30):5628–5644, 2014.

[15] T. R. Kirkpatrick and P. G. Wolynes. *Phys. Rev. A*, 35(7):3072–3080, 1987.

[16] T. R. Kirkpatrick and D. Thirumalai. *Phys. Rev. Lett.*, 58(20):2091–2094, 1987.

[17] V. Lubchenko and P. G. Wolynes, editors. *Structural Glasses and Supercooled Liquids: Theory, Experiment, and Applications*. Wiley, 2012.

[18] Patrick Charbonneau, Jorge Kurchan, Giorgio Parisi, Pierfrancesco Urbani, and Francesco Zamponi. *Annu. Rev. Condens. Matter Phys.*, 8:265–288, 2017.

[19] D. J. Gross, I. Kanter, and H. Sompolinsky. *Phys. Rev. Lett.*, 55:304–307, 1985.

[20] E. Gardner. *Nucl. Phys. B*, 257:747–765, 1985.

[21] Silvio Franz, Giorgio Parisi, Pierfrancesco Urbani, and Francesco Zamponi. *Proc. Natl. Acad. Sci. U.S.A.*, 112(47):14539–14544, 2015.

[22] Giulio Biroli and Pierfrancesco Urbani. *Nature Physics*, 12:1130–1133, 2016.

[23] Silvio Franz and Stefano Spigler. *Phys. Rev. E*, 95(2):022139, 2017.

[24] Yuliang Jin and Hajime Yoshino. *Nature Communications*, 8:14935, 2017.

[25] Markus Müller and Matthieu Wyart. *Annu. Rev. Condens. Matter Phys.*, 6(1):177–200, 2015.

[26] HGE Hentschel, Smarajit Karmakar, Edan Lerner, and Itamar Procaccia. *Phys. Rev. E*, 83(6): 061101, 2011.

[27] Ludovic Berthier, Patrick Charbonneau, Yuliang Jin, Giorgio Parisi, Beatriz Seoane, and Francesco Zamponi. *Proc. Natl. Acad. Sci. U.S.A.*, 113(30):8397–8401, 2016.

[28] A. Seguin and O. Dauchot. *Phys. Rev. Lett.*, 117:228001, 2016.

[29] Carolina Brito and Matthieu Wyart. *J. Stat. Mech.*, 2007(08):L08003, 2007.

[30] S. Kooij and E. Lerner. Unjamming in models with analytic pairwise potentials. `arXiv:1610.02843`, 2017.

[31] W. Götze. *Complex dynamics of glass-forming liquids: A mode-coupling theory*, volume 143. OUP, USA, 2009.

[32] Corrado Rainone, Pierfrancesco Urbani, Hajime Yoshino, and Francesco Zamponi. *Phys. Rev. Lett.*, 114(1):015701, 2015.

[33] Silvio Franz and Giorgio Parisi. *J. Phys. I France*, 5(11):1401–1415, 1995.

[34] Corrado Rainone and Pierfrancesco Urbani. *J. Stat Mech.*, 2016(5):P053302, 2016.

[35] A. Montanari and F. Ricci-Tersenghi. *Eur. Phys. J. B*, 33:339, 2003.

[36] Pierfrancesco Urbani and Giulio Biroli. *Phys. Rev. B*, 91(10):100202, 2015.

[37] Tommaso Rizzo. *Phys. Rev. E*, 88:032135, 2013.

[38] Derek Larson, Helmut G. Katzgraber, M. A. Moore, and A. P. Young. *Phys. Rev. B*, 87:024414, 2013.

[39] Marco Baity-Jesi et al. *J. Stat. Mech.*, 2014(5):P05014, 2014.

[40] Maria Chiara Angelini and Giulio Biroli. *Phys. Rev. Lett.*, 114(9):095701, 2015.

[41] T. Aspelmeier, Helmut G. Katzgraber, Derek Larson, M. A. Moore, Matthew Wittmann, and Joonhyun Yeo. *Phys. Rev. E*, 93:032123, 2016.

[42] Patrick Charbonneau and Sho Yaida. *Phys. Rev. Lett.*, 118(21):215701, 2017.

[43] M. A. Moore and A. J. Bray. *Phys. Rev. B*, 83:224408, 2011.

[44] T.S. Grigera and G. Parisi. *Phys. Rev. E*, 63(4):45102, 2001.

[45] R. Gutiérrez, S. Karmakar, Y. G. Pollack, and I. Procaccia. *Europhys. Lett.*, 111(5):56009, 2015.

[46] Andrea Ninarello, Ludovic Berthier, and Daniele Coslovich. *Phys. Rev. X*, 7:021039, 2017.

[47] H. J. C. Berendsen, J. P. M. Postma, W. F. van Gunsteren, A. DiNola, and J. R. Haak. *J. Chem. Phys.*, 81(8):3684–3690, 1984.

[48] Patrick Charbonneau, Yuliang Jin, Giorgio Parisi, Corrado Rainone, Beatriz Seoane, and Francesco Zamponi. *Phys. Rev. E*, 92(1):012316, 2015.

[49] G. Biroli and P.Urbani. Liu-nagel phase diagrams in infinite dimension. `arXiv:1704.04649`, 2017.

[50] Carl P Goodrich, Andrea J Liu, and Sidney R Nagel. *Phys. Rev. Lett.*, 109(9):095704, 2012.

[51] C. L. Hicks, M. J. Wheatley, M. J. Godfrey, and M. A. Moore. The gardner transition in physical dimensions. 1708.05644, 2017.

[52] Beatriz Seoane, D. R. Reid, J. J. de Pablo, and Francesco Zamponi. Low-temperature anomalies of a vapor deposited glass. arXiv:1709.04930, 2017.

[53] Hans C. Andersen, John D. Weeks, and David Chandler. *Phys. Rev. A*, 4:1597–1607, 1971.

[54] Ludovic Berthier and Gilles Tarjus. *J. Chem. Phys.*, 134:214503, 2011.

[55] R. Mari and J. Kurchan. *J. Chem. Phys.*, 135:124504, 2011.

[56] Edan Lerner, Gustavo Düring, and Eran Bouchbinder. *Phys. Rev. Lett.*, 117:035501, 2016.

[57] Hideyuki Mizuno, Hayato Shiba, and Atsushi Ikeda. Continuum limit of the vibrational properties of amorphous solids. arXiv:1703.10004, 2017.

[58] Aaron S. Keys, Lester O. Hedges, Juan P. Garrahan, Sharon C. Glotzer, and David Chandler. *Phys. Rev. X*, 1:021013, 2011.

[59] R. Candelier, A. Widmer-Cooper, J. K. Kummerfeld, O. Dauchot, G. Biroli, P. Harrowell, and D. R. Reichman. *Phys. Rev. Lett.*, 105:135702, 2010.

[60] Ekin D Cubuk, Samuel S Schoenholz, Jennifer M Rieser, Brad D Malone, Joerg Rottler, Douglas J Durian, Efthimios Kaxiras, and Andrea J Liu. *Phys. Rev. Lett.*, 114(10):108001, 2015.

[61] Robert L Jack and Juan P Garrahan. *Phys. Rev. Lett.*, 116(5):055702, 2016.

[62] ML Falk and JS Langer. *Phys. Rev. E*, 57(6):7192, 1998.

[63] Peter Schall, David A Weitz, and Frans Spaepen. *Science*, 318(5858):1895–1899, 2007.

[64] H. G. E. Hentschel, Smarajit Karmakar, Edan Lerner, and Itamar Procaccia. *Phys. Rev. Lett.*, 104:025501, 2010.

[65] F. Puosi, J. Rottler, and J-L. Barrat. *Phys. Rev. E*, 94:032604, 2016.

Article

# Nature of defects and excitations in structural glasses

C. Scalliet, L. Berthier and F. Zamponi, Nature Communications 10, 5102 (2019).

**The nature of defects in amorphous materials, analogous to vacancies and dislocations in crystals, remains elusive. Here we explore their nature in a three-dimensional microscopic model glass-former which describes granular, colloidal, atomic and molecular glasses by changing the temperature and density. We find that all glasses evolve in a very rough energy landscape, with a hierarchy of barrier sizes corresponding to both localized and delocalized excitations. Collective excitations dominate in the jamming regime relevant for granular and colloidal glasses. By moving gradually to larger densities describing atomic and molecular glasses, the system crosses over to a regime dominated by localized defects and relatively simpler landscapes. We quantify the energy and temperature scales associated to these defects and their evolution with density. Our result pave the way to a systematic study of low-temperature physics in a broad range of physical conditions and glassy materials.**

## I Introduction

Amorphous solids may be prepared via two distinct routes. Atomic and molecular glasses are obtained by crossing a glass transition, by cooling a dense liquid at constant pressure, or by a compression at constant temperature [1]. Disordered assemblies of grains, droplets and large colloids solidify by crossing a jamming transition upon compression from a fluid state [2]. In a seminal work, Liu and Nagel [3] proposed a unified phase diagram for glass and jamming transitions. Subsequent work investigated amorphous solidification by interpolating continuously between these two limits [4], to understand similarities and differences between them.

Zero-temperature amorphous solids are minima of the many-body interaction potential, and their low-temperature properties are determined by the structure of the potential energy landscape around these minima [5, 6]. The low-frequency vibrational modes around a minimum define the excitations of the solid (analogous to phonons in a crystal), and the structure of energy barriers

separating nearby energy minima define the defects (analogous to vacancies and dislocations in a crystal). The nature of excitations and defects can be different in systems undergoing jamming or glass transitions.

Understanding the nature of excitations and defects in amorphous solids is one of the major goals of condensed matter physics, because these features are relevant for mechanical, thermal and transport properties [7, 6], such as specific heat and thermal conductivity [8, 9], sound attenuation [10], energy dissipation [11] (with important technological consequences, e.g. for gravitational wave detection [12]), solid elasticity and plasticity [13, 14, 15, 16, 17].

In dense atomic glasses, typically modeled by simple Lennard-Jones (LJ) interaction potentials, low-frequency excitations are phonon-like (with peculiar properties) [18, 19, 20, 21], and defects are localized, with a few particles jumping between two local minima and slightly perturbing their neighbors, giving rise to two-level systems that play an important role in the low-temperature thermal properties of glasses [22, 7]. This phenomenology has been numerically confirmed in simple LJ-like glass models [6, 23, 24].

A different situation holds near jamming where particles interact essentially via short-range repulsive forces and mechanical stability is controlled by particle contacts. The minimal number of contacts required for stability is the isostatic number, which is exactly reached at the jamming transition. In the vicinity of the transition, the solid is marginally stable [2, 25]: a small perturbation can remove a few contacts and destabilize the entire solid [26, 27]. This geometrical feature gives rise to low-frequency collective excitations that are extremely different from phonons [28, 21, 29]. The energy landscape features a large number of minima [30], separated by low barriers. The corresponding defects are thus extended and involve collective particle motion, as numerically observed in simulation of Hard Sphere (HS) glasses [31, 32].

The mean-field theory of the glass transition has attempted to describe this phenomenology, coming to two important conclusions [30]. First, glass and jamming transitions are distinct phase transitions, where solidity emerges at thermal equilibrium (glass transition) or at zero temperature (jamming transition). Second, for repulsive particles, the jamming transition is buried deep inside a glass phase, which is split in two distinct phases, containing either trivial excitations ('simple glass'), or collective ones ('marginal glass'). Mean field theory predicts that a sharp Gardner phase transition separates these two glass phases [30]. These mean field results, however, conflict with several finite dimensional studies. First, the nature of the Gardner transition in three dimensions is not fully understood [33]. Second, the quasi-localised excitations [20, 21] and localized defects [23, 34] numerically observed in glassy systems are not described by mean-field theory.

In summary, the two extreme cases of LJ-like and HS glasses, which have been thoroughly investigated by numerical simulations, together with the insight coming from mean field theory, highlight the conceptually distinct nature of excitations and defects in glassy and jammed states. Yet, many questions are currently open. Are extended, marginally stable excitations restricted to HS glasses [35]? How do excitations and defects evolve between the jamming and glass regimes? What is the region where marginal stability influences glass properties? Do localized and collective excitations coexist in some regime?

We address this broad set of questions by introducing two main technical tools. First, we simulate a three-dimensional system of particles interacting via the Weeks-Chandler-Andersen (WCA) potential [36]. Varying a physical control parameter, i.e. the density, allows to capture all relevant glassy regimes. At high density, the WCA potential becomes equivalent to a Lennard-Jones potential, widely used for atomic glasses. At lower density, the finite range of the WCA potential makes it suitable to study jamming. Second, we perform a systematic investigation of the distribution of

minima and barriers in the potential energy landscape, by means of a state-of-the-art reaction path finding protocol.

Our analysis leads to two main findings. First, the HS phenomenology extends in a wide region of the phase diagram of the soft WCA system, centered around the jamming transition. Marginal stability, and its associated collective excitations and defects, is then relevant not only for hard colloids, but also for softer systems such as foams and emulsions. Second, marginal stability can coexist with localized defects over a wide range of physical conditions. Collective modes are typically associated to low-energy barriers, whereas localized modes correspond to the motion of a few particles in a rigid elastic matrix, controlled by higher energy barriers. The two phenomena are thus controlled by different energy and temperature scales that we quantify numerically. In the vicinity of jamming, all defects are collective. At intermediate density, collective defects exist only under a characteristic temperature 'dome', as predicted by mean-field theory [17, 37], while localized defects dominate at higher temperatures. At high density, collective defects disappear. Our results thus establish the extent of the region in which marginal stability impacts glass physics, and open the way for a systematic study of low-temperature glass physics (including quantum effects) across the whole range of experimentally relevant conditions.

# II Results

## II.1 Equilibrium phase diagram

We first discuss the packing fraction, $\varphi$, and temperature, $T$, equilibrium phase diagram of the three-dimensional polydisperse, non-additive WCA model we simulate (see Sec. IV for technical details). We focus in particular on the determination of the fluid region, and its boundary, the glass transition, below which physical dynamics fail to reach equilibrium.

For each packing fraction, we study the temperature evolution of the relaxation time $\tau_\alpha$ of density correlations in the equilibrium fluid, using molecular dynamics (MD) simulations. The relaxation time is measured through the self-intermediate scattering function $F_s(k,t)$, by the condition $F_s(k = 7.0, t = \tau_\alpha) = e^{-1}$, and it follows an Arrhenius law at high temperature, while deviations from the Arrhenius law appear below an onset temperature $T_0$, where $\tau_\alpha(T = T_0) \equiv \tau_0$. Standard algorithms such as MD fail to reach equilibrium below $T_d$, defined by $\tau_\alpha(T = T_d) = 10^4\tau_0$. We refer to $T_d$ as the "computer glass transition". Glasses prepared at the computer glass transition lie much higher in the energy landscape than any experimental glass, which are created after up to twelve decades of glassy dynamical slowdown.

In order to bypass the computer glass transition and access deeper glassy minima, relevant to describe real materials, we use a hybrid swap Monte Carlo algorithm [38]. This unphysical dynamical scheme, which accelerates greatly equilibrium sampling [39, 40], achieves thermalization down to temperatures around $0.6T_d$ almost independently of the packing fraction.

In Fig. 1 we indicate by circles the state points for which equilibrium is reached, either by MD or swap. The state points below the computer glass transition line $T_d(\varphi)$ have been fully equilibrated by swap. In this article, we present results for glasses prepared well below the computer glass transition, highlighted by red squares in Fig. 1. They lie along a line $T_g \approx 0.65\ T_d$ of similar glass stabilities, which corresponds roughly to the experimental glass transition temperature. The latter is defined by $\tau_\alpha = 10^{12}\tau_0$, and estimated by extrapolating the physical relaxation time with a parabolic law. These glasses lie so deep in the landscape that when their physical dynamics is simulated with MD, diffusion is suppressed over accessible timescales, and only vibrations around

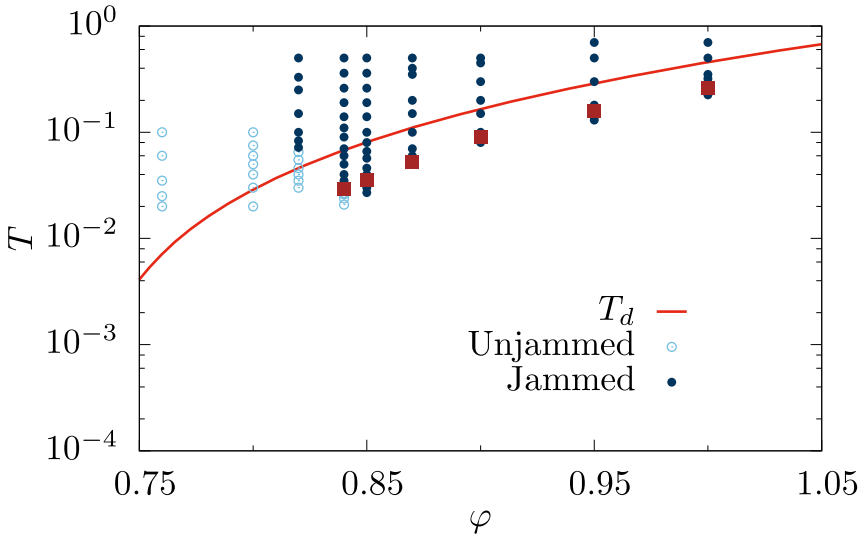


Figure 1: **Equilibrium phase diagram of the WCA model.** The red line corresponds to the computer glass transition, below which conventional molecular dynamics simulations fail to reach equilibrium over accessible time scales. State points are studied in equilibrium conditions with the hybrid swap method (circles). After energy minimization, their potential energy is either zero (open circles, unjammed), or positive (full circles, jammed). The equilibrium glassy states analyzed in more detail are indicated with red squares.

the initial equilibrated configuration are observed. The landscape picture of a well-defined glassy basin, from which the system does not escape, is thus relevant. The nature of the glassy basin, either smooth, rough, etc., determines the physical properties of the material. In this work, we study how the properties of glassy basins are affected by varying density.

More precisely, our strategy is to prepare equilibrium configurations at various state points $(\varphi_g, T_g)$ using hybrid swap, in order to select a glass basin, which we then follow out of equilibrium using ordinary MD simulations across the phase diagram $(\varphi, T)$. We determine how the properties of a given glass depend on the preparation state $(\varphi_g, T_g)$, which encodes its degree of stability, and the state point $(\varphi, T)$ at which it is studied. The glass properties depend both on initial and final state points. To each initial glass selected in the plane of Fig. 1, corresponds a two-dimensional state following phase diagram [17, 37]. This makes a representation of the complete phase diagram difficult. Instead, we focus on a few well-chosen initial glasses, and follow their evolution with both $\varphi$ and $T$.

In order to connect the glassy physics to that of the jamming transition occurring at zero temperature, we use a conjugate gradient method to minimize all equilibrated state points in Fig. 1 to their inherent structure [5, 6]. The potential being purely repulsive with a finite interaction range, the potential energy of the inherent structures can be either positive (indicating that some particles overlap), or zero (no overlap). We call "jammed" the former and "unjammed" the latter inherent structures, and the jamming transition separates the two regimes [2]. In Fig. 1, open (full) circles reach unjammed (jammed) inherent structures under minimization. Depending on the preparation of the glass basin, in our model the jamming transition can occur over a range of packing fractions $\varphi_J \in [0.78 - 0.84]$. The lower value is found when minimizing random configurations, while the higher bound corresponds to the jamming transition of deeply thermalized samples. Note that the

unusually high values of $\varphi_J$ (for a $3d$ system) stem from both polydispersity and non-additivite interactions of our mixture (see Methods).

## II.2 Ergodicity breaking inside a glassy minimum

Configurations prepared by hybrid swap at a state point $(\varphi_g, T_g)$ are equilibrated, but their dynamics, when simulated by MD, is arrested, and no diffusion is observed. Yet, at long times, molecular dynamics ergodically samples the glass basin selected by the initial configuration. We now study how this ergodicity is broken when temperature and packing fraction are changed. Let us stress that we are looking at an ergodicity breaking transition inside the glass, i.e. within the vibrational dynamics [30, 31], which is very different from the more familiar ergodicity breaking transition occurring in the diffusive dynamics when quickly cooling the liquid into the glass phase.

Ergodicity breaking inside glassy minima can be detected using the isoconfigurational ensemble [41]. We prepare $n_c$ identical clones of each equilibrium configuration, initialized with independent velocities. Their dynamical evolution is studied at a new state point $(\varphi, T)$ with MD. We measure $\Delta_{AB}(t_{\rm w})$, the mean-squared displacement (MSD) between two clones after a time $t_{\rm w}$ spent at the new state point, and $\Delta(t_{\rm w}, t_{\rm w}+\tau)$, the MSD of particles between time $t_{\rm w}$ and $t_{\rm w}+\tau$, in a single clone. Both quantities are averaged over clones and initial glasses (see Methods for details). The full time and waiting-time dependence of these quantities is studied below. Here we focus on their long time behavior. In the temperature regime studied, diffusion is suppressed and the MSDs typically show a plateau at long times, which we characterize by their value at $t_{\rm w} = 8192$, $\tau = 10^4$. If the glass basin is sampled ergodically, the average distance between two clones must coincide with the average displacement performed by one clone, and $\Delta$ and $\Delta_{AB}$ should coincide [31]. Ergodicity breaking inside the glass is indicated by a strict inequality $\Delta < \Delta_{AB}$ in the long time limit.

We first consider the glasses prepared at $(\varphi_g, T_g) = (0.84, 0.029)$, $(0.85, 0.0353)$, $(0.87, 0.053)$, $(0.9, 0.09)$, $(0.95, 0.16)$, $(1, 0.26)$ shown in Fig. 1. These glasses are subjected to constant-density temperature quenches. The long-time limits of $\Delta$ and $\Delta_{AB}$ after the quenches are presented in Fig. 2. For all glasses, $\Delta = \Delta_{AB}$ around $T_g$ and slightly below. At lower temperatures however, we find that $\Delta_{AB}$ is systematically greater than $\Delta$. This means that the particles in different clones are further apart than what thermal fluctuations allow them to explore. The different clones become confined in distinct minima, which are dynamically inaccessible at low temperature: ergodicity is lost inside the glass. This ergodicity breaking transition inside the glass is conceptually different from the usual ergodicity breaking transition observed as the fluid transforms into a glass. The latter corresponds to the freezing of translational degrees of freedom while the phenomena discussed here corresponds to the freezing of vibrational degrees of freedom [31].

To better characterize this loss of ergodicity, we empirically define the temperature $T_G$ at which the two MSD separate as $\Delta_{AB} = 1.06\Delta$ (both values taken at $t_{\rm w} = 8192$, $\tau = 10^4$). The arrows in Fig. 2 indicate the value $T_G$ for each glass studied.

We can also follow glasses both in temperature and packing fraction. We focus on two extreme regimes: $(\varphi_g, T_g) = (0.85, 0.0353)$ and $(1, 0.26)$, see Fig. 1. The glasses are brought instantaneously to a new state point $(\varphi, T)$, where the long-time limit of the MSDs is measured. Using the same criterion as above, we now look for the line $T_G(\varphi)$ at which ergodicity is broken. We report in Fig. 3 the $T_G$ line for the two initial glasses. Despite differences in the protocols, all the resulting ergodicity breaking temperatures $T_G(\varphi)$ behave qualitatively similarly and grow monotonically from zero above $\varphi \approx 0.81$. Hence, ergodicity within a glass basin is highly sensitive to the final state $(\varphi, T)$ to which the glass is brought, and the preparation history of the glass seems to simply set

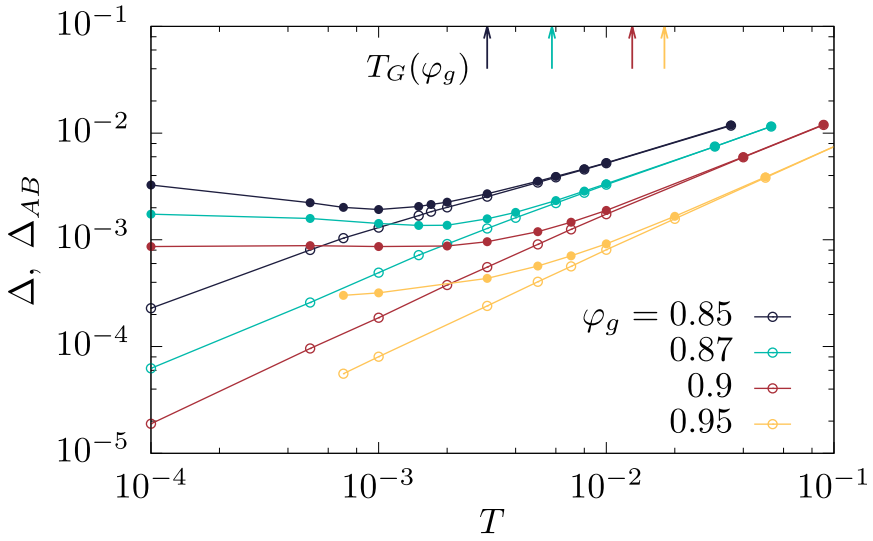


Figure 2: **Loss of ergodicity at low temperature.** Glasses prepared at various $(\varphi_g, T_g)$ and comparable stabilities are quenched to $T$ at fixed packing fraction. The long-time limit ($t_{\rm w} = 8192$, $\tau = 10^4$) of the mean-squared displacement $\Delta$ (open symbols) and mean-squared distance $\Delta_{AB}$ (closed symbols) are shown as a function of the quench temperature. For each $\varphi_g$, a vertical arrow indicates the temperature $T_G$ at which the two MSD separate, signaling loss of ergodicity inside the glass basin.

the overall scale of the barriers inside the glass. Consequently, we can use isochoric temperature quenches or compression/cooling protocols interchangeably.

The phase diagram in Fig. 3 suggests the following picture. At temperatures slightly below the preparation state $(\varphi_g, T_g)$, thermal fluctuations enable an ergodic sampling of the restricted portion of phase space defining a glass basin. When temperature is lowered, the clones retain the same particle arrangement, defined by the initial equilibrium configuration, but may fall into different sub-basins. The sub-basins may differ by the positions of a few particles, or the whole system, as discussed extensively below. The barrier crossing between the different sub-basins is associated to a temperature-dependent timescale. Ergodicity is lost when this timescale becomes much larger than the simulation time and clones then explore separate regions of phase space.

### II.3 Collective and heterogeneous dynamics

In order to reveal the mechanism behind ergodicity breaking and the corresponding growing timescale, we investigate the existence of a growing lengthscale associated to microscopic vibrational dynamics. We use a dynamical susceptibility $\chi_{AB}(t_{\rm w})$, which provides an estimate of the number of correlated particles in the vibrational dynamics at time $t_{\rm w}$. Its definition, given in Sec. IV, ensures $\chi_{AB} \simeq 1$ for uncorrelated dynamics.

We present in Fig. 4 the time evolution of $\chi_{AB}(t_{\rm w})$ after quenching a glass prepared at $(\varphi_g, T_g) = (0.85, 0.0353)$ down to various temperatures $T$. For quenches slightly below $T_g$, the value of $\chi_{AB}$ remains of order unity at all times. The dynamics is ergodic and spatially uncorrelated. The susceptibility increases gradually in time and in amplitude with decreasing the target temperature. For quenches at very low temperature, the initial growth of the susceptibility with time is abrupt,

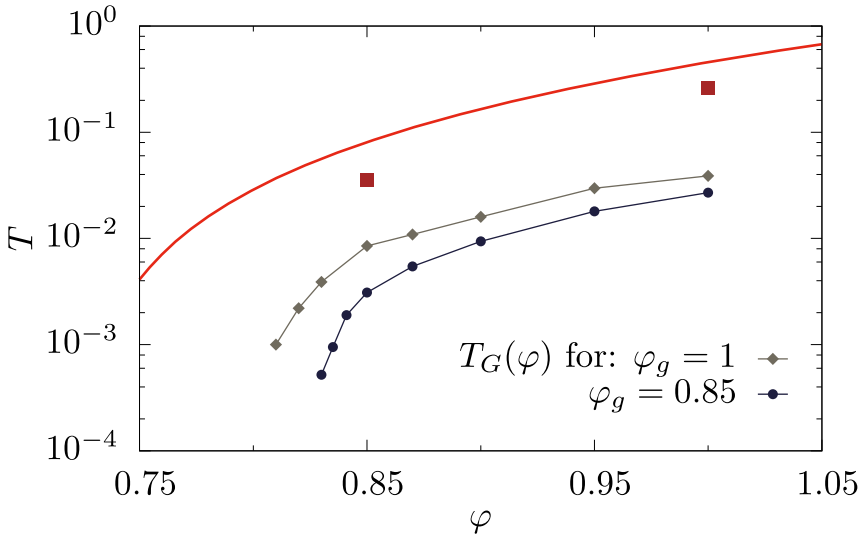


Figure 3: **Loss of ergodicity for various glasses.** Glasses are prepared in equilibrium conditions with the swap method at $(\varphi_g, T_g) = (0.85, 0.0353)$ and $(1, 0.26)$ (red squares), below the computer glass transition (red line). The glasses are rapidly brought to another state point $(\varphi, T)$ in the phase diagram. We compare the long-time limit of the mean-squared displacement and the mean-squared distance between clones of the glass at the new state point. Both values are equal around $(\varphi_g, T_g)$ where the glass basin is sampled ergodically. Ergodicity inside the glass is broken below $T_G(\varphi)$. The ergodicity breaking line $T_G(\varphi)$ depends on glass preparation, encoded in $(\varphi_g, T_g)$. We find that the lines $T_G(\varphi)$ for different glass preparations have the same qualitative behavior.

but slows down dramatically at larger times. The value $\chi_{AB}(t_w = 10^4)$ is thus non-monotonic with $T$. While this behavior resembles qualitatively that reported in hard sphere glasses [31, 32] and $3d$ spin glass models in an external field [42], to our knowledge, this is the first numerical evidence for a growing correlation lengthscale associated with vibrational dynamics in a model relevant to describe bulk thermal systems with soft interactions. The non-monotonicity can be interpreted as a competition between the emergence of an increasingly complex landscape, which tends to increase the susceptibility, and the dynamic slowdown due to the reduction of thermal fluctuations, which makes the exploration of that landscape more difficult at small $T$.

We now determine the extent of the region in which the physics is governed by a complex landscape and spatially correlated dynamics. As in Sec. II.2, we follow glasses initially prepared at $(\varphi_g, T_g) = (0.85, 0.0353)$ to state points $(\varphi, T)$, at which we measure the susceptibility $\chi_{AB}$, in particular its long-time value $\chi_{AB}(t_w = 10^4)$. In Fig. 5, we present iso-$\chi_{AB}(t_w = 10^4)$ lines which connect the state points at which the susceptibility reaches a value of $8, 12$, or $16$. The lines have a similar 'dome' shape, and delimit a region of the phase diagram which shrinks, both in temperature and packing fraction, as $\chi_{AB}$ increases. In this region of the phase diagram, the vibrational dynamics of the glass is slow, correlated in space, and heterogeneous. In Sec. II.5, we characterize the structure of glassy minima in this region, and confirm that it has a highly complex organization.

We locate the jamming transition $(\varphi_J, T = 0)$ of the same glasses by slow decompression, followed by a gradual cooling of the system to $T = 0$. We find $\varphi_J \simeq 0.8404(5)$, indicated by an arrow in Fig. 5. Interestingly, the jamming transition is located inside the dome where the dynamics

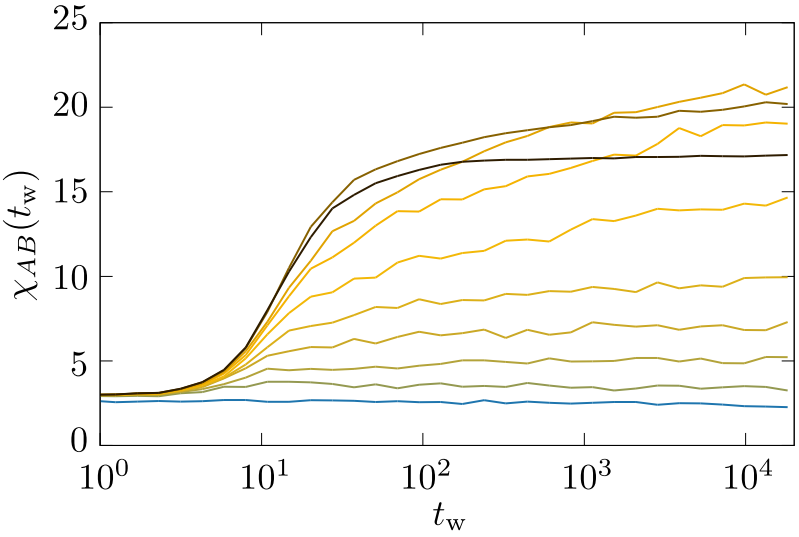


Figure 4: **Growing susceptibility after a temperature quench.** Glasses prepared at $(\varphi_g, T_g) = (0.85, 0.0353)$ are rapidly quenched to temperature $T$. From bottom to top, $T = 0.0353$, 0.005, 0.003, 0.002, 0.0015, 0.001, $7 \times 10^{-4}$, $5 \times 10^{-4}$, $10^{-4}$, $2 \times 10^{-5}$. The susceptibility $\chi_{AB}$, which quantifies the number of particles moving collectively, increases with time after quenches at $T < 0.002$. The value at long time $\chi_{AB}(t_w \simeq 10^4)$ increases with decreasing $T$, until a reverse of trend at $T < 5 \times 10^{-4}$. The non-monotonicity stems from the competition between the emergence of an increasingly complex landscape, which increases the susceptibility, and the dynamic slowdown due to the reduction of thermal fluctuations, which makes the exploration of that landscape more difficult at small temperature.

is governed by a complex landscape. We find a qualitatively similar behavior for glasses prepared at $\varphi_g = 1, T_g = 0.26$. As a result of our extensive exploration of all glassy regimes, we find that the emergence of an incredibly complex landscape at finite temperature, revealed by a growth of the dynamical susceptibility, always takes place close to the jamming transition in the phase diagram. Both phenomena are however distinct, since the 'dome' delimited by the iso-$\chi_{AB}$ lines extends up to temperature orders of magnitude larger than that of jamming criticality [43].

An important observation is that the loss of ergodicity and the increase of lengthscale do not coincide for all densities. In particular, for $\varphi \gtrsim 0.875$ the line $T_G(\varphi)$ is located at higher temperature than the iso-$\chi_{AB}$ lines. We conclude that the loss of ergodicity may have a different origin in different regions of the phase diagram. At lower densities, the loss of ergodicity is accompanied by a growth of $\chi_{AB}$, *i.e.* increasingly collective excitations. At higher packing fraction, the loss of ergodicity is not accompanied by a growing lengthscale, suggesting that it stems from localized defects. These results show that marginal stability, and its associated extended excitations, is not restricted to hard spheres, but can also be found for soft thermal systems in a region around jamming, which is our first important result.

## II.4 Time-evolution of the mean-squared displacement

We investigate the time-evolution of the MSD $\Delta$, and show that the vibrational dynamics becomes increasingly slow as it becomes more collective. We examine the dynamics of the glass at state

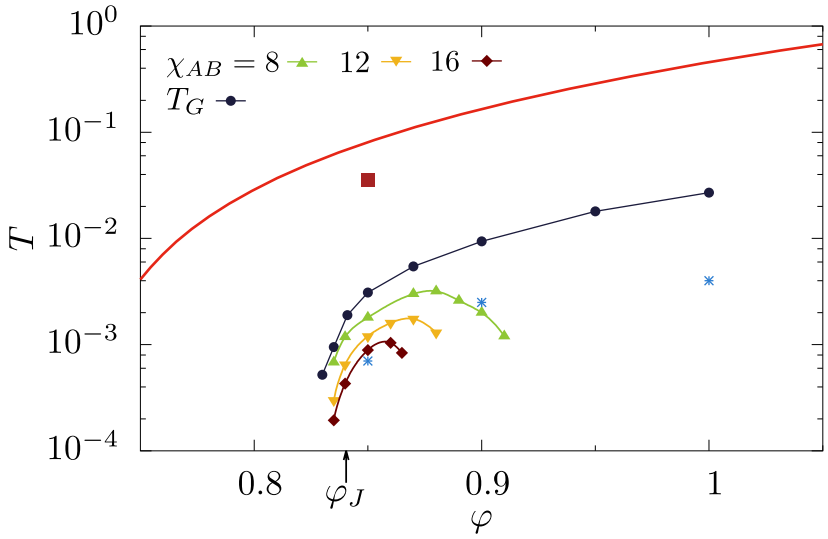


Figure 5: **Ergodicity breaking versus collective dynamics.** Glasses prepared at $(\varphi_g, T_g) = (0.85, 0.0353)$ (red square), below the computer glass transition (red line), are followed in the $\varphi - T$ phase diagram. We indicate the iso-$\chi_{AB}(t_w = 10^4)$ lines at which the dynamical susceptibility reaches 8, 12 and 16. The dynamics is increasingly collective in the dome delineated by theses lines. Ergodicity breaking, observed at the line $T_G(\varphi)$, may be due to collective defects (low $\varphi$), or not (high $\varphi$). The jamming transition $\varphi_J$ of the glass, indicated by an arrow, takes place under the dome where dynamics is collective. We show in Fig. 6 the microscopic dynamics after bringing the glass (red square) to three state points (blue stars) at which ergodicity is lost, and the dynamics is more or less collective (labelled a, b, c from left to right).

points below the ergodicity breaking line $T_G(\varphi)$. We concentrate on three state points indicated by blue stars in Fig. 5. At these points, $\Delta_{AB}/\Delta$ takes a similar value, making their comparison meaningful.

We show in Fig. 6 the time evolution of the MSD $\Delta$ as a function of the waiting time $t_w$ after the quench. We observe very different behavior depending on the target state point. The microscopic dynamics exhibits a strong waiting-time dependence after a quench into the 'dome' (a). This represents a novel type of aging, different from more mundane aging effects observed after rapidly cooling a liquid below the glass transition. In our work, the glass is first equilibrated below the computer glass transition (which kills all diffusive processes), before being quenched to a lower temperature. The aging effect observed in Fig. 6 are related to the vibrational dynamics within a glass basin, whose bottom is so rough that relaxation processes involved after the quench are non-trivial, and have not reached steady state after a time $t_w = 8192$. Quenches further away from the dome, to $\varphi = 0.9, T = 0.0025$ (b), at which $\chi_{AB} \simeq 4$, lead to the same effects, but the amplitude of the decrease of $\Delta$ with waiting time is diminished than for (a). Compressions to higher density $\varphi = 1, T = 0.004$ (c), where the dynamics is not collective, lead to stationary dynamics. This suggests that the glassy basin has a simpler structure at this state point. We explored compressions to $\varphi = 1$ and temperatures ranging from $T_G$ to very low temperature, and never observed any aging effects. We conclude that aging dynamics is a direct signature of the collective excitations taking place inside the glass [44]. We will confirm this picture in Figs. 7 and 8 below.

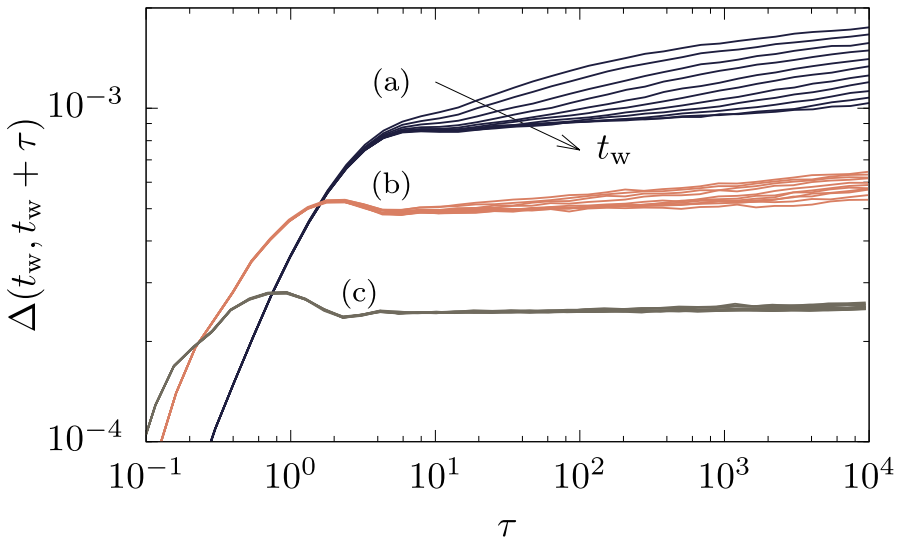


Figure 6: **Microscopic dynamics after quenching a glass.** Mean-squared displacement of glasses prepared in equilibrium at $(\varphi_g, T_g) = (0.85, 0.0353)$ then rapidly quenched to (a) $\varphi = 0.85, T = 7 \times 10^{-4}$; (b) $\varphi = 0.9, T = 0.0025$; (c) $\varphi = 1, T = 0.004$. For each set of curves, the time $t_w$ spent at low temperature increases from top to bottom: $t_w = 8, 16, 32, ..., 4096, 8192$. The three state points (a-c) are shown in Fig. 5 (blue stars). Strong aging effects are observed in (a), mild aging in (b) and no aging in (c). The aging effect evidenced here takes place after further cooling dynamically arrested glasses. This effect is different from the common aging effect observed after rapidly cooling a liquid into the glass phase.

### II.5 Defects: from extended near jamming to localized in dense liquids

The phase diagram in Fig. 5, together with the aging results in Sec. II.4, suggest the following picture. At low densities, $\varphi \sim 0.85$, the relaxation processes responsible for the loss of ergodicity are collective and extended, which naturally explains the growth of $\chi_{AB}$ and collective aging dynamics observed at low temperature. At high densities, $\varphi \sim 1.1$, these processes are localized and do not give rise to an increasing $\chi_{AB}$ or to aging dynamics. The crossover between these two extremes takes place around $\varphi \sim 0.95$ by a mechanism in which the barriers associated to extended defects are pushed towards lower energies, while localized defects with higher energy barriers appear. Ergodicity breaking and susceptibility growth are observed on these different temperature scales, since the former is caused by the localized defects, and the latter by extended ones.

To confirm this physical picture, we analyze the energy landscape of glasses prepared at $(\varphi_g, T_g) = (0.85, 0.0353)$, $(0.95, 0.16)$ and $(1.1, 0.46)$. For each state point, we select randomly one equilibrium configuration, which defines a glassy basin. In order to characterize its structure, we run simulations in the isoconfigurational ensemble. We create $n_c = 100$ clones of each initial equilibrium configuration. The clones are cooled to $T = 0.0005$, $0.005$, and $0.0005$, respectively. Our results do not depend on this choice of temperature. After a simulation time of $t_w = 10^4$, each clone is brought to its inherent structure (IS), where its potential energy $E_{IS}$ is measured. Different clones may or may not end up in the same inherent structure, depending on the complexity of the landscape. In each glass, we analyze all pairs $AB$ of clones after minimization. We compute: (i) the mean-squared distance $\Delta^0_{AB}$ between clones in their IS, (ii) the participation ratio $P_{AB}$ which indi-

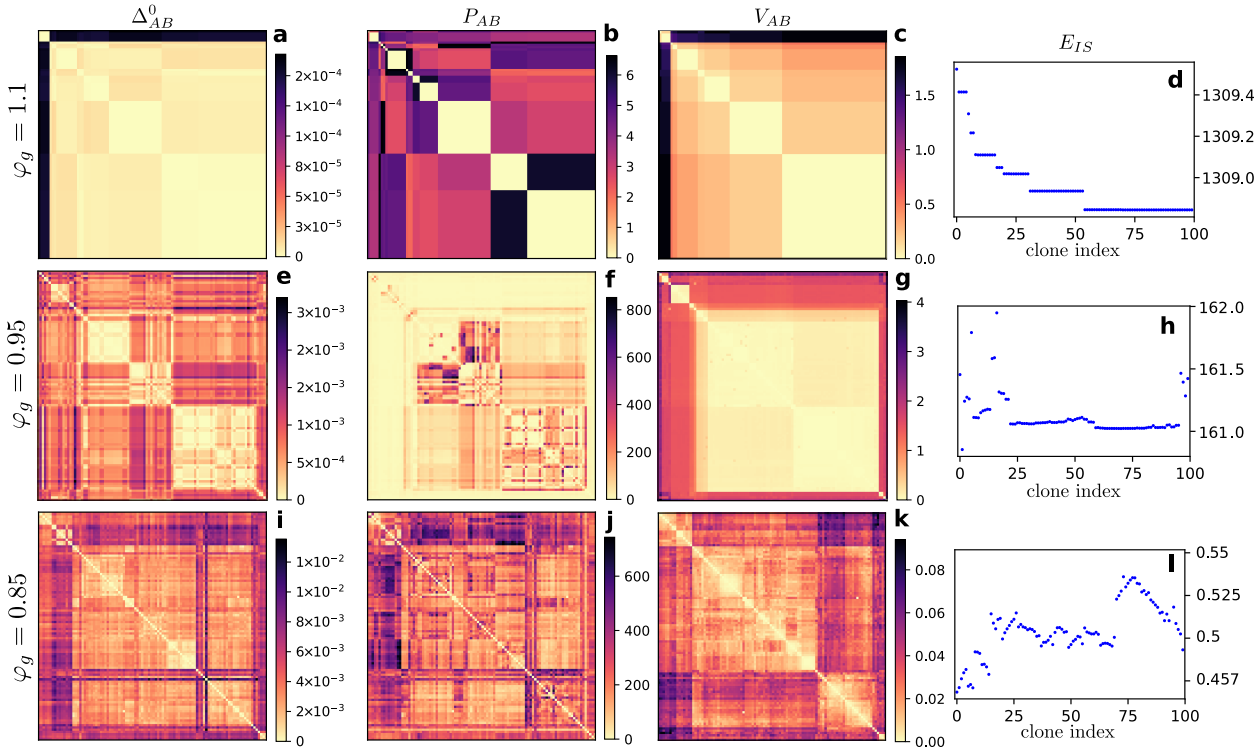


Figure 7: **Crossover from simple to hierarchical landscapes** in glasses prepared at $\varphi_g = 1.1$ (top row), 0.95 (middle), 0.85 (bottom). The potential energy landscape of glasses is sampled by $n_c = 100$ independent clones. We characterize the landscape by several observables $O$, presented as matrices $O_{AB}$, where $A$ and $B$ denote different clones, minimized to their inherent structure. We show the real-space distance $\Delta^0_{AB}$ (a,e,i), participation ratio $P_{AB}$ (b,f,j), and potential energy barrier $V_{AB}$ (c,g,k) between all pairs of clones. The potential energy $E_{IS}$ of the clones in their inherent structure is presented in (d,h,l). The clones indexes are ordered by running a hierarchical clustering algorithm on the matrix $V_{AB}$. For each glass preparation $\varphi_g$, all observables are presented with the same clone ordering.

cates how many particles dominate the displacement field between the two IS, and (iii) the energy barrier $V_{AB}$ between the two IS (see Sec. IV.4 for technical details). To the best of our knowledge, such a complete study of the distribution of minima and barriers inside a glass basin has not been previously reported in the literature.

Representative results for the four observables $(\Delta^0_{AB}, P_{AB}, V_{AB}, E_{IS})$, and three glasses are presented in Fig. 7. The observables defined for pairs of clones are presented as square matrices. The clones are reordered to reveal a possible hierarchical structure of the landscape. In practice, this clustering is performed on the matrix of energy barriers $V_{AB}$ (see Sec. IV.4), and is kept identical for all observables. The clustering allows to visualize easily the topology of the glass energy landscape (Fig. 7: c,g,k), and to follow its evolution with the glass preparation density.

We first describe Fig. 7 (a-d), which correspond to the glass prepared at high density $\varphi_g = 1.1$. We identify mainly two clusters of clones in (a,c): one cluster contains only a few clones (top left), and the other contains the majority of clones. The clones inside a single cluster are close to one another (a), have similar energies (d), and are separated by low energy barriers (c). The two clusters are separated by a large energy barrier (c). The glass basin has little structure: it consists in two sub-basins separated by a high barrier. Each sub-basin contains a small number of IS (d). Whereas the distance between the sub-basins is relatively large (a), they differ only by the position of a few particles, as shown by the maximum participation ratio $P_{AB} = 6$ (b). The defects inside this glass are simple: a few particles hop from one sub-basin to another. These localized defects control the separation of $\Delta_{AB}$ and $\Delta$ which arises at a temperature $T_G$ set by the large barrier $V_{AB}$ between the two clusters. Because they are simple and highly localized, these defects cannot give rise to aging dynamics (Fig. 6), or a growing susceptibility $\chi_{AB}$. Localized defects are crucial to understand the low-temperature thermal properties of glasses [8, 22, 7]. In light of the remarkable ability of the swap algorithm to create glasses with quench rates comparable to those found in vapor deposition studies, it would be interesting to analyze how the classical and quantum properties of these localized defects depend on glass preparation [45].

We then analyze in Fig. 7 (i-l) the other extreme of a glass prepared at $\varphi_g = 0.85$. In this case, the landscape is instead very rough and extremely complex. The glass basin is characterized by a large number of distinct minima (l), separated by barriers of all sizes (k). The clustering in (k) suggests that the landscape is organized hierarchically. Contrary to the glass at $\varphi_g = 1.1$, there is little correlation between the energy barrier separating two minima (k) and the distance between them (i). There is however a good correlation between the distance (i) and participation ratio (j) matrices: extended excitations typically correspond to larger displacements. In summary, the glassy minimum contains barriers of all sizes and of all nature, from localized to extended. This explains why in this glass, the separation of $\Delta_{AB}$ and $\Delta$ around $T_G$ is concomitant with the growth of the susceptibility (Fig. 5) and the emergence of rejuvenation effects (Fig. 6(a)). To the best of our knowledge, this is the first time that such effects are reported in a model for thermal soft particles, relevant for dense colloidal suspensions, and emulsions.

We complete the above picture by providing a microscopic description of how defects transform from localized to extended as packing fraction decreases. Several scenarios could explain this transformation. The density of defects could remain the same, but individual defects become gradually extended. Alternatively, more and more localized defects could appear, and eventually percolate to form extended defects. We show in Figs. 7(e-h) that both types of defects and excitations coexist in the intermediate regime of densities, $\varphi_g = 0.95$. As for $\varphi_g = 1.1$, the glassy minimum is separated into a few sub-minima separated by large barriers. The barriers inside each sub-minimum are much smaller (g-h). Yet, the number of distinct minima inside each cluster is quite large (h). Strikingly,

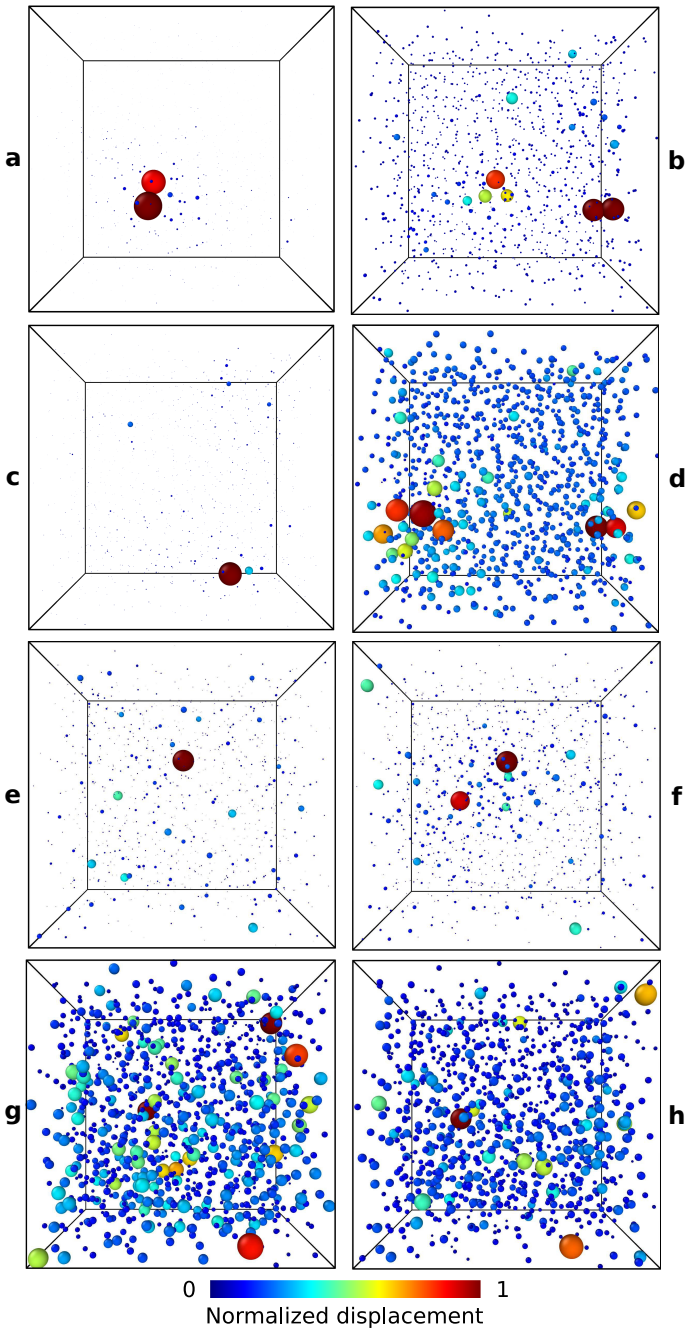


Figure 8: **Coexistence of localized and extended defects in glasses.** Snapshots of particle displacements between pairs of inherent structures of the same glass for (a) $\varphi_g = 1.1$; (b,c,d) $\varphi_g = 0.95$; (e,f,g,h) $\varphi_g = 0.85$. (a) $\varphi_g = 1.1$: localized defect, high energy barrier; $\varphi_g = 0.95$: (b) localized, small barrier, (c) localized, high barrier, (d) delocalized, low barrier; $\varphi_g = 0.85$: (e) localized, small barrier; (f) localized, high barrier; (g) delocalized, small barrier; (h) delocalized, high barrier. Particle size and color are proportional to the particle displacement, normalized to the largest displacement in the sample.

while the large energy barriers (g) have a low participation ratio (f), the barriers found inside the sub-basins can be very collective, as for $\varphi_g = 0.85$. The landscape is clearly organized around two main energy scales: the scale $T_G$, at which ergodicity is lost due to the highest energy barriers associated to localized defects, which explains why neither a significant growth in the susceptibility, nor aging dynamics are observed around this temperature scale; and a lower scale, associated to extended defects, which controls the growth of $\chi_{AB}$ and the emergence of aging, Fig. 6(b). We believe that this coexistence of extended and localized excitations, which is our second important result, will be manifested in the physical properties of the corresponding glasses, e.g. in transport properties [8], in the response to localized probes [7], and in the aging/rejuvenation dynamics after a sudden temperature change [44].

We accompany these conclusions with real-space snapshots illustrating the difference between distinct inherent structures in Fig. 8 resolved at the particle scale. For $\varphi_g = 1.1$, we show the localized defect responsible for the loss of ergodicity (a). Two particles move between two local minima, and the surrounding particles move slightly due to the elasticity of the solid. For $\varphi_g = 0.95$, localized excitations can correspond to a low (b) or high (c) energy barrier. Delocalized excitations only correspond to the bottom of the landscape, i.e. to small barriers (d). For $\varphi_g = 0.85$, we find localized (e,f) and delocalized (g,h) excitations, which are either associated to small barriers (e,g) or high energy barriers (f,h) demonstrating the variety and increasing complexity of the potential energy landscape when moving closer to the jamming transition.

# III Discussion

We study the nature of excitations and defects through extensive simulations of a three-dimensional WCA glass former. Our main finding is that the nature of the energy landscape can be sensitively tuned by changing density. At high densities, in the regime relevant for molecular and atomic glasses, the landscape is rather simple, characterized by few minima. The dynamical behavior of the glass is dictated by highly localized defects, which correspond to a few particles hopping between nearby configurations. This corresponds to the standard picture of two-level systems in glasses [22, 7]. By contrast, at lower densities, relevant for granular materials, soft and hard colloidal suspensions, the landscape is very rough and has a hierarchical structure. There exist barriers over a broad range of energy scales, with a degree of localization that spans very localized and highly extended defects. This first result extends to finite temperatures earlier results about the marginality associated to athermal jamming [28, 2, 25, 29]. Most interestingly, in the intermediate regime of densities, relevant for soft colloidal particles and emulsions, the landscape is characterized by both features. Localized defects dominate at higher temperature, and are responsible for ergodicity breaking inside the glass. The freezing of these defects, which involve a few particles, defines a small number of sub-basins. Each sub-basin, however, possesses a complex structure at lower energy scales, with extended defects associated to low barriers that appear similar to the ones found at lower densities. This second result leads us to predict that soft colloidal glasses and emulsions should be characterized by a complex hierarchical landscape, giving rise to interesting new physics, such as ergodicity breaking transitions, aging in the glass, rejuvenation and memory effects [44].

We showed that in all physical regimes, low-temperature glasses evolve inside an energy basin composed of a potentially large number of sub-minima. This sub-structure gives rise to a new type of ergodicity breaking transition in glasses at low temperature. The ergodicity breaking transition may or may not be accompanied by a growing lengthscale, dynamic heterogeneity and aging effects, depending on the preparation density of the glass. One can thus expect a variety of behaviors in

distinct materials, depending on their location in the phase diagram analyzed in our work. Our study paves the way to a complete numerical and experimental characterization of the low-temperature behavior of glasses, including in the quantum regime where tunneling properties are likely to be strongly influenced by the spatial nature of defects.

**Acknowledgments.** – We thank M. Baity-Jesi, W. Ji, D. Khomenko, B. Seoane, and D. Reichman for interesting discussions, and C. Dennis for hierarchical clustering tips. This project has received funding from the European Research Council (ERC) under the European Union's Horizon 2020 research and innovation programme (grant agreement num. 723955 - GlassUniversality). This work was supported by a grant from the Simons Foundation (#454933, L. Berthier, #454955, F. Zamponi).

## Bibliography

[1] A. Cavagna. *Physics Reports*, 476(4-6):51–124, 2009.

[2] Andrea J Liu and Sidney R Nagel. *Annual Review of Condensed Matter Physics*, 1(1):347–369, 2010.

[3] Andrea J. Liu and Sidney R. Nagel. *Nature*, 396(6706):21, 1998.

[4] L. Berthier and T. A. Witten. *EPL (Europhysics Letters)*, 86(1):10001, 2009.

[5] Frank H. Stillinger and Thomas A. Weber. *Phys. Rev. A*, 25(2):978, Feb 1982.

[6] Andreas Heuer. *Journal of Physics: Condensed Matter*, 20(37):373101, 2008.

[7] WA Phillips. *Reports on Progress in Physics*, 50(12):1657, 1987.

[8] RC Zeller and RO Pohl. *Physical Review B*, 4(6):2029, 1971.

[9] DA Parshin, HR Schober, and VL Gurevich. *Physical Review B*, 76(6):064206, 2007.

[10] W Schirmacher, G Ruocco, and T Scopigno. *Physical Review Letters*, 98(2):025501, 2007.

[11] T Damart, A Tanguy, and D Rodney. *Physical Review B*, 95(5):054203, 2017.

[12] R Flaminio, J Franc, C Michel, N Morgado, L Pinard, and B Sassolas. *Classical and Quantum Gravity*, 27(8):084030, 2010.

[13] David Rodney, Anne Tanguy, and Damien Vandembroucq. *Modelling and Simulation in Materials Science and Engineering*, 19(8):083001, 2011.

[14] HGE Hentschel, Smarajit Karmakar, Edan Lerner, and Itamar Procaccia. *Physical Review E*, 83(6):061101, 2011.

[15] Jie Lin, Alaa Saade, Edan Lerner, Alberto Rosso, and Matthieu Wyart. *EPL (Europhysics Letters)*, 105(2):26003, 2014.

[16] Sylvain Patinet, Damien Vandembroucq, and Michael L Falk. *Physical review letters*, 117(4): 045501, 2016.

[17] Giulio Biroli and Pierfrancesco Urbani. *Nature Physics*, 12:1130–1133, 2016.

[18] Francesco Sette, Michael H Krisch, Claudio Masciovecchio, Giancarlo Ruocco, and Giulio Monaco. *Science*, 280(5369):1550–1555, 1998.

[19] TS Grigera, V Martin-Mayor, Giorgio Parisi, and Paolo Verrocchio. *Nature*, 422(6929):289, 2003.

[20] Edan Lerner, Gustavo Düring, and Eran Bouchbinder. *Phys. Rev. Lett.*, 117(3):035501, 2016.

[21] Hideyuki Mizuno, Hayato Shiba, and Atsushi Ikeda. *Proceedings of the National Academy of Sciences*, 114:E9767, 2017.

[22] P W Anderson, BI Halperin, and C M Varma. *Philosophical Magazine*, 25(1):1, 1972.

[23] C. Scalliet, L. Berthier, and F. Zamponi. *Phys. Rev. Lett.*, 119:205501, Nov 2017.

[24] T Damart and D Rodney. *Physical Review B*, 97(1):014201, 2018.

[25] Markus Müller and Matthieu Wyart. *Annual Review of Condensed Matter Physics*, 6:177, 2015.

[26] Thibault Bertrand, Carl F. Schreck, Corey S. O'Hern, and Mark D. Shattuck. *Phys. Rev. E*, 89:062203, Jun 2014.

[27] Qikai Wu, Thibault Bertrand, Mark D. Shattuck, and Corey S. O'Hern. *Phys. Rev. E*, 96: 062902, Dec 2017.

[28] M. Wyart, SR Nagel, and TA Witten. *Europhysics Letters*, 72(3):486–492, 2005.

[29] Masanari Shimada, Hideyuki Mizuno, Matthieu Wyart, and Atsushi Ikeda. *Phys. Rev. E*, 98 (6):060901, 2018.

[30] Patrick Charbonneau, Jorge Kurchan, Giorgio Parisi, Pierfrancesco Urbani, and Francesco Zamponi. *Nature communications*, 5:3725, 2014.

[31] Ludovic Berthier, Patrick Charbonneau, Yuliang Jin, Giorgio Parisi, Beatriz Seoane, and Francesco Zamponi. *Proceedings of the National Academy of Sciences*, 113(30):8397–8401, 2016.

[32] Qinyi Liao and Ludovic Berthier. *Phys. Rev. X*, 9:011049, Mar 2019.

[33] M. A. Moore and A. J Bray. *Phys. Rev. B*, 83(22):224408, 2011.

[34] C. L. Hicks, Michael J. Wheatley, Michael J. Godfrey, and Micheal A. Moore. *Phys. Rev. Lett.*, 120:225501, May 2018.

[35] Giorgio Parisi, Yoav G. Pollack, Itamar Procaccia, Corrado Rainone, and Murari Singh. *Phys. Rev. E*, 97:063003, Jun 2018.

[36] John D. Weeks, David Chandler, and Hans C. Andersen. *J. Chem. Phys.*, 54(12):5237, 1971.

[37] Camille Scalliet, Ludovic Berthier, and Francesco Zamponi. *Phys. Rev. E*, 99:012107, Jan 2019.

[38] Ludovic Berthier, Elijah Flenner, Christopher J Fullerton, Camille Scalliet, and Murari Singh. *Journal of Statistical Mechanics: Theory and Experiment*, page 064004, 2019.

[39] T.S. Grigera and G. Parisi. *Physical Review E*, 63(4):45102, 2001.

[40] Andrea Ninarello, Ludovic Berthier, and Daniele Coslovich. *Phys. Rev. X*, 7(2):021039, 2017.

[41] Asaph Widmer-Cooper, Peter Harrowell, and H. Fynewever. *Phys. Rev. Lett.*, 93:135701, Sep 2004.

[42] Beatriz Seoane and Francesco Zamponi. *Soft Matter*, 14:5222, 2018.

[43] A. Ikeda, L. Berthier, and G. Biroli. *J. Chem. Phys.*, 138:12A507, 2013.

[44] Camille Scalliet and Ludovic Berthier. *Phys. Rev. Lett.*, 122:255502, Jun 2019.

[45] Tomás Pérez-Castañeda, Cristian Rodríguez-Tinoco, Javier Rodríguez-Viejo, and Miguel A. Ramos. *Proceedings of the National Academy of Sciences*, 111(31):11275–11280, 2014.

[46] S. Franz and G. Parisi. *Journal de Physique I*, 5(11):1401–1415, 1995.

[47] Lenka Zdeborová and Florent Krzakala. *Phys. Rev. B*, 81:224205, Jun 2010.

[48] Hannes Jónsson, Greg Mills, and Karsten W Jacobsen. Nudged elastic band method for finding minimum energy paths of transitions. In B. J. Berne, G. Ciccotti, and D. F. Coker, editors, *Classical and Quantum Dynamics in Condensed Phase Simulations*. World Scientific, Singapore, 1998. URL `https://www.worldscientific.com/doi/abs/10.1142/9789812839664_0016`.

[49] Graeme Henkelman, Blas P Uberuaga, and Hannes Jónsson. *J. Chem. Phys.*, 113(22):9901,

2000.

[50] C. C. Aggarwal and C. K. Reddy. *Data Clustering: Algorithms and Applications*. CRC Press, 2006.

# IV Supplementary Information - Methods

## IV.1 Model

We study a three-dimensional Weeks-Chandler-Andersen (WCA) model of soft repulsive particles [36]. The pair interaction between particles $i$ and $j$ reads

$$V = \begin{cases} 4\epsilon \left[ \left( \frac{\sigma_{ij}}{r_{ij}} \right)^{12} - \left( \frac{\sigma_{ij}}{r_{ij}} \right)^{6} \right] + 1 \ , & r_{ij} < 2^{1/6}\sigma_{ij} \\ 0 & \text{otherwise.} \end{cases} \tag{1}$$

The potential and its first derivative are smooth at the cutoff distance $\bar{\sigma}_{ij} = 2^{1/6}\sigma_{ij}$. We use a non-additive polydisperse mixture to stabilize the homogeneous fluid against fractionation or crystallization [40], $\sigma_{ij} = \frac{1}{2}(\sigma_i + \sigma_j)\,(1 - 0.2|\sigma_i - \sigma_j|)$. Although the potential is non-additive, the quantity $\bar{\sigma}_i = 2^{1/6}\sigma_i$ acts as an effective particle diameter. The $\sigma_i$ are distributed continuously with the distribution $P(\sigma_m \leq \sigma \leq \sigma_M) \sim 1/\sigma^3$, with a size ratio $\sigma_m/\sigma_M = 0.45$, and $\langle\sigma\rangle = \int P(\sigma)\mathrm{d}\sigma = 1$. The polydispersity of the system is 23%. We study systems of $N = 1000$ particles of mass $m$, in a box of linear size $L$ and volume $V = L^3$. The relevant control parameters are the temperature $T$ and the packing fraction $\varphi$, defined as $\varphi = \pi/(6V)\sum_i \bar{\sigma}_i^3 = \sqrt{2}\pi/(6V)\sum_i \sigma_i^3$. The effect of polydispersity and non-additivity is to shift all packing fractions to higher values. For example the jamming transition of random packings is equal to $\varphi_J \simeq 0.78$ in our model, instead of 0.64 for monodisperse $3d$ packings with additive interactions. Energies, lengths and times are respectively expressed in units of $\epsilon$, $\sqrt{\epsilon/m\langle\sigma\rangle^2}$, and $\langle\sigma\rangle$.

## IV.2 Preparation protocols

We employ a two-step protocol. First, we generate equilibrated configurations at various state points $(\varphi_g, T_g)$, for which the physical dynamics is completely arrested on accessible time scales (see Fig. 1) but where thermalization can be achieved using a hybrid swap Monte Carlo technique [40]. For the hybrid swap, we use the implementation of Ref. [38]. For each state point $(\varphi_g, T_g)$, we first generate $n_g = 200$ independent equilibrium configurations. Second, we use these very stable equilibrium configurations as input for molecular dynamics (MD) simulations. The equations of motion are solved with an integration timestep $dt = 0.0035$. The temperature of the system is imposed by a Berendsen thermostat with a timescale $\tau_B = 1.0$. We consider thermodynamic conditions where particle diffusion is fully arrested, so that simulations always remain confined within a single glass basin, selected by the initial configuration. In addition, we produce $n_c = 20$ clones for each of the $n_g$ initial configurations (we use $n_c = 100$ in Sec. II.5). Clones share the same initial positions, but are given initial velocities randomly sampled from the appropriate Maxwell distribution. Each configuration is then studied at various $(\varphi, T)$ by instantaneously changing the control parameters. This two-step process emulates the 'state following' construction employed in mean-field analytical studies [46, 47], that we have recently applied to the WCA model [37]. This protocol is also a fair numerical implementation of an experimental protocol where glasses are produced by cooling, and the glassy state frozen at the experimental glass transition temperature is then studied at various state points within the glass phase.

## IV.3 Observables for ergodicity breaking in the glass basin

From a given initial equilibrated configuration at $(\varphi_g, T_g)$, we run $n_c$ independent MD simulations using the clones as initial conditions. At the beginning of the simulation, the control parameters $(\varphi, T)$ are changed instantaneously. It takes a time $t \sim 10$ for the kinetic temperature to reach the desired value. The origin for waiting times $t_{\rm w} = 0$ is defined as the time at which the kinetic temperature, averaged over a time $t = 1$, reaches the imposed value. We focus on two measures of distance: the mean-squared displacement (MSD) $\Delta_{AB}$ between the same particles in different clones of a glass,

$$\Delta_{AB}(t_{\rm w}) = \frac{1}{N_b}\sum_{i=1}^{N_b}\langle|\mathbf{r}_i^A(t_{\rm w}) - \mathbf{r}_i^B(t_{\rm w})|^2\rangle \ , \tag{2}$$

and the MSD $\Delta$, which quantifies the dynamics of the particles within a single clone,

$$\Delta(t_{\rm w}, t_{\rm w}+\tau) = \frac{1}{N_b}\sum_{i=1}^{N_b}\langle|\boldsymbol{r}_i(t_{\rm w}+\tau) - \boldsymbol{r}_i(t_{\rm w})|^2\rangle \ . \tag{3}$$

Here, $\boldsymbol{r}_i$ is the coordinate of particle $i$, and $\mathbf{r}_i^A$ and $\mathbf{r}_i^B$ the positions of particle $i$ in two different clones, which are generically referred to as $A$ and $B$. The average is made using the $N_b = N/2$ particles having the largest diameter. We find that smaller particles are more mobile and sometimes dominate the average. The brackets indicate an average both on disorder (using the $n_g = 200$ independent initial configurations), and thermal history (using the $n_c = 20$ clones for each glass). In the case of $\Delta_{AB}$, the thermal average is performed over the $n_c(n_c-1)/2$ pairs of clones.

We define the susceptibility associated to the global fluctuations of the mean-squared distance between clones [31, 23],

$$\chi_{AB} = N_b\frac{\langle\Delta_{AB}^2\rangle - \langle\Delta_{AB}\rangle^2}{\langle{\Delta_{AB}^i}^2\rangle - \langle\Delta_{AB}^i\rangle^2}, \tag{4}$$

where $\Delta_{AB}$ is defined in Eq. (2), and $\Delta_{AB}^i$ represents its single-particle version. The time dependence in Eq. (4) is omitted to ease the reading, but just as $\Delta_{AB}$, $\chi_{AB}(t_{\rm w})$ is a time-dependent observable. The normalization in $\chi_{AB}$ ensures that $\chi_{AB} = 1$ for spatially uncorrelated dynamics. Using this definition, $\chi_{AB}$ is also a direct measure of a correlation volume, and it is the direct analogue of a spin-glass susceptibility.

## IV.4 Exploration of the potential energy landscape

To explore the energy landscape associated to a given initial equilibrium configuration we first create $n_c = 100$ clones. The clones are cooled to a lower temperature: $T = 0.0005, 0.005$, and $0.0005$, for the glasses prepared at $\varphi_g = 1.1, 0.95, 0.85$, respectively. We simulate the dynamics of these systems at these low temperatures $T$ during a total time $t_{\rm w} = 10^4$. At the end of the simulation, the configuration is minimized using a conjugate gradient algorithm to bring each clone to its inherent structure (IS). We measure the potential energy $E_{IS}$ of each IS found inside each glass basin.

We then compare all pairs of IS found inside each glass. We compute the distance between two IS, taking into account all $N$ particles:

$$\Delta_{AB}^0 = \frac{1}{N}\sum_i|\mathbf{r}_i^{A,0} - \mathbf{r}_i^{B,0}|^2, \tag{5}$$

where $\mathbf{r}_i^{A,0}$ is the position of particle $i$ in the IS of clone $A$. In order to have a more refined information on how many particles contribute to the value of $\Delta_{AB}$, we compute a participation ratio

$$P_{AB} = \frac{\left[\sum_{\mu,i}(\delta r_{AB}^{\mu,i})^2\right]^2}{\sum_{\mu,i}(\delta r_{AB}^{\mu,i})^4}, \tag{6}$$

where $\delta r_{AB}^{\mu,i} = \mu_i^{A,0} - \mu_i^{B,0}$ ($\mu = x, y, z$). The sum runs over all $N$ particles. With this definition, the participation ratio directly estimates the number of particles which dominate the difference between pairs of IS.

For each pair of IS, we estimate an energy barrier using the nudge elastic band (NEB) method [48]. Note that this approximate method only provides an upper bound for the lowest energy barrier separating the two energy minima. We use 40 intermediate images of the system, initialized by linear interpolation between two IS. We relax the chain of images using the potential energy Eq. (1) in directions transverse to the chain, and elastic springs in the parallel direction. We use a climbing version of the method [49], which ensures that one image is at the saddle point. The energy barrier $V_{AB}$ is the energy difference between the saddle point and the lowest energy minimum.

We find that for $\varphi \lesssim 0.9$, the NEB method does not converge properly. The reason is that at low temperature in this density regime, the particles behave more and more like hard sphere particles, for which the potential energy cost of overlapping particles diverges. In some cases, the linear interpolation creates strongly overlapping particles, and a singularity in the potential energy of the chain of images. To work around this problem, we first perform a NEB minimization using a harmonic repulsion between particles, instead of WCA. The harmonic potential used is $V = 18 \times 2^{2/3}(r_{ij}/\sigma_{ij} - 2^{1/6})^2$ if $r_{ij} < 2^{1/6}\sigma_{ij}$ and zero otherwise. The WCA and this harmonic potential have the same first two derivatives at the cutoff. Both potentials behave similarly at small overlaps, but the harmonic one does not create diverging potential energies due to particle overlaps. The initial NEB minimization run with harmonic repulsion converges smoothly at all densities, and removes spurious particle overlaps. The relaxed chain of images is then minimized with the NEB method using the original WCA potential. We have checked that both methods (WCA versus harmonic + WCA) yield similar results at high densities $\varphi_g = 1.1$ and $\varphi_g = 0.95$. This validates the two-step NEB minimization using the combination of harmonic and WCA interactions that we implement at $\varphi_g = 0.85$.

The hierarchical clustering is performed on the barrier matrix $V_{AB}$ using the `linkage` function of the 'hierarchical clustering' python package, which is an agglomerative algorithm [50]. Initially, each clone starts in its own cluster. The clusters are gradually merged until they form one large cluster. The merging rule is defined by giving: a distance between individual clones (here, the energy barrier $V_{AB}$), and a 'linkage criterion' which defines the distance between clusters. At each step, clusters with the smallest distance are merged. We find empirically that an 'average' linkage (the distance between clusters is the average of the energy barriers on all pairs) gives a good enough clustering.

The snapshots shown in Fig. 8 highlight the displacement of particles between two IS. The particle positions are those of one IS, and the size and color code for the particles is proportional to the displacement $|\mathbf{r}_i^{A,0} - \mathbf{r}_i^{B,0}|$ between the IS. The particle with largest displacement is set to a diameter 1. This allows to compare visually snapshots of systems for which the displacement may vary by orders of magnitude. The snapshots should therefore be read in parallel with Figs. 7(a,e,i), which provide the scale for particle displacements in each case.

Article

# Rejuvenation and Memory Effects in a Structural Glass

C. Scalliet and L. Berthier, Phys. Rev. Lett. 122 (25), 255502 (2019) – Editor's Suggestion.

**We show numerically that a three-dimensional model for structural glass displays aging, rejuvenation and memory effects when subjected to a temperature cycle. These effects indicate that the free energy landscape of structural glasses may possess the complex hierarchical structure that characterizes materials such as spin and polymer glasses. We use the theoretical concept of marginal stability to interpret our results, and explain in which physical conditions a complex aging dynamics can emerge in dense supercooled liquids, paving the way for future experimental studies of complex aging dynamics in colloidal and granular glasses.**

The behavior of many disordered materials is dominated by their failure to reach equilibrium, leading to extremely slow relaxations, non-linear responses, and time-dependent behavior. This aging behavior is observed in a broad variety of condensed-matter systems as microscopically distinct as polymers [1], spin glasses [2], molecular glasses [3, 4], colloidal gels [5, 6], disordered ferroelectrics [7, 8], and crumpled paper sheets [9]. The widespread occurrence of aging phenomena is theoretically understood as a general consequence of frustration leading to a complex free-energy landscape [10, 11].

Specific experimental protocols, such as temperature cycles, are used to better characterize the nonequilibrium dynamics of glasses [2, 12]. Temperature cycles within the glass phase were first performed in spin glasses, revealing spectacular dynamical effects [13, 14, 15, 16, 17, 18]. Aging is reinitialized after a second downward jump in temperature (rejuvenation), but when the first temperature is restored, the system recalls the state reached before that jump (memory). However, when similar protocols are applied to molecular glasses, such as glycerol, no rejuvenation is observed [3], although some memory can be found [19, 20, 21]. Both effects were however reported in gelatin gels [22]. Aging is a simple consequence of long relaxation timescales, but rejuvenation and memory effects require a specific, hierarchical organization of the free-energy landscape [23, 24, 25, 26]. This is exactly realized in mean field models for spin-glasses [27, 28, 29], and can directly be confirmed in spin-glass simulations [30, 31, 32, 33].

Recently, the mean-field theory for structural glasses predicted the existence of marginally stable

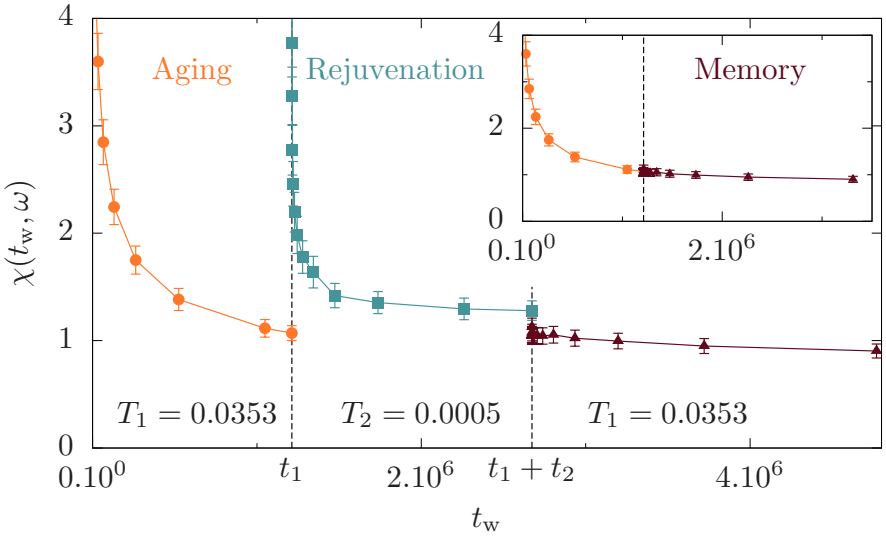


Figure 1: **Aging, rejuvenation and memory** in a structural glass subjected to a temperature cycle. We show the time evolution of $\chi(t_w, \omega = 10^{-5})$ in each step of the cycle, delimited by vertical dashed lines. Aging is observed as the liquid is quenched into the glass phase (circles). The glass rejuvenates as it is cooled further (squares), but retains perfect memory when heated back (triangles). In the inset, the intermediate step is removed to better demonstrate the memory effect.

glass phases characterized by a hierarchical free energy landscape, with strong similarities with spin glasses [34, 35]. Although the existence of a sharp phase transition between normal and marginally stable glass phases remains debated in finite dimensions [36, 37, 38, 39], the theory makes crisp predictions regarding the physical conditions where the glassy landscape becomes hierarchical [40, 41, 42, 43]. There are numerical evidences that a complex aging dynamics emerges in the hard sphere model [44, 45, 46], but simulations of model atomic glasses [47, 48] did not find those signatures.

We numerically study the nonequilibrium dynamics of soft repulsive spheres in $d = 3$. This choice is motivated by both theoretical results in the mean-field limit [43] and by a numerical exploration of the complete temperature/density phase diagram to detect the state points where marginal stability can be expected to become physically relevant [49]. By carefully choosing the state points where signs of marginal stability can be observed [49] to perform the present temperature cycles, we successfully observe rejuvenation and memory effects in our model for structural glasses. Our central result is presented in Fig. 1, where we adopt the same representation as in experiments, showing the evolution of a dynamic susceptibility $\chi(t_w, \omega)$ (Eq. 3) during the cycle. A high-temperature liquid is rapidly cooled to $T_1$ in the glass phase. Aging dynamics is signaled by a slowly decreasing $\chi$ (circles). The glass is aged for a given time before being cooled to a lower temperature $T_2$. The glass then rejuvenates, since a strong restart of the aging dynamics takes place at $T_2$ (squares). When the glass is reheated to $T_1$ (triangles), it recovers memory of the initial aging (Fig. 1, inset), despite the strong rejuvenation in the intermediate step. We attribute these effects to the hierarchical landscape of structural glasses in a marginally stable phase.

**Model and methods** – We study a three-dimensional glass former composed of $N = 3000$ continuously polydisperse particles. Two particles $i$ and $j$ at positions $\mathbf{r}_i$ and $\mathbf{r}_j$ interact via the

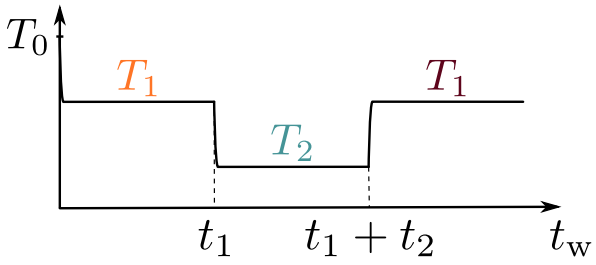


Figure 2: **Protocol:** Sketch of the temperature cycle, where $T_1$ and $T_2$ are both in the glass phase while $T_0$ is in the fluid.

Weeks-Chandler-Andersen (WCA) potential [50]

$$v(r_{ij}) = 4\epsilon \left[(\sigma_{ij}/r_{ij})^{12} - (\sigma_{ij}/r_{ij})^{6}\right] + 1 \quad , \tag{1}$$

only if they are at a distance $r_{ij} = |\mathbf{r}_i - \mathbf{r}_j| < 2^{1/6}\sigma_{ij}$, with a non-additive interaction rule $\sigma_{ij} = \frac{\sigma_i+\sigma_j}{2}(1 - 0.2|\sigma_i - \sigma_j|)$. The potential and forces are continuous at the physical cut-off distance. For each particle, $\sigma_i$ is drawn from the normalized distribution $P(\sigma_m \leq \sigma \leq \sigma_M) \sim 1/\sigma^3$, where $\sigma_m = 0.73$ and $\sigma_M = 1.62$. This model is chosen for its excellent glass-forming ability when simulated either with molecular dynamics, or particle-swap dynamics [51], and represents a canonical model for dense supercooled liquids [52].

The aging dynamics is studied with molecular dynamics (MD). The simulations are performed with a time discretization $dt = 0.003$, within a cubic box of linear size $L$, using periodic boundary conditions. The temperature is controlled by a Berendsen thermostat with damping parameter $\tau_B = 1$ [53]. We reset the total momentum to zero every $10^6$ MD steps. Lengths, times and energies are expressed in units of $\overline{\sigma} = \int \sigma P(\sigma) d\sigma$, $\sqrt{\epsilon/m\overline{\sigma}^2}$ and $\epsilon$, respectively. The state of the system is determined by temperature $T$, and packing fraction $\varphi = \pi/(3\sqrt{2}L^3)\sum_i \sigma_i^3$. For this non-additive polydisperse mixture, the jamming transition occurs near $\varphi_J \sim 0.78$. Here, we focus on a fixed packing fraction $\varphi = 0.85$, and discuss later this choice. At this density, the onset of glassy dynamics is near $T_{\rm onset} = 0.2$, and at $T_{\rm c} = 0.07$ the dynamics has slowed down by a factor $10^4$, below which conventional MD simulations do not reach equilibrium. In addition, we use a hybrid Swap Monte Carlo method [54] to prepare equilibrated configurations deep in the glass phase, down to $T = 0.035 \sim T_{\rm c}/2$, to better analyze rejuvenation effects.

**Protocol and observables** – We investigate the nonequilibrium dynamics of glasses during a temperature cycle sketched in Fig. 2. In the first step, an equilibrium liquid at $T_0 = 0.36$ is quenched rapidly (with a rate of $3.10^{-3}$) to $T_1 = 0.0353 < T_{\rm c}$. The liquid falls out of equilibrium and slowly ages for a duration $t_1$. In the second step, the aged glass is rapidly cooled to a lower temperature $T_2 < T_1$. It stays there during a time $t_2 = t_1$, after which the system is heated back to $T_1$. We measure the mean-squared displacement (MSD):

$$\Delta(t_{\rm w}, t_{\rm w} + \tau) = \frac{1}{N}\sum_{i=1}^{N} \langle |\boldsymbol{r}_i(t_{\rm w} + \tau) - \boldsymbol{r}_i(t_{\rm w})|^2 \rangle \quad , \tag{2}$$

where $t_{\rm w}$ is the waiting time after a temperature change. This protocol is repeated using 200 independent equilibrium liquids. The brackets in Eq. (2) represent an average over these independent

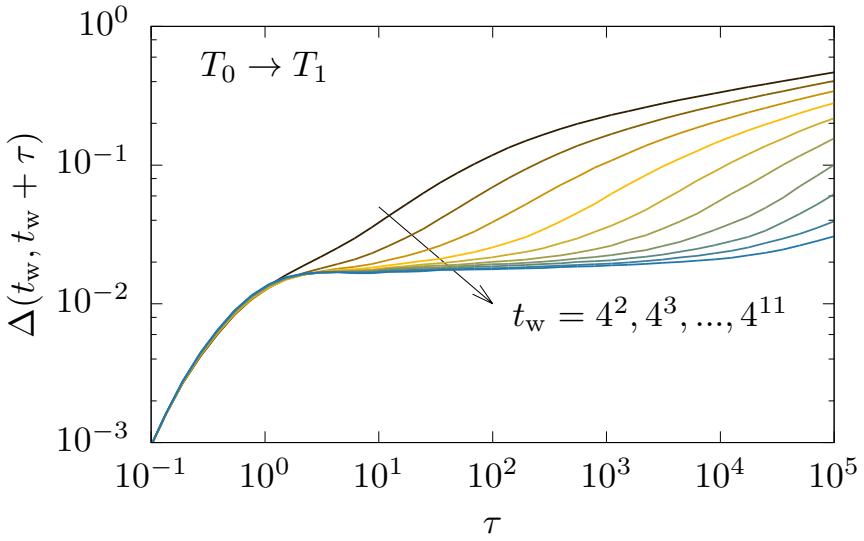


Figure 3: **Aging** of the mean-squared displacement after a quench from the liquid $T_0 = 0.36$ to the glass phase $T_1 = 0.0353$. Each curve corresponds to a given waiting time $t_w$ after the quench, and reveals a slower motion in older systems.

runs. To make a connection with experiments, we define a dynamic susceptibility [30]

$$\chi(t_w, \omega) = \frac{\Delta(t_w, t_w + \omega^{-1})}{T} \quad , \tag{3}$$

which plays a role analogous to the ac magnetic or dielectric susceptibility at frequency $\omega$ in experiments. This quantity also conveniently compares results at different temperatures, since typical displacements are scaled by $T$, which is the natural scale for particle motion. Note that our choice does not affect the time dependence, in which rejuvenation and memory effects are encoded.

We shall study the role of temperature $T_2$ on the non-equilibrium dynamics of glasses during a temperature cycle as well as the influence of time $t_1$ spent at temperature $T_1$. In particular, we can easily study the limiting case $t_1 \to \infty$, which corresponds to reaching equilibrium at $T_1$ by generating equilibrium configurations at this temperature using the Swap Monte Carlo method. These very stable glasses would be inaccessible by conventional MD.

**Aging** – Let us focus on the first step of the temperature cycle, where liquids thermalized at $T_0 = 0.36$ are rapidly cooled to low temperature, $T_1 = 0.0353 < T_c$. The waiting time $t_w$ measures the time spent at $T_1$. The resulting MSD is presented in Fig. 3, each curve corresponding to a given waiting time $t_w$. The curves share a similar trend. The MSD increases quadratically at small times $\tau$, before crossing over to a plateau value during a time that depends on $t_w$, and eventually departs from this plateau at larger times. In terms of microscopic dynamics, this corresponds to a short-time ballistic motion, transient trapping within an amorphous cage of neighboring particles, and eventual rearrangement of the cage. Diffusive behavior is not observed within the accessible timescale and particles actually move very little, as the MSD is typically one tenth of particle diameter or less. At the largest $t_w = 4^{11} \simeq 4.10^6$, the MSD plateaus over 4 orders of magnitude in time, meaning that the amorphous structure of the glass remains frozen over very long times. We observe a clear

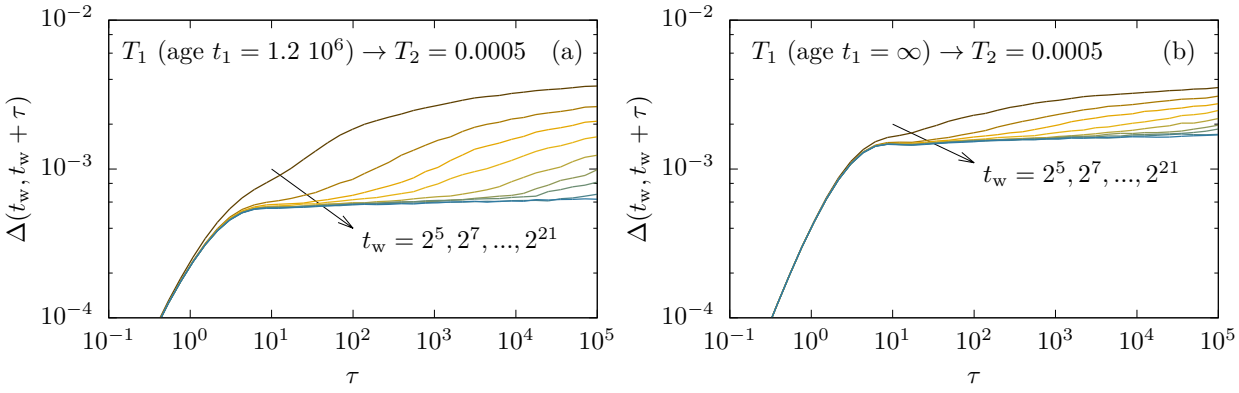


Figure 4: **Rejuvenation effect**, or restart of aging dynamics, as glasses aged for (a) $t_1 = 1.2\ 10^6$ and (b) $t_1 = \infty$ (equilibrium) at $T_1 = 0.0353$ are cooled down to $T_2 = 0.0005$.

waiting-time dependence in the dynamics in Fig. 3. The dynamics becomes slower with the age $t_w$ of the system, a typical property of aging systems [55, 56]. This slowing down implies that the large $\tau$-data obey a sub-aging $\tau/t_w^\mu$ scaling (we find $\mu \simeq 0.9$), widely known and observed in glasses of various materials [1, 10, 57].

Aging can be seen as a consequence of the rugged nature of the landscape of glasses. This corresponds to the thermally-activated crossing of barriers, which leads the system to slowly relax towards lower energy states, where it stays for longer times [10]. The common wisdom in structural glasses is to view these glassy states as energy minima with no (or simple) internal structure [58], suggesting that no interesting dynamic effect should take place by further cooling the glass. We now present results challenging this view.

**Rejuvenation** – We consider the second step of the cycle. The glasses aged during a time $t_1$ at temperature $T_1$ are suddenly cooled to $T_2 < T_1$. To investigate the influence of $T_2$, we present data for $T_2 = 0.01$ and $T_2 = 0.0005$. We also consider glasses of two different ages, $t_1 = 1.2\ 10^6$ (corresponding to $t_w \simeq 4^{10}$ in Fig. 3) and $t_1 = \infty$, the latter being obtained using the hybrid Swap method. As before, we measure the MSD, with $t_w$ now being the time spent at $T_2$.

We start with a large temperature jump to $T_2 = 0.0005$, and report data for $t_1 = 1.2\ 10^6$ and $t_1 = \infty$ in Fig. 4(a-b). In both panels, a strongly aging dynamics is observed, similar to the one observed in the first step in Fig. 3. The MSD evolves continuously over 5 orders of magnitude in time, with strong waiting-time dependence and a variation of one order of magnitude in amplitude. Such strong aging effects would not be observed if the system simply had to readjust, over a fast timescale, to the new imposed temperature. Remarkably, these strong effects survive in Fig. 4(b) for $t_1 = \infty$. This implies that the aging dynamics at $T_2$ is not simply the continuation of the one at $T_1$, but that new slow processes emerge at low temperature. This is precisely the rejuvenation effect first reported in spin glasses, since very old glasses (up to $t_1 = \infty$) behave as young glasses at lower temperatures.

Rejuvenation is not observed if $T_2$ is too high. We show in Fig. 5 the results of cooling from $T_1 = 0.0353$ and $t_1 = \infty$ down to $T_2 = 0.01$. Here, the dynamics does not depend on $t_w$, signaling the absence of aging. The frozen amorphous structure adjusts over a microscopic timescale at the new temperature $T_2$, and this process is not slowed down by free energy barriers. This is again

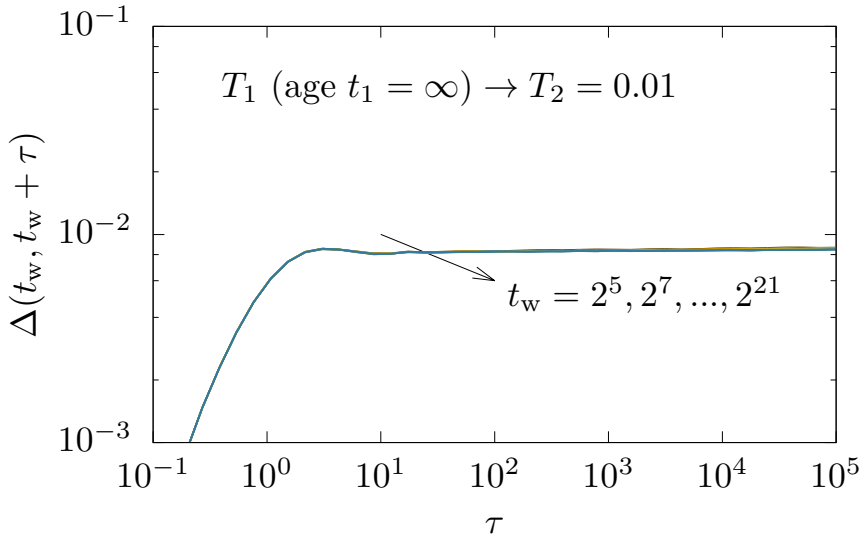


Figure 5: **No rejuvenation** if $T_2$ is too large. Here, glasses aged for $t_1 = \infty$ at $T_1 = 0.0353$ are cooled down to $T_2 = 0.01$.

similar to observations in spin glasses [26, 30].

**Memory** – We complete the thermal cycle by heating the glass aged for $t_2 = 1.4\ 10^6 \simeq t_1$ at $T_2 = 0.0005$ back to $T_1 = 0.0353$. The MSD measured after the heating is shown in Fig. 6, along with the MSD at the last $t_w$ of the first step of the cycle. After going back to $T_1$, the relaxation dynamics is the direct continuation of the aging which took place in the first step. Despite the strong rejuvenation effect observed at $T_2$ in the intermediate step, the glass has kept a perfect memory of its age at temperature $T_1$. The aging dynamics then continues as if the second step had not taken place at all. This is the memory effect [2, 12].

We gather all these results in Fig. 1 by reporting the time evolution of $\chi(t_w, \omega = 10^{-5})$, defined in Eq. (3), during the complete temperature cycle. Aging in the first part of the cycle corresponds to a slow decay of $\chi(t_w, \omega)$, while rejuvenation corresponds to a strong restart of a similar aging. Memory is very clear as the third step appears to be the direct continuation of the first one, as emphasized in the inset where the second step is removed. The aging dynamics in the third step proceeds as a simple continuation of the first. This figure mirrors similar results obtained in spin glass materials [2, 30, 32, 59]. The simultaneous observation of both rejuvenation and memory effects is highly non-trivial, and confirms the idea that the landscape inside glassy minima can be rugged and hierarchical in systems of soft repulsive particles that describe structural glasses [43, 49].

**Separation of lengthscales** – We have studied the probability distribution function (pdf) of single particle displacements in the three steps of the temperature protocol. At each temperature, we measure the pdf of $\Delta r^2 = |\boldsymbol{r}(t_w + \tau) - \boldsymbol{r}(t_w)|^2$ towards the end of the step, for $t_w = 2^{20}$ and $\tau = 10^5$. These distributions give additional information on the typical scale of particle displacements at each temperature (the average value is plotted in Figs. 3-6), and, more importantly on the heterogeneity of the particle displacements.

Results for the three steps are reported in Fig. 7. We observe that the pdf of displacements

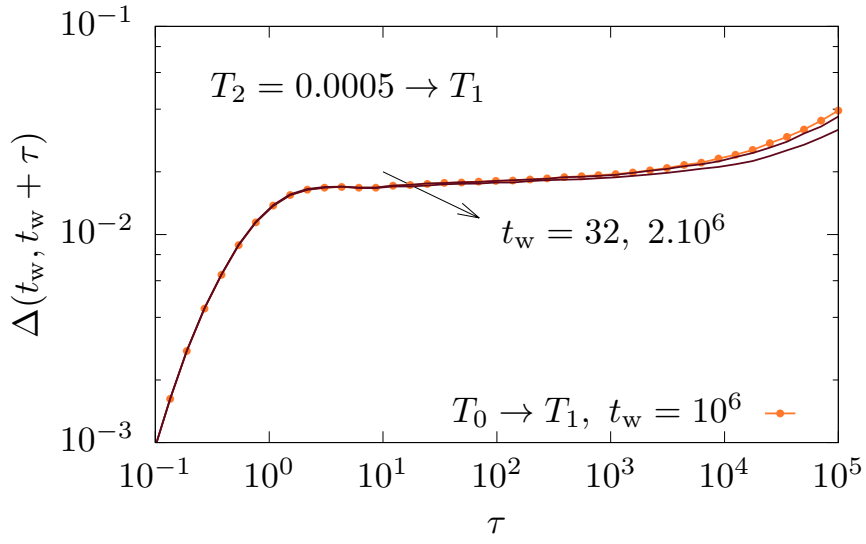


Figure 6: **Memory effect** after heating the glass from $T_2 = 0.0353$ (age $t_2 = 1.4\ 10^6$) back to $T_1 = 0.0353$. We report the MSD after heating for $t_w = 32$ and $t_w = 2.10^6$ (lines). The glass has kept memory of its state at temperature $T_1$, as the dynamics smoothly continues that of the first cycle shown for $t_w = 10^6$ (circles).

during aging is broad but relatively featureless, indicating that all particles are involved in the aging dynamics. A similar shape is obtained during the rejuvenation, but at a much smaller scale. This indicates that the aging dynamics in the second step is again due to very collective particle motion involving the entire system, but it involves displacements on much smaller lengthscales. This explains why memory of the first step is retained, as the structure obtained at the end of the first step is essentially unperturbed during the second step. Dynamics is hierarchical both in timescales and in lengthscales [26, 57].

**Discussion** – We have shown that subjecting a three-dimensional model for structural glasses to a temperature cycle reveals rich non-equilibrium dynamical effects, such as rejuvenation and memory effects that were first observed in spin glasses, but not in molecular glasses. Are these effects ubiquitous? Varying more broadly the parameters reported in this work, we find that for $\varphi = 0.85$ and $T_1 = 0.0353$, only quenches below $T_2 \approx 0.001$ will lead to rejuvenation effects in the dynamics. We also analyzed the density dependence of these effects and found that no such rejuvenation effect can be found for packing fractions beyond $\varphi \approx 0.9$. These findings are consistent with a systematic search for marginally stable glassy phases in the present numerical model [49], which suggest that soft repulsive spheres at packing fractions relevant to describe soft colloids and granular materials are characterized by a complex free energy landscape, which should thus give rise to rejuvenation and memory effects, whereas this physics is absent in the regime describing dense supercooled liquids [47, 48]. These conclusions are broadly consistent with mean-field analysis [43], and can explain the absence of rejuvenation reported for glycerol [3], and should guide future experimental studies of the dynamics of glassy materials.

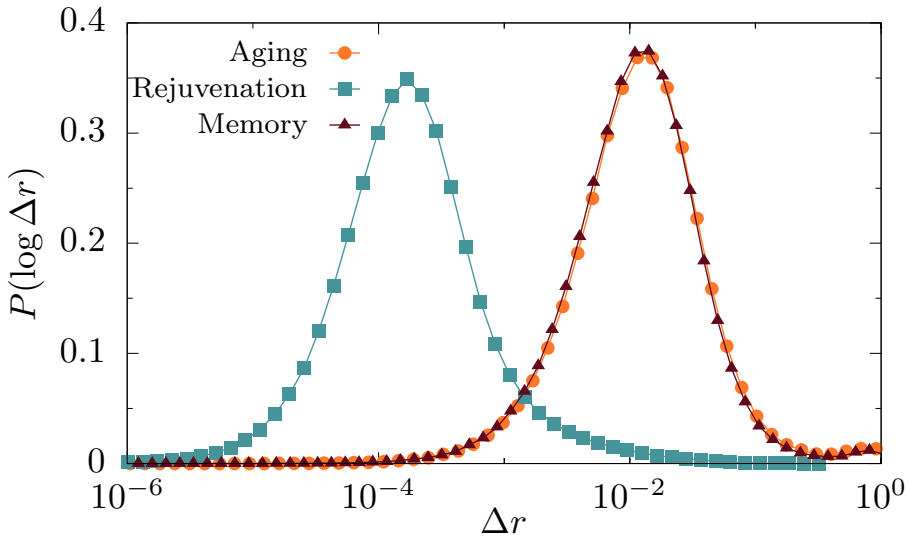


Figure 7: **Hierarchy of lengthscales** in the probability distribution function of particle displacements $\Delta r^2$ during aging (circle), rejuvenation (square), and memory (triangle) for $t_w = 2^{20}$ and $\tau = 10^5$. All particles contribute collectively to each step, but at a different scales.

**Acknowledgments** – We thank S. R. Nagel for inspiring discussions. We thank F. Zamponi, Q. Liao, H. Yoshino and E. Vincent for useful exchanges. This work was supported by a grant from the Simons Foundation (#454933, L. Berthier).

## Bibliography

[1] LGE Struik. *Publ. Comp., Amsterdam-Oxford-New York*, 1978.

[2] Eric Vincent, Jacques Hammann, Miguel Ocio, Jean-Philippe Bouchaud, and Leticia F. Cugliandolo. Slow dynamics and aging in spin glasses. In Miguel Rubí and Conrado Pérez-Vicente, editors, *Complex Behaviour of Glassy Systems*, pages 184–219, Berlin, Heidelberg, 1997. Springer Berlin Heidelberg.

[3] Robert L. Leheny and Sidney R. Nagel. *Phys. Rev. B*, 57:5154–5162, 1998.

[4] P. Lunkenheimer, R. Wehn, U. Schneider, and A. Loidl. *Phys. Rev. Lett.*, 95:055702, 2005.

[5] Luca Cipelletti, S. Manley, R. C. Ball, and D. A. Weitz. *Phys. Rev. Lett.*, 84:2275–2278, 2000.

[6] A Knaebel, M Bellour, J.-P Munch, V Viasnoff, F Lequeux, and J. L Harden. *Europhysics Letters (EPL)*, 52(1):73–79, 2000.

[7] F. Alberici, P. Doussineau, and A. Levelut. *J. Phys. I France*, 7(2):329–348, 1997.

[8] Eugene V. Colla, Lambert K. Chao, M. B. Weissman, and Dwight D. Viehland. *Phys. Rev. Lett.*, 85:3033–3036, 2000.

[9] Yoav Lahini, Omer Gottesman, Ariel Amir, and Shmuel M. Rubinstein. *Phys. Rev. Lett.*, 118: 085501, 2017.

[10] J. P. Bouchaud. *J. Phys. I France*, 2(9):1705–1713, 1992.

[11] Jean-Philippe Bouchaud, Leticia F Cugliandolo, Jorge Kurchan, and Marc Mezard. *Spin glasses and random fields*, pages 161–223, 1998.

[12] Ludovic Berthier, Virgile Viasnoff, Olivia White, Vladimir Orlyanchik, and Florent Krzakala. *arXiv preprint cond-mat/0211106*, 2002.

[13] F Lefloch, J Hammann, M Ocio, and E Vincent. *Europhysics Letters (EPL)*, 18(7):647–652, 1992.

[14] J. O. Andersson, J. Mattsson, and P. Nordblad. *Phys. Rev. B*, 48:13977–13980, 1993.

[15] V. Dupuis, E. Vincent, J.-P. Bouchaud, J. Hammann, A. Ito, and H. Aruga Katori. *Phys. Rev. B*, 64:174204, 2001.

[16] P. E. Jönsson, H. Yoshino, and P. Nordblad. *Phys. Rev. Lett.*, 89:097201, 2002.

[17] P. E. Jönsson, R. Mathieu, P. Nordblad, H. Yoshino, H. Aruga Katori, and A. Ito. *Phys. Rev. B*, 70:174402, 2004.

[18] F. Bert, V. Dupuis, E. Vincent, J. Hammann, and J.-P. Bouchaud. *Phys. Rev. Lett.*, 92:167203, 2004.

[19] H Yardimci and R. L Leheny. *Europhysics Letters (EPL)*, 62(2):203–209, 2003.

[20] L Bellon, S Ciliberto, and C Laroche. *Europhysics Letters (EPL)*, 51(5):551–556, 2000.

[21] Ludovic Bellon, Sergio Ciliberto, and Claude Laroche. *The European Physical Journal B-Condensed Matter and Complex Systems*, 25(2):223–231, 2002.

[22] Alan Parker and Valéry Normand. *Soft Matter*, 6:4916–4919, 2010.

[23] J Hammann, F Lefloch, E. Vincent, M. Ocio, and J-P Bouchaud. In Beyermann, Huang-Liu, and MacLaughlin, editors, *Random Magnetism and High-Temperature Su- perconductivity*, Singapore, 1994. World Scientific.

[24] E. Vincent, J. P. Bouchaud, J. Hammann, and F. Lefloch. *Philosophical Magazine B*, 71(4): 489–500, 1995.

[25] J.-P. Bouchaud and D.S. Dean. *J. Phys. I France*, 5(3):265–286, 1995.

[26] Jean-Philippe Bouchaud, Vincent Dupuis, Jacques Hammann, and Eric Vincent. *Physical review B*, 65(2):024439, 2001.

[27] Marc Mézard, Giorgio Parisi, and Miguel A Virasoro. *Spin glass theory and beyond*. World Scientific, Singapore, 1987.

[28] G. Parisi. Mean field theory of glasses: Statics and dynamics. In J.-P. Bouchaud, M. Mézard, and J. Dalibard, editors, *Complex Systems*, Les Houches, France, 2007. Elsevier.

[29] Bernard Derrida. *Phys. Rev. B*, 24:2613–2626, 1981.

[30] Ludovic Berthier and Jean-Philippe Bouchaud. *Physical Review B*, 66(5):054404, 2002.

[31] L. Berthier and A. P. Young. *Phys. Rev. B*, 69:184423, 2004.

[32] Ludovic Berthier and A. P. Young. *Physical Review B*, 71(21):214429, 2005.

[33] Helmut G. Katzgraber and I. A. Campbell. *Phys. Rev. B*, 72:014462, 2005.

[34] Jorge Kurchan, Giorgio Parisi, Pierfrancesco Urbani, and Francesco Zamponi. *The Journal of Physical Chemistry B*, 117(42):12979–12994, 2013.

[35] Patrick Charbonneau, Jorge Kurchan, Giorgio Parisi, Pierfrancesco Urbani, and Francesco Zamponi. *Annu. Rev. Condens. Matter Phys.*, 8:265–288, 2017.

[36] Pierfrancesco Urbani and Giulio Biroli. *Phys. Rev. B*, 91(10):100202(R), 2015.

[37] Patrick Charbonneau and Sho Yaida. *Phys. Rev. Lett.*, 118:215701, 2017.

[38] C. L. Hicks, Michael J. Wheatley, Michael J. Godfrey, and Micheal A. Moore. *Phys. Rev. Lett.*, 120:225501, 2018.

[39] Patrick Charbonneau, Yi Hu, Archishman Raju, James P Sethna, and Sho Yaida. *arXiv e-prints*, art. arXiv:1808.02767, 2018.

[40] Corrado Rainone, Pierfrancesco Urbani, Hajime Yoshino, and Francesco Zamponi. *Phys. Rev. Lett.*, 114(1):015701, 2015.

[41] Giulio Biroli and Pierfrancesco Urbani. *Nature Physics*, 12:1130–1133, 2016.

[42] Giulio Biroli and Pierfrancesco Urbani. *SciPost Phys.*, 4:20, 2018.

[43] Camille Scalliet, Ludovic Berthier, and Francesco Zamponi. *Phys. Rev. E*, 99:012107, 2019.

[44] Ludovic Berthier, Patrick Charbonneau, Yuliang Jin, Giorgio Parisi, Beatriz Seoane, and Francesco Zamponi. *Proc. Natl. Acad. Sci. U.S.A.*, 113(30):8397–8401, 2016.

[45] Beatriz Seoane and Francesco Zamponi. *Soft Matter*, 14:5222–5234, 2018.

[46] Qinyi Liao and Ludovic Berthier. *arXiv e-prints*, art. arXiv:1810.10256, 2018.

[47] Camille Scalliet, Ludovic Berthier, and Francesco Zamponi. *Phys. Rev. Lett.*, 119:205501, 2017.

[48] Beatriz Seoane, Daniel R. Reid, Juan J. de Pablo, and Francesco Zamponi. *Phys. Rev. Materials*, 2:015602, 2018.

[49] Camille Scalliet, Ludovic Berthier, and Francesco Zamponi. In preparation (2019).

[50] John D. Weeks, David Chandler, and Hans C. Andersen. *The Journal of Chemical Physics*, 54 (12):5237–5247, 1971.

[51] Andrea Ninarello, Ludovic Berthier, and Daniele Coslovich. *Phys. Rev. X*, 7:021039, 2017.

[52] Ludovic Berthier and Gilles Tarjus. *J. Chem. Phys.*, 134:214503, 2011.

[53] H. J. C. Berendsen, J. P. M. Postma, W. F. van Gunsteren, A. DiNola, and J. R. Haak. *J. Chem. Phys.*, 81(8):3684–3690, 1984.

[54] Ludovic Berthier, Elijah Flenner, Christopher J Fullerton, Camille Scalliet, and Murari Singh. *arXiv e-prints*, art. arXiv:1811.12837, 2018.

[55] Walter Kob and Jean-Louis Barrat. *Phys. Rev. Lett.*, 78:4581–4584, 1997.

[56] Djamel El Masri, Ludovic Berthier, and Luca Cipelletti. *Phys. Rev. E*, 82:031503, 2010.

[57] Jean-Philippe Bouchaud. Aging in glassy systems: new experiments, simple models, and open questions. In M. E. Cates and M. R. Evans, editors, *Soft and Fragile Matter: Nonequilibrium Dynamics, Metastability and Flow*, pages 285–304, Bristol and Philadelphia, 2000. IOP Publishing.

[58] P. G. Debenedetti and F. H. Stillinger. *Nature*, 410:259, 2001.

[59] Ph Refregier, E Vincent, J Hammann, and M Ocio. *Journal de Physique*, 48(9):1533–1539, 1987.

Article

# Depletion of two-level systems in ultrastable computer-generated glasses

D. Khomenko*, C. Scalliet*, L. Berthier, F. Zamponi, D. Reichman, preprint arXiv: 1910.11168, under review at Physical Review Letters.

**Amorphous solids exhibit quasi-universal low-temperature thermal anomalies whose origin has been ascribed to a distribution of localized tunneling defects. Using an advanced Monte Carlo procedure, we create *in silico* glasses spanning from hyperquenched to vapor-deposited ultrastable glasses. Using a multidimensional path-finding protocol, we locate tunneling defects with energy splittings smaller than $k_B T_Q$, with $T_Q$ the temperature below which quantum effects are relevant ($T_Q \approx 1\,\mathrm{K}$ in most experiments). We find that the evolution of the energy landscape with the quench rate, as well as the manner in which the landscape is explored, conspire to deplete the density of tunneling defects in well-annealed glasses, as observed in recent experiments. We systematically explore the real-space nature of tunneling defects, finding that they are mostly localized to the participation of a few atoms, but are occasionally dramatically delocalized.**

## I Introduction

The theory of low-temperature properties of perfect crystals stands as one of the most profound early tests of the power of quantum statistical mechanics. In particular, Debye's seminal calculation of the observed $T^3$ behavior of the low-temperature specific heat highlighted the importance of long wavelength phonons as low energy excitations in ordered solids [1]. Given that the wavelength of populated phonon modes in the temperature range $T \sim 1\,\mathrm{K}$ is significantly longer than the interparticle distance in a typical solid, it came as a major surprise in 1971 when Zeller and Pohl [2] measured large deviations from the expected Debye behavior of the specific heat and the thermal conductivity of vitreous silica and other selenium and germanium-based glasses. An explanation for this puzzling behavior was almost immediately put forward by Anderson, Halperin and Varma [3]

*These authors contributed equally to the work

and by Phillips [4]. They posited that, due to the disorder intrinsic to amorphous solids, the energy landscape of a glass contains many local minima. Rare, nearly degenerate, adjacent local minima support tunneling defects or two-level systems (TLS) with energy splittings of the order of 1 K, which provide a large excess contribution to the specific heat and a new mode of scattering that determines the thermal conductivity. In the subsequent decades, the generic behavior described by Zeller and Pohl has been observed in numerous other amorphous materials, and the TLS theory has withstood essentially all experimental tests [5, 6, 7, 8, 9]. Despite this great progress in our understanding, the microscopic real-space structure of the tunneling defects remains debated, as do the factors that determine the density and distribution of TLS in amorphous solids [10, 11, 12, 13, 14, 15, 16, 17, 18, 19, 20, 21, 22].

A powerful platform for addressing the aforementioned issues is the use of computer simulation to prepare amorphous materials *in silico* and to interrogate the simulated energy landscape for TLS *ab initio* [23]. Such a program was initiated in the pioneering work of Heuer and Silbey nearly three decades ago [24, 25, 26, 27]. Limited by the computational power and the algorithms available at the time, they created model glasses formed with cooling rates roughly nine orders of magnitude larger that those found in the laboratory setting, and were able to locate only a handful of TLS with the requisite tunnel splittings, necessitating uncontrolled extrapolations. In the subsequent years the situation has incrementally improved [28, 29, 30], although until very recently the algorithmic ability to simulate amorphous materials which are cooled in an experimentally realistic fashion has remained completely out of reach. This obstacle has greatly limited the ability to microscopically understand the universal anomalous thermal behavior of low-temperature amorphous solids from a computational viewpoint.

In this work we leverage the remarkable ability of the swap Monte Carlo algorithm to produce *in silico* amorphous materials with fictive temperatures that range from those found in typical experiments to the significantly slower rates found in recent vapor deposition studies [31]. We find a dramatic depletion of active TLS (those with a tunnel splitting $\sim 1$ K) as a function of decreasing quench rate, just as found in recent experiments [32, 33, 34, 35, 36, 37]. Use of a state-of-the-art reaction path-finding protocol [38, 39] allows us to efficiently locate double-well potentials in the multi-dimensional potential energy landscape, yielding a *direct sampling* of active tunneling states with sufficient statistics to avoid any extrapolation. This sampling enables the determination of the degree of localization associated with individual TLS, and hence provides a detailed, real-space understanding of how atoms participate in tunneling motion and how the thermal exploration of the energy landscape in well-annealed amorphous materials determines the effective density of tunneling centers.

## II Glass preparation

Past work on the local landscape of low temperature glasses has focused on simple models for real systems such as NiP [24] and silica [29, 30]. Here we study a polydisperse mixture of particles interacting through an inverse power law potential [31]. Our choice is motivated by the fact that the peculiar low-temperature behavior of glasses was observed in a variety of materials, and should not depend on the particular form of the interactions between atoms or molecules. Given the vast palette of existing glass-forming models, our particular model was chosen to enable the thermalization of the system on the computer in a manner that makes direct connection to experiments. We thus choose a system for which swap Monte Carlo is maximally efficient [31].

We provide minimal details on the system and measures of equilibration in the main text;

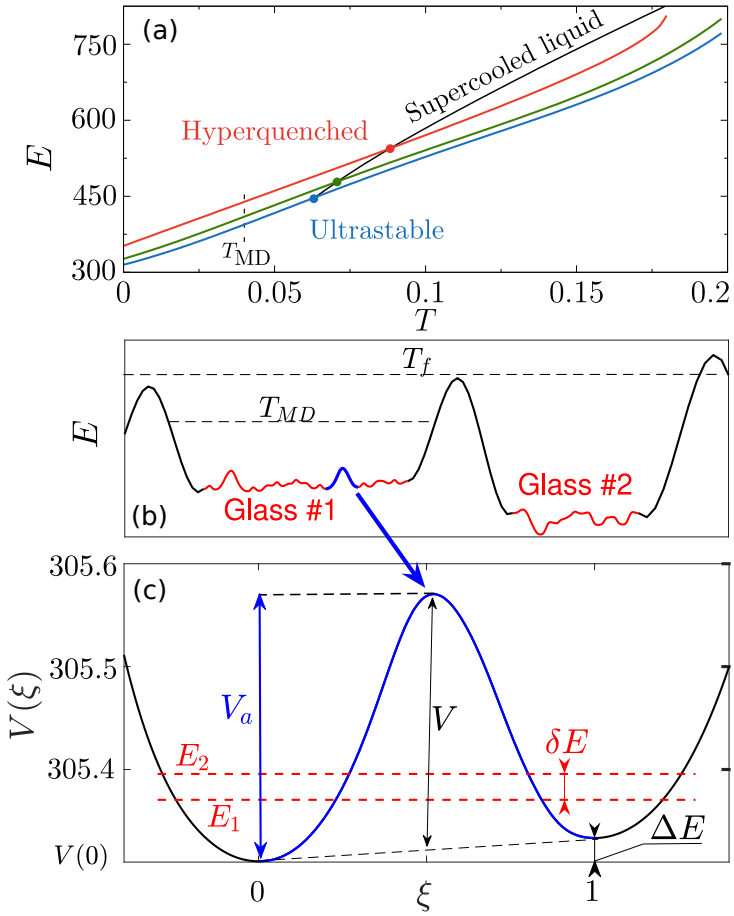


Figure 1: (a) Glasses are prepared at equilibrium (black line) at temperatures $T_f = 0.092, 0.07, 0.062$ (bullets), ranging from hyperquenched to ultrastable. Their potential energy is followed after rapid temperature changes (colored lines). (b) One-dimensional sketch of the potential energy landscape. Molecular dynamics simulations performed at $T_{\rm MD} = 0.04$ are employed to detect double-well potentials (blue). (c) Zoom of one double well potential $V(\xi)$ detected in a glass prepared at $T_f = 0.062$. The classical asymmetry $\Delta E$, activation energy $V_a$, and energy barrier $V = V_a - \Delta E/2$ are illustrated, as well as the energy levels $E_1$ and $E_2$ of the ground state doublet, obtained by solving the 1d Schrödinger equation.

additional information may be found in the Appendix. We simulate a non-additive polydisperse mixture of $N = 1500$ particles of mass $m_0$. Two particles $i$ and $j$ separated by a distance $r_{ij}$ interact via the potential

$$v(r_{ij}) = \epsilon \left( \frac{\sigma_{ij}}{r_{ij}} \right)^{12} + \epsilon F(r_{ij}/\sigma_{ij}) \tag{1}$$

only if $r_{ij} < r_{cut} = 1.25\sigma_{ij}$, $\sigma_{ij}$ being the non-additive interaction length scale. The function $F$ is a fourth-order polynomial which guarantees the continuity of the potential up to the second derivative at $r_{cut}$. We characterize the physical classical dynamics of the model using molecular dynamics (MD) with energies and lengths expressed in units of $\epsilon$ and the average diameter $\sigma$, respectively. Times measured during MD simulations are expressed in units of $\sqrt{\epsilon/m_0\sigma^2}$. In these units, the number density is $\rho = 1$. The relaxation time $\tau_\alpha$ of the equilibrium fluid is measured from the self-intermediate scattering function $F_s(k = 7.0, \tau_\alpha) = e^{-1}$. The onset of glassy dynamics, signaled by deviations from Arrhenius behavior of $\tau_\alpha$, takes place at $T_o = 0.18$, where $\tau_\alpha(T_o) \equiv \tau_o$, while the mode-coupling crossover temperature is located at $T_{MCT} = 0.104$ [31].

We analyze *in silico* glasses by preparing fully equilibrated configurations, using the swap Monte Carlo algorithm, at various preparation temperatures $T_f$, which are then rapidly cooled to lower temperatures using regular molecular dynamics. Therefore, $T_f$ represents the "temperature at which the glass would find itself in equilibrium if suddenly brought to it from its given state," which is precisely the definition of the fictive temperature given by Tool [40]. The temperature $T_f$ characterizes the degree of stability of the computer glasses, see Fig. 1(a). In experiments, $T_f$ would be determined by the cooling rate [41, 42], or by the substrate temperature in a vapor deposition experiment [43, 44, 45, 46, 47]. To maximise the analysed range of glass stabilities, we present results for poorly annealed (or, hyperquenched) glasses ($T_f = 0.092$, slightly below $T_{MCT}$ with $\log(\tau_\alpha/\tau_o) = 4.9$), liquid-cooled experimental glasses ($T_f = 0.07 \simeq T_g$, with $\log(\tau_\alpha/\tau_o) = 10.7$), and ultrastable vapor-deposited glasses ($T_f = 0.062$, with $\log(\tau_\alpha/\tau_o) = 14.8$). To obtain statistically significant results, we analyze $N_g$ independent samples ($N_g = 200, 50, 15$ for increasing $T_f$).

## III Landscape exploration

Our goal is to identify transitions between nearby minima, or double well potentials (DWPs) of the potential energy landscape (PEL) of our glassy configurations. Detailed information may be found in the Appendix. Briefly, starting from the configurations equilibrated at $T_f$, we run MD simulations at a temperature $T_{\rm MD} = 0.04$, which is sufficiently low to confine each glass in a single metabasin but is high enough that the system can rapidly visit many distinct minima (or, inherent structures) within the metabasin [23], see Fig. 1(b).

By repeatedly sampling inherent structures during MD trajectories, we obtain a library of visited local minima. We then identify pairs of minima that are dynamically connected. For each of the $N_g$ starting configurations, we use the isoconfigurational ensemble [48], and run up to 200 simulations starting from the same initial configuration with randomly assigned velocities. The number of isoconfigurational runs, as well as their duration, needs to be large enough for the probability distributions of the inherent structures potential energy $P(E_i)$, and the number of transitions $P(T_{ij})$, to converge to stationary results. While we reach convergence of the probability distributions, we do not sample all potential energy minima and transitions, and their absolute numbers keep increasing with time. We however obtain a significant amount of them, namely 13252, 26898, 848698 minima for $T_f = 0.062, 0.07, 0.092$, respectively. As shown below, these numbers are large enough to directly

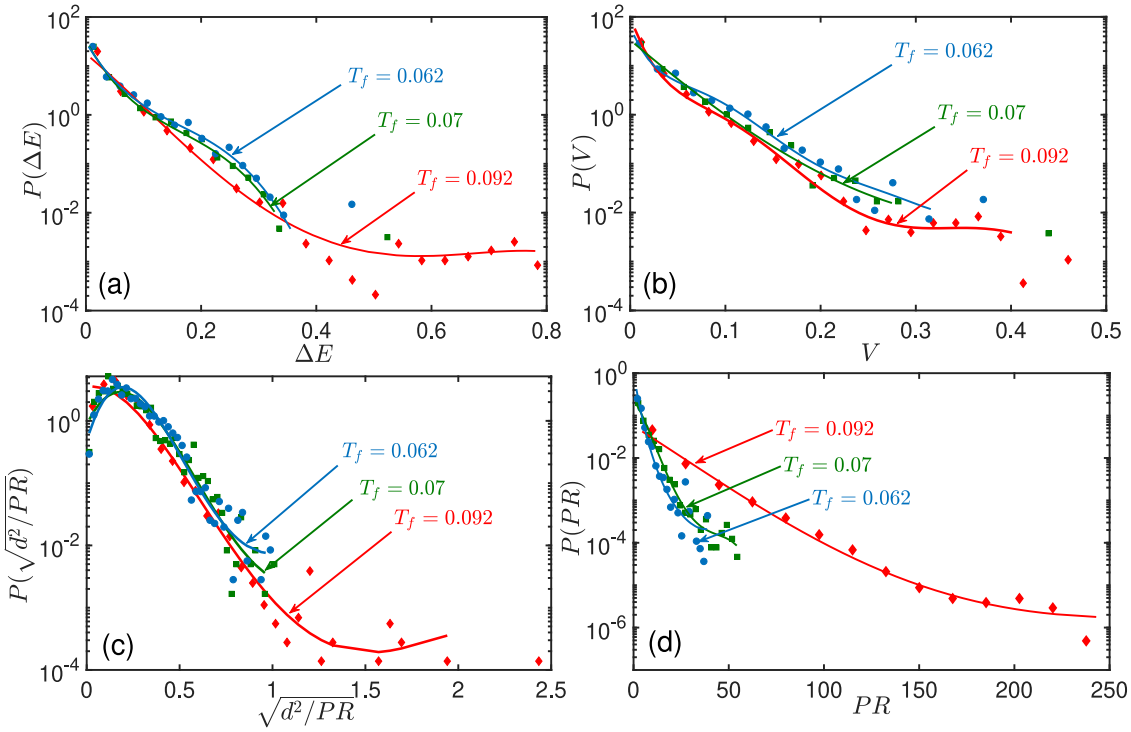


Figure 2: Probability distribution functions of DWP parameters as a function of glass preparation temperature $T_f$: (a) asymmetry $\Delta E$, (b) energy barrier $V$, (c) distance $d$ normalized by $\sqrt{PR}$, which characterizes the typical individual displacement of particles that participate actively in a double-well transition, and (d) participation ratio $PR$. Lines are a guide for the eye.

determine the density of tunneling TLS, which is our main goal.

We select transitions between adjacent minima as described in the Appendix, for which we compute the minimum energy paths connecting them using a climbing image Nudged Elastic Band (NEB) algorithm [38, 39], which ensures that one of the images lies at the saddle point and provides a smooth potential energy profile. In most cases, double wells are obtained. Occasionally, especially for $T_f = 0.092$, the energy profile contains intermediate minima. In such cases, we apply an iterative method to split multiple wells into distinct DWPs, which are then analyzed similarly to the other ones.

We parametrize the minimum energy path of a DWP by $\xi$ such that $\xi = 0$ and $\xi = 1$ correspond to the locations of the two minima (we arbitrarily choose $\xi = 0$ for the deepest minimum), see Fig. 1(c). A DWP is characterized by its asymmetry $\Delta E = V(1) - V(0)$, its energy barrier $V = V_a - \Delta E/2$, where $V_a$ is the activation energy, and by the distance $d$ between minima. The distance is calculated along the reaction coordinate given by the NEB, as the sum of Euclidean distances between images of the system: $d^2 = \sum_{i,\mu} d_{i,\mu}^2$, where $d_{i,\mu}$ is the displacement of particle $i$ in direction $\mu = x, y, z$. The number of particles participating in the transition is characterized by the participation ratio, defined as $PR = (\sum_{i,\mu} d_{i,\mu}^2)^2/(\sum_{i,\mu} d_{i,\mu}^4)$.

The statistics of the classical DWP parameters are shown in Fig. 2. The probability distribution function (pdf) for each quantity is given for different preparation temperatures $T_f$. The pdfs for $T_f = 0.062$ and 0.07 agree quantitatively, within noise, while we observe an evolution of the pdfs from $T_f \leq 0.07$ to $T_f = 0.092$. In particular, the pdfs of asymmetries and energy barriers are almost

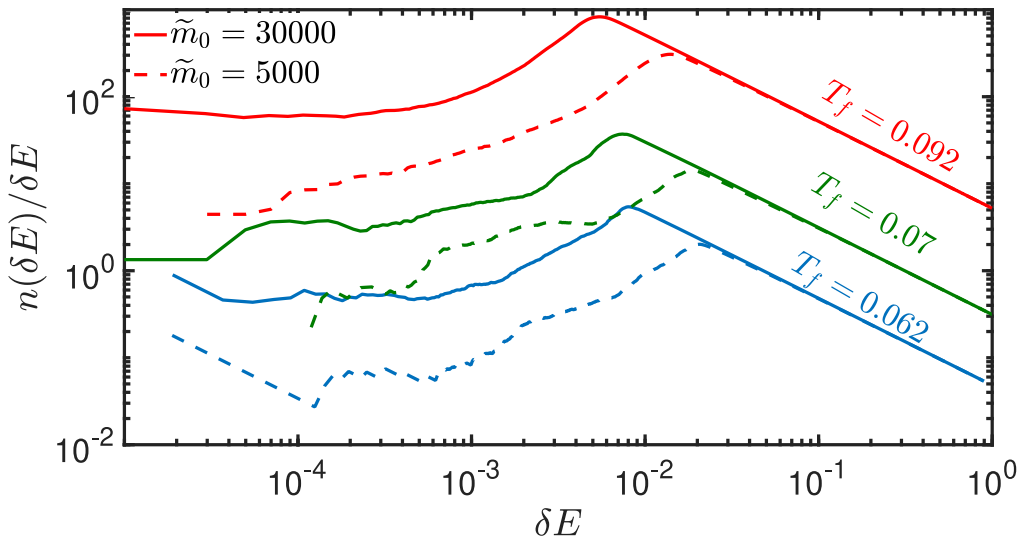


Figure 3: Cumulative distribution of energy splitting from hyperquenched to ultrastable glasses (top to bottom curve). The two values of $\widetilde{m}_0$ are chosen for comparison with real materials. The plateau at small $\delta E$ affords a direct determination of the TLS density $n_0$, which is suppressed by two orders of magnitude as glass preparation is varied.

exponential in all glasses, although the relevant TLS will typically not be found in those tails. The mild dependence of these tails may stem from the fact that the sampling temperature $T_{\rm MD}$ sets a limit on the DWPs that can be detected, independently of $T_f$ (see Appendixfor the effect of $T_{\rm MD}$). The pdfs of distances (not shown) and participation ratios vary more significantly between $T_f \leq 0.07$ and $T_f = 0.092$. Since $d \propto \sqrt{PR}$, an increase of $PR$ will affect the distribution of $d$. To eliminate this effect we present the pdf of $d/\sqrt{PR}$ instead of $d$. This quantity can be interpreted as an average displacement of the particles that participate in the transition. On average, the number of particles involved in DWPs is larger in poorly annealed glasses, while the displacements of individual particles remain comparable. To our knowledge, a dependence on the quench rate of the classical parameters of DWPs has not been reported before.

## IV Density of two-level systems

At sufficiently low temperatures, thermal activation over the energy barrier $V$ is suppressed, but quantum tunneling becomes important [49]. For all subsequent analysis, we reduce our problem to a one dimensional (1d) effective Schrödinger equation along the reaction coordinate. Following Vineyard [50], the effective mass remains $m_0$, with a reaction coordinate $x \in [0, d]$. Using the normalized variable $\xi = x/d$, and scaling energies by $\epsilon$, we obtain

$$-\frac{\hbar^2}{2m_0 d^2 \epsilon}\partial_\xi^2 \Psi(\xi) + V(\xi)\Psi(\xi) = E\Psi(\xi), \tag{2}$$

where the "quantumness" of the problem is controlled by the adimensional mass $\widetilde{m}_0 = m_0\sigma^2\epsilon/\hbar^2$ (see Fig. 3). In general, the Laplacian should take into account curvature effects, which are neglected here for simplicity. Additionally, the potential $V(\xi)$ obtained from the NEB is defined only for $\xi \in [0, 1]$. An extrapolation outside this interval is needed to solve Eq. (2), see the Appendix.

We solve Eq. (2) for all DWPs analyzed in Fig. 2. In particular, we compute the first two energy levels of the double well, $E_1$ and $E_2$, and define the tunnel splitting $\dot{\mathrm{E}} \equiv E_2 - E_1$. As an illustration, we show in Fig. 1(c) the two energy levels and the tunnel splitting of a DWP. The tunnel splitting $\dot{\mathrm{E}}$ is the relevant parameter when it comes to low-temperature properties. When $T$ is low, the transitions that occur by quantum tunneling have a tunnel splitting $\dot{\mathrm{E}} \sim T$ [6]. These particular DWPs are called tunneling two-level systems (TLS).

We characterize the distribution of TLS using a cumulative distribution of tunnel splittings $n(\dot{\mathrm{E}})$, defined as the number of DWPs with tunnel splitting smaller than $\dot{\mathrm{E}}$, normalized by the number of particles $N$ in the glass, and the number of independent analyzed samples $N_g$. In TLS theory, $n(\delta E)$ can be expanded as $n(\dot{\mathrm{E}}) \simeq n_0 \dot{\mathrm{E}} + \mathcal{O}(\dot{\mathrm{E}}^2)$ for small tunnel splittings, and the specific heat at low temperature is linear with $T$, with $n_0$ entering the prefactor [3, 6].

In order to estimate the density $n_0$ of TLS and to analyze its dependence on glass stability, we plot $n(\dot{\mathrm{E}})/\dot{\mathrm{E}}$ as a function of tunnel splitting in Fig. 3. The curves have a similar shape, indicating a saturation to a plateau value, $n_0$, at low tunnel splittings. The existence of a plateau in these curves demonstrates our ability to directly estimate the density of TLS $n_0$ without any extrapolation or uncontrolled hypothesis. The key physical result is that the TLS density $n_0$ (as estimated for example by the values of the curves for $\dot{\mathrm{E}}$ in the range $10^{-3} - 10^{-4}$) decreases by two orders of magnitude when exploring glasses from the hyperquenched to the ultrastable regime. We find almost no TLS with splitting $\dot{\mathrm{E}} < 10^{-4}$ in the most stable glasses. To our knowledge, this constitutes the first numerical evidence for a significant suppression of TLS with increasing glass stability.

## V Microscopic nature of TLS

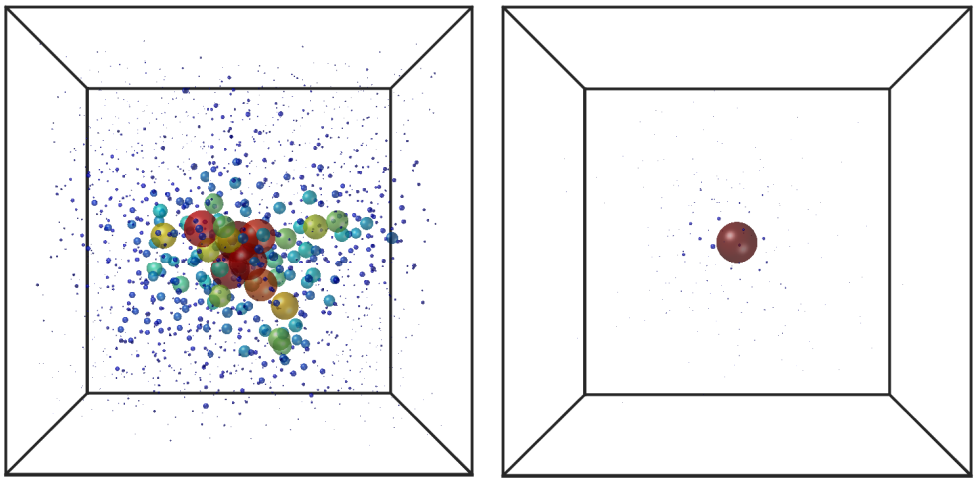


Figure 4: Snapshots of TLS with low tunnel splitting $\dot{\mathrm{E}}$ for $T_f = 0.092$ and $\widetilde{m}_0 = 30000$. (a) $PR \approx 126$ with $\delta E = 8.9 \times 10^{-5}$. (b) $PR \approx 1.6$ and similarly low $\delta E = 5.4 \times 10^{-5}$. The size and color of particles are proportional to their displacement between the initial and final configurations of the TLS, normalized to the highest displacement.

How many particles are involved in the tunneling motion of a TLS? [28, 29, 30] To establish

an accurate picture, we analyzed how the participation ratio $PR$ of transitions correlates with the tunnel splitting $\dot{E}$. We focus on the low-temperature active TLS with tunnel splittings $\dot{E} \sim 10^{-3} - 10^{-4}$, and find that the participation ratio can vary from 1 to 200 (see the Appendix). Higher participation ratios ($PR \sim 200$) are found for hyperquenched glasses, while the most collective TLS found in ultrastable glasses have $PR \sim 30$. Our study thus provides a systematic numerical evidence that TLS are typically very localized, but active TLS are occasionally associated with collective excitations. We provide two snapshots in Fig. 4, corresponding to a collective TLS (left) and a very localized TLS (right) identified in a hyperquenched glass.

# VI Discussion

Our detailed analysis of tunneling TLS in a simple computer model demonstrates their importance to understand low-temperature glass anomalies. We show that the density $n_0$ of TLS directly controls the linear temperature dependence of the specific heat at low temperatures. Several recent works advocated the idea that quantized low-frequency harmonic modes alone could explain this behavior [10, 51, 52, 18, 53, 54, 55]. These soft modes are known for our glasses [56], but we find that their contribution to the low-temperature specific heat is subdominant (see Appendix), suggesting that the specific heat of structural glasses is dominated by tunneling TLS, as originally proposed in [3, 6].

To relate our data to experiments we must convert our simulation units into physical units. The temperature scale below which quantum effects become important is obtained by comparing the thermal wavelength to the interparticle distance: $T_Q = \frac{2\pi\hbar^2}{m_0\sigma^2 k_B}$. We thus consider DWPs with $\dot{E} < k_B T_Q$ as low-temperature active TLS, and their total number for $N$ particles and $N_g$ glass samples is $n_{active} = N N_g n(\dot{E} = k_B T_Q)$.

A detailed analysis for experimental comparisons may be found in the Appendix. Let us first consider Argon parameters: $\sigma = 3.4\times10^{-10}$m, $\epsilon/4 = 1.65\times10^{-21}$J, $m_0 = 6\times10^{-26}$kg [57]. This gives $T_g \sim 32\,\mathrm{K}$, $T_Q \sim 0.73\,\mathrm{K}$, and $\widetilde{m}_0 \sim 4000$. For this $\widetilde{m}_0$, our values of $n_0$ can be estimated from Fig. 3, within statistical noise, as $n_0^{sim} \sim 4, 0.4, 0.04$ for $T_f$=0.092, 0.07, 0.062, which gives $n_0^{exp} \sim 10^{49}$, $10^{48}$, $10^{47}$ J$^{-1}$m$^{-3}$. Active TLS have $\dot{E} < k_B T_Q = 0.0015\epsilon$ and we find $n_{active} = 1008$, 291, 61 such TLS for $T_g = 0.092$, 0.07, 0.062 respectively. A second choice would be to use Nickel as a reference material as motivated by NiP metallic glasses [24], where $\sigma = 2.21 \times 10^{-10}$m, $\epsilon = 6.14 \times 10^{-20}$J, $m_0 = 1.02 \times 10^{-25}$kg [58]. In this case, we have $T_g \sim 298\,\mathrm{K}$, $T_Q \sim 0.9\,\mathrm{K}$, and $\widetilde{m}_0 \sim 30000$. For this value of $\widetilde{m}_0$, from Fig. 3 we find $n_0^{sim} \sim 60, 6, 0.6$ for $T_f = 0.092$, 0.07, 0.062, which gives $n_0^{exp} \sim 10^{50}, 10^{49}, 10^{48}$ J$^{-1}$m$^{-3}$. Active TLS have $\delta E < k_B T_Q = 0.0002\epsilon$ and we find $n_{active} = 248$, 46, 28 such TLS for $T_g = 0.092$, 0.07, 0.062 respectively.

Experimentally, a typical value of $n_0 \sim 10^{46}$J$^{-1}$m$^{-3}$ is reported [6, 7]. Our corresponding estimate for $T_f = 0.07$ is larger by a factor of $\sim 10^2$ for Argon and $\sim 10^3$ for Nickel. This discrepancy may be explained by the fact that we include in our estimates all DWPs detected at temperature $T_{\mathrm{MD}} = 0.04 \gg T_Q$, while in the real experiment the glass is brought directly to $T_Q$ and only a small fraction of DWPs that lie at the very bottom of the energy metabasin is observed. In fact, it is well known that $n_0 \sim \log(\tau)$ where $\tau$ is the observation time at $T_Q$ [6]. This behavior should exist up to a natural cutoff corresponding to the timescale of complete exploration of the energy landscape. Our exploration protocol at $T_{\mathrm{MD}} \gg T_Q$ should then correspond to artificially setting the value of $\tau$ larger than this natural cutoff.

Despite this, the reduction of $n_0$ by two orders of magnitude when moving from hyperquenched to ultrastable glasses is very robust and in very good agreement with recent experimental results [34,

37]. Our results also demonstrate that glass ultrastability (rather than the potentially anisotropic vapor-deposition process) is responsible for the depletion of TLS.

**Acknowledgments.** – We thank M. Ediger, D. Rodney and W. Ji for interesting discussions. This work benefited from access to the University of Oregon high performance computer, Talapas. This project has received funding from the European Research Council (ERC) under the European Union's Horizon 2020 research and innovation program (grant agreement n. 723955 - GlassUniversality). C. Scalliet acknowledges the Fondation l'Oréal for a For Women in Science Fellowship. This work was supported by a grant from the Simons Foundation (#454933, L. Berthier, #454955, F. Zamponi, #454951 D. R. Reichman).

## Bibliography

[1] N. W. Ashcroft and N. D. Mermin, *Solid State Physics* (Thomson Learning, 1976).

[2] R. C. Zeller and R. O. Pohl, Phys. Rev. B **4**, 2029 (1971).

[3] P. W. Anderson, B. I. Halperin, and C. M. Varma, Philosophical Magazine **25**, 1 (1972).

[4] W. Phillips, Journal of Low Temperature Physics **7**, 351 (1972).

[5] M. Loponen, R. Dynes, V. Narayanamurti, and J. Garno, Physical Review B **25**, 1161 (1982).

[6] W. A. Phillips, Reports on Progress in Physics **50**, 1657 (1987).

[7] J. Berret and M. Meissner, Zeitschrift für Physik B Condensed Matter **70**, 65 (1988).

[8] A.-M. Boiron, P. Tamarat, B. Lounis, R. Brown, and M. Orrit, Chemical physics **247**, 119 (1999).

[9] A. L. Burin, J. M. Leveritt III, G. Ruyters, C. Schötz, M. Bazrafshan, P. Fassl, M. von Schickfus, A. Fleischmann, and C. Enss, EPL (Europhysics Letters) **104**, 57006 (2013).

[10] Y. M. Galperin, V. Karpov, and V. Kozub, Advances in Physics **38**, 669 (1989).

[11] S. Coppersmith, Physical review letters **67**, 2315 (1991).

[12] A. J. Leggett, Physica B: Condensed Matter **169**, 322 (1991).

[13] A. Burin and Y. Kagan, Physics Letters A **215**, 191 (1996).

[14] D. R. Reichman, P. Neu, and R. J. Silbey, Molecular Crystals and Liquid Crystals Science and Technology. Section A. Molecular Crystals and Liquid Crystals **291**, 65 (1996).

[15] V. Lubchenko and P. G. Wolynes, Physical Review Letters **87**, 195901 (2001).

[16] V. Gurarie and J. Chalker, Physical Review B **68**, 134207 (2003).

[17] V. Lubchenko and P. G. Wolynes, Proceedings of the National Academy of Sciences **100**, 1515 (2003).

[18] D. Parshin, H. Schober, and V. Gurevich, Physical Review B **76**, 064206 (2007).

[19] D. C. Vural and A. J. Leggett, Journal of Non-Crystalline Solids **357**, 3528 (2011).

[20] A. J. Leggett and D. C. Vural, The Journal of Physical Chemistry B **117**, 12966 (2013).

[21] D. Zhou and A. J. Leggett, arXiv:1510.05538 (2015).

[22] H. M. Carruzzo and C. C. Yu, arXiv:1909.09258 (2019).

[23] A. Heuer, Journal of Physics: Condensed Matter **20**, 373101 (2008).

[24] A. Heuer and R. Silbey, Physical review letters **70**, 3911 (1993).

[25] A. Heuer and R. Silbey, Physical Review B **49**, 1441 (1994).
[26] D. Dab, A. Heuer, and R. Silbey, Journal of luminescence **64**, 95 (1995).
[27] A. Heuer and R. J. Silbey, Physical Review B **53**, 609 (1996).
[28] J. Reinisch and A. Heuer, Physical Review B **70**, 064201 (2004).
[29] J. Reinisch and A. Heuer, Physical review letters **95**, 155502 (2005).
[30] T. Damart and D. Rodney, Physical Review B **97**, 014201 (2018).
[31] A. Ninarello, L. Berthier, and D. Coslovich, Physical Review X **7**, 021039 (2017).
[32] D. Queen, X. Liu, J. Karel, T. Metcalf, and F. Hellman, Physical review letters **110**, 135901 (2013).
[33] T. Pérez-Castañeda, R. J. Jiménez-Riobóo, and M. A. Ramos, Physical review letters **112**, 165901 (2014).
[34] T. Pérez-Castañeda, C. Rodríguez-Tinoco, J. Rodríguez-Viejo, and M. A. Ramos, Proceedings of the National Academy of Sciences **111**, 11275 (2014).
[35] X. Liu, D. R. Queen, T. H. Metcalf, J. E. Karel, and F. Hellman, Physical review letters **113**, 025503 (2014).
[36] M. Ediger, Proceedings of the National Academy of Sciences **111**, 11232 (2014).
[37] D. R. Queen, X. Liu, J. Karel, H. C. Jacks, T. H. Metcalf, and F. Hellman, Journal of Non-Crystalline Solids **426**, 19 (2015).
[38] H. Jónsson, G. Mills, and K. W. Jacobsen, in *Classical and Quantum Dynamics in Condensed Phase Simulations*, edited by B. J. Berne, G. Ciccotti, and D. F. Coker (World Scientific, Singapore, 1998).
[39] G. Henkelman, B. P. Uberuaga, and H. Jónsson, The Journal of chemical physics **113**, 9901 (2000).
[40] A. Q. Tool, Journal of the American Ceramic society **29**, 240 (1946).
[41] M. D. Ediger, C. A. Angell, and S. R. Nagel, The Journal of Physical Chemistry **100**, 13200 (1996).
[42] A. Cavagna, Physics Reports **476**, 51 (2009).
[43] S. F. Swallen, K. L. Kearns, M. K. Mapes, Y. S. Kim, R. J. McMahon, M. D. Ediger, T. Wu, L. Yu, and S. Satija, Science **315**, 353 (2007).
[44] K. L. Kearns, S. F. Swallen, M. D. Ediger, T. Wu, Y. Sun, and L. Yu, The Journal of Physical Chemistry B **112**, 4934 (2008).
[45] M. Tylinski, Y. Chua, M. Beasley, C. Schick, and M. Ediger, The Journal of chemical physics **145**, 174506 (2016).
[46] M. D. Ediger, The Journal of Chemical Physics **147**, 210901 (2017).
[47] J. Ràfols-Ribé, M. Gonzalez-Silveira, C. Rodríguez-Tinoco, and J. Rodríguez-Viejo, Physical Chemistry Chemical Physics **19**, 11089 (2017).
[48] A. Widmer-Cooper, P. Harrowell, and H. Fynewever, Physical review letters **93**, 135701 (2004).
[49] M. Gillan, Journal of Physics C: Solid State Physics **20**, 3621 (1987).
[50] G. H. Vineyard, Journal of Physics and Chemistry of Solids **3**, 121 (1957).
[51] L. Gil, M. A. Ramos, A. Bringer, and U. Buchenau, Phys. Rev. Lett. **70**, 182 (1993).
[52] D. Parshin, Physical Review B **49**, 9400 (1994).
[53] W. Ji, M. Popović, T. W. J. de Geus, E. Lerner, and M. Wyart, Phys. Rev. E **99**, 023003

(2019).

[54] S. Franz, T. Maimbourg, G. Parisi, and A. Scardicchio, Proceedings of the National Academy of Sciences **116**, 13768 (2019).

[55] M. Baggioli, R. Milkus, and A. Zaccone, arXiv:1903.05237 (2019).

[56] L. Wang, A. Ninarello, P. Guan, L. Berthier, G. Szamel, and E. Flenner, Nature communications **10**, 26 (2019).

[57] J.-P. Hansen and I. R. McDonald, *Theory of simple liquids (Third edition)* (Academic Press, 1986).

[58] W. Ching and C. C. Lin, in *Amorphous Magnetism II* (Springer, 1977) pp. 469–477.

# I Supplementary information - Model

We study a three-dimensional, non-additive, continuously polydisperse mixture of particles interacting via the pair potential Eq. (1). The particle diameters $\sigma_i$ are drawn from the normalized distribution $P(0.73 < \sigma < 1.62) \sim 1/\sigma^3$, with average diameter $\langle\sigma\rangle = \int P(\sigma)\mathrm{d}\sigma = 1$ (simply denoted as $\sigma$ in the main text). We employ a non-additive cross-diameter $\sigma_{ij} = 0.5(\sigma_i + \sigma_j)\,(1 - 0.2|\sigma_i - \sigma_j|)$. This model is efficiently simulated with the swap Monte Carlo algorithm. The choice of particle dispersity and non-additivity make the homogeneous fluid robust against fractionation and crystallization at all temperatures numerically explorable [31]. As in the main text, classical quantities are given in units of $\epsilon, \sigma, m_0$.

We characterize the dynamic slowdown of the supercooled liquid using molecular dynamics (MD) simulations. The temperature evolution of the relaxation time $\tau_\alpha$ provides three temperatures relevant to this work. The onset of glassy dynamics, signaled by deviations from Arrhenius behavior, takes place at $T_o = 0.18$, where $\tau_\alpha(T_o) = \tau_o$. The mode-coupling crossover temperature $T_{MCT} = 0.104$ is measured by fitting the relaxation time data to $\tau_\alpha \sim (T - T_{MCT})^{-\gamma}$ in a limited window of relatively high temperatures. At $T_{MCT}$, the dynamics is four orders of magnitude slower than at the onset temperature, $\tau_\alpha(T_{MCT}) \simeq 10^4\tau_o$. We take the mode-coupling crossover temperature $T_{MCT}$ as a proxy for the computer glass transition, below which standard MD fail to equilibrate the homogeneous fluid. The experimental glass transition $T_g = 0.067$ is located by fitting the relaxation time data to a parabolic law, using $\tau_\alpha(T_g) = 10^{12}\tau_o$ [31].

This glass-forming model is efficiently simulated at equilibrium with the swap Monte Carlo algorithm. Supercooled liquid configurations can be generated down to $T = 0.062$, i.e. below the experimental glass transition $T_g$. In this work, we focus on configurations prepared in equilibrium conditions at temperatures $T_f = 0.092, 0.07, 0.062$. For the two lowest $T_f$ values, standard MD dynamics initialized from an equilibrium configuration is completely arrested: no diffusion is observed and the system is trapped within a glass metabasin. For the higher $T_f = 0.092$, some diffusion is observed in equilibrium; but if the system is rapidly cooled at lower temperatures, once again no diffusion is observed and a glass state is obtained. Borrowing from experimental conventions [40], we call this the "fictive temperature" of the glasses, as discussed in the main text.

# II Supplementary information - Landscape exploration

The amorphous configurations generated at $T_f$ are first thermalized to $T_{\mathrm{MD}} = 0.04$ using a Berendsen thermostat. At this temperature, no diffusion is observed for all glasses. The system is then simulated in the NVE ensemble, using an integration time step of $dt = 0.01$. Configurations along the MD trajectory are frequently minimized using a conjugate gradient algorithm, bringing them to their inherent structure (IS), i.e. the nearest local minimum in the potential energy landscape (PEL). We minimize the MD trajectory every 20, 10, 5 time steps for $T_f = 0.062, 0.07, 0.092$. The high frequency of minimization is chosen to identify nearby local minima, separated by an energy barrier.

From the MD simulations, we obtain a time series of inherent structures. We are interested in transitions between two different inherent structures, identified by comparing two consecutive minima. We recorded 70970, 130859, and 1593359 transitions between inherent structures, for $T_f = 0.062, 0.07, 0.092$ respectively. We wish to characterize the potential energy barriers corresponding to the transitions. This analysis is computationally costly. Given the large number of transitions detected, we chose to analyze transitions detected at least 4 times, regardless of the direction of the

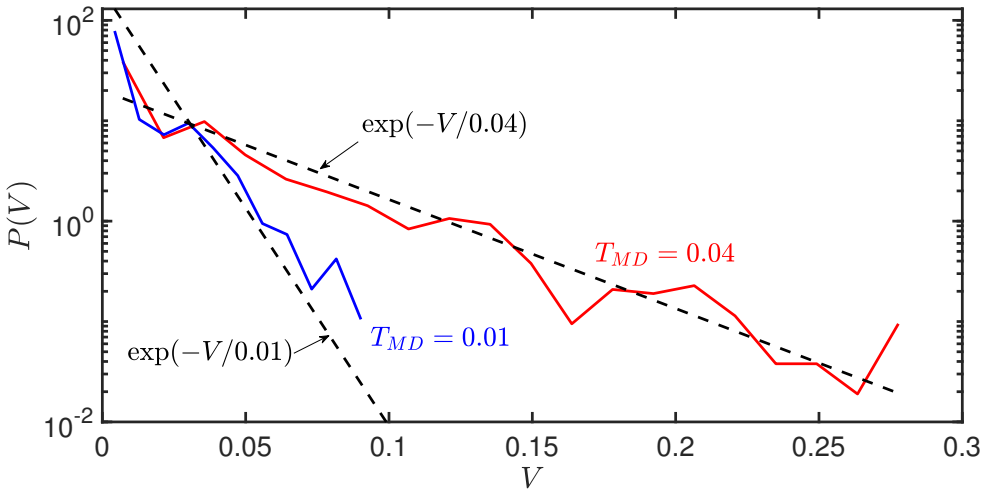


Figure S1: Probability distribution of the potential energy barriers $V$ sampled at temperatures $T_{\rm MD} = 0.01$ and 0.04.

transition ($A \to B$, or $B \to A$). The number of transitions analyzed is equal to 14195, 23535, and 117361, for $T_f = 0.062, 0.07, 0.092$ respectively.

In order to investigate the influence of the temperature $T_{\rm MD}$ on the characteristics of the double well potentials identified, we present in Fig. S1 the probability distribution function of potential energy barriers identified with $T_{\rm MD} = 0.01$, and 0.04 (used in the main text). The sampling temperature $T_{\rm MD}$ influences the tail of the distribution only, which decays as $\exp(-V/T_{\rm MD})$. We conclude that the sampling of relevant TLS is not affected by a variation of $T_{\rm MD}$ within a reasonable interval.

## III Supplementary information - Tunnel splitting

For each analyzed transition, the Nudged Elastic Band (NEB) algorithm outputs a one-dimensional potential defined for the reduced coordinate $\xi$, between the two minima only. We run the algorithm using 40 images of the system. We need to extrapolate the potential in order to obtain a full double well potential. We tested various extrapolation schemes, such as parabolic fitting of the minima, and mirroring around each minima, defining $V(-\xi) = V(\xi)$ for $\xi < \xi_a$ and $V(2-\xi) = V(\xi)$ for $\xi > \xi_a$, where $\xi_a$ is the coordinate of the potential maximum: $V(\xi_a) = V(0) + V_a$. In the main text, we used a linear extrapolation of the reaction path obtained with the NEB. Let us denote $\mathbf{r}_1$ and $\mathbf{r}_2$ the coordinates of the particles in the first two images of the system along the reaction path ($\mathbf{r}_1$ is an energy minimum). We measure the potential energy of the configuration, starting from $\mathbf{r}_1$, and moving in the direction $\mathbf{r}_1 - \mathbf{r}_2$. We perform a similar extrapolation at the other minimum. We show in Fig. 1 a double-well potential obtained from the NEB algorithm (blue part), and by linear extrapolation of the reaction path (black part). We have compared all methods and found that while each scheme gives a slightly different potential, the statistics of tunnel splittings remains unaffected by our choice. In the main text, we use the most physical scheme, namely the linear extrapolation of the reaction path.

Once the classical potential $V(\xi)$ is obtained by extrapolation as discussed above, we solve

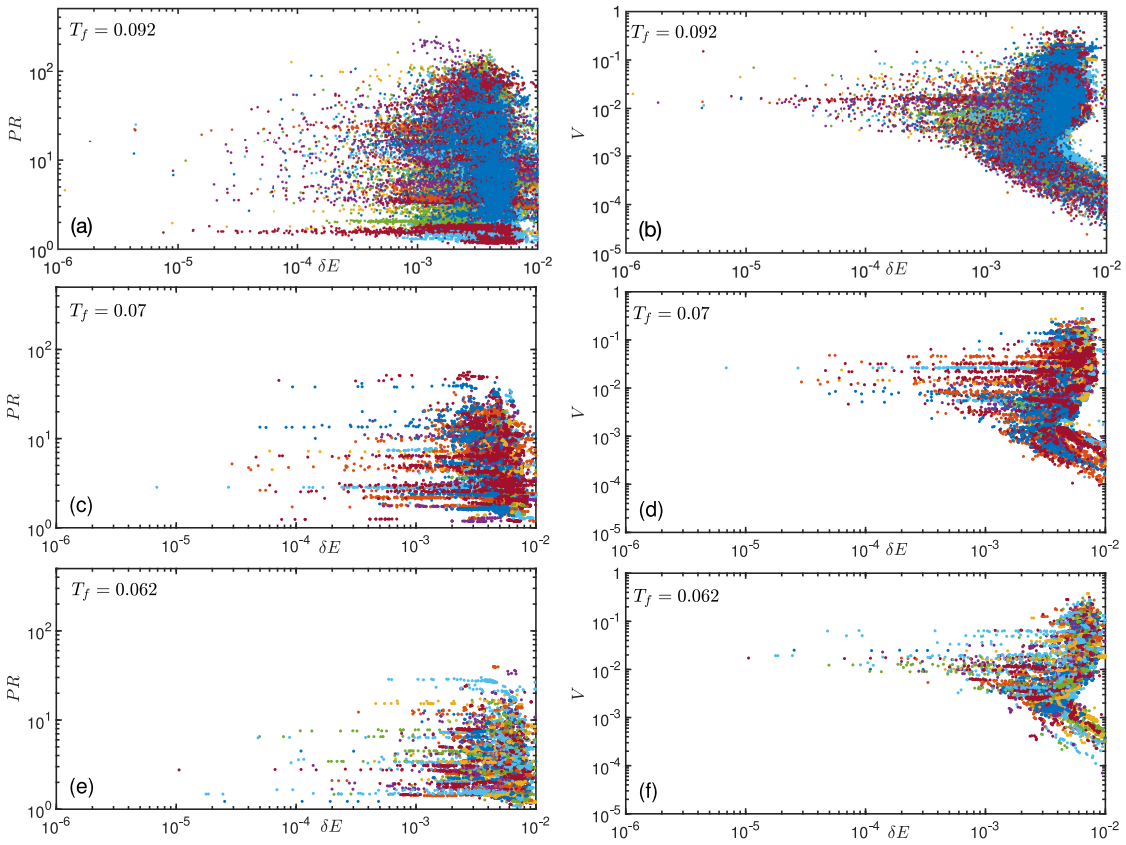


Figure S2: Scatter plot of the participation ratio $PR$ (a,c,e) and the potential energy barrier $V$ (b,d,f) versus the tunnel splitting $\delta E$, of double-well potentials in glasses prepared at $T_f = 0.092$ (a-b), $T_f = 0.07$ (c-d), and $T_f = 0.062$ (e-f). The data for DWPs found in the same glass sample (there are $N_g$ of them) are presented with the same color. The tunnel splittings are computed using an adimensional mass $\widetilde{m}_0 = 30000$.

numerically the Schrödinger Eq. (2) using a standard Python package. Note that, in general, the Laplacian term should take into account curvature effects along the reaction coordinate, $\nabla^2_\xi = \partial^2_\xi + (\det g)^{-1/2}\partial_\xi[(\det g)^{1/2}\partial_i] + (\det g)^{-1/2}\partial_i[(\det g)^{1/2}\partial_\xi]$, where $g$ is a metric tensor and $\xi_i$ are coordinates orthogonal to $\xi$. For simplicity, we neglect these effects and use the standard second derivative along the reaction coordinate.

We present in Fig. S2 a scatter plot of the tunnel splitting $\delta E$ as a function of participation ratio $PR$ and energy barrier $V$ for DWPs identified in glasses from hyper-quenched (top) to ultrastable (bottom). In Fig. S2 (a,c,e) we observe that in the relevant range of $\dot{\mathrm{E}} \lesssim 10^{-3}$ the value of $PR$ can be as large as $\sim 200$ for $T_f = 0.092$ and $\sim 30$ for $T_f = 0.062$. In Fig. S2 (b,d,f) we observe that in the same relevant range, the barrier is always $V \gtrsim 10^{-2} \gg \dot{\mathrm{E}}$, indicating that the relevant DWP are indeed TLS. We also checked (not shown) that in the same range, one always has $E_3 - E_1 \gg \dot{\mathrm{E}}$, where $E_3$ is the third energy level.

Finally, we checked that for most TLS in the relevant range, the wavefunctions of the first two levels are delocalized over the two wells, indicating that tunnelling is active. However, the barrier $V$ has a relatively wide distribution (see Fig. S2), and there exist TLS with large barriers and hence very

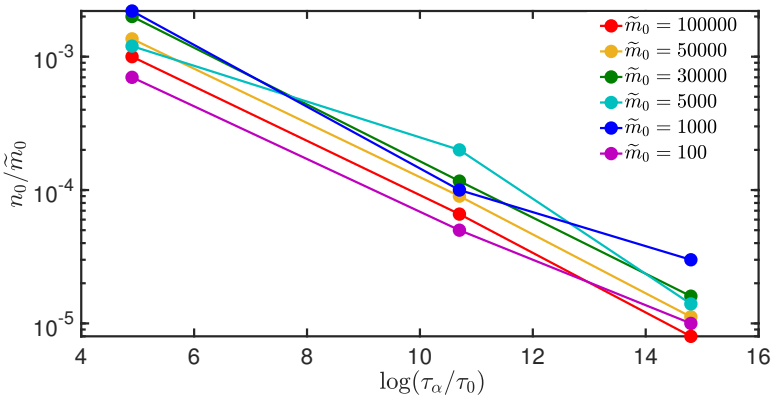


Figure S3: The TLS density $n_0$, as extrapolated from $n(\dot{E})/\dot{E}$ in the limit $\dot{E} \to 0$, divided by $\widetilde{m}_0$, as a function of glass stability, encoded by the value of $\log(\tau_\alpha/\tau_o)$ for the three values of $T_f$ and different $\widetilde{m}_0$. A reduction of $n_0$ by two orders of magnitude is robustly observed, independently of $\widetilde{m}_0$. Furthermore, we find $n_0 \propto \widetilde{m}_0$ independently of $T_f$.

small tunnelling matrix elements. For those TLS, the wavefunctions are almost localized, indicating that tunnelling is highly suppressed. These TLS would be frozen in experimental conditions. The wide distribution of $V$ is known to be responsible for a logarithmic growth of $n_0$ with observation time $\tau$, $n_0 \propto \log \tau$ [6], which also provides an additional explanation for why our simulations overestimate $n_0$ with respect to experiments.

# IV Supplementary information - Dimensional scaling analysis for unit conversion

The number of TLS per particle in a given glass sample with a tunnel splitting less than $\delta E$, for $\delta E \to 0$, is $n_0 \delta E$. Hence, $n_0$ has the dimensions of an inverse energy, expressed in units of $\epsilon^{-1}$. However, because in our simulation units the number density is $\rho = 1$, $n_0$ is also the number of TLS per unit volume, in units of $\epsilon^{-1}\sigma^{-3}$, i.e.

$$n_0^{exp} = n_0^{sim} \times \epsilon^{-1}\sigma^{-3} \ . \tag{3}$$

For Argon, $\epsilon^{-1}\sigma^{-3} \sim 3.85 \times 10^{48} \mathrm{J}^{-1}\mathrm{m}^{-3}$, while for Nickel $\epsilon^{-1}\sigma^{-3} \sim 1.51 \times 10^{48} \mathrm{J}^{-1}\mathrm{m}^{-3}$, which allows one to convert our numerical results for $n_0^{sim}$ into experimental values for these two materials.

Because the glass transition temperature in the simulation is $T_g = 0.067$, the corresponding glass transition temperature in physical units is

$$T_g = 0.067 \times \frac{\epsilon}{k_B} \ . \tag{4}$$

Finally, the temperature $T_Q$ at which quantum effects become relevant is that at which the thermal wavelength equals the interparticle distance. Since our simulation density is $\rho = 1/\sigma^3$, we get

$$T_Q = \frac{2\pi\hbar^2}{m_0 \sigma^2 k_B} = \frac{2\pi}{\widetilde{m}_0} \frac{\epsilon}{k_B} \ , \tag{5}$$

and we recall that $\widetilde{m}_0 = m_0\sigma^2\epsilon/\hbar^2$ is the adimensional mass that appears in the Schrödinger equation. Finally, note that the relevant (active) TLS are those with $\delta E < k_B T_Q$, and their total number in our simulation is given by

$$\begin{aligned} n_{active} &= NN_g n\left(\delta E = k_B T_Q\right) \\ &\sim NN_g n_0^{sim} \frac{k_B T_Q}{\epsilon} = 2\pi NN_g \frac{n_0^{sim}}{\widetilde{m}_0} \ . \end{aligned} \tag{6}$$

We find that $n_0/\widetilde{m}_0$ is roughly constant for a given glass stability $T_f$, as shown in Fig. S3. This results implies that the choice of $\widetilde{m}_0$ can be quite arbitrary, within a reasonable range. In particular, $\widetilde{m}_0$ cannot be too small otherwise the condition $T_Q \ll T_g$ would be violated.

# V Supplementary information - Vibrational and TLS contributions to the specific heat

Here, we compare the contributions to specific heat coming from TLS and from harmonic vibrations around an inherent structure. To obtain the TLS contribution, for a given $T_f$ and $\widetilde{m}_0$, we collect all the TLS found in all the $N_g$ glasses, with splitting $\delta E_i$, and compute [6, 3]

$$C_{\rm TLS} = \frac{1}{NN_g} \sum_i \frac{x_i^2}{\cosh(x_i)^2} \ , \qquad x_i = \frac{\delta E_i}{2k_B T} \ . \tag{7}$$

To obtain the vibrational contribution, we considered a single glass prepared at $T_f = 0.062$, and all the $N_{\rm IS}$ inherent structures found within that glass. For each inherent structure, we diagonalize the Hessian matrix of the classical potential, to obtain a set of eigenvalues (spring constants) $\kappa_\alpha$. Each of these provides a quantum harmonic oscillator contribution to the vibrational specific heat, which is

$$C_{\rm vib} = \frac{1}{NN_{\rm IS}} \sum_\alpha \frac{x_\alpha^2}{\sinh(x_\alpha)^2} \ , \qquad x_\alpha = \frac{\hbar\omega_\alpha}{2k_B T} \ , \qquad \omega_\alpha = \sqrt{\frac{\kappa_\alpha}{m_0}} \ . \tag{8}$$

Note that the finite size of the system imposes a cutoff on the low-frequency Debye behavior. In fact, the lowest frequency found in our system is $\hbar\omega_\alpha/k_B = 0.0038$ (in simulation units) for $\widetilde{m}_0 = 5000$, and $\hbar\omega_\alpha/k_B = 0.0016$ for $\widetilde{m}_0 = 30000$. To avoid this problem we used data of larger system with $N = 192000$ particles [56] and extrapolate the quadratic region of the density of states to the $\omega \to 0$ limit.

Yet, from Fig. S4 we conclude that the vibrational contribution decays much faster than the TLS one upon lowering temperature, and that already at $T \sim 10^{-4}$ we have $C_{\rm vib} \ll C_{\rm TLS}$ for all considered values of $\widetilde{m}_0$ and $T_f$.

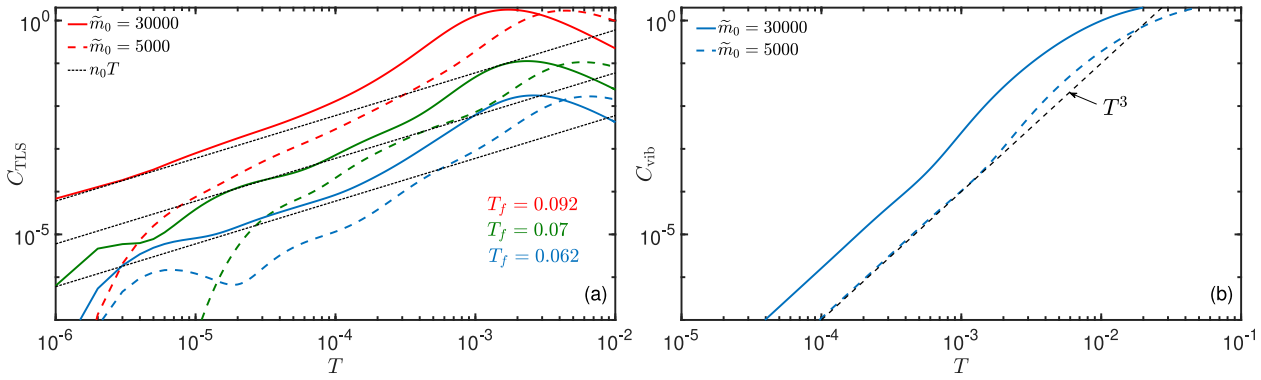


Figure S4: (a) TLS contribution to the specific heat per particle, as a function of $T$. Dotted-dashed lines are the asymptotic low-temperature scaling, $C_{\rm TLS} \sim T$, for $\widetilde{m}_0 = 30000$ (for $\widetilde{m}_0 = 5000$ the statistics is not sufficient for a good extrapolation). (b) Vibrational contribution to the specific heat per particle, as a function of $T$, for $T_f = 0.062$, averaged over inherent structures in a typical glass metabasin.

Chapter 4

# Efficient algorithms for the simulation of equilibrium supercooled liquids

The development of the SWAP algorithm opened the way to computer studies of supercooled liquids and glasses in a previously inaccessible temperature regime. Most of our numerical work was made possible by this recent advance.

The optimization of the swap Monte Carlo algorithm, combined to the design of new computer glass-forming models allowed thermalization at temperatures below the experimental glass transition. Surprisingly, this is achieved by bringing a small modification to the original Monte Carlo algorithm. The massive acceleration of dynamics offered by the addition of local swap moves raises questions on the origin of the glassy slowdown [230, 231]. It also reveals that smarter algorithms may be able to bypass the dramatic slowdown of supercooled liquids.

This sudden leap forward motivated efforts to take things one step further. Being able to reach even lower temperatures in equilibrium, or thermalizing larger system sizes, is an important goal. The putative Kauzmann transition could be approached even closer [232, 233]. Large computer samples are needed to investigate the melting mechanism of ultrastable films [234]. Large samples are also needed to study the mechanical stability of stable glasses [235], their vibrational properties [236], or to address the nature of the Gardner transition in $3d$ glasses by finite-size scaling analysis.

A first attempt to increase the efficiency of the swap algorithm is to implement a parallel version of the algorithm, *i.e.* running on several processors. In the following article, we explore this possibility by proposing a Hybrid molecular dynamics/SWAP Monte Carlo method. This method is implemented in the LAMMPS simulation package, for which MD is readily parallelized. We optimize the algorithm and its parameters to achieve the best efficiency, which we compare to the SWAP Monte Carlo method. We find that this method is as efficient as SWAP MC when run in serial (one processor). Our implementation within the LAMMPS package makes the algorithm accessible to a broad community of users. When run in parallel, however, the current version of the algorithm does not allow to gain in efficiency. In fact, the speedup gained in the MD part of the algorithm is counterbalanced by a greater cost of parallelizing the swap MC part.

In a second part of the work, we present a fully continuous version of the SWAP algorithm. The size of particles are treated as continuous variables which evolve in an external potential. A generalized Hamiltonian is defined for the system of interacting particles. The equations of motion

for the position and particle size are derived and solved numerically, as done in molecular dynamics. In this continuous method, the distribution of particle sizes, which defines a glass-forming model, is not fixed. It fluctuates in order to minimizes the potential energy of the system. This makes this method difficult to use in practice, since the potential for particle radii must be adjusted at all temperatures. Moreover, crystallization becomes almost inevitable at low temperature: the particle size distribution deforms in order to facilitate crystallization. While this method could be easily parallelized (the dynamics is deterministic), it is cumbersome to implement and does not compete with the SWAP and Hybrid methods.

In practice, Elijah Flenner initially proposed and implemented a version of the SWAP algorithm in the LAMMPS package. Christopher Fullerton and myself worked on a better implementation of the code, in order to make the parallel version as efficient as possible. Despite our efforts, the current version, run for $3d$ systems, is not more efficient when run in parallel. I performed the efficiency tests of the Hybrid method, which are presented in Figs. 2-7 of the article. I implemented several pair interaction potentials, such as the WCA potential, inverse power law potential, and harmonic potential. Murari Singh implemented, optimized and studied the continuous version of the swap method.

This Hybrid method is used to prepare the stable configurations studied in the article 'Nature of defects and excitations in structural glasses' of Chapter 3, as well as constant-pressure simulations, for which the results are presented in Chapter 5.

Article

# Efficient swap algorithms for molecular dynamics simulations of equilibrium supercooled liquids

L. Berthier, E. Flenner, C. J. Fullerton, C. Scalliet, M. Singh, J. Stat. Mech. (2019) 064004

**It was recently demonstrated that a simple Monte Carlo (MC) algorithm involving the swap of particle pairs dramatically accelerates the equilibrium sampling of simulated supercooled liquids. We propose two numerical schemes integrating the efficiency of particle swaps into equilibrium molecular dynamics (MD) simulations. We first develop a hybrid MD/MC scheme combining molecular dynamics with the original swap Monte Carlo. We implement this hybrid method in LAMMPS, a software package employed by a large community of users. Secondly, we define a continuous time version of the swap algorithm where both the positions and diameters of the particles evolve via Hamilton's equations of motion. For both algorithms, we discuss in detail various technical issues as well as the optimisation of simulation parameters. We compare the numerical efficiency of all available swap algorithms and discuss their relative merits.**

## I Introduction

Simulations are a useful tool to understand the equilibrium properties of supercooled liquids approaching a glass transition [1]. They offer microscopic insight into static and dynamic properties for well-defined and usually quite simple model systems. A major obstacle in this approach is the difficulty of simulating large enough timescales in order to get closer to experimentally-relevant studied materials. Recently, the gap between simulated timescales and experimental ones has been closed [2, 3] using a simple Monte Carlo (MC) scheme, where ordinary translational moves of the particles (that mimic the physical dynamics) are complemented by the swap of unlike particle pairs [4, 5]. The method is thus broadly applicable to models composed of discrete or continuous mixtures of distinct particles. In practice, this encompasses virtually all types of glass-formers [1].

While having many advantages, such as simplicity and efficiency, Monte Carlo is not necessarily

the most commonly used simulation technique for supercooled liquids. Molecular dynamics (MD) techniques are often preferred, because the microscopic dynamics is closer to that of real molecular fluids [6]. For colloidal particles, Brownian dynamics may be more adapted. For several models of supercooled liquids, the equivalence of all these different microscopic dynamics to those of MC simulations is fully established [7, 8, 9, 10]. This implies in particular that the chosen numerical method to simulate supercooled liquids is essentially one of personal convenience. Since particle swaps were first introduced in the context of MC studies [5, 2], it is natural to ask whether it is possible to extend the method in the more general context of MD simulations.

One potential advantage of MD simulations is that they are easier to parallelize than MC techniques, mainly because the positions of the particles are all updated simultaneously in MD rather than sequentially in MC. This makes simulating large systems prohibitively slow when using MC simulations. Although spatial correlations remain relatively modest in supercooled liquids [1, 11], larger and larger systems are required to analyse the deeply supercooled states that swap MC simulations can now potentially access [12, 13, 14, 15]. It is therefore natural to ask if it is possible to introduce swap moves into molecular dynamics, a simulation method which is readily parallelized.

As a first step we consider a hybrid MC/MD simulation scheme where blocks of swap Monte Carlo moves are inserted at regular time intervals into a conventional molecular dynamics simulation. This method has already been used long ago [4], in a different context. We show how to best tune the parameters of this hybrid technique to obtain maximum efficiency, and carefully discuss the numerical efficiency of the technique. We implement the method into the LAMMPS open software for MD simulations [16]. In a second effort, we implement a continuous time version of the swap MC into a generalized MD scheme where both the positions and the diameters of the particles obey Newton's equations of motion for a suitably defined Hamiltonian. This second scheme bears similarities with semi-grand MC techniques for polydisperse fluids [17, 4, 18]. When properly optimised, we find that all three simulations techniques provide essentially the same (potentially very large) speedup over conventional MD and MC techniques, so that again the choice of one swap algorithm over another is mostly one of personal convenience.

This article is organised in the following way. In Sec. II, we discuss the hybrid MC/MD method: numerical scheme, details of the studied models, thermalisation speedup. These results are of general interest and do not depend on the specific implementation of the algorithm. We then present the computational efficiency obtained with our implementation of the method in the LAMMPS package. In Sec. III, we present the continuous time version of the swap algorithm. The relative merits of all swap algorithms are discussed in Sec. IV.

# II Hybrid MC/MD method

## II.1 Microscopic model

We study numerically a system composed of $N$ size polydisperse particles of identical masses $m$ in a cubic box of linear size $L$ with periodic boundary conditions. The system is defined by the $3N$ particle position coordinates $\mathbf{r}^N = \{\mathbf{r}_1, \mathbf{r}_2, \ldots, \mathbf{r}_N\}$, and the particle sizes $\sigma^N = \{\sigma_1, \sigma_2, \ldots, \sigma_N\}$.

Two particles $i \neq j$ at a distance $r_{ij} = |\mathbf{r}_i - \mathbf{r}_j|$ interact only if $r_{ij} < 1.25\sigma_{ij}$. We model the

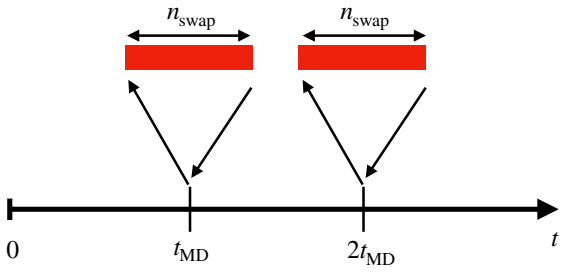


Figure 1: The hybrid scheme consists of a regular succession of blocks of molecular dynamics simulations and blocks of particle-swap Monte Carlo steps. Every $t_{\rm MD}$, the molecular dynamics is paused and $n_{\rm swap}$ swap Monte Carlo steps are performed, which are not counted in the total elapsed MD time.

interactions between particles via a soft repulsive pair potential

$$\begin{aligned} u(r_{ij},\sigma_{ij})/\epsilon &= \left(\frac{\sigma_{ij}}{r_{ij}}\right)^{12} + F(r_{ij},\sigma_{ij}) \quad , \\ \text{where } F(r_{ij},\sigma_{ij}) &= c_0 + c_2\left(\frac{r_{ij}}{\sigma_{ij}}\right)^2 + c_4\left(\frac{r_{ij}}{\sigma_{ij}}\right)^4 \end{aligned} \tag{1}$$

is a function that smooths the potential at the cutoff distance $1.25\sigma_{ij}$. The coefficients $c_0$, $c_2$, and $c_4$ ensure the continuity of the potential up to the second derivative at the cutoff. The total potential energy of the system is $U(\mathbf{r}^N,\sigma^N) = \sum_{i<j} u(r_{ij},\sigma_{ij})$. In order to obtain a good glass-forming model, we study a continuously polydisperse system. The particle diameters follow the distribution $P(\sigma_m \leq \sigma \leq \sigma_M) = A/\sigma^3$, where $A$ is a normalizing constant, $\sigma_m = 0.73$ and $\sigma_M = 1.62$. To ensure the structural stability of the polydisperse mixture, we employ a nonadditive interaction rule for the cross diameters $\sigma_{ij} = \frac{\sigma_i+\sigma_j}{2}(1-0.2|\sigma_i-\sigma_j|)$, following previous work [3]. Lengths and times are respectively expressed in units of $\overline{\sigma} = \int \sigma P(\sigma) d\sigma$ and $\sqrt{\epsilon/m\overline{\sigma}^2}$. In the following, we present results for this model at number density $\rho = N/L^3 = 1$, mostly for $N = 1500$. In Sec. II.7, we study systems with larger sizes to check the scalability of the algorithm with system size.

## II.2 Hybrid scheme

We introduce the hybrid scheme used to simulate the glass-forming model presented in Sec. II.1. The method consists of alternating between ordinary molecular dynamics simulation sequences during which the particle positions evolve with a fixed particle size, and particle-swap Monte Carlo sequences during which the particles exchange their sizes at fixed positions. The hybrid method is illustrated in the schematic diagram of Fig. 1.

The trajectories of particles in the MD blocks are generated in the canonical ensemble ($NVT$) by integrating Nosé-Hoover chain equations of motion [19, 20, 21, 22]. We use a chain of thermostats of length three. The time integration of the equations of motion is performed by a time-reversible measure-preserving Verlet algorithm, with a time discretization $dt = 0.01$ [23]. The damping parameter associated to the heat bath variables is equal to 1. The particles positions and velocities are evolved during sequences of duration $t_{\rm MD}$. This defines the MD blocks. At the end of each MD block, the time is paused, and the particle positions and velocities are frozen. A series of particle-swap Monte Carlo moves are then performed, and this defines a swap Monte Carlo (SMC) block.

These blocks are composed of $N_{\rm swap}$ attempted elementary swap moves. During each elementary move, two particles are chosen randomly and the exchange of their diameters is accepted or rejected based on the Metropolis criterion. The swap moves preserve detailed balance and guarantee an equilibrium sampling of phase space in the $NVT$ ensemble. The duration of the swap Monte Carlo blocks is defined in a system-size independent way through $n_{\rm swap} = N_{\rm swap}/N$.

We combine the parameters $t_{\rm MD}$ and $n_{\rm swap}$ together as

$$\rho_{\rm swap} = \frac{n_{\rm swap}}{t_{\rm MD}}, \tag{2}$$

which represents the density of particle-swap Monte Carlo moves per particle and unit MD time. In the following, we will study how the parameters $t_{\rm MD}$ and $n_{\rm swap}$ affect the efficiency of the algorithm. In particular, we will study the competition between the thermalisation speedup offered by the swap moves and the additional CPU time entailed by the addition of swap MC blocks.

We have implemented the hybrid scheme into the LAMMPS open software, because it is widely used and versatile. We have already used this method to study other model systems, such as Lennard-Jones and its truncated Weeks-Chandler-Andersen version [24, 25, 26]. Very deeply supercooled states have been successfully obtained for all these models. Details about how size polydispersity is handled and other LAMMPS-specific details are presented in Appendix V.

## II.3 Proper sampling of the canonical ensemble

In the previous section, we presented the hybrid scheme as a succession of molecular dynamics and swap Monte Carlo blocks. Inside each block, the dynamics (MD or MC) is carefully designed to sample the canonical $NVT$ ensemble. However, given the different nature of both algorithms, we need to ensure that the combination of both methods continues this equilibrium sampling.

In the hybrid method, the MD simulation is regularly interrupted to perform particle-swap moves. In the MD blocks, both the potential and kinetic energies fluctuate. By contrast, the SMC blocks only affect the potential energy of the system, since only the diameters of particles are changed, at fixed positions and velocities. As a new MD block starts, the particles have the same positions and velocities as in the previous MD block, but they now possess a different potential energy. It takes a short but finite time (of the order $t \sim 0.1$) for the kinetic energy to relax after the SMC block has been performed. As a result, MD blocks cannot be made arbitrarily short. When hybrid simulations are run with $t_{\rm MD} < 0.1$, we have found that the system heats. In the limit $t_{\rm MD} = dt$, which amounts to alternating MC and MD at each integration step, the kinetic energy is up to 3% higher than the imposed temperature and the Nosé-Hoover thermostat does not work properly.

However, when the hybrid simulations are run with $t_{\rm MD} > 0.1$, the probability distributions of the potential and kinetic energies follow the canonical ones, and coincide with those obtained from standard $NVT$ simulations without the SMC blocks.

## II.4 Equilibration speedup

In this section, we study the equilibrium dynamics of the model presented in Sec. II.1 simulated with the hybrid method.

We first run equilibration simulations during which we monitor the evolution of the potential energy $U$ and the structure factor of the liquid, to detect aging effects and potential instabilities of

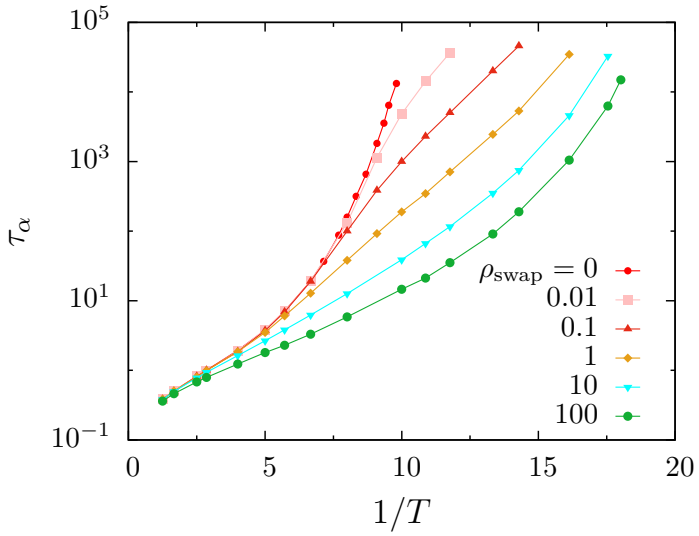


Figure 2: Evolution of the equilibration time $\tau_\alpha$ with inverse temperature $1/T$ in hybrid MD/MC simulations of the three-dimensional soft polydisperse model of Sec. II.1 at number density 1. The swap density $\rho_{\rm swap}$ is varied between $\rho_{\rm swap} = 0$ (ordinary molecular dynamics) and $\rho_{\rm swap} = 100$. The dynamics at intermediate $\rho_{\rm swap}$ smoothly interpolates between these two limits.

the homogeneous fluid. When equilibrium is reached, we compute the self-part of the intermediate scattering function

$$F_s(k,t) = \left\langle \frac{1}{N} \sum_j e^{i\mathbf{k}\cdot[\mathbf{r}_j(t)-\mathbf{r}_j(0)]} \right\rangle \quad . \tag{3}$$

We spherically average over wavevectors of magnitude $k = 7.0$, which corresponds to the first diffraction peak in the static structure factor of the liquid. The brackets indicate averages over independent equilibrated configurations. We do not insist that times are taken immediately or long after the Monte Carlo swap moves. Following common practice, we define the structural relaxation time of the liquid $\tau_\alpha$ as the time at which $F_s(k,\tau_\alpha) = e^{-1}$.

We study the influence of gradually adding SMC blocks to standard MD simulations. We compute the equilibrium relaxation time of the liquid varying temperature and swap density $\rho_{\rm swap}$ and report the results in Fig. 2. For $\rho_{\rm swap} \geq 0.1$, we use $t_{\rm MD} = 0.1$, and different lengths $n_{\rm swap}$ for swap blocks. To access the lowest density of swap $\rho_{\rm swap} = 0.01$, we use instead $t_{\rm MD} = 1$. The resulting swap density $\rho_{\rm swap}$ then varies from 0.01 to 100. Conventional molecular dynamics simulations correspond to $\rho_{\rm swap} = 0$.

For standard molecular dynamics, the relaxation time of the liquid increases sharply as temperature decreases. We evaluate empirically $T_{MCT} \approx 0.1$ through a mode-coupling theory power-law fit to the relaxation time data [27]. In practice, the numerical study of equilibrium supercooled liquids with molecular dynamics simulations are confined to temperatures above $T_{MCT}$, as the relaxation time near $T_{MCT}$ corresponds typically to the maximal computer time accessed in conventional MD. As such the mode-coupling temperature crossover $T_{MCT}$ is a useful temperature scale in the context of computer simulation studies of supercooled liquids.

The situation changes gradually as $\rho_{\rm swap}$ increases. For low values $\rho_{\rm swap} = 0.01 - 0.1$, the relaxation time of the system at high temperature is equal to that of the standard MD simulation.

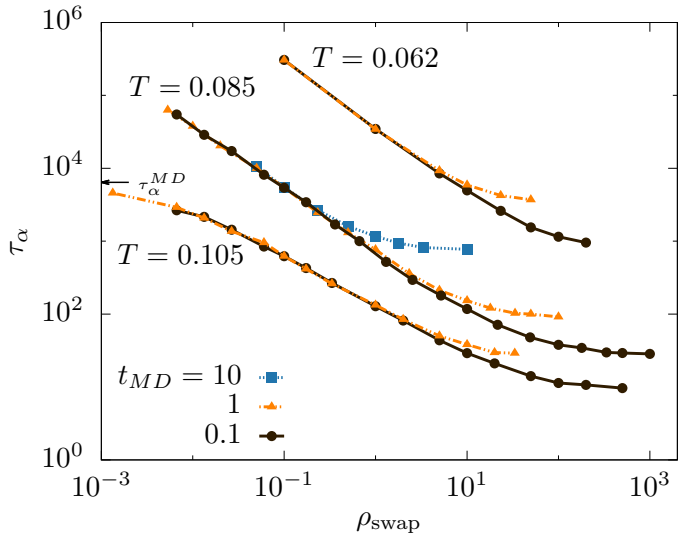


Figure 3: Relaxation time as a function of $\rho_{\mathrm{swap}}$ for three selected temperatures: $T = 0.105, 0.085, 0.062$. At fixed temperature, each data set corresponds to a given duration of the MD blocks, $t_{\mathrm{MD}} = 0.1, 1, 10$, and each single point to one value of $n_{\mathrm{swap}}$. The arrow labeled $\tau_\alpha^{MD}$ indicates the relaxation time of the liquid at $T = 0.105$ for ordinary MD simulations; this time cannot be directly measured for the two lowest temperatures.

In this regime, the dynamics is not slow enough to be affected by the addition of a small number of swap moves. Around $T_{MCT}$ and below, the addition of short SMC blocks becomes key to observing the liquid relax in numerically accessible timescales. Strikingly, equilibrium is easily reached at $T < T_{MCT}$ with a density of swap as small as $\rho_{\mathrm{swap}} = 0.01$, i.e., when only 1% of the $N$ particles are swapped per unit time. As the swap density $\rho_{\mathrm{swap}}$ increases, the relaxation time departs more strongly from the one obtained with pure MD simulations.

For large swap densities such as $\rho_{\mathrm{swap}} = 100$, the dynamics are affected so much that the high-temperature Arrhenius behavior of the normal dynamics now persists almost down to $T_{MCT}$, before eventually increasing with a super-Arrhenius law at lower temperatures. We find that the hybrid method can achieve thermalization of supercooled liquids down to $0.6T_{MCT}$. We point out that Fig. 2 resembles results obtained with the swap Monte Carlo method, in which the role of $\rho_{\mathrm{swap}}$ was played by the probability, $p$, to perform a particle-swap move over a translational move [28]. This suggests a close correspondence between $\rho_{\mathrm{swap}}$ in the hybrid method and $p$ in the original swap MC method, which we explore further in Sec. II.6.

In order to optimize the hybrid method, we investigate the separate influence of the parameters $n_{\mathrm{swap}}$ and $t_{\mathrm{MD}}$ on the thermalization speedup of supercooled liquids. We select three temperatures of interest, one above $T_{MCT}$ and two below: $T = 0.105$, 0.085, and 0.062. For each temperature, we report the relaxation time $\tau_\alpha$ measured with the hybrid simulations at different $n_{\mathrm{swap}}$ and $t_{\mathrm{MD}}$ in Fig. 3. Each data set corresponds to a fixed duration $t_{\mathrm{MD}}$ of the MD blocks, so that increasing $\rho_{\mathrm{swap}}$ corresponds to increasing the duration $n_{\mathrm{swap}}$ of the SMC blocks.

The qualitative evolution of the relaxation time with swap density is similar at all temperatures. Starting from the limit $\rho_{\mathrm{swap}} = 0$ (conventional MD simulations), $\tau_\alpha$ decreases with the swap density, roughly as $\tau_\alpha \sim 1/\rho_{\mathrm{swap}}$ [3]. At $T = 0.085, 0.062$, this behaviour is observed over a few decades of $\rho_{\mathrm{swap}}$. At large $\rho_{\mathrm{swap}}$, all curves saturate to a plateau value: increasing the length of SMC blocks at

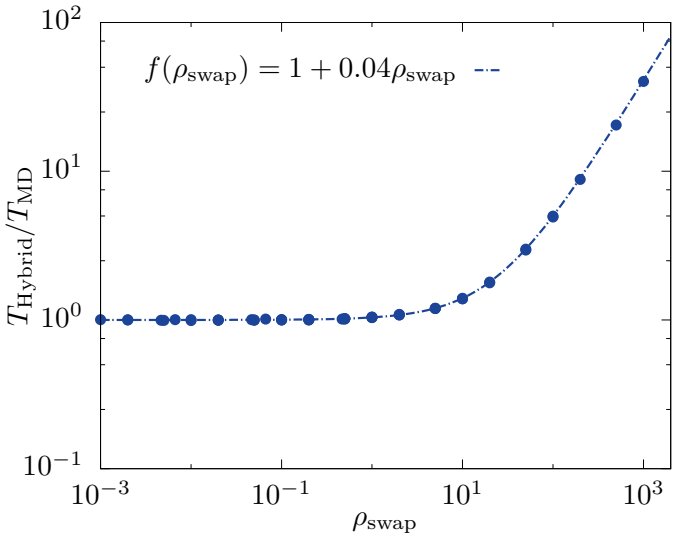


Figure 4: Ratio of the CPU time $T_{\mathrm{Hybrid}}$ of Hybrid simulations compared to the CPU time of standard molecular dynamics $T_{\mathrm{MD}}$, both running for the same total MD length. The trivial limits of $T_{\mathrm{Hybrid}}/T_{\mathrm{MD}}$ at small and large $\rho_{\mathrm{swap}}$ are well captured by a simple empirical fitting function shown with a dashed line.

fixed interval $t_{\mathrm{MD}}$ does not speedup further the dynamics. Indeed, as $n_{\mathrm{swap}}$ increases more particle-swap attempts are performed in a SMC block. But since the particles' positions are frozen during such SMC blocks, the saturation of $\tau_\alpha$ reflects the thermalization of the particles' diameters within a frozen configuration. At a given temperature, the plateau value at larger $\rho_{\mathrm{swap}}$ depends on $t_{\mathrm{MD}}$: the longer $t_{\mathrm{MD}}$, the higher $\tau_\alpha$ is at the plateau. Since molecular dynamics is inefficient at relaxing the structure of the liquid in this temperature regime, longer MD blocks do not help speedup the structural relaxation. We emphasise that MD blocks are nonetheless essential to the hybrid method, since swap moves and particle displacements work hand in hand to decorrelate the structure of the liquid [3].

The optimal value $t_{\mathrm{MD}} = 0.1$ emerges from optimizing the physical efficiency (see Fig. 3) of the hybrid simulation which requires a small $t_{\mathrm{MD}}$ value, together with the constraint that $t_{\mathrm{MD}}$ must be large enough for a proper sampling of the canonical ensemble (see Sec. II.3).

## II.5 Efficiency of the hybrid method on a single CPU

In this section, we focus on the efficiency of the hybrid method executed on a single CPU. More specifically, we are interested in quantifying the competition between the added CPU cost due to increasing the number of swap moves and the speedup in thermalisation offered by the swap moves observed in Fig. 2. Such results, therefore, will be a combination of the physical efficiency of the algorithm, the efficiency of our implementation of the hybrid method, and the hardware that we run it on. However, our discussion is generic and should be useful to anyone willing to employ the hybrid method. We present results obtained with our implementation of the hybrid method in the LAMMPS package. We expect these results to be broadly applicable, as there is little flexibility in implementing such a serial program, apart from well-known optimizations [6].

To characterize the influence of $\rho_{\mathrm{swap}}$ on the CPU time in the hybrid method, we measure the time in seconds to run hybrid simulations which last the same total MD time, using different

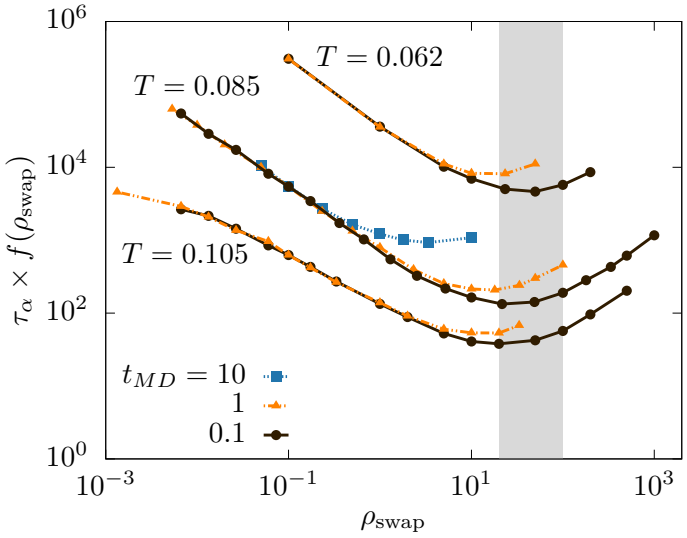


Figure 5: The product of the measured relaxation time $\tau_\alpha$ with the computational cost $f(\rho_{\text{swap}})$ of increasing the swap density in the hybrid method presents a minimum at all temperature. The hybrid method is the most efficient with the parameters yielding a minimum in the curves. The best trade-off between physical speedup and CPU cost is reached for $n_{\text{swap}} = 2 - 10, t_{\text{MD}} = 0.1$, as highlighted by the shaded region.

combinations of $n_{\text{swap}}$ and $t_{\text{MD}}$. The computational time should of course not depend on how the MD and SMC blocks are distributed, but rather on the total duration of each type of blocks. We therefore report times as a function of $\rho_{\text{swap}}$ in Fig. 4. As expected, we see that all points collapse on a single master curve, confirming that the CPU time indeed depends on $\rho_{\text{swap}}$ only. In the range $\rho_{\text{swap}} = 0 - 10$, the CPU time of the hybrid method is dominated by that of the MD blocks. Around $\rho_{\text{swap}} = 10$, the CPU time becomes dominated by particle-swaps, and eventually grows linearly with $\rho_{\text{swap}}$ with a slope controlled by the CPU cost of an individual swap move. This simple dependence of the CPU time with $\rho_{\text{swap}}$ is well captured by a fitting function $f(\rho_{\text{swap}}) = 1 + 0.04\rho_{\text{swap}}$ (dashed line in Fig. 4), which captures these two limits.

To finally determine the optimal parameters of the hybrid method, we combine the dynamical gain shown in Fig. 3 and the computational cost discussed in Fig. 4. The product of both quantities quantifies the time needed to achieve a given number of MD steps in units of the relaxation time of the system. In other words, this quantifies how long (in CPU time) it takes to equilibrate the system at a particular state point. This quantity should be minimal for the hybrid method to be the most efficient.

The numerical results are shown in Fig. 5. All the curves shown in this figure present a minimum for a given value of $\rho_{\text{swap}}$, and the location and value of this minimum both depend on $t_{\text{MD}}$. For a given temperature, the global minimum occurs for $t_{\text{MD}} = 0.1$. The location of the minimum varies over a narrow range of $\rho_{\text{swap}}$, slightly shifting to higher $\rho_{\text{swap}}$ at lower temperatures. This range is highlighted by the shaded region in Fig. 5, and corresponds to $\rho_{\text{swap}} = 20 - 100$ and thus to $n_{\text{swap}} = 2 - 10$. This represents the best trade-off between the speedup offered by increasing the number of swap moves, and the added CPU cost of performing these moves.

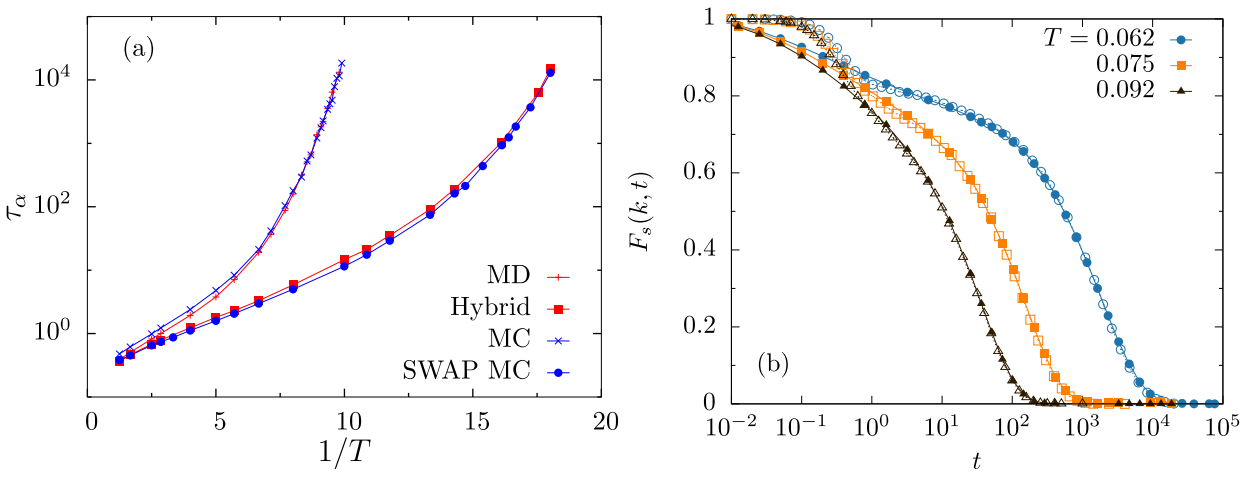


Figure 6: Comparison between the hybrid ($n_{\rm swap} = 10$, $t_{\rm MD} = 0.1$) and swap MC algorithms ($p = 0.2$). (a) Equilibrium relaxation times of the liquid $\tau_\alpha$ as a function of the inverse temperature in hybrid and swap MC methods, as well as in standard MD and MC simulations. Relaxation times for hybrid and MD methods are in MD units. For swap and conventional MC, we convert 1 MD step into $a = 3.2$ MC steps. (b) Self-intermediate scattering function $F_s(k,t)$ measured in swap MC (close symbols) and hybrid simulations (open symbols) at $T = 0.062, 0.075, 0.092$ using the same time units as in (a). These data demonstrate the full equivalence between swap MC and hybrid simulations, which offer the same equilibration speedup over conventional MC and MD methods.

## II.6 Comparison between the hybrid and swap MC methods

We now compare the efficiency and physical dynamics obtained in both the hybrid and the swap MC methods. Both methods have their own set of optimised parameters. For the hybrid method, $t_{\rm MD}$ and $n_{\rm swap}$ must be tuned, whereas for swap MC one must adjust the relative probability $p$ to attempt a particle-swap move instead of a translational move. Within the MC approach the typical size of the translational moves must also be adjusted [7]. In order to compare the two methods, we present results for simulations run with the optimal parameters in each case. The optimal efficiency of the swap MC algorithm is reached around $p = 0.2$ [3]. In this section, we consider hybrid simulations with $n_{\rm swap} = 10, t_{\rm MD} = 0.1$.

To compare MD and MC methods, we need to employ a dictionary between timescales, which correspond to very different processes in both approaches. To this end, we first measure the relaxation time of supercooled liquids measured in standard MC and MD simulations, i.e. with no swap moves at all. These are respectively expressed in numbers of MC steps and MD time. As found before in a different system [7], we observe that the structural relaxation time in both dynamics follows a similar temperature dependence, see Fig. 6a. Rescaling the MC curve on top of the MD curve, we find that $t = 1$ in MD units corresponds to $t \approx 320$ MC steps. Using a time discretisation $dt = 0.01$, this implies that 1 MD step corresponds roughly to $a = 3.2$ MC steps, a conversion similar to the one found for a Lennard-Jones model [7].

This conversion factor allows us to convert the simulation parameters used in optimal hybrid simulations, $n_{\rm swap} = 10, t_{\rm MD} = 0.1$, into an equivalent probability of performing swap moves: $p^{\rm equiv} = (n_{\rm swap}/a)/(n_{\rm swap}/a + t_{\rm MD}/dt) \approx 0.238$, which is indeed very close to the optimal $p \approx 0.2$ determined in Ref. [3].

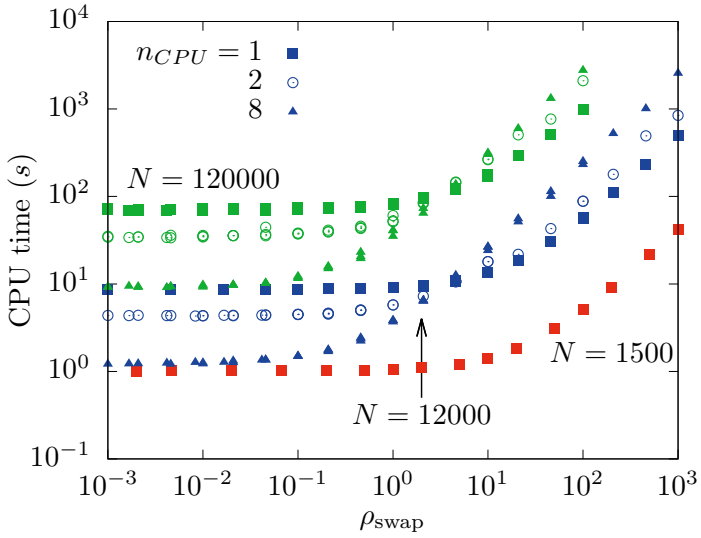


Figure 7: CPU time (in seconds) as a function of the swap density $\rho_{\text{swap}}$ for hybrid simulations of systems composed of $N = 1500$ (red), 12000 (blue), 120000 (green) particles, running on one (square), two (circle) or eight (triangle) processors. All the simulations run for a total time of 10 (in MD units), obtained by varying both $t_{\text{MD}}$ and $n_{\text{swap}}$.

In Fig. 6b, we show self-intermediate scattering functions $F_s(k,t)$ measured in hybrid and swap MC simulations at three temperatures below $T_{MCT}$. We have converted Monte Carlo steps in MD units using the above conversion factor. We see that the equivalence between MC and MD dynamics discussed before for conventional simulations [7, 8] now extends to swap algorithms. Apart from small differences at short times, the decay of time correlation functions using swap MC and the hybrid methods are very similar.

We obtain the relaxation time for these two swap dynamics and present the results in Fig. 6a along with the results for the ordinary dynamics. It is clear from this figure that the relaxation times of the swap MC and hybrid methods are again equivalent. We conclude that the hybrid method is able to speedup the equilibration of supercooled liquids with an efficiency comparable to the one of the original swap MC algorithm. Given the above conversion factor of order unity between MC and MD steps, we finally conclude that both methods give an equivalent equilibration speedup at an equivalent CPU cost.

We have shown that the hybrid method MC/MD is as powerful as the swap Monte Carlo algorithm when it comes to generating computer supercooled liquids at temperatures lower than the laboratory glass transition. The implementation in the LAMMPS package that we propose should in addition makes this algorithm a very powerful and versatile tool accessible to the glass community.

## II.7 Efficiency of the hybrid method in parallel

In essence, the hybrid method converts the translational moves of the original swap MC algorithm into MD integration steps, while keeping the much less frequent swap moves unchanged. An important difference between translational MC steps and MD steps is that the former need to be performed sequentially, which makes MC intrinsically difficult to parallelise. Existing solutions to

this problem only become advantageous for extremely large system sizes [29]. Converting MC steps to MD steps in the hybrid method thus makes it possible to easily parallelise the translational part of the swap algorithm. This is an important objective of the present work.

The LAMMPS package, a "Massively Parallel Simulator", provides a good starting point to implement the hybrid scheme on several CPUs. In LAMMPS, the molecular dynamics is already well optimized to run on several processors. It is possible to parallelize MD simulations because the algorithm is deterministic, so each processor can be in charge of a subset of the total system without having to perform time-costly inter-processor communications frequently. To work within the existing framework of LAMMPS, some inter-processor communication is necessary during the SMC blocks. We now determine how much of an effect this has on the efficiency of the hybrid method when run in parallel.

We simulate at temperature $T = 0.062$ systems composed of $N = 1500$, 12000, 120000 particles. The simulations have been run on one, two and eight processors. For a given system size and number of CPUs, we run simulations at different values of $n_{\mathrm{swap}}$ and $t_{\mathrm{MD}}$. All the simulations are run for the same total MD length. In Fig. 7 we report the CPU time in seconds for this large set of hybrid simulations.

We observe two regimes in this figure. At low density of swap moves, $\rho_{\mathrm{swap}} < 1$, the CPU time of the simulation is dominated by the MD blocks. In this regime, the CPU time depends essentially on the number of particles per processor. For example, $N = 12000$ particles on 8 CPUs takes about the same CPU time as $N = 1500$ particles on one processor. In this regime of modest swap density, the hybrid algorithm allows us to efficiently simulate very large systems by using more than one processor. In other words, we benefit from the optimal parallelisation offered by the MD algorithm, as implemented in LAMMPS. In this regime of system sizes, no such improvement would be gained for the original swap MC method.

At larger $\rho_{\mathrm{swap}}$, the CPU time becomes dominated by the SMC blocks, and it increases linearly with $\rho_{\mathrm{swap}}$, as found already in Fig. 4. The relative position of the curves corresponding to different numbers of CPUs is inverted compared to the low $\rho_{\mathrm{swap}}$ regime. In other words, running simulations on more processors does not decrease the CPU time of a simulation, bur rather increases it.

The difficulty in parallelising Monte Carlo algorithms is well-known and intrinsic to their stochastic sequential nature. In LAMMPS, information about particles in different parts of the box is stored on different processors. Adding SMC moves to LAMMPS therefore means that processors need to exchange information during most swap moves. These communications are time-consuming, and more frequent than during parallelised MD simulations. This means that swap moves in this implementation are less efficient in parallel than they are in serial. The CPU time in this regime of $\rho_{\mathrm{swap}}$ is completely dominated by these inter-processors communications, hence the increase in CPU time when running on more processors. More details are given in Appendix V.

There is a crossover between the two regimes discussed above, at which the CPU time is the same for a given system size, regardless the number of processors. This crossover occurs at a value around $\rho_{\mathrm{swap}} \sim 10$, which tends to decrease as system size increases.

In order to get the global efficiency of the hybrid method in parallel, we have reproduced the analysis done in Fig. 5. We multiply the physical relaxation time by the CPU time for simulations run in parallel. The optimal parameters for the hybrid method in serial are around $\rho_{\mathrm{swap}} = 20 - 100$ (see Fig. 5) but this corresponds to the swap-dominated regime. As a result, the global efficiency of the hybrid method does not increase with the number of processors. In other words, for a large system, it is advantageous to use a larger number of swap moves on a single CPU than a smaller number of swap moves on many CPUs, at least using our current implementation of the algorithm

on the LAMMPS package.

### II.8 Future directions

In order to improve the efficiency of the hybrid method, in particular in the parallel case, several future directions are possible because some improvements could be made to our current implementation of the scheme in the LAMMPS package. One possibility would be to use a separate serial architecture for performing swap moves, while running the MD blocks in parallel. The SMC block would be performed on one processor only, avoiding costly inter-processor communication. In this case the MD blocks would be more efficient in parallel than in serial and the efficiency of the SMC blocks would be the same, meaning that overall this implementation should be faster. However, this method requires copying data from the LAMMPS parallel architecture and building neighbor lists from scratch before every SWAP block. Then, at the end of SMC blocks the new particle sizes would be sent back to each processor and the neighbour lists and parallel architecture updated again. It may be that these extra calculations will have a strong effect on the computational efficiency.

Another way to improve the speedup and circumvent the issues encountered while dealing with LAMMPS architecture would be to write a handmade molecular dynamics code that could be more versatile, and optimized for hybrid simulations. The MD part of the code in this case would be designed to run in parallel and integrate efficiently with a completely serial SMC routine.

## III Continuous time swap MD algorithm

### III.1 Equations of motion

In this section, we introduce an algorithm that includes the physics of swap MC moves in a fully continuous time MD framework. The swap MC algorithm used in the context of supercooled liquids [5, 3] uses swap moves where the diameter of pairs of particles is exchanged, which leaves the particle size distribution fixed. In older versions of the swap MC algorithm [4], particle diameters were exchanged with an external bath in a semi-grand canonical ensemble. This ensemble is conveniently used to describe theoretically [17] and numerically [30] mixtures with a continuous size polydispersity. In this approach, the particle diameters are considered as fluctuating variables along with the particle positions. The diameters are constrained by an external potential (a chemical potential), and the particle size distribution becomes the result of the equilibrium sampling. The approach used in this section is a continuous time version of this idea. A zero-temperature version of the algorithm is discussed in Refs. [18, 31], which study the nature of energy minima generated by the Hamiltonian shown below in Eq. (4).

To study instead the finite temperature version of this approach, we introduce a generalised Hamiltonian where the diameters of particles are considered as dynamical variables, alongside their positions. For a system of $N$ particles, given the $3N$ particle coordinates $\mathbf{r}^N \equiv \{\mathbf{r}_1, \mathbf{r}_2, \ldots, \mathbf{r}_N\}$, their $3N$ conjugate momenta $\mathbf{p}_\mathbf{r}^N \equiv \{\mathbf{p}_{1,\mathbf{r}}, \mathbf{p}_{2,\mathbf{r}}, \ldots, \mathbf{p}_{N,\mathbf{r}}\}$, the $N$ particle diameters $\sigma^N \equiv \{\sigma_1, \sigma_2, \ldots, \sigma_N\}$ and their $N$ conjugate momenta $p_\sigma^N \equiv \{p_{1,\sigma}, p_{2,\sigma} \ldots, p_{N,\sigma}\}$, we define the Hamiltonian

$$\begin{aligned} H(\mathbf{r}^N, {\mathbf{p}_\mathbf{r}}^N, \sigma^N, p_\sigma^N) &= \sum_i \frac{\mathbf{p}_{i,r}^2}{2m} + U(\mathbf{r}^N, \sigma^N) \\ &\quad + \sum_i \frac{p_{i,\sigma}^2}{2M} + V(\sigma^N), \end{aligned} \tag{4}$$

where $m$ is the mass conjugate to position momenta $p_r$, and $M$ is the mass conjugate to diameter momenta $p_\sigma$. The potential energy due to inter-particle interactions is given by $U(\mathbf{r}^N, \sigma^N)$, which can be an ordinary pair potential. Each particle is additionally subject to a potential $v(\sigma_i)$ that constrains its diameter $\sigma_i$, so that $V(\sigma^N) = \sum_i v(\sigma_i)$ in Eq. (4). Examples of this potential will be given below.

The equations of motion follow from Hamilton's equations, and read

$$\frac{\mathrm{d}\mathbf{p}_{i,\mathbf{r}}}{\mathrm{d}t} = -\frac{\partial H}{\partial \mathbf{r}_i} = -\frac{\partial U(\mathbf{r}^N, \sigma^N)}{\partial \mathbf{r}_i} \quad , \tag{5}$$

$$\frac{\mathrm{d}p_{i,\sigma}}{\mathrm{d}t} = -\frac{\partial H}{\partial \sigma_i} = -\frac{\partial [U(\mathbf{r}^N, \sigma^N) + V(\sigma^N)]}{\partial \sigma_i} \quad , \tag{6}$$

$$\frac{\mathrm{d}\mathbf{r}_i}{\mathrm{d}t} = \frac{\partial H}{\partial \mathbf{p}_{i,r}} = \frac{\mathbf{p}_{i,r}}{m} \quad , \tag{7}$$

$$\frac{\mathrm{d}\sigma_i}{\mathrm{d}t} = \frac{\partial H}{\partial p_{i,\sigma}} = \frac{p_{i,\sigma}}{M} \quad . \tag{8}$$

Similarly to standard molecular dynamics, we discretise in time these equations of motion and obtain an enlarged version of the standard velocity-Verlet algorithm. We solve the equations of motion using this algorithm with a time discretization $dt = 0.001$. As a result, we obtain trajectories for the particles coordinates and diameter. In the following, we simulate systems of $N = 500$ particles at number density $N/L^3 = 1.0$ in canonical ensemble $NVT$ in cubic box with periodic boundary conditions.

We consider two temperatures $T_r$ and $T_\sigma$ related to particle translational momenta and diameter momenta, respectively. They are defined as

$$T_r = \frac{1}{3N} \sum_i \frac{\mathbf{p}_{i,r}^2}{2m_i} \quad , \tag{9}$$

$$T_\sigma = \frac{1}{N} \sum_i \frac{p_{i,\sigma}^2}{2M_i} \quad . \tag{10}$$

The temperatures are kept constant and equal, $T_r = T_\sigma$, during the simulations using a Berendsen thermostat [32] with coupling time constant $\tau = 5.0$. In the following, we refer to the temperature simply as $T$. The reduced units are defined exactly as in Sec. II.1.

### III.2 Microscopic model

A glass-forming model is typically defined by the interactions between the particles and their size dispersity. We model the interaction between two particles $i$ and $j$ by the pair potential defined in Eq. (1). In the continuous method, we cannot use the same nonadditive cross diameter rule as presented in Sec. II.1 because its derivative is not continuous. As a first step, we have simulated an additive rule for the diameters but we could easily generalise the nonadditive rule replacing the absolute value $|\sigma_i - \sigma_j|$ by a smooth function with equivalent properties, such as for instance $[1 - \exp(-(\sigma_i - \sigma_j)^2)]$.

We focus on continuously polydisperse systems characterized by their diameter distribution, $P(\sigma)$. Contrary to the hybrid and swap MC methods in which particles exchange their diameters leaving the global distribution $P(\sigma)$ unaffected, the present method does not directly impose the

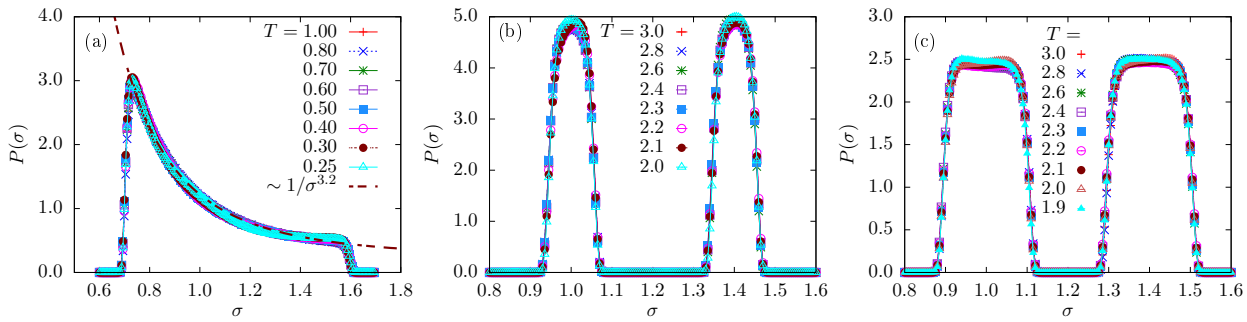


Figure 8: Probability distribution of diameters $P(\sigma)$ measured in equilibrium at different temperatures $T$ for: (a) the continuous polydisperse system with $P(\sigma) \approx 1/\sigma^{3.2}$; binary systems with uniform distribution of width $\Delta\sigma = 0.1$ (b) and $\Delta\sigma = 0.2$ (c).

diameter distribution $P(\sigma)$. Instead, one must impose an external potential for the diameters, $v(\sigma)$, to constrain the fluctuations of the diameters $\sigma^N$ and the particle size distribution is obtained as the result of the equilibrium simulations. This is a major difficulty if one wants to perform simulations at a series of state points, since $P(\sigma)$ would evolve if $v(\sigma)$ is left unchanged. Therefore, this approach needs an additional iteration step where the potential $v(\sigma)$ is adjusted at each state point in order to keep $P(\sigma)$ constant. This additional step becomes time consuming at low temperatures, where the equilibration of the system is slow and controls in particular the convergence of the distribution $P(\sigma)$ itself.

We simulate two classes of systems which were shown to be structurally stable against crystallization at low temperature using swap MC. The first system is analogous to the continuously polydisperse one presented in Sec. II.1, and is characterized by $P(\sigma) \sim 1/\sigma^{3.2}$ in a finite range $[\sigma_m, \sigma_M]$. In order to obtain this diameter distribution at equilibrium, we design the diameter potential $v(\sigma)$ as follows. The hard boundaries of the distribution at $\sigma_m$ and $\sigma_M$ are imposed by two very steep exponential functions. To generate a power law distribution $P(\sigma) \sim 1/\sigma^{3.2}$ in between, we employ a smooth power law form. The diameter potential used to enforce this distribution thus reads

$$\begin{aligned} v(\sigma) &= \exp[A(-\lambda_1\sigma + \sigma_m)] + \exp[A(\lambda_2\sigma - \sigma_M)] - D\sigma^n \\ &= v_\sigma(A, \lambda_1, \lambda_2, D, n) \quad , \end{aligned} \tag{11}$$

where the parameters $(A, \lambda_1, \lambda_2, D, n)$ need to be tuned at each temperature in order to obtain the desired size distribution in equilibrium. More quantitative details on this procedure are given in Appendix VI, where all simulated parameters are tabulated. We show in Fig. 8a the measured probability distribution function at equilibrium across a range of temperatures. Therefore, we have successfully designed a diameter potential that imposes a constant diameter distribution that resembles the one studied in Sec. II with the hybrid method.

The second type of glass-forming model we study is a continuously polydisperse version of a discrete binary mixture, using a 50:50 mixture of particles with a typical size ratio $\sigma_B/\sigma_A = 1.4$. In this model, the original delta peaks at $\sigma_A$ and $\sigma_B$ in the distribution $P(\sigma)$ are broadened uniformly over a typical width $\Delta\sigma$. We have considered two such binary systems of width $\Delta\sigma = 0.1$ and $\Delta\sigma = 0.2$. These diameter distributions are again designed by using the same functional form $v_\sigma$ as in Eq. (11) but using two distinct types of particles. This approach means we must now adjust 10 independent parameters at each simulated temperature. We show in Fig. 8b-c the measured

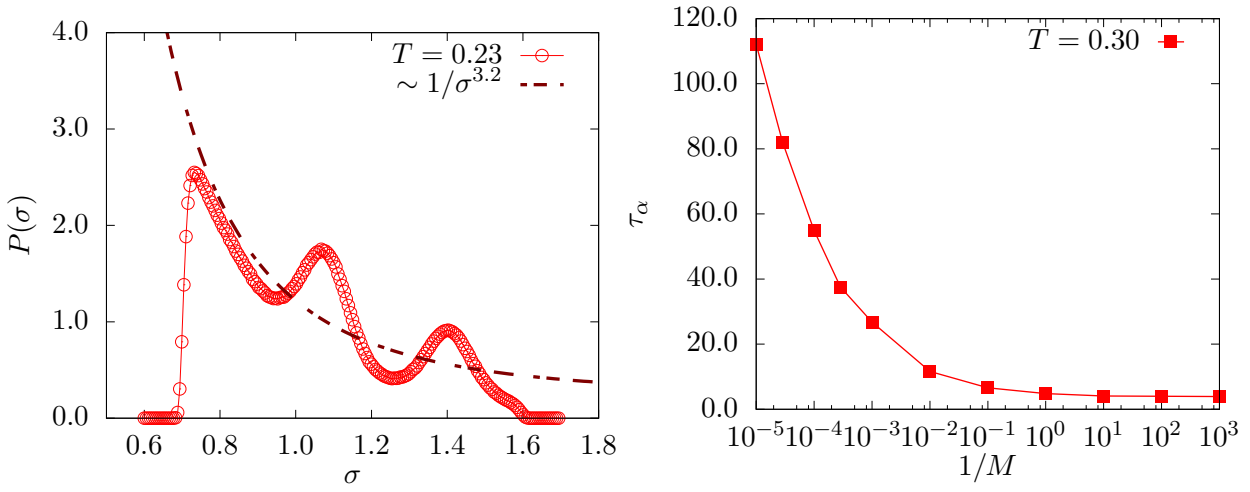


Figure 9: (a) Probability distribution $P(\sigma)$ of diameters $\sigma$, measured for continuous polydisperse system at $T = 0.23$, where phase separation and crystallisation is observed. The energy cost in diameter space due to the distortion of the particle size distribution is more than compensated by an ordering in position space. (b) Dependence of the equilibrium relaxation time $\tau_\alpha$ with inverse diameter mass $1/M$ for continuous polydisperse liquids $P(\sigma) \sim 1/\sigma^{3.2}$ at temperature $T = 0.3$.

probability distribution functions measured at equilibrium across a broad range of temperatures for the two systems considered. The quantitative details about the parameters used in these simulations are also tabulated in Appendix VI.

We demonstrate in Fig. 8 that we are successful in designing diameter potentials and sets of parameters which produce a desired diameter distribution $P(\sigma)$ across different temperatures. This method, however, is relatively cumbersome. At each temperature, one has to make many trials in order to find the parameters for the diameter potential that yields the desired probability distribution at equilibrium. As temperature decreases, relaxation times increase and the trial and error procedure becomes increasingly costly in terms of CPU time. In our effort to design new algorithms and methods to simulate supercooled liquids at ever lower temperature, this method therefore does not necessarily appear as the most efficient one, as it introduces the need to perform a large number of runs to prepare the system before making any measurement. Of course, the temperature evolution of the potential $v(\sigma)$ is very smooth, and thus training at high temperatures and some educated guesses help converge that procedure faster.

### III.3 Structural instability and crystallization

Crystallisation, fractionation and ordering are problems that need to be faced when dealing with supercooled liquids. To push the swap MC method to its maximal efficiency, new models of supercooled liquids were developed that better resist ordering and are therefore better glass-formers. Recent investigations have demonstrated that swap MC is able to crystallise polydisperse models of hard spheres relatively easily [28, 33, 34], whereas the ordinary dynamics would only allow one to probe the metastable fluid.

We expect that the hybrid method and swap MC behave similarly with respect to crystallisation, but we find that the fully continuous version shows qualitatively distinct behaviour, as we now explain. In Fig. 8a, we show that a continuous polydispersity can be easily maintained down to

$T = 0.25$ by a proper choice of the potential $v(\sigma)$. If we use this insight to attempt thermalising the system at $T < 0.25$ we observe that the system becomes unstable. An example is shown in Fig. 9(b) which shows the measured $P(\sigma)$ for $T = 0.23$, compared to the functional form $\sigma^{-3.2}$ observed at higher temperatures. It is clear that the shape of the particle size distribution is now completely different since it develops peaks near $\sigma \sim 1.0$ and $\sigma \sim 1.4$. Simultaneously, direct visualisation reveals that the system has partially crystallised and phase separated between large and small particles.

The physical interpretation is that the system is distorting the particle size distribution (thus paying an energetic cost in diameter space due to the potential $v(\sigma)$) in order to gain free energy by ordering the system in position space. Such instability is typically not observed using hybrid and swap MC algorithm because the particle size distribution is by construction not allowed to vary over the course of a simulation. Of course, in the large system size limit, the phase separation and crystallisation reported in Fig. 9(b) should also occur when swap MC is used, because concentration fluctuations would occur. These fluctuations are presumably too slow to lead to crystallisation in hybrid and swap MC approaches.

We conclude, therefore, that the type of semi-grand canonical simulation that we perform when employing the continuous time swap algorithm may unfortunately accelerate the crystallisation of the system. To cure this problem, new models should be developed that are even more robust against ordering and could then be simulated using the continuous time swap algorithm. For instance, one could attempt to use a finite nonadditivity to the pair interaction as a first step in this direction.

### III.4 Choice of the diameter mass

In standard molecular dynamics the diameter of the particles is constant. This corresponds to the limit of an infinite diameter mass $M$ in the continuous method described by Eq. (8). As the diameter mass decreases from $M = \infty$, the diameters become dynamical variables and start to vary and influence the structural relaxation.

We look for the diameter mass that optimizes the continuous method. To do so, we compute the relaxation time $\tau_\alpha$ of a liquid as a function of the diameter mass $M$. The relaxation time is computed as in Sec. II.4, taking Eq. (3) at wavevectors of magnitude $k = 6.7$. We report in Fig. 9(b) the measured relaxation time $\tau_\alpha$ as a function of inverse diameter mass $1/M$ in the continuously polydisperse system $P(\sigma) \sim 1/\sigma^{3.2}$, at a fixed temperature $T = 0.30$.

The qualitative behavior of $\tau_\alpha$ in Fig. 9(b) is qualitatively similar to the one in Fig. 3. The parameter $1/M$ plays a role similar to the swap density $\rho_{\text{swap}}$ or the probability $p$ of particle-swap moves in the hybrid and swap MC algorithms, respectively. When they increase, the typical timescale for the diameter dynamics decreases, which speeds up the physical relaxation of liquids. We observe a clear decrease in the structural relaxation time as the mass $M$ of diameters decreases, starting from a very large value $M = 10^5$. Around $M = 1$, the relaxation time reaches a plateau, and decreasing further the diameter mass $M$ does not speed up the structural relaxation of the liquid.

While any choice $M < 1$ minimizes the time needed to relax the liquid, a very small diameter mass is not suitable. Indeed, when $M$ is too small, large variations of the diameters occur on very short time scales, which requires a very small integration time step $dt$. This effectively increases the CPU time of the simulations, which is undesired. In the following, we choose $M = 1$ as the optimal compromise between physical speedup and computational efficiency.

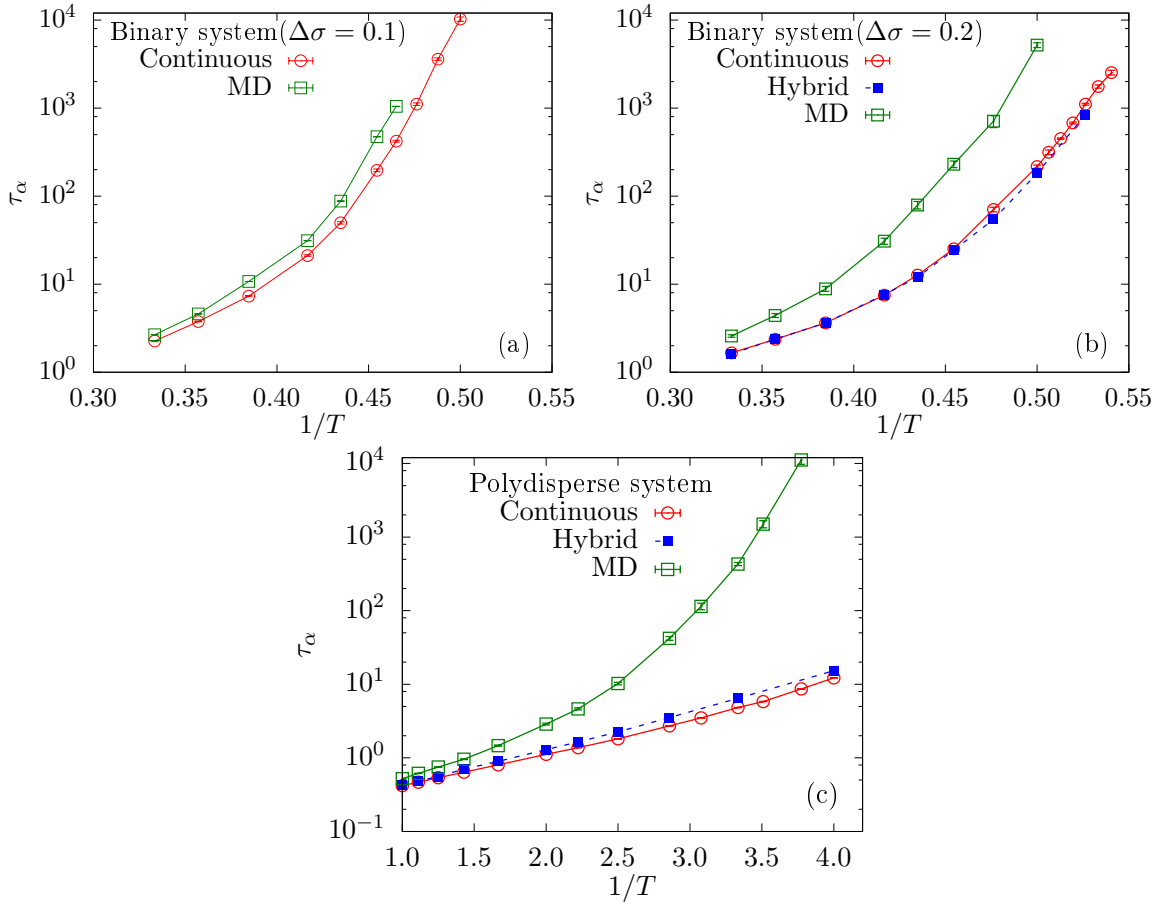


Figure 10: Relaxation time as a function of inverse temperature measured in: (a) binary system with $\Delta\sigma = 0.1$, (b) $\Delta\sigma = 0.2$, and (c) continuous polydisperse system. Relaxation times have been computed using three different methods continuous time swap method, hybrid method and standard MD.

### III.5 Physical Efficiency

We now compare the relaxation dynamics of the three glass-forming models presented in Sec. III.2 when simulated both with the continuous swap method and standard MD simulations. We first have to determine iteratively the correct parameters for the diameter potential at each temperature, as described above. Then, we run simulations with the continuous method at a temperature $T$ to obtain equilibrium configurations. We also measure the equilibrium relaxation time of the system using the continuous time swap algorithm. Finally, the equilibrated configurations are taken as initial conditions for standard MD simulations, during which the relaxation time is measured. By construction, then, the MD simulations run the dynamics for the same particle size distribution as the continuous time swap algorithm. These configurations will also serve as starting points for hybrid MD/MC simulations, to be discussed below in Sec. III.6.

The results for the equilibrium relaxation time $\tau_\alpha$ of the three models and three numerical algorithms are reported in Fig. 10. The binary systems with $\Delta\sigma = 0.1$ and $\Delta\sigma = 0.2$ can be simulated down to quite low temperature without crystallizing. In both cases, the efficiency of the continuous

time swap method over MD simulations is temperature dependent, with an efficiency increasing as temperature decreases. The speedup in thermalization offered by the continuous method depends on the width $\Delta\sigma$ accessible to diameters. Larger variations in the particles' diameters are expected to ease even more the structural relaxation of the liquid. When $\Delta\sigma = 0.1$, diameters are more constrained than when $\Delta\sigma = 0.2$. The dynamical gain observed in Fig. 10(a) is about one order of magnitude in relaxation time for $\Delta\sigma = 0.1$, while for $\Delta\sigma = 0.2$, extrapolation of the data presented in Fig. 10b suggest that the continuous time swap method can more easily achieve thermalization in a region inaccessible to MD simulations, with a speedup estimated at about 2 orders of magnitude. Clearly these two binary systems do not yield as large a speedup as fully polydisperse models [3], and as a result are less prone to crystallisation.

In the case of the continuous polydisperse model with diameter distribution $P(\sigma) \sim 1/\sigma^{3.2}$, shown in Fig. 10c, the dynamical gain with the continuous method is even greater, similarly to what was measured with the swap MC algorithm[3]. While the dynamical gain is very interesting with this model, the continuous time method cannot simulate supercooled liquids at temperatures lower than $T < 0.25$, the last point studied, because of structural instability discussed in Sec. III.3, and we can thus not benefit from the efficiency of the swap algorithm as much as when the hybrid method is used.

### III.6 Comparison with the hybrid method

In this section, we compare the physical efficiency of the continuous time swap algorithm with the hybrid method. To that effect, we use configurations equilibrated with the continuous method as initial condition for hybrid simulations using parameters ($n_{\text{swap}} = 10$, $t_{\text{MD}} = 0.1$), and measure the relaxation time of the liquid. Results for the binary system with $\Delta\sigma = 0.2$ and the continuous polydisperse system with $P(\sigma) \sim 1/\sigma^{3.2}$ are presented in Fig. 10b-c. We observe that both methods give physical relaxation times that are extremely close to one another, and have a very similar temperature dependence. Note that we did not tune the parameters of each method in order to obtain the exact same relaxation times, but rather used each technique with its own set of optimal parameters. The agreement between the two methods suggests that the continuous time swap method, once optimised, captures the same physics as the other swap algorithms (hybrid MC/MD and pure MC). Overall, we conclude that all three algorithms have the same efficiency in terms of speedup of the structural relaxation.

Finally, we also plot the self-intermediate scattering functions measured at different temperatures in hybrid and continuous time methods in Fig. 11. At each temperature, the curves corresponding to the two methods have the same time dependence. Both the relaxation dynamics at long times and microscopic dynamics are very similar. This implies that the two methods are equivalent as far as the relaxation of the liquid is concerned. The different nature of the microscopic rules for the dynamics do not matter. Performing discrete particle-swap moves or continuously modifying the diameters of particles has no influence on the physical relaxation of supercooled liquids at long times. What matters, eventually, is the strong coupling between diameter and position degrees of freedom that relax in a strongly correlated manner [3], the diameter fluctuations allowing the system to efficiently relax the positional degrees of freedom even in a temperature regime where the physical dynamics is extremely slow.

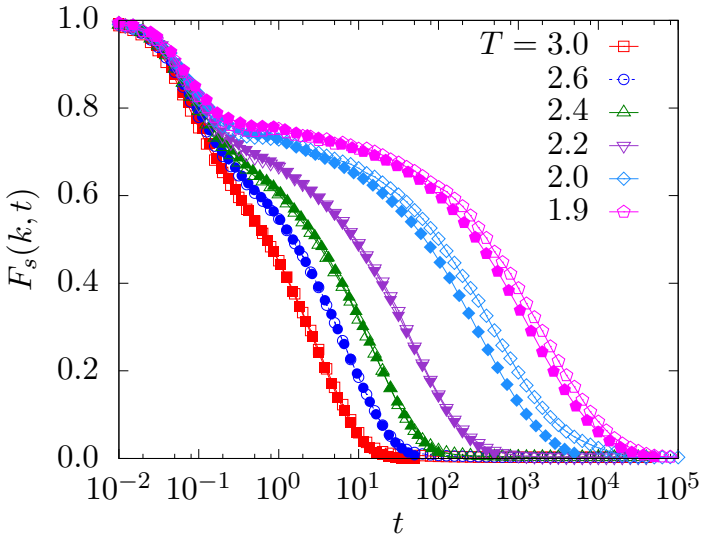


Figure 11: Self-intermediate scattering function $F_s(k,t)$ calculated for the binary system with $\Delta\sigma = 0.2$ using the continuous time (open symbols) swap and hybrid (filled symbols) algorithms at different temperatures.

### III.7 Computational performance

The continuous time swap algorithm runs similarly to conventional MD simulations, with the difference that particles have one more degree of freedom (the diameter) in addition to the positions. This implies that running this algorithm is essentially as costly in terms of CPU time as running a conventional MD simulations. But the speedup offered in terms of structural relaxation time is the same as with swap MC method. This method thus offers a valuable alternative to swap MC, especially for users that are not familiar to Monte Carlo simulations.

Attempts to parallelize the hybrid method did not bring significant improvements in terms of CPU time. This was due to the difficulty to parallelize efficiently the Monte Carlo blocks present in the hybrid method. The continuous time swap method offers the same advantages as standard molecular dynamics simulations in terms of parallelisation. Since the dynamics is continuous and deterministic, one can in principle implement this method to run it efficiently on several processors. The CPU time needed to run simulations of the same MD length is expected to scale with the number of particles per processor, as discussed in Sec. II.7.

## IV Discussion and perspectives

In this work, we provided two distinct generalisations of the swap Monte Carlo algorithm that has recently proved extremely successful in producing equilibrium configurations of supercooled liquids at very low temperatures. Both algorithms combine the idea of particle swaps with conventional Molecular Dynamics techniques. In the first version, we simply alternate periods of conventional MD with periods of swap MC moves, while in the second we solve Hamilton's equations of motion for both positions and diameters simultaneously, in a fully continuous time MD scheme.

After an adequate optimisation of all simulation parameters involved in each three swap-like algorithms, we find that the three algorithms provide a very similar (and quite impressive in some

cases) speedup of equilibration, which suggests that the same physics is at play in the three cases. Namely, the addition of diameter fluctuations strongly couples to positional degrees of freedom to relax the structure of the supercooled liquid. The equivalence between the three algorithms even extends to time correlation functions.

Our general conclusion is that all three algorithms can be equivalently used to produce low-temperature equilibrium configurations for model glass-formers, and which algorithm should be preferred depends is firstly a matter of personal convenience. The hybrid and swap MC are very close to one another in spirit and performances, and the implementation into the LAMMPS software of the hybrid method makes it user-friendly in case a different model needs to be studied. Regarding the continuous time swap algorithm, it is promising since it combines the efficiency of the swap MC to the simplicity of the MD technique, with great potential if large systems need to be studied. However, the iterative determination of the diameter potential makes it more cumbersome to use, and one must find ways to prevent the ordering that the semi-grand canonical ensemble seems to facilitate. In future work, it would therefore be interesting to develop more robust glass-forming models that can resist the crystallisation and phase separation observed when the particle size distribution is not conserved by the dynamics.

## Bibliography


[1] Ludovic Berthier and Giulio Biroli. *Rev. Mod. Phys.*, 83:587–645, Jun 2011.

[2] Ludovic Berthier, Daniele Coslovich, Andrea Ninarello, and Misaki Ozawa. `arXiv:1511.06182`, 2015.

[3] Andrea Ninarello, Ludovic Berthier, and Daniele Coslovich. *Phys. Rev. X*, 7:021039, 2017.

[4] W. G. T. Kranendonk and D. Frenkel. *Molecular Physics*, 72:679, 1991.

[5] T.S. Grigera and G. Parisi. *Phys. Rev. E*, 63(4):45102, 2001.

[6] M. P. Allen and D. J. Tildesley. *Computer Simulation of Liquids*. Clarendon Press, New York, NY, USA, 1989. ISBN 0-19-855645-4.

[7] L Berthier and W Kob. *Journal of Physics: Condensed Matter*, 19(20):205130, 2007.

[8] Ludovic Berthier. *Phys. Rev. E*, 76:011507, Jul 2007.

[9] L. Berthier, G. Biroli, J.P. Bouchaud, W. Kob, K. Miyazaki, and DR Reichman. *J. Chem. Phys.*, 126:184503, 2007.

[10] L. Berthier, G. Biroli, J.P. Bouchaud, W. Kob, K. Miyazaki, and DR Reichman. *J. Chem. Phys.*, 126:184504, 2007.

[11] L. Berthier, G. Biroli, J-P Bouchaud, L. Cipelletti, and W. van Saarloos, editors. *Dynamical Heterogeneities and Glasses*. Oxford University Press, 2011.

[12] Ludovic Berthier, Patrick Charbonneau, Daniele Coslovich, Andrea Ninarello, Misaki Ozawa, and Sho Yaida. *Proceedings of the National Academy of Sciences*, 2017. ISSN 0027-8424.

[13] L. Berthier, P. Charbonneau, A. Ninarello, M. Ozawa, and S. Yaida. *arXiv:1805.09035*, 2018.

[14] Christopher J. Fullerton and Ludovic Berthier. *EPL (Europhysics Letters)*, 119(3):36003, 2017.

[15] Misaki Ozawa, Ludovic Berthier, Giulio Biroli, Alberto Rosso, and Gilles Tarjus. *Proceedings of the National Academy of Sciences*, 115(26):6656–6661, 2018.

[16] S. Plimpton. *J. Comput. Phys.*, 117:1, 1995.

[17] J. G. Briano and E. D. Glandt. *J. Chem. Phys.*, 80:3336, 1984.

[18] C. Brito, E. Lerner, and M. Wyart. *Phys. Rev. X*, 8:031050, 2018.

[19] William G. Hoover. *Phys. Rev. A*, 31:1695–1697, Mar 1985.

[20] Mark E. Tuckerman, Yi Liu, Giovanni Ciccotti, and Glenn J. Martyna. *J. Chem. Phys.*, 115 (4):1678–1702, 2001.

[21] Glenn J. Martyna, Michael L. Klein, and Mark Tuckerman. *J. Chem. Phys.*, 97(4):2635–2643, 1992.

[22] Glenn J. Martyna, Mark E. Tuckerman, Douglas J. Tobias, and Michael L. Klein. *Molecular Physics*, 87(5):1117–1157, 1996.

[23] Mark E Tuckerman, José Alejandre, Roberto López-Rendón, Andrea L Jochim, and Glenn J Martyna. *Journal of Physics A: Mathematical and General*, 39(19):5629, 2006.

[24] Camille Scalliet, Ludovic Berthier, and Francesco Zamponi. In preparation (2019).

[25] Ludovic Berthier, Patrick Charbonneau, Elijah Flenner, and Christopher J. Fullerton. `arXiv:1903.09108`, 2019.

[26] Camille Scalliet, Ludovic Berthier, and Francesco Zamponi. *Phys. Rev. Lett.*, 119:205501, Nov 2017.

[27] Wolfgang Götze. *Journal of Physics: Condensed Matter*, 11(10A):A1–A45, 1999.

[28] Ludovic Berthier, Giulio Biroli, Jean-Philippe Bouchaud, and Gilles Tarjus. Can the glass transition be explained without a growing static length scale? `arXiv:1805.12378`, 2018.

[29] Joshua A. Anderson, Eric Jankowski, Thomas L. Grubb, Michael Engel, and Sharon C. Glotzer. *Journal of Computational Physics*, 254:27 – 38, 2013.

[30] D. A. Kofke and E. D. Glandt. *J. Chem. Phys.*, 87:4881, 2018.

[31] G. Kapteijns, W. Ji, C. Brito, M. Wyart, and E. Lerner. *arXiv:1808.00018*, 2018.

[32] H. J. C. Berendsen, J. P. M. Postma, W. F. van Gunsteren, A. DiNola, and J. R. Haak. *J. Chem. Phys.*, 81(8):3684–3690, 1984.

[33] Beth A. Lindquist, Ryan B. Jadrich, and Thomas M. Truskett. *The Journal of Chemical Physics*, 148(19):191101, 2018.

[34] P. K. Bommineni, N. R. Varela-Rosales, M. Klement, and M. Engel. *arXiv:1811.00061*, 2018.

# V Considerations for implementing the hybrid MD/MC swap algorithm in LAMMPS

In this section of the appendix we give some details about how the hybrid molecular dynamics/particle-swap Monte Carlo method is implemented in the LAMMPS package. We provide an outline of how several problems were overcome.

## V.1 Handling continuously polydisperse systems in LAMMPS

In LAMMPS, each particle has a type and all particles of a given type share the same values for certain properties. One of these shared properties is their size $\sigma$. This means that to simulate a system of $N$ particles with continuous polydispersity, $N$ different types of particle are needed. Defining $N$ types of particles in LAMMPS would be cumbersome, especially if we wish to simulate large numbers of particles.

To overcome this problem, we decided to define only one particle type, and to store the diameters of particles in a type-independent property. We used the existing `charge` property to store the diameter of each particle. We also created a modified version of `pair_style lj` called `pair_style lj_poly` that uses the `charge` in place of particle size when calculating the pair interaction energy.

## V.2 Avoiding neigbour list rebuilds after every swap move

To keep the neighbour list of particle $i$ as short as possible, LAMMPS takes the size of particle $i$ into account when generating its neighbour list. This means that if the size of $i$ should change (for example during a swap move), the neighbour list is incorrect and must be recalculated. Given that we typically attempt $N$ swap moves after every MD step, recalculating neighbour lists this frequently would overwhelm any computational time gained by using the swap algorithm.

To reduce this computational burden, we calculate the neighbour list for particle $i$ as if it had the largest size in the particle size distribution. This means that after a successful swap move, the neighbour list will still be valid. This modification comes at the price of longer neighbour lists, but the increase in the time to calculate pair interaction energies and to update a particle's neighbour list is offset by not having to recalculate the neighbour list after every swap move. We note that this means the simulation time for systems of particles with pair interactions that have short cutoffs will be significantly faster.

## V.3 Full and half neighbour lists

The neighbour lists required by Molecular Dynamics and Monte Carlo simulations are different. Due to the nature of the energy and force calculations being carried out at each step, Molecular Dynamics simulations require that a pair of particles appears once in the neighbour lists: that is if $j$ is in the neighbour list of $i$ then $i$ is not in the neighbour list of $j$. In a Monte Carlo simulation, particle $i$ must know about all the particles it could interact with: $i$ would appear in the neighbour list of $j$ and $j$ in that of $i$. In practice this means that the neighbour lists required for Monte Carlo simulations are twice the size of those for Molecular Dynamics. In LAMMPS, these are referred to as `full` and `half` neighbour lists. Since the energy and force calculations take up the bulk of computational time, we wish to avoid maintaining only `full` neighbour lists and thus doubling the length of the force calculations performed during each Molecular Dynamics move. The alternative

solution of maintaining only `half` neighbour lists and performing a sum over all particles for the energy calculations during Monte Carlo moves is even less desirable.

Thankfully LAMMPS has a method for updating `full` and `half` neighbour lists together at the same time - the computational overhead to do this is considerably less than that required for the two solutions described above. The class `pair_lj_poly` must be written to ensure that the correct neighbour list is used in each case: `full` for interaction energies and `half` for force calculations.

### V.4 Triggering blocks of swap moves

Due to some technical details about how blocks of swap moves are triggered during a LAMMPS simulation we had to modify the `run` function in the LAMMPS `verlet` class. The swap moves are triggered within a `modify->pre_exchange()` command and the position of this command in the `run` function means that neighbour lists are unnecessarily calculated every time a block of swap moves is attempted. We moved the position of the `modify->pre_exchange()` command within the `run` function to prevent this.

### V.5 The hybrid method and parallelisation

The final issue, which remains only partially resolved, arises due to integrating a serial simulation method (swap Monte Carlo) into a parallelized one (Molecular Dynamics, as performed by LAMMPS). This issue is caused by the particular way that LAMMPS implements parallel computation and could be avoided if custom Molecular Dynamics code was used. If this was done, the theoretical maximum computational efficiency for the parallelised hybrid method would be achieved.

LAMMPS spatially parallelises the system, meaning that a processor has responsibility for a subbox of the simulation box. A processor must keep track of particles on neighbouring processors that particles it has responsibility for may interact with. This means that during Molecular Dynamics bouts of inter-processor communication must be carried out with roughly the same frequency as the neighbour lists are rebuilt. Due to the non-local nature of the changes that take place during swap moves and the way that LAMMPS keeps track of particle identities, this inter-processor communication must be carried out much more frequently when attempting swap moves. We have tried to minimise it as much as possible, but it is impossible to eliminate without more serious modifications to LAMMPS. Unfortunately, these communications are sufficiently costly that our implementation of the hybrid method does not scale as well as it could when run on multiple processors.

## VI Designing diameter potentials in the continuous time swap algorithm

### VI.1 Continuously polydisperse model

In this method, in the absence of a diameter potential, *i.e.* when $v_\sigma = 0$, the particles sizes will all shrink to zero to minimize the potential energy. Therefore we must perform our simulations for a finite diameter potential to constrain the diameter sizes for a desired range and distribution. We employ Eq. (11) as defined in Sec. III.2 to generate continuously polydisperse systems with a size distribution $P(\sigma) \sim 1/\sigma^{3.2}$. In this equation, two exponential functions create the steep walls (the steepness is determined by the parameter $A$, here $A = 100.0$) at minimum $\sigma_m$ and maximum

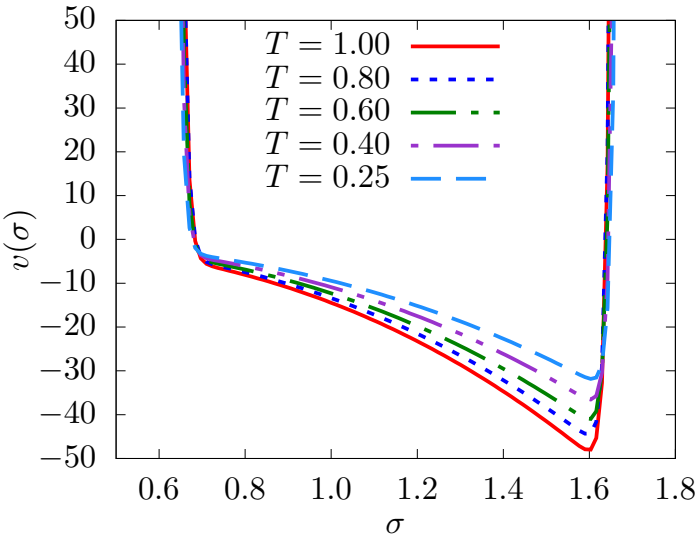


Figure 12: Diameter potential at different $T$ for suitable set of parameters to maintain the desirable distribution of particles with average diameters $\sigma \approx 1.0$ and polydispersity of $\approx 24\%$.

diameters $\sigma_M$. To generate the desired particle size distribution between $[\sigma_m, \sigma_M]$, we employ a power law form with proper combination of parameters $n$ and $D$. The power $n$ decides the nature of the distribution, while the prefactor $D$ set an energy scale in diameter space (and hence is $T$-dependent).

We start the process of tuning the parameters of diameter potential at some initial temperature. We first obtain $n = 2.6$ and $D = 14.46$ at $T = 1.0$. We know that for a given size distribution, the pair potential energy increases as $T$ increases. So if we fix these potential parameters $n$ and $D$ and investigate a higher $T$, the kinetic energy will not suffice to sample enough of the large particles and we need to increase the parameter $D$ to reobtain the correct distribution. Similarly we decrease the parameter $D$ as we decrease $T$. Also, we notice that after fixing the parameters $A$, $n$ and $D$, then while going from high to low $T$, the particle size distribution becomes systematically narrower and therefore we need to choose two more parameters, $\lambda_1$ and $\lambda_2$, to maintain the correct width of the size distribution.

Here we tune our potential parameters such that the average size $\overline{\sigma} \approx 1.0$ and the average polydispersity is $\approx 24\%$. The resulting potential is continuous in its first and second derivative and is thus convenient for MD simulations. Representative potential $v(\sigma)$ are shown in Fig. 12 and the corresponding values of the parameters at different temperatures are reported in Table 1.

## VI.2 Binary polydisperse model

The second class of system that we consider is an equimolar mixture of particles having average size ratio 1.4 (*i.e.*, $\sigma_A/\sigma_B = 1.4$) with uniform distributions centered around their respective average diameters $\sigma_A$ and $\sigma_B$, of width $\Delta\sigma = 0.1$ and $\Delta\sigma = 0.2$.

To generate the diameter potential we employ the same functional forms as in Eq. (11). There are six terms in this diameter potential. Four exponential functions (with steepness parameter $A = 100$) define the steep walls delimiting the range of the particle size distributions of width $\Delta\sigma$, and two power law functions with suitable power of $\sigma$ ($n_1 = 2.5$ and $n_2 = 2.4$) produce uniform

distributions centered around $\sigma_A = 1.0$ and $\sigma = 1.4$.

In this case, the average diameter is therefore $\overline{\sigma} \approx 1.2$. For the case of $\Delta\sigma = 0.1$, the polydispersity for $A$-type particles is is $\approx 3.2\%$ and around $\sigma_B = 1.4$ it is $\approx 2.2\%$. For the case of $\Delta\sigma = 0.2$, the polydispersity around $\sigma_A = 1.0$ is $\approx 6\%$ and around $\sigma_B = 1.4$ it is $\approx 4.2\%$. The parameters used at different temperatures are listed in Table 2.

| $T$ | $D$ | $\lambda_1$ | $\lambda_2$ |
|---|---|---|---|
| 1.00 | 14.4600 | 1.000 | 1.0000 |
| 0.90 | 13.9400 | 1.000 | 1.0000 |
| 0.80 | 13.3900 | 1.000 | 1.0000 |
| 0.70 | 12.8830 | 1.004 | 0.9995 |
| 0.60 | 12.2998 | 1.006 | 0.9980 |
| 0.50 | 11.6840 | 1.009 | 0.9950 |
| 0.45 | 11.3139 | 1.010 | 0.9950 |
| 0.40 | 10.8932 | 1.010 | 0.9950 |
| 0.35 | 10.5277 | 1.013 | 0.9950 |
| 0.30 | 10.0566 | 1.016 | 0.9950 |
| 0.25 | 9.44502 | 1.017 | 0.9920 |

Table 1: Parameters for internal potential $v(\sigma)$ to generate distribution of size of particles $P(\sigma) \sim 1/\sigma^{3.2}$

| $T$ | $D_1$ | $D_2$ | $\lambda_1$ | $\lambda_2$ |
|---|---|---|---|---|
| 3.000 | 68.7081 | 72.1031 | 0.996 | 1.003 |
| 2.800 | 67.5904 | 71.1848 | 0.997 | 1.002 |
| 2.600 | 65.7046 | 69.3978 | 0.997 | 1.002 |
| 2.400 | 64.3770 | 68.3707 | 0.998 | 1.001 |
| 2.300 | 63.9399 | 67.8369 | 0.999 | 1.001 |
| 2.200 | 63.5409 | 67.3381 | 0.999 | 1.000 |
| 2.150 | 62.8426 | 66.8393 | 0.999 | 1.000 |
| 2.100 | 62.6431 | 66.6398 | 0.999 | 1.000 |
| 2.050 | 61.6456 | 66.2408 | 0.999 | 1.000 |
| 2.000 | 61.2466 | 65.9415 | 0.999 | 1.000 |
| 3.000 | 69.0051 | 72.8954 | 0.996 | 1.003 |
| 2.800 | 67.5200 | 71.3107 | 0.996 | 1.002 |
| 2.600 | 65.8695 | 69.5649 | 0.998 | 1.002 |
| 2.400 | 64.5384 | 68.5352 | 0.999 | 1.001 |
| 2.300 | 63.9399 | 67.8369 | 0.999 | 1.001 |
| 2.200 | 63.2000 | 67.2000 | 1.000 | 1.000 |
| 2.100 | 62.3200 | 66.5500 | 1.000 | 1.000 |
| 2.000 | 61.2000 | 65.7000 | 1.000 | 1.000 |
| 1.975 | 60.9500 | 65.4500 | 1.000 | 1.000 |
| 1.950 | 60.6500 | 65.2000 | 1.000 | 1.000 |
| 1.925 | 60.3000 | 64.9000 | 1.000 | 1.000 |
| 1.900 | 60.0500 | 64.8000 | 1.000 | 1.000 |
| 1.875 | 59.9000 | 64.6500 | 1.000 | 1.000 |
| 1.850 | 59.5550 | 64.4560 | 1.000 | 1.000 |

Table 2: Parameters used to design the potential $v(\sigma)$ to generate a binary distribution of diameters with width $\Delta\sigma = 0.1$ (top) and $\Delta\sigma = 0.2$ (bottom).

Chapter 5

# The role of the configurational entropy in glassy slowdown

In the Introduction, we presented theoretical arguments for an underlying thermodynamic glass transition.They associate the configurational entropy decrease with the dramatic slowdown of supercooled liquids. This picture is motivated by the existence of a finite-temperature entropy crisis in the mean field theory of structural glasses.

We argued that a 'configurational entropy' cannot be unambiguously defined in finite-dimensional liquids. It is supposed to count the number of metastable states available to the system, but defining 'metastable states' beyond mean field is intricate. Several numerical methods were employed in the past to measure a configurational entropy. The first estimates crudely counted the number of minima in the potential energy landscape. Recently, refined methods were developed, inspired by theoretical constructions.

The article 'Configurational entropy of glass-forming liquids' has been published as a Perspective in The Journal of Chemical Physics. It is based on a series of lectures given by Ludovic Berthier at the 2017 Boulder summer school 'Disordered and Frustrated systems', which I attended. I organized and complemented the lecture notes, in order to provide a review and perspective on configurational entropy measurements in computer simulations. My initial effort was then supported by Misaki Ozawa, who implemented and developed some of the numerical schemes.

In the second article 'Does the Adam-Gibbs relation hold in simulated supercooled liquids?', we address the validity of the Adam-Gibbs (AG) relation, introduced in Sec. 1.4.1, which relates the configurational entropy and relaxation time in the supercooled liquid regime. We also address the generalized Adam-Gibbs (gAG) relation (Eq. 1.18), which contains the non-trivial exponents $\theta$ and $\psi$. They correspond to an interface term, and the dynamical exponent, respectively. Using the thermalization speedup of particle-swap methods, we revisit previous numerical tests of the AG relations. Most importantly, we address their validity in a broad temperature regime, relevant to test theoretical predictions.

This work was initiated by Ludovic Berthier, Misaki Ozawa and Andrea Ninarello. The paper analyzes data for several glass-forming models, published in previous works. My contribution was to extend these results to supercooled liquids prepared in conditions closer to experimental

ones, namely at constant pressure. My work aimed at identifying glass-forming models which were as fragile as experimental liquids, and stable against crystallization using the SWAP algorithm. Interestingly, it was realized that good glass-formers model in constant volume conditions can crystallize easily at constant pressure. Using the Hybrid algorithm presented in Chapter 4, I was able to generate supercooled liquids at constant pressure, down to temperatures below the experimental glass transition temperature. Misaki Ozawa then performed configurational entropy measurements. I was able to measure the equilibrium relaxation time down to unprecedentedly low temperatures in a three-dimensional model. The dynamical slowdown is followed on almost 6 orders of magnitude (Fig. 2 (c)). Such high-quality data allows to perform precise fitting and extrapolation of the relaxation time, which are needed to test accurately the Adam-Gibbs relation.

We find that the Adam-Gibbs relation is not verified when addressed over the relevant temperature regime $T < T_d$, in four different glass-forming models. Interestingly, we gather high-quality experimental data and find that the relation is also not verified in experimental systems. The data is fitted to a generalized Adam-Gibbs relation, in order to estimate the exponents $\theta$ and $\psi$. The values measured numerically are in agreement with theoretical predictions.

Most importantly, deviations from the Adam-Gibbs relation were previously invoked to question the thermodynamic nature of the glass transition. We show that recent thermodynamic theories rather predict a generalized Adam-Gibbs relation. We show that experimental and numerical data follow the gAG relation, and thus do not invalidate thermodynamic theories for the glass transition.

Article

# Perspective: Configurational entropy of glass-forming liquids

L. Berthier, M. Ozawa, and C. Scalliet, The Journal of chemical physics 150 (16), 160902 (2019).

**The configurational entropy is one of the most important thermodynamic quantities characterizing supercooled liquids approaching the glass transition. Despite decades of experimental, theoretical, and computational investigation, a widely accepted definition of the configurational entropy is missing, its quantitative characterization remains fraud with difficulties, misconceptions and paradoxes, and its physical relevance is vividly debated. Motivated by recent computational progress, we offer a pedagogical perspective on the configurational entropy in glass-forming liquids. We first explain why the configurational entropy has become a key quantity to describe glassy materials, from early empirical observations to modern theoretical treatments. We explain why practical measurements necessarily require approximations that make its physical interpretation delicate. We then demonstrate that computer simulations have become an invaluable tool to obtain precise, non-ambiguous, and experimentally-relevant measurements of the configurational entropy. We describe a panel of available computational tools, offering for each method a critical discussion. This perspective should be useful to both experimentalists and theoreticians interested in glassy materials and complex systems.**

# I Configurational entropy and glass formation

## I.1 The glass transition

When a liquid is cooled, it can either form a crystal or avoid crystallization and become a supercooled liquid. In the latter case, the liquid remains structurally disordered, but its relaxation time increases so fast that there exists a temperature, called the glass temperature $T_g$, below which structural relaxation takes such a long time that it becomes impossible to observe. The liquid is then trapped virtually forever in one of many possible structurally disordered states: this is the basic phenomenology of the glass transition. [1, 2, 3, 4] Clearly, $T_g$ depends on the measurement timescale and shifts to lower temperatures for longer observation times. The experimental glass transition is not a genuine phase transition, as it is not defined independently of the observer.

The rich phenomenology characterizing the approach to the glass transition has given rise to a thick literature. It is not our goal to review it, and we refer instead to previous articles. [1, 2, 3, 4, 5, 6, 7, 8, 9] There are convincing indications that the dynamic slowing down of supercooled liquids is accompanied by an increasingly collective relaxation dynamics. This is seen directly by the measurement of growing lengthscales for these dynamic heterogeneities, [10, 11, 12] or more indirectly by the growth of the apparent activation energy for structural relaxation, as seen in its non-Arrhenius temperature dependence. These observations suggest an interpretation of the experimental glass transition in terms of a generic, collective mechanism possibly controlled by a sharp phase transition. [13] 'Solving the glass problem' thus amounts to identifying and obtaining direct experimental signatures about the fundamental nature and the mathematical description of this mechanism.

Why is this endeavor so difficult as compared to other phase transformations encountered in condensed matter? [14, 15] The core problem is illustrated in Fig. 1 by two particle configurations taken from a recent computer simulation. [16] The left panel shows an equilibrium configuration of a two-dimensional liquid with a relaxation time of order $10^{-10}$ s, using experimental units appropriate for a molecular system. The right panel shows another equilibrium configuration now produced close to $T_g$ with an estimated relaxation timescale of order 100 s. The system on the right flows $10^{12}$ times slower than the one on the left, but to the naked eye both configurations look quite similar. In conventional phase transitions, [14, 15] a structural change takes place and some form of (crystalline, nematic, ferromagnetic, etc.) order appears. Glass formation is not accompanied by such an obvious structural change. Therefore, the key to unlock the glass problem is to first identify the correct physical observables to distinguish between the two configurations in Fig. 1.

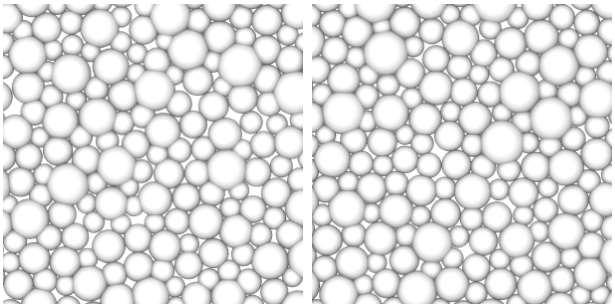

Figure 1: Two equilibrium configurations of a two-dimensional glass-forming model characterized by relaxation times that differ by a factor $10^{12}$. The two density profiles appear to the naked eye similarly featureless. These two states in fact differ by the number of available equilibrium states and the configurational entropy quantifies this difference.

Several theories, scenarios and models have been developed in this context. [5, 17, 18, 19, 20, 21, 22, 23, 24, 25, 26, 27] Some directly focus on the rich dynamical behavior approaching the glass transition, [24] while others advocate some underlying phase transitions of various kinds, [17, 19, 20] possibly involving some 'hid-

den' or amorphous order.

In this perspective, we explore one such research line, in which configurational entropy associated with a growing amorphous order plays the central role. [19, 20, 28] We argue that recent developments in computational techniques offer exciting perspectives for future work, allowing the determination of complex observables that are not easily accessible in experiments, as well as the exploration of temperature regimes relevant to experiments.

## I.2 Why the configurational entropy?

The fate of equilibrium supercooled liquids followed below $T_g$ with inaccessibly long observation times was discussed 70 years ago by Kauzmann in a seminal work. [29] Since the supercooled liquid is metastable with respect to the crystal, Kauzmann compiled data for the excess entropy, $S_{exc} \equiv S_{liq} - S_{xtal}$, where $S_{liq}(T)$ and $S_{xtal}(T)$ are the liquid and crystal entropies, respectively. Kauzmann observed that $S_{exc}(T)$ decreases sharply with decreasing the temperature of the equilibrium supercooled liquid.

An extrapolation of the temperature evolution of $S_{exc}$ from equilibrium data to lower temperatures suggests that $S_{exc}$ becomes negative at a finite temperature, which led Kauzmann to comment: [29] *'Certainly it is unthinkable that the entropy of the liquid can ever be very much less than that of the solid.'* To avoid this paradoxical situation, referred to as the Kauzmann paradox or entropy crisis, he mentioned the possibility of a thermodynamic glass transition occurring well below $T_g$, at a temperature now called the Kauzmann temperature, $T_K$. Although Kauzmann suggested that crystallization eventually prevents the occurrence of an entropy crisis, Kauzmann's intuition remains very influential, for good reasons.

Gibbs and DiMarzio were the first to give theoretical insights to the temperature evolution of $S_{exc}$, by analogy with a lattice polymer model whose entropy is purely configurational. [30, 31] Hence the conventional name, 'configurational entropy' and notation $S_{conf}$, widely used in the experimental literature. [32] We show below that there is no, and that there cannot be any, unique definition of $S_{conf}$. We nevertheless use the same symbol for all discussed estimates. In particular, $S_{conf} \approx S_{exc}$.

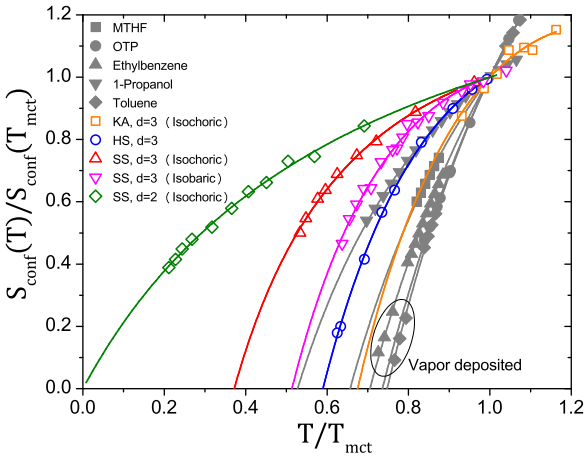


Figure 2: Experimental and numerical determinations of the equilibrium configurational entropy in various models [16, 33] and materials. [32, 34, 35] Data points extracted from vapor deposition experiments [35] are indicated by the ellipse. Both axis are rescaled using the mode-coupling crossover as a reference temperature at which the relaxation time is about $10^{-7}$s. For hard spheres, the inverse of the reduced pressure, $1/p$, replaces temperature. Extrapolation to low temperatures suggests the possibility of an entropy crisis at a finite $T_K$ in $d = 3$, whereas $T_K = 0$ in $d = 2$.

We compile state-of-the-art experimental [32, 34, 35] and numerical [16, 33] data of $S_{conf}$, and their extrapolation to low temperatures in Fig. 2. We employ a representation close to Kauzmann's original analysis, [29] rescaling $S_{conf}$ by its value at some high temperature (we choose the mode-coupling temperature $T_{mct}$, [36] for convenience).

In calorimetric experiments, the configurational entropy becomes constant below $T_g$ upon entering the non-equilibrium glass regime, defining a residual entropy. [29, 34] The glass residual entropy is a non-equilibrium effect that has been

extensively discussed. [37, 38, 39, 40, 41] Here, we focus on equilibrium supercooled liquids and do not discuss further the glass residual entropy and remove non-equilibrium measurements in Fig. 2.

The data for ethylbenzene and toluene are extended by combining conventional calorimetric measurements to data indirectly estimated from ultrastable glasses produced using vapor deposition. [35, 42] In that case, $T$ corresponds to the substrate temperature. Various computational models using hard, [43] soft, [44] and Lennard-Jones potentials, [45] along isochoric and isobaric paths, in spatial dimensions $d = 2$ [16] and 3 [33] are included along with experiments. [32, 34, 35] This representative data set demonstrates that all glass formers in dimension $d = 3$ display a sharp decrease of $S_{\rm conf}$, even down to a temperature regime unavailable to Kauzmann. These results reinforce the idea that $S_{\rm conf}$ can vanish at a finite temperature, $T_K > 0$. Simulation data in $d = 2$ suggest instead that $S_{\rm conf}$ vanishes only at $T_K = 0$, suggesting that a finite $T_K$ entropy crisis does not occur for $d < 3$. [16]

Of course, the data in Fig. 2 do not rule out the existence, at some yet inaccessible temperature, of a crossover in the behavior of $S_{\rm conf}$ that makes it smoothly vanish at $T = 0$, [46, 47] or remain finite with an equilibrium residual entropy in classical systems, [48, 49, 50, 51, 52] or a discontinuous jump due to an unavoidable crystallization, [29, 53, 54] or a liquid-liquid transition, [22] or a conventional (kinetic) glass transition. [55] These alternative possibilities are not supported by data any better than the entropy crisis they try to avoid. It is impossible to comment on the many articles supporting the absence of a Kauzmann transition [46, 50, 56, 57, 58, 59], but we clarify below that none of them resists careful examination. The existence of a thermodynamic glass transition remains an experimentally and theoretically valid, but unproven, hypothesis. Thus, extending configurational entropy measurements to even lower temperatures remains an important research goal. [60]

As emphasized repeatedly, a negative $S_{\rm exc}$ is not prohibited by thermodynamic laws. [56] This is also not 'unthinkable' since entropy is not a general measure of disorder. As a first counterexample, think of hard spheres for which the crystal entropy is larger than that of the fluid above the melting density under constant volume condition. A second example under constant pressure condition would be materials showing inverse melting. [61] A stronger reason to 'resolve' the Kauzmann paradox is that if $S_{\rm liq}$ continues to decrease further below $S_{\rm xtal}$, the third law of thermodynamics could be violated. [62] However, the third law is conventionally interpreted as a consequence of the quantum nature of the system. [63] This implies that the Kauzmann paradox is not really problematic if considered within the realm of classical physics. In summary, *there is no theoretical need* to avoid the entropy crisis.

However, theoretical treatments rooted in Gibbs and DiMarzio's theory [30, 31] relate the configurational entropy to the (logarithm of the) number of distinct glass states available to the system at a given temperature. A proper enumeration of those states must therefore result in a non-negative configurational entropy. In this interpretation, Fig. 2 suggests that a fundamental change in the properties of the free-energy landscape must underlie glass formation.

A strong decrease of the configurational entropy answers the question raised by the apparent structural similarity suggested by the snapshots in Fig 1. Conventional phase transitions deal with the 'structure' of a single configuration, [14, 15] for instance the periodic order of the density profile for crystallization, see Fig. 3(a). By contrast, it is not the *nature* of the density profile that changes across the glass transition, but rather the *number* of distinct available profiles. [1] There are many distinct states available to the liquid, leading to a finite configurational entropy, but only a subextensive number in the putative thermodynamic glass phase, where $S_{\rm conf} = 0$. 'Glass order' can thus only be revealed by the enumeration of equilibrium accessible states, see Fig. 3(b).

A final general question is: how can a purely thermodynamic quantity be useful to under-

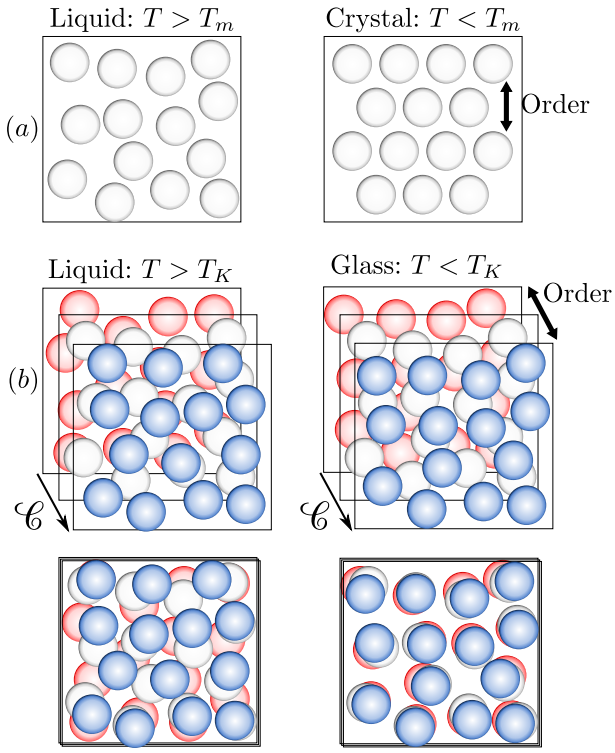


Figure 3: (a) Crystallization at the melting temperature $T_{\rm m}$ corresponds to the emergence of periodic order in the density profile of a single configuration. (b) The glass transition at $T_{\rm K}$ is detected by enumerating equilibrium configurations in configuration space $\mathscr{C}$. Glass order is revealed by comparing the degree of similarity (in practice, the overlap in Eq. (7)) of amorphous density profiles.

stand slow dynamics? After all, the above phenomenological description of the glass transition relies on dynamics, and a connection to configurational entropy is not obvious. The first quantitative connection arose in 1965, when Adam and Gibbs proposed that the timescale for structural relaxation increases exponentially with $1/(TS_{\rm conf})$. [17] Quantitatively, the modest decrease of $S_{\rm conf}(T)$ in Fig. 2 could then be sufficient to account for the modest increase in the apparent activation energy, and for the large increase of relaxation times although this view remains heavily debated, to this day. [64, 65]

Testing the Adam-Gibbs relation has become a straw man for a deeper issue: [32, 58, 66, 67] how can one (dis)prove the existence of a causal link between the rarefaction of equilibrium states and slow dynamics? In essence, the physical idea to be tested is that the driving force behind structural relaxation for $T > T_K$ is the configurational entropy gained by the system exploring distinct disordered states. Slower dynamics then arises when fewer states are available at lower $T$, since the system hardly finds new places to go. In this view, the two configurations in Fig. 1 relax at a much different rate not because there structure is different, but because much fewer equilibrium configurations are accessible to the configuration on the right. This is indeed hard to recognize by the naked eye.

### I.3 Mean-field theory of the glass transition

Despite the diversity of theoretical work related to glass formation, the configurational entropy plays a central role. This is natural for theories rooted in thermodynamics and describe an entropy crisis, [17, 18, 68] but theories based on a different mechanism must also explain the observed behavior of $S_{\rm conf}$, and the role played by a (possibly avoided) entropy crisis. [21, 22, 46] Finally, theories based on dynamics must explain why a rapidly changing $S_{\rm conf}$ is an irrelevant factor. [24, 69, 70, 71] This makes the concept of configurational entropy, a careful understanding of its physical content, and the development of precise numerical measurements important research goals.

The first theory 'predicting' an entropy crisis appeared about a decade after Kauzmann's work. [30, 31] Inspired by lattice polymer studies, [72] Gibbs and DiMarzio identified the decrease of $S_{\rm exc}$ presented by Kauzmann with the reduction of the entropy computed within a set of mean-field approximations. In their lattice model, 'states' were identified with microscopic configurations, with no need to subtract any vibrational contribution, $S_{\rm conf} \approx S_{\rm tot}$. An approximate statistical mechanics treatment of their

model yields $S_{\rm tot} \to 0$ at a finite temperature.

Revisions and extensions of the Gibbs-DiMarzio work abound. [48, 73, 74] Modern studies offer more detailed treatments of the polymer chain and refined approximations. [75] The entropy may or may not vanish, depending on the approximations used and the ingredients entering the model. [52, 76] An entropy crisis is thus not always present within the Gibbs-DiMarzio line of thought, but one cannot draw general conclusions about the existence of an entropy crisis in supercooled liquids. Moreover, the distinction between individual configurations and free-energy minima is generally not considered, which may be problematic. [77] Finally, these works rely heavily on the polymeric nature of the molecules to make predictions whose validity for simpler particle models or molecular systems is not guaranteed. These works nevertheless suggest that the presence of a Kauzmann transition could well be system-dependent. This is demonstrated by some specific colloidal models in which the entropy crisis is indeed avoided with a finite configurational entropy at zero temperature. [49, 51]

A coherent mean-field theory of the glass transition was recently derived for classical, off-lattice, point particle systems interacting with generic isotropic pair interactions. [78, 79, 80, 81, 82] The 'mean-field' nature of the theory stems from the fact that it becomes mathematically exact in the limit of $d \to \infty$, whereas it amounts to an approximate analytic treatment for physical dimensions $d < \infty$. The nature of the glass transition found in this mean-field limit agrees with results obtained in the past in a variety of approximate treatments, starting with density functional theory of hard spheres, [83] replica calculations of fully-connected spin glass models, [18, 84, 85, 86, 87, 88] and others. [89, 90, 91]

The fact that distinct models and treatments yield similar results reflects a universal evolution of the free-energy landscape in glassy systems, with results rediscovered in a variety of contexts. [28, 92] The theory reveals the existence of sharp temperature scales where the topography of the free-energy landscape changes qualitatively. There exists a first temperature scale, $T_{\rm onset}$, above which a single global free energy minimum exists, and below which a large number, $\mathcal{N}$, of free-energy minima appear. This number scales exponentially with the system size, which allows for the definition of an entropy, $\Sigma = \ln \mathcal{N}$, [1] also called complexity. At a second temperature scale, $T_{\rm mct} < T_{\rm onset}$, the partition function becomes dominated by those multiple free-energy minima. This transition shares many features with the dynamic transition first discovered in the context of mode-coupling theory. [36] The third critical temperature is $T_K < T_{\rm mct}$, below which the number of free-energy minima becomes subextensive, resulting in a vanishing complexity, $\Sigma(T \to T_K) \to 0$.

An entropy crisis is thus an analytic result in mean-field theory, which provides a clear physical interpretation of the configurational entropy as the logarithm of the number of free-energy minima, $S_{\rm conf} \approx \Sigma = \ln \mathcal{N}$. A Kauzmann transition is exactly realized, and is referred to as a random first order transition (RFOT).

The idea that the existence, number, and organization of distinct free-energy minima control the glass transition was elegantly captured by an approach developed by Franz and Parisi. [93, 94] As in Landau theory, they expressed the free-energy, or effective potential $V(Q)$, as a function of a global order parameter $Q$. As illustrated in Fig. 3(b), the distinction between liquid and glass phases stems from the degree of similarity of particle configurations drawn from the Boltzmann distribution. Let us define an overlap, $Q$, as the degree of similarity of the density profiles of two equilibrium configurations, such that $Q \approx 0$ for uncorrelated profiles (liquid phase), and $Q \approx 1$ for similar profiles (glass phase); see Eq. (7) below.

The free-energy $V(Q)$ can be computed analytically for mean-field glass models, as shown in Fig. 4. As expected, the global minimum of $V(Q)$ is near $Q \approx 0$ for $T > T_K$ as there exist so many distinct available states that two equilibrium configurations chosen at random have no simi-

[1] In this paper, we set the Boltzmann constant to unity.

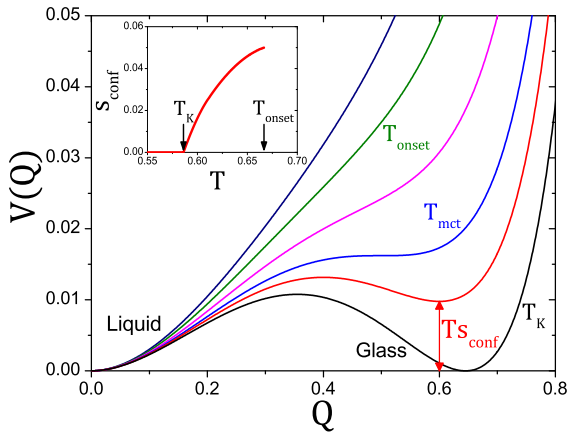


Figure 4: Schematic plot of the Franz-Parisi free energy in mean-field theory. Inset: Temperature evolution of the configurational entropy.

larity. All critical temperatures mentioned above have a simple interpretation in this representation. The free-energy $V(Q)$ has non-convexity when $T < T_{\rm onset}$, it develops a secondary minimum when $T < T_{\rm mct}$, and this local minimum becomes the global one when $T$ reaches $T_K$. The secondary minimum occurs for $Q$ slightly smaller than 1, due to thermal fluctuations. [95] In this description, mean-field glass theory shares similarities with ordinary first-order transitions.

In the interesting regime, $T_{\rm K} < T < T_{\rm mct}$, the glass phase at high $Q$ is metastable with respect to the liquid phase at low $Q$. The free-energy difference between the liquid and glass phases results from confining the system within a restricted part of the configuration space. Preventing the system to explore the multiplicity of available free-energy minima entails an entropic loss, precisely given by the complexity, $T\Sigma(T)$. The temperature evolution of the configurational entropy $S_{\rm conf}$ is thus readily visualised and quantified from the Franz-Parisi free-energy as shown in Fig. 4. The inset of Fig. 4 shows that a finite configurational entropy emerges discontinuously at $T_{\rm onset}$, and vanishes continuously at $T_K$.

The entropy crisis captured by the random first-order transition universality class is now validated by exact calculations performed in the large dimensional limit, $d \to \infty$. [82] This confers to RFOT a status similar to van der Waals theory for the liquid-gas transition. With its well-defined microscopic starting point, mean-field theory confirms that the configurational entropy is central to the understanding of supercooled liquids, and the rigorous treatment it offers puts phenomenological and approximate ideas introduced earlier by Kauzmann, Gibbs, DiMarzio, Adam, and others on a solid basis. This now serves as a stepping stone to describe finite dimensional effects. [96, 97, 98, 99, 100, 101]

## I.4 Conceptual and technical problems

Physically, the configurational entropy quantifies the existence of many distinct *glass states* that the system can access in equilibrium conditions. There are two main routes to measure $S_{\rm conf}$.

First, one can subtract from the total entropy a contribution that comes from small thermal vibrations performed in the neighborhood of a given reference configuration: $S_{\rm conf}(T) \approx S_{\rm tot}(T) - S_{\rm glass}(T)$. In this view, $S_{\rm glass}(T)$ should be the entropy of an equilibrium system that does not explore distinct states at temperature $T$. This quantity can be measured straightforwardly in equilibrium for $T < T_K$, whereas some approximations are by construction needed to measure $S_{\rm glass}$ for $T > T_K$.

Experimentally, it is often assumed that $S_{\rm glass} \approx S_{\rm xtal}$, because it is possible to measure $S_{\rm xtal}$ in equilibrium using reversible thermal histories. [32] This represents a well-defined and physically plausible proxy. It has been tested for some systems, [102, 103, 104, 105, 106, 107] and its validity seems to be non-universal. [107] We shall introduce in Sec. III.5 a computational method to determine $S_{\rm glass}$ that makes no reference to the crystal. [108, 109, 110]

The second general route to $S_{\rm conf}$ is to directly enumerate the number of distinct glass states available to the system in equilibrium, $\mathcal{N}$, and use $S_{\rm conf} = \ln \mathcal{N}$. Here, mean-field theory provides a rigorous definition of glass states as free-

energy minima. However, just as for ordinary phase transitions (e.g. van der Waals theory) local free-energy minima are no longer infinitely long-lived when physical dimension is finite, and states can no longer be defined precisely. Thus, strictly speaking, the complexity that vanishes at $T_K$ in mean-field theory *is not defined in finite dimensional systems*. Again, approximations must be performed to measure a physical analog. Two such methods based on the Franz-Parisi free energy [93, 94] and glassy correlation length, [68] are now available, as discussed in Secs. IV and V. The existence of an entropy crisis in finite dimension is not directly challenged by the approximate nature of these estimates. To determine whether a Kauzmann transition can occur in finite $d$, one should rather study the effect of finite-dimensional fluctuations within a $d$-dimensional field theory using the Franz-Parisi free-energy as a starting point.[96, 97, 98, 99, 100, 101] There exists no 'proof' that the Kauzmann transition should be destroyed in finite dimensions as divergent conclusions were obtained using distinct approximate field-theoretical treatments. This is a difficult, but pressing, theoretical question for future work.

A popular alternative is the enumeration of potential energy minima using the potential energy landscape (PEL), which was actually proposed long before the development of mean-field theory, first by Goldstein, [111] and further formalized by Stillinger and Weber. [112, 113] The PEL approach assumes that an equilibrium supercooled liquid resides very close to a minimum of the potential energy, also named inherent structure. Assuming further that each inherent structure corresponds to a distinct glass state, the number of inherent structures, $\mathcal{N}_{\rm IS}$, provides a proxy for the configurational entropy, $S_{\rm conf} \approx \ln \mathcal{N}_{\rm IS}$. This assumption offers precise and simple computational methods to estimate the configurational entropy, [46, 114, 115] discussed below in Sec. III.

The identification between inherent structures and the free-energy minima entering the mean-field theory should not be made, as explicit examples were proposed to show that it is generally incorrect. [77, 116] Physically, it is believed that free-energy minima may contain a large number of inherent structures. The concept of 'metabasins' [117] has been empirically introduced to capture this idea, but there is no available method to enumerate the number of metabasins to obtain a configurational entropy. The hard sphere model is a striking example of the difference between energy and free energy minima. In large dimensions, hard spheres undergo an entropy crisis, but it does not correspond to a decrease of the number of inherent structures, which are not defined for due to the discontinous nature of the pair potential.

Using the PEL approach, several arguments were given to question the existence of a Kauzmann transition in supercooled liquids. By considering localized excitations above inherent structures, Stillinger provided a physical argument showing that the PEL approximation to the configurational entropy can not vanish at a finite temperature. [46] The effect of such excitations on the free-energy landscape has not been studied, and so this argument does not straightforwardly apply to the random first order transition itself. In the same vein, Donev *et al.* directly constructed dense hard disk packings of a binary mixture model to suggest that $\mathcal{N}_{\rm IS}$ cannot yield a vanishing configurational entropy. This again does not question the Kauzmann transition of that system, since it should be demonstrated that the equilibrium free-energy landscape is sensitive to these artifical inherent states, whose relevance to the equilibrium supercooled fluid is not established.[2] Finally, the ambiguous nature of inherent structures becomes obvious when considering colloidal systems composed of a continuous distribution of particle sizes. Starting from a given inherent structure, each permutation of the particle identity provides a different energy minimum and a naive enumeration of the configurational entropy [118] would contain a divergent

[2] In addition, the constructed dense packings are largely demixed and partially crystallized, and it is unclear that these states are relevant for the (metastable) fluid branch.

mixing entropy contribution, again incorrectly suggesting the absence of a Kauzmann transition. [116] A similar argument was proposed for a binary mixture. [119] The problem of the mixing entropy in the PEL approach is considered further, and solved, in Sec. III.6.

# II Computer simulations of glass-forming liquids

## II.1 Why perform computer simulations to measure the configurational entropy?

Let us start with some major steps in computer simulations of supercooled liquids, referring to broader reviews for a more extensive perspective. [120, 121] Early computational studies date back to the mid-1980s, [122, 123, 124, 125, 126] followed by intensive works strongly coupled to the development of mode-coupling theory during the 1990s. [45] The nonequilibrium aging dynamics of glasses, [127] along with concepts of effective temperatures, [128, 129, 130] rheology [131, 132] and dynamical heterogeneities [10, 131, 133, 134] were in the spotlight at the end of the 20th century. The search for a growing static lengthscale, [135] linked to a Kauzmann transition and configurational entropy, [114, 115] have continuously animated the field until today. Over this period spanning about 3 decades, the numerically-accessible time window increased about as many orders of magnitude, mainly due to improvements in computer hardware. Until 2016, computer studies lagged well behind experiments in terms of equilibrium configurational entropy measurements, but recent developments in computer algorithms have been able to generate, for highly polydisperse systems, equilibrium configuration comparable to experimental data. [44] For these models, temperatures *below* the experimental glass transition are now numerically accessible in equilibrium conditions, making computer simulations an essential tool for configurational entropy studies in supercooled liquids. [16, 136]

As illustrated in Fig. 1, theories for the glass transition need to make predictions for complex observables that reflect nontrivial changes in the supercooled liquid, such as multi-point time correlation functions, [137] point-to-set correlations, [135, 138] non-linear susceptibilities, [139, 140] as well as properties of the potential and free-energy landscapes. [141, 142, 143] Most of these quantities are extremely challenging, or sometimes even impossible, to measure in experiments. Computer simulations are particularly suitable because they generate equilibrium density profiles from which any observable can be computed. Obtaining the same information in experiments is possible to some extent in colloidal glasses, but still a challenge in atomistic or molecular glasses.

Computer simulations take place under perfectly controlled conditions, and are therefore easier to interpret than experiments. All settings are well-defined: microscopic model, algorithm for the dynamics, statistical ensemble (isobaric or isochoric conditions), external parameters, etc. Computer simulations are also very flexible. Since the mean-field theory for the glass transition provides exact predictions for the configurational entropy in infinite dimensions, it is crucial to understand how finite-dimensional fluctuations affect them. Along with current efforts that strive to develop renormalization group approaches to this problem, numerical simulations give precious insights into the effect of dimensionality on the physics of glass formation. Numerical simulations can be performed in any physical dimensions, and the range $d = 1 - 12$ was explored in that context. [144, 145, 146, 147] Even the space topology can be varied. [148, 149] One can study the effect of freezing a subset of particles with arbitrary geometries by means of computer simulations. [138, 150, 151, 152, 153] The size of the system under study can be tuned and finite-size scaling analysis can reveal important lengthscales for the glass problem. [154, 155]

## II.2 Simple models for supercooled liquids

The features associated with the glass transition, such as a dramatic dynamical slowdown and dynamic heterogeneities, are observed in a wide variety of glassy materials composed of atoms, molecules, metallic compounds, colloids and polymers. It may be useful to focus on simple models exhibiting glassy behavior to understand universal features of the glass transition. We consider classical point-like particles with no internal degrees of freedom that interact via isotropic pair potentials. These models may not capture all detailed aspects of glass formation, e.g. $\beta$-relaxations due to slow intramolecular motion in molecules, but their configurational entropy can nevertheless be measured. The numerical study of simple models is especially relevant in the context of configurational entropy, since mean-field theory was precisely derived for such simple models, which allow direct comparison between theory and simulations. [82]

For this perspective, we use results for three simple glass-formers to illustrate generic features of entropy measurements. The Lennard-Jones (LJ) potential was first introduced to model the interaction between neutral atoms and molecules. The interaction potential between two particles separated by a distance $r$ reads

$$v_{\rm LJ}(r) = 4\varepsilon\left[\left(\frac{\sigma}{r}\right)^{12} - \left(\frac{\sigma}{r}\right)^{6}\right], \qquad (1)$$

where $\varepsilon$ and $\sigma$ set the energy and length scales. The stiffness of the repulsion in the soft-sphere (SS) potential $v_{\rm SS}(r) = \varepsilon(\sigma/r)^{\nu}$ can be tuned with $\nu$. [44] The hard-sphere (HS) potential, defined as $v_{\rm HS}(r) = \infty$ if $r < \sigma$, and $v_{\rm HS}(r) = 0$ otherwise, models hard-core repulsion between particles of diameter $\sigma$. This highly-idealized model efficiently captures the glass transition phenomenology.[156, 157] We recall that for hard spheres, pressure and temperature are no longer independent control parameters, but enter together in the adimensional pressure, $p = P/(\rho T)$, so that $1/p$ replaces the temperature for that system, [156] and directly controls the packing fraction $\phi$ via the equation of state, $\phi = \phi(p)$.

The homogeneous supercooled liquid is metastable with respect to the crystal in the temperature regime where the configurational entropy is measured, and so the expression "equilibrium supercooled liquid" represents, strictly speaking, an abuse of language. Designing glass-forming models in which crystallization is frustrated, and defining strict protocols to detect crystallization is crucial.[44] Mixtures of different species are good experimental glass-formers: colloidal glasses are made of polydisperse suspensions, [158] and metallic glasses are alloys of atoms with different sizes. [159] Inspired by experiments, numerical models use particles of different species which differ by their size $\sigma$ or interaction $\varepsilon$. The Kob-Andersen (KA) model is a bidisperse mixture with 80% larger particles and 20% smaller particles, interacting via the LJ potential with adjusted parameters $\sigma$ and $\varepsilon$ to describe amorphous $Ni_{80}P_{20}$ metallic alloys.[45] Many numerical models with good glass-forming ability have been developed, [44, 45, 124, 126, 160, 161] although development in computational power now leads to crystallization for some of those models. [44, 162, 163, 164] Thus, developing new models robust against crystallization is an important research goal.

While the situation may seem satisfactory to theorists, numerical glass-formers are probably too simplistic for many experimentalists. A wide variety of more realistic glass forming models have been developed and studied [165, 166, 167, 168]. Future developments should aim at designing minimal models for more complex systems and powerful algorithms for efficient simulations, in order to also close this conceptual gap.

## II.3 Molecular dynamics simulations

The two main classical methods used to simulate the above models are Monte Carlo (MC) and Molecular Dynamics (MD) simulations.[169, 170] Quantum effects, partially included in *ab initio*

simulations, are irrelevant in the present context.

The course of a numerical simulation is very similar to an experiment. A sample consisting of $N$ particles is prepared and equilibrated (using either MC or MD dynamics) at the desired state point, until its properties no longer change with time. After equilibration is achieved, the measurement run is performed. Common problems are just as in experiments: the sample is not equilibrated correctly, the measurement is too short, the sample undergoes an irreversible change during the measurement, etc.

A noticeable difference between computer and experimental supercooled liquid samples is their size. Numerical studies of the configurational entropy are limited to around $10^4$ particles, to be compared to around $10^{23}$ atoms or molecules in experimental samples. Periodic boundary conditions are applied to the simulation box in order to avoid important boundary effects, and simulate the bulk behavior of 'infinitely' large samples. Lengthscales larger than the system size are numerically inaccessible. Up to now, this limit was not really problematic since all relevant lengthscales associated with the glass transition are not growing to impossibly large values, in particular for static quantities. Analysis of dynamic heterogeneity have shown that systems larger than $10^4$ particles are sometimes needed. [10, 12, 154]

The difference between MD and MC is the way the system explores phase space. The molecular dynamics method simulates the physical motion of $N$ interacting particles. As an input, one defines a density profile $\mathbf{r}_0^N$, particle velocities $\mathbf{v}_0^N$, and an interaction potential between particles. The method solves the classical equations of motion step by step using a finite difference approach. As an output, one obtains physical particle trajectories $(\mathbf{r}^N(t), \mathbf{v}^N(t))$ from which thermodynamic quantities can be computed, see Sec. II.5. By construction, the trajectories sample the microcanonical ensemble. Other ensembles can be simulated by adding degrees of freedom which simulate baths which generate equilibrium fluctuations in any statistical ensemble.[169, 171, 172]

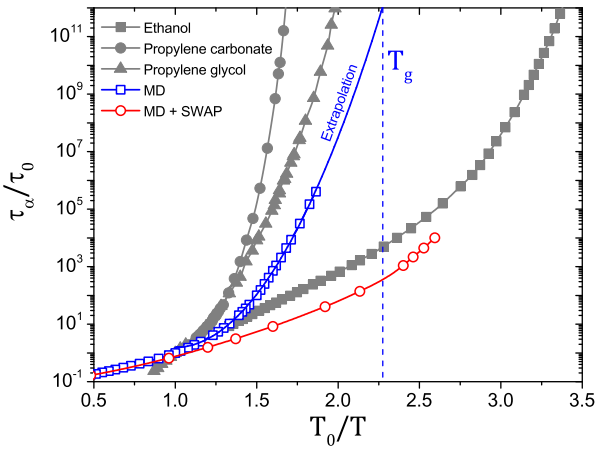


Figure 5: Isobaric relaxation time of supercooled liquids as a function of the inverse temperature for ethanol, [173] propylene carbonate, [174] and propylene glycol, [175] as well as the standard molecular dynamics (open squares) and its combination with the swap Monte-Carlo algorithm (open circles) [176] for three-dimensional polydisperse soft spheres [44]. We renormalize axis using the onset of glassy dynamics, ($\tau_0 = 10^{-10}$s in experiments), and the corresponding $T_0$. We fit MD results with a parabolic fit, which provides a reasonable estimate of $T_g$ for this system (vertical dashed line). The SWAP algorithm (open circles) can equilibrate the numerical model well below that $T_g$ value.

Molecular dynamics mimics the physical motion of particles, very much as it takes place in experiments, but computers are much less efficient than Nature. Long MD simulations of a simple glass model (about a month) can only track the first 4-5 orders of magnitude of dynamical slowdown in supercooled liquids approaching the glass transition, to be compared to 12-13 orders of magnitude in real molecular liquids. In Fig. 5, we show relaxation time $\tau_\alpha$ of some molecular liquids of various fragilities, [173, 174, 175, 177] and MD simulations of polydisperse soft spheres under isobaric condition. The temperature range accessible with MD simulations is far from the experimentally relevant regime, and stops well before $T_g$ is reached (estimated from a parabolic

fit [178]).

Recently, efficient software packages for MD have been developed that use the power of graphic cards. [179, 180] They typically yield a speed-up of about two orders of magnitude over normal MD, which is sufficient to get below the mode-coupling crossover, and thus access interesting new physics and dynamics. [164, 179]

## II.4 Beating the timescale problem: Monte Carlo simulations

Monte Carlo simulations aim at efficiently sampling the configurational space with Boltzmann statistics.[181, 182] A stochastic Markov process is generated in which a given configuration $\mathbf{r}^N$ is visited with a probability proportional to the Boltzmann factor $e^{-\beta U(\mathbf{r}^N)}$, where $\beta = 1/T$ and $U$ are the inverse of the temperature and the potential energy, respectively. The method only considers configurational, and not kinetic, degrees of freedom, and is suitable for configurational entropy measurements.

A Markov process is defined by the transition probability $T(\mathbf{r}^N \to \mathbf{r'}^N)$ to go from configurations $\mathbf{r}^N$ to $\mathbf{r'}^N$. To sample configurations with a probability $P(\mathbf{r}^N)$ given by the Boltzmann factor, the global balance condition should be verified

$$\sum_{\mathbf{r'}^N} P(\mathbf{r}^N) T(\mathbf{r}^N \to \mathbf{r'}^N) = \sum_{\mathbf{r'}^N} P(\mathbf{r'}^N) T(\mathbf{r'}^N \to \mathbf{r}^N) . \tag{2}$$

We consider a stronger condition and impose the equality in Eq. (2) to be valid for each new state $\mathbf{r'}^N$. This detailed balance condition reads

$$\frac{T(\mathbf{r}^N \to \mathbf{r'}^N)}{T(\mathbf{r'}^N \to \mathbf{r}^N)} = \frac{P(\mathbf{r'}^N)}{P(\mathbf{r}^N)} = \exp\left[-\beta\left(U(\mathbf{r'}^N) - U(\mathbf{r}^N)\right)\right] \tag{3}$$

In practice, $T(\mathbf{r}^N \to \mathbf{r'}^N) = \alpha(\mathbf{r}^N \to \mathbf{r'}^N) \times \mathsf{acc}(\mathbf{r}^N \to \mathbf{r'}^N)$, where $\alpha$ and $\mathsf{acc}$ are the probabilities to propose a trial move and to accept it, respectively. We consider a symmetric matrix $\alpha$ for trials such that the matrix $\mathsf{acc}$ obeys the same equation as $T$ in Eq. (3). If trial moves are accepted with probability $\mathsf{acc}(\mathbf{r}^N \to \mathbf{r'}^N) = \min\left\{1, \exp\left[-\beta(U(\mathbf{r'}^N) - U(\mathbf{r}^N))\right]\right\}$ (Metropolis criterion), [181] the configurations are drawn from the canonical distribution at equilibrium at the desired temperature.

Contrary to MD simulations, dynamics in a Monte Carlo simulation is not physical, since it results from a random exploration of configurational space. This is actually good news, since there is a considerable freedom in the choice of trial moves, opening the possibility to beat the numerical timescale problem illustrated in Fig. 5. The choice of trial move depends on the purpose of the numerical simulation. A standard trial move consists in selecting a particle at random and slightly displacing it. For small steps, the dynamics obviously resembles the (very physical) Brownian dynamics. [183]

Efficient Monte Carlo simulations should in principle be possible using lattice models for glasses, which would use discrete rather than continuous degrees of freedom. This approach has been heavily used to analyse models based on dynamic facilitation such as kinetic Ising models [184], or plaquette models [185] but the entropy does not play any central role in these models. Lattice glass models were introduced as lattice models that have, in some controlled mean-field limit, a random first order transition, [90, 91] but simulation studies of finite dimensional versions of these models remain scarce, [186] and we are aware of no study of configurational entropy in such lattice models.

If instead efficient equilibration is targeted, more efficient but less physical trial moves should be preferred. In the SWAP algorithm, [44, 161, 187, 188, 189, 190, 191] trial moves combine standard displacement moves and attempts to swap the diameters of two randomly chosen particles. Since the trial moves satisfy detailed balance in Eq. (3), the SWAP algorithm by construction generates equilibrium configurations from the canonical distribution.

Using continuously polydisperse samples, this algorithm outperforms standard MC or MD, as equilibrium liquids can be generated at temperatures below the experimental glass transi-

tion. [44] In Fig. 5, we show the equilibrium relaxation time $\tau_\alpha$ of an Hybrid scheme of MD and SWAP MC developed recently in Ref. [176]. The relaxation dynamics with this scheme is significantly faster than with standard MD, which makes equilibration of the system possible even below the estimated experimental glass transition temperature $T_g$. Accessing numerically these low temperatures is crucial to compare simulations and experiments. From a theoretical perspective, the concept of metastable state applies far better at low temperatures. In particular, numerical estimates for the configurational entropy become more meaningful in these extreme temperature conditions.

To conclude, Monte Carlo simulations are very relevant in the present context, because their flexibility allows us to compute and compare different estimates for the configurational entropy of supercooled liquids. [33, 136] These measurements are done under perfectly controlled conditions, in a temperature regime relevant to experimental works, and even at lower temperatures. [16]

### II.5 From microscopic configurations to observables

The output of a numerical simulation consists in a series of equilibrium configurations. To measure an observable numerically, one must first express it as a function of the positions of the particles.

Static quantities describing the structure of the liquid are easily computed.[192] In particular, the density field is given by

$$\rho(\mathbf{r}) = \sum_{i=1}^{N} \delta(\mathbf{r} - \mathbf{r}_i) \ . \tag{4}$$

Two-point static density correlation functions such as the pair correlation function

$$g(\mathbf{r}) = \frac{1}{\rho N} \left\langle \sum_{i \neq j} \delta(\mathbf{r} + \mathbf{r}_i - \mathbf{r}_j) \right\rangle \ , \tag{5}$$

where $\rho = N/V$ is the number density and the bracket indicate an ensemble average at thermal equilibrium, and the structure factor

$$S(\mathbf{k}) = \frac{1}{N} \langle \rho_{\mathbf{k}} \rho_{-\mathbf{k}} \rangle \ , \tag{6}$$

are evaluated, where $\rho_{\mathbf{k}} = \sum_{i=1}^{N} e^{i\mathbf{k}\cdot\mathbf{r}_i}$ is the Fourier transform of the density field. Even if these quantities are not relevant to describe the dynamical slowdown of the supercooled liquid (see Fig. 1), they are convenient to detect instabilities of the homogeneous fluid (crystallization, fractionation). Thermodynamic quantities (such as energy, pressure), and their fluctuations (e.g. specific heats, compressibility), related to macroscopic response functions, can be computed directly from the two-point structure of the liquid.

As presented in Sec. I.3, the relevant order parameter for the glass transition is the overlap $Q$ that quantifies the similarity of equilibrium density profiles. This quantity compares the coarse-grained density profiles of two configurations, to remove the effect of short-time thermal vibrations. Numerically, the following definition is very efficient

$$Q = \frac{1}{N} \sum_{i,j} \theta(a - |\mathbf{r}_{1i} - \mathbf{r}_{2j}|) \ , \tag{7}$$

where $\mathbf{r}_1$ and $\mathbf{r}_2$ are the positions of particles in distinct configurations, and $\theta(x)$ is the Heaviside step function. The parameter $a$ is usually a small fraction (typically $0.2-0.3$) of the particle diameter. The overlap is by definition equal to 1 for two identical configurations, it is slightly smaller than 1 due to the effect of vibrations, and becomes close to zero (more precisely $4\pi a^3\rho/3 \ll 1$) for uncorrelated liquid configurations at density $\rho$.

## III Configurational entropy by estimating a 'glass' entropy

### III.1 General strategy

The configurational entropy enumerates the number of distinct glass states. One possible strategy to achieve this enumeration is to first

estimate the total number of configurations, or phase space volume, $\mathcal{N}_{\rm tot}$. If one can then measure the number of configurations belonging to the same glass state, $\mathcal{N}_{\rm glass}$, the number of glass states $\mathcal{N}_{\rm conf}$ can be deduced, $\mathcal{N}_{\rm conf} = \mathcal{N}_{\rm tot}/\mathcal{N}_{\rm glass}$. Taking the logarithm of $\mathcal{N}_{\rm conf}$ yields the configurational entropy

$$S_{\rm conf} = S_{\rm tot} - S_{\rm glass}. \tag{8}$$

Whereas the measurement of the total entropy $S_{\rm tot}$ is straightforward, the art of measuring the configurational entropy lies in the quality of the unavoidable approximation made to determine $S_{\rm glass}$. Recall that experimentalists typically use $S_{\rm glass} \approx S_{\rm xtal}$. This is not a practical method for simulations, because numerical models which can crystallize are generally very poor glass-formers. In this section, we describe several possible strategies to measure $S_{\rm glass}$ which do not rely on the knowledge of the crystal state, and present their limitations.

Let us now introduce our notations for entropy calculations. We consider a $M$-component system in the canonical ensemble in $d$ spatial dimensions, with $N$, $V$, and $T = 1/\beta$ the number of particles, volume, and temperature, respectively. We fix the Boltzmann constant to unity. We take $M = N$ to treat continuously polydisperse systems. The concentration of the $m$-th species is $X_m = N_m/N$, where $N_m$ is the number of particles of the $m$-th species ($N = \sum_{m=1}^{M} N_m$). A point in position space is denoted as $\mathbf{r}^N = (\mathbf{r}_1, \mathbf{r}_2, \cdots, \mathbf{r}_N)$. For simplicity, we consider equal masses, irrespective of the species, which we set to unity.

For this system, the following partition function in the canonical ensemble is conventionally used [193]

$$Z = \frac{\Lambda^{-Nd}}{\Pi_{m=1}^{M} N_m!} \int_V {\rm d}\mathbf{r}^N e^{-\beta U(\mathbf{r}^N)}, \tag{9}$$

where $\Lambda$ and $U(\mathbf{r}^N)$ are respectively the de Broglie thermal wavelength and the potential energy. The only fluctuating variables are the configurational degrees of freedom $\mathbf{r}^N$, since momenta are already traced out in Eq. (9).

## III.2 Total entropy $S_{\rm tot}$

An absolute estimate of the total entropy at a given state point can be obtained by performing a thermodynamic integration from a reference point where the entropy is exactly known, [110, 114, 194, 195] typically the ideal gas at $\rho \to 0$ or $\beta \to 0$. This approach works for all state points which can be studied in equilibrium conditions, and are connected to the reference point by a series of equilibrium state points. This is usually doable also in most experiments. However, this constraint prevents a direct analysis of the entropy of vapor-deposited ultrastable glasses produced directly at very low temperature. In practice, to perform the thermodynamic integration and access $S_{\rm tot}$, we need to distinguish between continuous 'soft' interaction potentials, such as the Lennard-Jones potential, and discontinuous 'hard' potentials, as in the hard sphere model:

$$S_{\rm tot} = S_{\rm id} + \beta E_{\rm pot}(\beta) - \int_0^\beta {\rm d}\beta' E_{\rm pot}(\beta') \quad \text{(soft)}, \tag{10}$$

$$S_{\rm tot} = S_{\rm id} - N \int_0^\rho {\rm d}\rho' \frac{(p(\rho')-1)}{\rho'} \quad \text{(hard)}, \tag{11}$$

where $S_{\rm id}$, $E_{\rm pot}$ and $p = P/(\rho T)$ are the ideal gas entropy, the averaged potential energy, and the reduced pressure, respectively. The ideal gas entropy $S_{\rm id}$ can be written as

$$S_{\rm id} = N\frac{(d+2)}{2} - N\ln\rho - N\ln\Lambda^d + S_{\rm mix}^{(M)}, \tag{12}$$

where $S_{\rm mix}^{(M)}$ is the mixing entropy of the ideal gas,

$$S_{\rm mix}^{(M)} = \ln\left(\frac{N!}{\Pi_{m=1}^{M} N_m!}\right). \tag{13}$$

When $M$ is finite and $N_m \gg 1$, Stirling's approximation can be used, $\ln N_m! \simeq N_m \ln N_m - N_m$, and Eq. (13) reduces to $S_{\rm mix}^{(M)}/N = -\sum_{m=1}^{M} X_m \ln X_m$.

As a representative example, Fig. 6(a) shows the temperature dependence of the numerically measured total entropy in the Kob-Andersen model. [45] It decreases monotonically with decreasing the temperature.

### III.3 Inherent structures as glass states

The first strategy that we describe to identify glass states and estimate $S_{\rm glass}$ is based on the potential energy landscape (PEL). [111, 112, 113, 117, 143] The central idea is to assume that each configuration can be decomposed as

$$\mathbf{r}^N = \mathbf{r}^N_{\rm IS} + \Delta\mathbf{r}^N, \tag{14}$$

where $\mathbf{r}^N_{\rm IS}$ is the position of the 'inherent structure', *i.e.* the potential energy minimum closest to the original configuration. This trivial decomposition becomes meaningful if one makes the central assumption that *different inherent structures represent distinct glass states*. It follows immediately that the glass entropy, $S_{\rm glass}$, then quantifies the size of the basin of attraction of inherent structures.

Assuming that temperature is low, $\Delta\mathbf{r}^N$ can be treated in the harmonic approximation. Expanding the potential energy $U(\mathbf{r}^N)$ around the inherent structure $\mathbf{r}^N_{\rm IS}$, one gets

$$U_{\rm harm}(\mathbf{r}^N) \simeq U(\mathbf{r}^N_{\rm IS}) + \frac{1}{2}\sum_{i,j}\frac{\partial^2 U(\mathbf{r}^N_{\rm IS})}{\partial\mathbf{r}_i\partial\mathbf{r}_j}\Delta\mathbf{r}_i\Delta\mathbf{r}_j. \tag{15}$$

Injecting this expansion in the partition function, Eq. (9), gives

$$Z_{\rm harm} = e^{-\beta U(\mathbf{r}^N_{\rm IS})}\Pi_{a=1}^{Nd}(\beta\hbar\omega_a)^{-1}, \tag{16}$$

where $\omega_a^2$ are the eigenvalues of the Hessian matrix. We also considered that each inherent structure is realized $\Pi_{m=1}^{M}N_m!$ times in the phase space volume, as permuting the particles within each specie leaves the configuration unchanged (see related argument in mean-field theory) [196, 197, 198]. This factorial term cancels out with the denominator in Eq. (9).

We have implicitly assumed that exchanging two distinct particles produces a different inherent structure, [118] which is consistent with the identification of energy minima as glass states. Physically, this implies that there is no mixing entropy associated with inherent structures. As realized recently, [116] this assumption produces

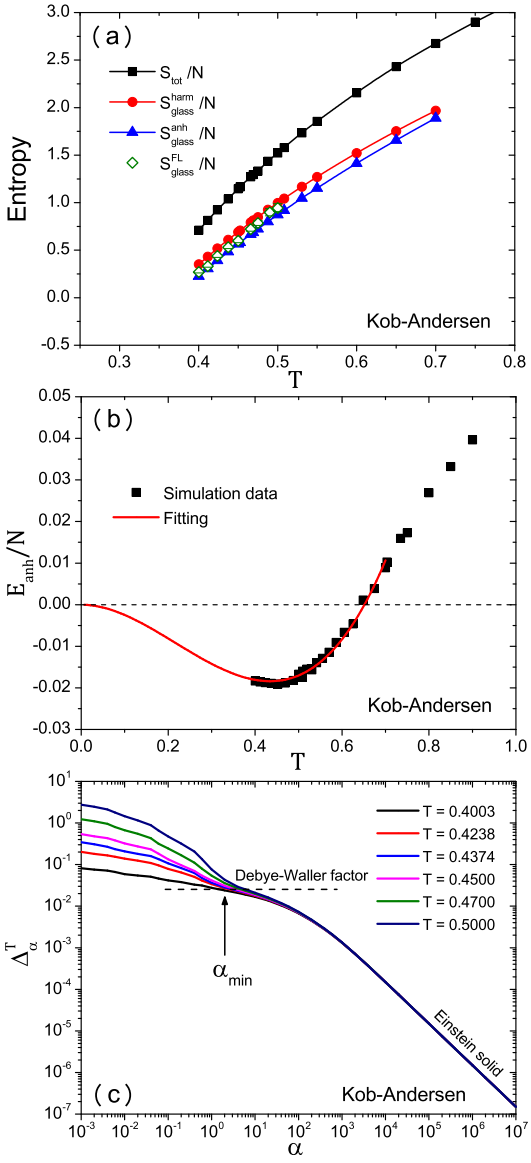


Figure 6: (a) Total entropy $S_{\rm tot}$ and various estimates of the glass entropy $S_{\rm glass}$: harmonic $S^{\rm harm}_{\rm glass}$, with anharmonic correction $S^{\rm anh}_{\rm glass}$, and the Frenkel-Ladd entropy $S^{\rm FL}_{\rm glass}$. (b) Anharmonic energy $E_{\rm anh}$ from simulations (black points) and polynomial fitting to third order (red line). (c) Constrained mean-squared displacement in the Frenkel-Ladd method. The dashed horizontal line correspond to the Debye-Waller factor independently measured in the bulk dynamics at the lowest temperature. The vertical arrow indicates $\alpha_{\rm min}$.

unphysical results for systems with continuous polydispersity.

Averaging over independent inherent structures (denoted by $\langle(\cdots)\rangle_{\rm IS}$), the free energy of the harmonic solid is obtained,

$$\begin{aligned} -\beta F_{\rm harm} &= \langle \ln Z_{\rm harm}\rangle_{\rm IS} \qquad (17)\\ &= -\beta \left\langle U(\mathbf{r}_{\rm IS}^N)\right\rangle_{\rm IS} - \left\langle \sum_{a=1}^{Nd} \ln(\beta\hbar\omega_a)\right\rangle_{\rm IS} \end{aligned}$$

The internal energy of the harmonic solid is

$$E_{\rm harm} = \frac{Nd}{2}T + \left\langle U(\mathbf{r}_{\rm IS}^N)\right\rangle_{\rm IS} + \frac{Nd}{2}T, \qquad (18)$$

where the first and last terms are the kinetic and harmonic potential energies. Using Eqs. (17) and (18), we finally obtain the glass entropy in the harmonic approximation:

$$\begin{aligned} S_{\rm glass}^{\rm harm} &= \beta\left(E_{\rm harm} - F_{\rm harm}\right),\\ &= \left\langle \sum_{\rm a=1}^{Nd} \{1 - \ln(\beta\hbar\omega_a)\}\right\rangle_{\rm IS}. \qquad (19) \end{aligned}$$

In practice, this method requires the production of a large number of independent inherent structures, obtained by performing energy minimizations from equilibrium configurations using widespread algorithms such as the steepest decent or conjugate gradient methods, [199] or FIRE. [200] The energy $U(\mathbf{r}_{\rm IS})$ is measured, and the Hessian matrix is diagonalized to get the eigenvalues $\omega_a^2$. Using Eq. (19), these measurements then provide the glass entropy $S_{\rm glass}^{\rm harm}$. The numerical results for $S_{\rm glass}^{\rm harm}(T)$ in the Kob-Andersen model are shown in Fig. 6(a). The difference $S_{\rm tot} - S_{\rm glass}^{\rm harm}$ is a widely used practical definition of the configurational entropy in computer simulations. [114, 115, 153, 194, 201, 202]

## III.4 Anharmonicity

Although presumably not the biggest issue, it is possible to relax the harmonic assumption in the above procedure. [143] First, the anharmonic energy, $E_{\rm anh}$, is obtained by subtracting the harmonic energy in Eq. (18) from the total one,

$$E_{\rm anh} = E_{\rm pot} - \left\langle U(\mathbf{r}_{\rm IS}^N)\right\rangle_{\rm IS} - \frac{Nd}{2}T. \qquad (20)$$

The anharmonic contribution to the entropy can then be estimated as

$$S_{\rm anh} = \int_0^T \frac{dT'}{T'}\frac{\partial E_{\rm anh}(T')}{\partial T'}, \qquad (21)$$

which requires a low-temperature extrapolation of the measured $E_{\rm anh}(T)$. This can be done using an empirical polynomial fitting, $E_{\rm anh}(T) = \sum_{k\geq 2} a_k T^k$, where the sum starts at $k = 2$ to ensure a vanishing anharmonic specific heat at $T = 0$. By substituting this expansion in Eq. (21), we obtain

$$S_{\rm anh}(T) = \sum_{k\geq 2} \frac{k}{k-1} a_k T^{k-1}. \qquad (22)$$

We show the numerically measured $E_{\rm anh}$ for the Kob-Andersen model, along with its polynomial fit in Fig. 6(b). The non-trivial behavior of $E_{\rm anh}$ suggests that the harmonic description overestimates phase space at low $T$, but underestimates it at high $T$, a trend widely observed across other fragile glass-formers. [143, 165] The resulting $S_{\rm anh}$ using Eq. (22) is thus negative and is of the order of $S_{\rm anh}/N \approx -0.1$, which is a small but measurable correction to $S_{\rm conf}$. As a result, the improved glass entropy $S_{\rm glass}^{\rm anh} = S_{\rm glass}^{\rm harm} + S_{\rm anh}$ is slightly smaller than the harmonic estimate, as shown in Fig. 6(a).

## III.5 Glass entropy without inherent structures

The identification of inherent structures with glass states is a strong assumption which can be explicitly proven wrong in some model systems. [77, 116, 203] Moreover, inherent structures cannot be defined in the hard sphere model (because minima of the potential energy cannot be defined), which is obviously an important theoretical model to study the glass transition.

A more direct route to a glass entropy which automatically includes all anharmonic contributions and can be used for hard spheres is obtained by using the following decomposition, [108, 109, 110, 136, 194, 203, 204, 205]

$$\mathbf{r}^N = \mathbf{r}_{\rm ref}^N + \delta\mathbf{r}^N, \qquad (23)$$

where $\mathbf{r}^N_{\rm ref}$ is a reference equilibrium configuration. The first difference with Eq. (14) is that inherent structures do not appear, since deviations are now measured from a given equilibrium configuration.

The second difference is the strategy to estimate the size of the basin surrounding $\mathbf{r}^N_{\rm ref}$, which makes use of a constrained thermodynamics integration about the fluctuating variables $\delta\mathbf{r}^N$. The potential energy of the system is $\beta U(\mathbf{r}^N)$, is augmented by a harmonic potential to constrain $\delta\mathbf{r}^N$ to remain small, leading to

$$\beta U_\alpha(\mathbf{r}^N,\mathbf{r}^N_{\rm ref}) = \beta U(\mathbf{r}^N) + \alpha\sum_{i=1}^N |\mathbf{r}_i-\mathbf{r}_{{\rm ref},i}|^2. \tag{24}$$

We consider the statistical mechanics of a given basin, specified by $\mathbf{r}^N_{\rm ref}$, under the harmonic constraint. The partition function and the corresponding statistical average are

$$Z_\alpha = \Lambda^{-Nd}\int_V {\rm d}\mathbf{r}^N e^{-\beta U_\alpha(\mathbf{r}^N,\mathbf{r}^N_{\rm ref})}, \tag{25}$$

$$\langle(\cdots)\rangle^{\rm T}_\alpha = \frac{\int_V {\rm d}\mathbf{r}^N(\cdots)e^{-\beta U_\alpha(\mathbf{r}^N,\mathbf{r}^N_{\rm ref})}}{\int_V {\rm d}\mathbf{r}^N e^{-\beta U_\alpha(\mathbf{r}^N,\mathbf{r}^N_{\rm ref})}}. \tag{26}$$

Note that the factorial term $\Pi_{m=1}^M N_m!$ in Eq. (25) is treated as in Eq. (16) within the PEL approach. We consider the entropy of a constrained system as $S_\alpha = \beta(E_\alpha - F_\alpha)$, where $\beta E_\alpha = \frac{Nd}{2} + \beta\left\langle U_\alpha(\mathbf{r}^N,\mathbf{r}^N_{\rm ref})\right\rangle^{\rm T}_\alpha$ and $\beta F_\alpha = -\ln Z_\alpha$ are the internal energy and free energy, respectively.

In the glass phase, the system remains close to the reference configuration for any value of $\alpha$, including $\alpha = 0$. For the liquid, this is true only for times smaller than the structural relaxation time. For $\alpha$ small but finite, however, the system must remain close to the reference configuration and explore the basin whose size we wish to estimate. We therefore define the glass entropy in the Frenkel-Ladd method as [108]

$$S^{\rm FL}_{\rm glass} = \lim_{\alpha_{\rm min}\to 0}\overline{S_{\alpha_{\rm min}}}, \tag{27}$$

where $\overline{(\cdots)}$ represents an average over the reference configuration. The limit in Eq. (27) is a central approximation in this method, which is directly related to conceptual problems summarised in Sec. I.4. Because metastable glass states are not infinitely long-lived in finite dimensions, a finite value of $\alpha$ is needed to prevent an ergodic exploration of the configuration space, and the limit in Eq. (27) is difficult to take in practice. The choice of $\alpha_{\rm min}$ amounts to defining 'by hand' the glass state as the configurations that can be reached at equilibrium for a spring constant $\alpha_{\rm min}$.

The practical details are as follows. At very large $\alpha$ ($= \alpha_{\rm max}$), the entropy is known exactly because the second term in the right hand side of Eq. (24) is dominant. The entropy of the system is described by the Einstein solid,

$$S_{\alpha_{\rm max}} = \frac{Nd}{2} - N\ln\Lambda^d - \frac{Nd}{2}\ln\left(\frac{\alpha_{\rm max}}{\pi}\right). \tag{28}$$

By performing a thermodynamic integration from $\alpha_{\rm max}$, one gets $S_{\alpha_{\rm min}}$, and thus $S^{\rm FL}_{\rm glass}$ from Eq. (27)

$$S^{\rm FL}_{\rm glass} = S_{\alpha_{\rm max}} + N\lim_{\alpha_{\rm min}\to 0}\int_{\alpha_{\rm min}}^{\alpha_{\rm max}} {\rm d}\alpha\Delta^{\rm T}_\alpha, \tag{29}$$

where $\Delta^{\rm T}_\alpha$ is defined by

$$\Delta^{\rm T}_\alpha = \frac{1}{N}\overline{\left\langle\sum_{i=1}^N |\mathbf{r}_i-\mathbf{r}_{{\rm ref},i}|^2\right\rangle^{\rm T}_\alpha}. \tag{30}$$

To perform the integration and take the limit $\alpha_{\rm min}\to 0$ in Eq. (27), we write:

$$\lim_{\alpha_{\rm min}\to 0}\int_{\alpha_{\rm min}}^{\alpha_{\rm max}}{\rm d}\alpha\Delta^{\rm T}_\alpha \simeq \alpha_{\rm min}\Delta^{\rm T}_{\alpha_{\rm min}} + \int_{\alpha_{\rm min}}^{\alpha_{\rm max}}{\rm d}\alpha\Delta^{\rm T}_\alpha. \tag{31}$$

The practical choice for $\alpha_{\rm max}$ is simple, as it is sufficient that it lies deep inside the Einstein solid regime where $\Delta^{\rm T}_\alpha = d/(2\alpha)$ is satisfied. For $\alpha_{\rm min}$, a more careful look at the simulation results is needed.

In Fig. 6(c), we show $\Delta^{\rm T}_\alpha$ for the Kob-Andersen model at low temperature. The Einstein solid limit is satisfied for large $\alpha$, and we can fix $\alpha_{\rm max} = 10^7$. When $\alpha$ decreases, deviations from Einstein solid behavior are observed, and

a plateau emerges. Decreasing $\alpha$ further, the harmonic constraint for $\Delta_\alpha^{\rm T}$ becomes too weak and the glass metastability is not sufficient to prevent the system from diffusing away from the reference configuration, which translates into an upturn of $\Delta_\alpha^{\rm T}$ at small $\alpha$. It is instructive to compare the plateau level with the Debye-Waller factor measured from the bulk dynamics, [164] indicated by a dashed line. This comparison shows that $\alpha_{\rm min} \approx 2$ is a good compromise: it is in the middle of the plateau, and corresponds to vibrations comparable to the ones observed in the bulk. Using this value for $\alpha_{\rm min}$, we obtain the Frenkel-Ladd glass entropy shown in Fig. 6(a). We observe that $S_{\rm glass}^{\rm FL}$ is smaller than $S_{\rm glass}^{\rm harm}$, and becomes comparable to the anharmonic estimate using inherent structures, $S_{\rm glass}^{\rm anh}$, as temperature decreases, confirming that anharmonicities are automatically captured by the Frenkel-Ladd method. [203]

We show the resulting $S_{\rm conf} = S_{\rm tot} - S_{\rm glass}^{\rm FL}$ in Fig. 2. Comparing with experimental data, the temperature range where $S_{\rm conf}$ can be measured is limited since the SWAP algorithm is not efficient for binary mixtures such as the Kob-Andersen model. [201] Nevertheless an extrapolation to lower temperature suggests that $S_{\rm conf}/N$ may vanish at a finite $T_{\rm K}$. [33]

### III.6 Mixing entropy in the glass state

Using multi-component mixtures is essential to study supercooled liquids and glasses for spherical particle systems, as exemplified by metallic [159] and colloidal [158, 206] glasses. This is also true for most computer simulations, since monocomponent systems crystallize too easily, except for large spatial dimensions [147] or exotic mean-field like model systems. [207] For such multi-components systems, a mixing entropy term appears in the total entropy, see Eq. (12), with no analog in the glass entropy, see Eqs. (19) and (29). Physically, this is because we decided to treat two configurations where distinct particles had been exchanged as two distinct glass states.

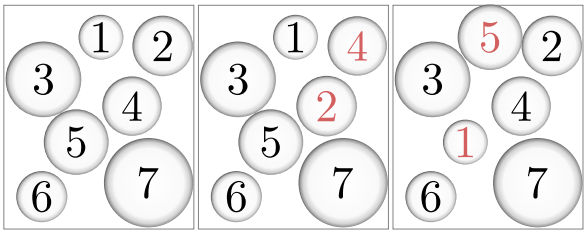


(a) (b) (c)

Figure 7: Mixing entropy conundrum for continuous polydispersity. Should one treat these 3 configurations as 3 distinct glass states, or only two by grouping (a) and (b) together? In Sec. III.7, a computational measurement is described that provides the correct answer, instead of guessing it.

For typical binary mixtures studied in computer simulations, the mixing entropy is about as large as the configurational entropy itself over the range accessible to molecular dynamics simulations. [110, 114] Therefore, neglecting the mixing entropy can change the configurational entropy by about 100%, which in turn produces a similar uncertainty on the estimate of the Kauzmann temperature. Properly dealing with the mixing entropy is thus mandatory. [116]

For discrete mixtures, such as binary and ternary mixtures, with large size asymmetries, the above treatment produces an accurate determination of $S_{\rm conf}$. [114, 115, 153, 194, 201, 202] However, for systems with a continuous distribution of particle sizes, such as colloidal particles and several computer models, this leads to unphysical results. In the liquid, the mixing entropy is formally divergent, since for $M = N$ it becomes $S_{\rm mix}^{(M=N)}/N = (\ln N!)/N \simeq \ln N - 1 \to \infty$. [208, 209] Because the glass entropy remains finite in conventional treatments, the configurational entropy also diverges, leading to the conclusion that no entropy crisis can take place in systems with continuous polydispersity. [116, 210] A similar argument was proposed by Donev *et al* to suggest that an entropy crisis does not exist in binary mixtures. [119]

In fact, the above treatments do not accu-

rately quantify the mixing entropy contribution in the glass entropy. This can be easily seen by considering a continuously polydisperse material with a very narrow size distribution, which should physically behave as a mono-component system, but has a mathematically divergent mixing entropy. In addition to this trivial example, the fundamental problem is illustrated in Fig. 7, which sketches three configurations which differ by the exchange of a single pair of particles. The inherent structure and the standard Frenkel-Ladd methods treat those three configurations as distinct. Physically, configurations (a) and (b) should instead be considered as the same glass state, since they differ by the exchange of two particles with nearly identical diameters. The glass entropy should contain some amount of mixing entropy, taking into account those particle permutations that leave the glass state unaffected. [116]

Recently, two methods were proposed to estimate the glass mixing entropy. The first method provides a simple approximation to the glass mixing entropy using information about the potential energy landscape. [116] We describe the second one in the next subsection, which leads to a direct determination of the glass mixing entropy using a generalized Frenkel-Ladd approach. [33]

### III.7 Generalized Frenkel-Ladd method to measure the glass mixing entropy

A proper resolution to the problematic glass mixing entropy is to directly measure the amount of particle permutations allowed by thermal fluctuations, instead of making an arbitrary decision. [33] Technically, one needs to include particle permutations in the statistical mechanics treatment of the system. In addition to the positions, we introduce the particle diameters, represented as $\Sigma^N = \{\sigma_1, \sigma_2, \cdots, \sigma_N\}$. Let $\pi$ denote a permutation of $\Sigma^N$, and $\Sigma^N_\pi$ represents the resulting sequence. There exist $N!$ such permutations. We define a reference sequence $\Sigma^N_{\pi^*} = (\sigma_1, \sigma_2, \sigma_3, \cdots, \sigma_N)$. The potential energy now depends on both positions and diameters, $U(\Sigma^N_\pi, \mathbf{r}^N)$. For simplicity, we write $U(\mathbf{r}^N) = U(\Sigma^N_{\pi^*}, \mathbf{r}^N)$ for the reference $\Sigma^N_{\pi^*}$.

Including particle diameters as additional degrees of freedoms, the partition function reads

$$\mathcal{Z} = \frac{1}{N!} \sum_\pi \frac{\Lambda^{-Nd}}{\Pi_{m=1}^M N_m!} \int_V \mathrm{d}\mathbf{r}^N e^{-\beta U(\Sigma^N_\pi, \mathbf{r}^N)}. \tag{32}$$

This partition function is the correct starting point to compute the configurational entropy in multi-component systems, including continuous polydispersity. The resulting method is a straightforward generalization of the Frenkel-Ladd method. [108]

As before, we introduce a reference configuration and a harmonic constraint,

$$\beta U_\alpha(\Sigma^N_\pi, \mathbf{r}^N, \mathbf{r}^N_{\mathrm{ref}}) = \beta U(\Sigma^N_\pi, \mathbf{r}^N) + \alpha \sum_{i=1}^N |\mathbf{r}_i - \mathbf{r}_{\mathrm{ref},i}|^2, \tag{33}$$

where $\mathbf{r}^N_{\mathrm{ref}}$ is a reference equilibrium configuration.

For the unconstrained system with $\alpha = 0$, the partition function in Eq. (32) reduces to the conventional partition function in Eq. (9), because diameter permutations can be compensated by the configurational integral. Therefore, the computation of $S_{\mathrm{tot}}$ is not altered by the introduction of the permutations. For the glass state with $\alpha > 0$, the partition function in Eq. (32) and the corresponding statistical average become

$$\mathcal{Z}_\alpha = \frac{1}{N!} \sum_\pi \frac{N! \Lambda^{-Nd}}{\Pi_{m=1}^M N_m!} \int_V \mathrm{d}\mathbf{r}^N e^{-\beta U_\alpha(\Sigma^N_\pi, \mathbf{r}^N, \mathbf{r}^N_{\mathrm{ref}})} \tag{34}$$

$$\langle (\cdots) \rangle^{\mathrm{T,S}}_\alpha = \frac{\sum_\pi \int_V \mathrm{d}\mathbf{r}^N (\cdots) e^{-\beta U_\alpha(\Sigma^N_\pi, \mathbf{r}^N, \mathbf{r}^N_{\mathrm{ref}})}}{\sum_\pi \int_V \mathrm{d}\mathbf{r}^N e^{-\beta U_\alpha(\Sigma^N_\pi, \mathbf{r}^N, \mathbf{r}^N_{\mathrm{ref}})}}, \tag{35}$$

We add a factor $N!$ in the numerator of Eq. (34), because there exist $N!$ configurations defined by the permutations of the particle identities of the reference configuration $\mathbf{r}^N_{\mathrm{ref}}$. More crucially, due to the presence of $\mathbf{r}^N_{\mathrm{ref}}$, the partition function in Eq. (34) is not identical to the one in Eq. (25).

Following the same steps as before we get the glass entropy by a generalized Frenkel-Ladd

method, defined as

$$S_{\rm glass}^{\rm GFL} = S_{\alpha_{\rm max}} + N \lim_{\alpha_{\rm min}\to 0} \int_{\alpha_{\rm min}}^{\alpha_{\rm max}} {\rm d}\alpha \Delta_\alpha^{\rm T,S} + S_{\rm mix}^{(M)} - \overline{\mathcal{S}_{\rm mix}(\mathbf{r}_{\rm ref}^N, \beta)}, \quad (36)$$

with

$$\Delta_\alpha^{\rm T,S} = \frac{1}{N} \overline{\left\langle \sum_{i=1}^{N} |\mathbf{r}_i - \mathbf{r}_{{\rm ref},i}|^2 \right\rangle_\alpha^{\rm T,S}}, \quad (37)$$

and $\mathcal{S}_{\rm mix}(\mathbf{r}_{\rm ref}^N, \beta)$ is obtained as

$$\mathcal{S}_{\rm mix}(\mathbf{r}_{\rm ref}^N, \beta) = -\ln\left( \frac{1}{N!} \sum_\pi e^{-\beta\left(U(\Sigma_\pi^N, \mathbf{r}_{\rm ref}^N) - U(\mathbf{r}_{\rm ref}^N)\right)} \right). \quad (38)$$

Note that in Eq. (36), the mean-squared displacement $\Delta_\alpha^{\rm T,S}$ is evaluated by simulations where both positions and diameters fluctuate, and we expect $\Delta_\alpha^{\rm T,S} \geq \Delta_\alpha^{\rm T}$. Practically, $\Delta_\alpha^{\rm T,S}$ is computed by Monte Carlo simulations including standard translational displacements and diameter swaps. In addition to this, $S_{\rm glass}^{\rm GFL}$ in Eq. (36) contains another non-trivial contribution, $S_{\rm mix}^{(M)} - \overline{\mathcal{S}_{\rm mix}}$, which requires Monte Carlo simulations of the diameter swaps for a fixed $\mathbf{r}_{\rm ref}^N$. In practice the entropy in Eq. (38) is evaluated by a thermodynamic integration. [33]

For mixtures with large size asymmetry such as the Kob-Andersen model, particle permutations of un-like particles rarely happen, [201] and the generalized Frenkel-Ladd method yields $\overline{\mathcal{S}_{\rm mix}} = S_{\rm mix}^{(M)}$ and $\Delta_\alpha^{\rm T,S} = \Delta_\alpha^{\rm T}$, so that Eq. (36) reduces to the conventional Frenkel-Ladd method in Eq. (29). On the other hand, for continuously polydisperse systems or mixtures with small size asymmetry, we expect $\overline{\mathcal{S}_{\rm mix}}/N < S_{\rm mix}^{(M)}/N \to \infty$ and $\Delta_\alpha^{\rm T,S} > \Delta_\alpha^{\rm T}$. In the limit case of a very narrow continuous distribution, we would have $\overline{\mathcal{S}_{\rm mix}}/N = 0$ and $\Delta_\alpha^{\rm T,S} = \Delta_\alpha^{\rm T}$, and we automatically get back to the treatment of a monocomponent material.

We finally obtain the configurational entropy as $S_{\rm conf} = S_{\rm tot} - S_{\rm glass}^{\rm GFL}$, which finally resolves the paradox raised by the mixing entropy in conventional schemes. For polydisperse systems, both the total entropy and the glass entropy in Eq. (36) contain the diverging mixing entropy term, which thus cancel each from the final expression of the configurational entropy. Instead, the physical mixing entropy contribution is quantified by $\overline{\mathcal{S}_{\rm mix}(\mathbf{r}_{\rm ref}^N, \beta)}$ in Eq. (38), which is finite, and whose value depends on the detailed particle size distribution of the system.

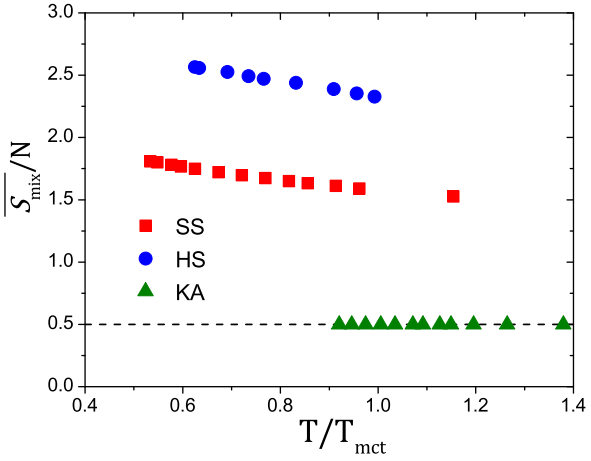


Figure 8: Mixing entropy $\overline{\mathcal{S}_{\rm mix}}/N$ as a function of the normalized temperature $T/T_{\rm mct}$ for polydisperse soft spheres (SS), hard spheres (HS), and the Kob-Andersen model (KA). The dashed-line corresponds to the combinatorial mixing entropy for the KA mixture.

In Fig. 8, we show the measured $\overline{\mathcal{S}_{\rm mix}(\mathbf{r}_{\rm ref}^N, \beta)}$ for three representative glass-forming models. For the Kob-Andersen binary mixture, the combinatorial mixing entropy, $S_{\rm mix}^{(M=2)}/N \approx 0.5$, [114, 194] is found, whereas for continuously polydisperse soft [44] and hard spheres [43] with polydispersity $\approx 23\%$, a finite value of the mixing entropy is measured, with a non-trivial temperature dependence. The data also directly confirms that the mixing entropy cannot be used to disprove the existence of a Kauzmann transition. [119]

Figure 2 shows the final result, $S_{\rm conf} = S_{\rm tot} - S_{\rm glass}^{\rm GFL}$, for polydisperse hard and soft spheres along isochoric [33] and isobaric paths (in preparation), in $d = 2$ [16] and 3. For the hard sphere model, we use the inverse of the reduced pres-

sure, $1/p = \rho T/P$, as the analog of the temperature. Thanks to the efficiency of the SWAP algorithm for these models, we can measure a reduction of the configurational entropy comparable to experimental molecular liquids, and even access values measured in vapor deposited ultrastable glasses. [211] Therefore, the simulation results presented here, together with experimental ones, offer the most complete and persuasive data set for existence of the Kauzmann transition at a finite temperature in $d = 3$ and at zero temperature in $d = 2$.

# IV Configurational entropy from free energy landscape

## IV.1 Franz-Parisi Landau free energy

The mean-field theory of the glass transition introduced in Sec. I.3 suggests a well-defined route to the configurational entropy, [212] based on free energy measurements of a Landau free energy $V(Q)$, expressed as a function of the overlap $Q$ between pairs of randomly chosen equilibrium configurations. [93, 94] A practical definition of the overlap was given in Eq. (7). The introduction of the appropriate global order parameter to detect the glass transition driven by an entropy crisis is the first key step.

The second key point is the assumption that $V(Q)$ contains, for finite dimensional systems, the relevant information about the configurational entropy. As illustrated in Fig. 4, mean-field theory suggests that the glass phase at large $Q$, for $T_K < T < T_{\rm mct}$, is metastable with respect to the equilibrium liquid phase at small $Q$, with a free-energy difference between the two phases that is controlled by the configurational entropy. To measure this configurational entropy, one should first demonstrate the existence of the glass metastability, and use it to infer $S_{\rm conf}$ as a free energy difference between liquid and glass phases.

The computational tools to study $V(Q)$ and metastability are not specific to the glass problem, but can be drawn from computer studies of ordinary first-order phase transitions. [189] To analyze the overlap and its fluctuations, we introduce a reference equilibrium configuration $\mathbf{r}^N_{\rm ref}$. We then define the overlap $Q_{\rm ref} = Q(\mathbf{r}^N, \mathbf{r}^N_{\rm ref})$ between the studied system $\mathbf{r}^N$ and the reference configuration, and introduce a field, $\varepsilon$, conjugate to the overlap,

$$U_\varepsilon(\mathbf{r}^N, \mathbf{r}^N_{\rm ref}) = U(\mathbf{r}^N) - \varepsilon N Q(\mathbf{r}^N, \mathbf{r}^N_{\rm ref}), \quad (39)$$

where $U$ is the potential energy of the unconstrained bulk system ($\varepsilon = 0$). The corresponding statistical mechanics and average become

$$Z_\varepsilon = \Lambda^{-Nd} \int_V {\rm d}\mathbf{r}^N e^{-\beta U_\varepsilon(\mathbf{r}^N, \mathbf{r}^N_{\rm ref})}, \quad (40)$$

$$\langle(\cdots)\rangle_\varepsilon = \frac{\int_V {\rm d}\mathbf{r}^N (\cdots) e^{-\beta U_\varepsilon(\mathbf{r}^N, \mathbf{r}^N_{\rm ref})}}{\int_V {\rm d}\mathbf{r}^N e^{-\beta U_\varepsilon(\mathbf{r}^N, \mathbf{r}^N_{\rm ref})}}, \quad (41)$$

and the related Helmholtz free energy is obtained as

$$-\beta F_\varepsilon = \overline{\ln Z_\varepsilon}, \quad (42)$$

where the overline denotes an average over independent reference configurations. All thermodynamic quantities can then be deduced from $F_\varepsilon$, such as the average overlap $\langle Q\rangle_\varepsilon = -(1/N)\partial F_\varepsilon/\partial\varepsilon$.

Following the spirit of the Landau free energy, [15] we express the free energy as a function of the order parameter $Q$, instead of $\varepsilon$. The Franz-Parisi free energy $V(Q)$ is obtained by a Legendre transform of $F_\varepsilon$,

$$V(Q) = \frac{1}{N}\left(\min_\varepsilon \{F_\varepsilon + \varepsilon N Q\} - F_0\right), \quad (43)$$

where $F_0 = -\beta^{-1}\ln Z_0$ is the free energy of the unconstrained system, which simply ensures that $V(Q) = 0$ for the equilibrium liquid phase at small $Q$. Following standard computational approaches for free-energy calculations, [189] $V(Q)$ is directly obtained by probing the equilibrium fluctuations of the overlap,

$$V(Q) = -\frac{T}{N}\overline{\ln \frac{\Lambda^{-Nd}}{Z_0}\int_V {\rm d}\mathbf{r}^N e^{-\beta U(\mathbf{r}^N)}\delta(Q - Q_{\rm ref})},$$
$$= -\frac{T}{N}\overline{\ln P(Q)}, \quad (44)$$

where $P(Q) = \langle \delta(Q - Q_{\rm ref}) \rangle$ is the probability distribution of the overlap function for the unconstrained bulk system.

This method naturally solves issues about the mixing entropy. [116] As captured in Eq. (43), this construction treats free energy differences, with no need to define absolute values for the entropy. The combinatorial terms in Eq. (41) are therefore not included since they eventually cancel out. Additionally, the constraint applied to the system acts only on the value of the overlap $Q$. Since particle permutations do not affect the value of the overlap, see Eq. (7), particle permutations within the same species can occur both in the liquid, near $Q_{\rm liq}$, and in the glass, near $Q_{\rm glass}$, with a probablity controlled by thermal fluctuations.

In finite dimensions, the secondary minimum in $V(Q)$ obtained in the mean-field limit (see Fig. 4) cannot exist, as the free energy must be convex, for stability reasons. [213] At best, $V(Q)$ should develop a small non-convexity for finite system sizes, and a linear part for larger systems, as for any first-order phase transition. In the presence of a finite field $\varepsilon$, a genuine first-order liquid-to-glass transition is predicted, [93, 94] where $\langle Q \rangle_\varepsilon$ jumps discontinuously to a large value as $\varepsilon$ is increased. This phase transition exists in the mean-field limit, and can in principle survive finite dimensional fluctuations.

The existence of this constrained phase transition induced by a field $\varepsilon$ in finite dimensional systems is needed to identify the Franz-Parisi free-energy with the configurational entropy in the unconstrained bulk system. If a metastable glass phase is detected in some temperature regime $T > T_K$, then it is possible to measure the free-energy difference between the equilibrium liquid and the metastable glass, namely $V(Q_{\rm glass})$. This quantity represents the entropic cost of localizing the system in a single metastable state: this is indeed the configurational entropy.

## IV.2 Computational measurement

The free-energy $V(Q)$ in Eq. (44) is the central physical quantity to measure in computer simulations. [136, 212, 214] It follows from the measurement of rare fluctuations of the overlap, since $P(Q) \sim e^{-\beta N V(Q)}$. Measuring such rare fluctuations (indeed, exponentially small in the system size) in equilibrium systems is a well-known problem that has received considerable attention and powerful solutions in the context of equilibrium phase transitions, [189] such as umbrella sampling. Physically, the idea is to perform simulations in an auxiliary statistical ensemble where the Boltzmann weight is biased by a known amount, and from which the unbiased canonical distribution is reconstructed afterwards. [215, 216] Combining this technique to the swap Monte Carlo [44] and parallel tempering methods [217] to sample more efficiently the relevant fluctuations makes possible the numerical measurement of $V(Q)$ over a broad range of physical conditions.

The same numerical techniques can also be used to probe the existence and physical properties of the phase transition induced by a field $\varepsilon$. The $\varepsilon$-transition has given rise to number of theoretical and computational analysis, which conclude that the transition is present in spatial dimensions $d > 2$. [212, 214, 216, 218, 219, 220] The phase transition emerges for temperatures lower than a critical temperature $T^*$, which is the analog of $T_{\rm onset}$ defined in the mean-field theory. For $T < T^*$, a first-order phase transition appears at a finite value $\varepsilon^*(T)$ of the field, where the overlap jumps discontinuously to a value $Q_{\rm glass}(T)$.

The existence of the transition allows the quantitative determination of the configurational entropy, namely

$$S_{\rm conf} = \frac{N}{T} V(Q = Q_{\rm glass}). \qquad (45)$$

A nearly equivalent determination can be obtained directly from the properties of the constrained phase transition, since $\varepsilon^*$ represents the field needed to tilt the Franz-Parisi free energy and make the local minimum at large $Q$ become

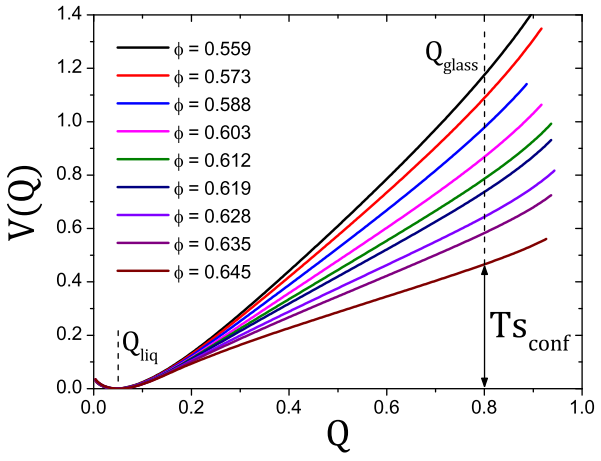


Figure 9: Franz-Parisi free energy in three dimensional polydisperse hard spheres, using a combination of swap Monte Carlo, parallel tempering, and umbrella sampling techniques. [136] $V(Q_{\rm glass})$ decreases progressively with increasing the volume fraction $\phi$. The vertical arrow indicates the estimate of $S_{\rm conf}$ as the free energy difference between the low-overlap ($Q_{\rm liq}$) and large-overlap ($Q_{\rm glass}$) phases. Estimated Kauzmann transition volume fraction, $\phi_{\rm K}$, at which $S_{\rm conf}$ vanishes is $\phi_{\rm K} \approx 0.68$. The system shows jamming transition by rapid compression of dilute configurations at $\phi_{\rm J} \approx 0.655$. [221]

the global one. [136, 212] Taking into account the small but positive $Q_{\rm liq} > 0$, we can estimate the configurational entropy as

$$S_{\rm conf} \simeq \frac{N}{T}\varepsilon^*(Q_{\rm glass} - Q_{\rm liq}). \qquad (46)$$

In Fig. 9, we show the evolution of the Franz-Parisi free energy $V(Q)$ for a system of continuously polydisperse hard spheres in three dimensions, with $N = 300$ particles. The value of $Q_{\rm glass}$ is identified by a separate study of the $\varepsilon$-transition, and is indicated as a vertical dashed line. For each value of the volume fraction $\phi$, $V(Q_{\rm glass})$ provides an estimate of the configurational entropy using Eq. (45), as shown by the vertical arrow.

More broadly, the data in Fig. 9 suggests that Kauzmann's intuition of an underlying thermodynamic phase transition connected to the rapid decrease of $S_{\rm conf}$ is realized in deeply supercooled liquid. The evolution of the Franz-Parisi free energy shows that the glass phase at large $Q$ is metastable as $\phi < \phi_{\rm K}$ (i.e., $T > T_{\rm K}$), but its stability increases rapidly as $\phi$ increases (i.e., $T$ decreases), controlled by the decrease of the configurational entropy. It is still not known whether a finite temperature entropy crisis truly takes place as a thermodynamic phase transition, but the key idea that glass formation is accompanied by the decrease of the associated free energy difference (and hence the configurational entropy) is no longer a hypothesis, but an established fact.

Finally, the evolution of the free-energy $V(Q)$ with supercooling is quite dramatic. This large change quantitatively answers the question raised by the apparent similarity of the two particle configurations shown in Fig. 1. The density profiles of those two state points do not seem very different, but their free energy profiles $V(Q)$ are. This means that to compare the two snapshots, one should monitor appropriate observables reflecting the reduction of available states in glass formation, instead of simple structural changes.

# V Configurational entropy from real space correlations

## V.1 A real space view of metastability

In finite dimensions, the long-lived metastable states envisioned by mean-field theory do not exist since the system will eventually undergo structural relaxation in a finite time. Therefore, metastable states can at best exist over a finite timescale. [18, 222] In the construction of Franz-Parisi, [93, 94] metastable states are therefore explored by introducing a global constraint on the system via a field conjugate to the macroscopic overlap. This strategy allows one to estimate the number of free energy minima for a given temperature.

The constraint envisioned in the Franz-Parisi is global and acts on the bulk system. In this section, we introduce another type of constraint

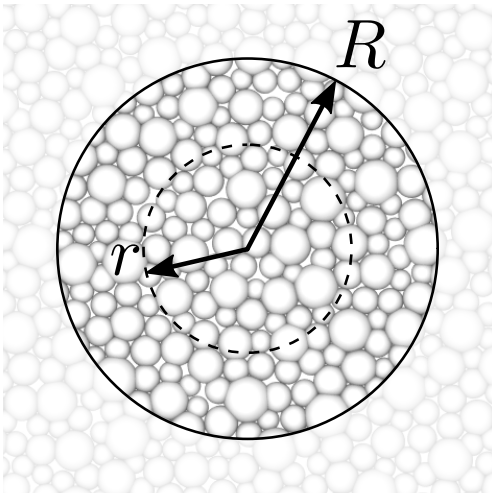


Figure 10: Sketch of the cavity construction to determine the point-to-set lengthscale. The positions of the particles outside a cavity of radius $R$ are given by a reference equilibrium configuration and are frozen, while particles inside the cavity evolve freely at thermal equilibrium in the presence of the frozen amorphous boundaries. The overlap profile $Q(r)$ is defined by comparing the density profile inside the cavity to the reference configuration.

that again allows a sharp distinction between the vicinity of a given configuration (the glass basin), and the rest of the free energy landscape. The key difference with the Franz-Parisi constraint is that we impose a spatially resolved constraint to the system using a cavity construction. [68] We shall argue that this provides a real space interpretation of the rarefaction of metastable states in terms of a growing spatial correlation length, the so-called point-to-set correlation length. This correlation length cannot emerge from the observation of the density profile in a single configuration, but stems once again from the comparison between the distinct density profiles available under some constraint.

The main idea is illustrated in Fig. 10. We prepare an equilibrium configuration of the system, which we take as a reference configuration, $\mathbf{r}^N_{\rm ref}$. We then consider a configuration $\mathbf{r}^N$ which is constrained to be equal to the reference configuration outside a cavity of radius $R$, but can freely fluctuate inside the cavity. Therefore, the constraint from the reference configuration is now only felt at the frozen amorphous boundary of the cavity. By varying the cavity size $R$, one can then infer how far the constraint propagates inside the cavity. As quantified below, one expects a crossover between small cavities where the constraint is so strong that particles inside the cavity can only remain close to the reference configuration, whereas for very large cavities particles inside the cavity will explore a large number of distinct states. The crossover between these two regimes is used to define the point-to-set correlation length. [68, 223, 224]

Why is this crossover length directly connected to the configurational entropy? This can be understood following a simple thermodynamic argument. Suppose the particles inside the cavity explore states that are very different from the reference configuration. This will allow them to sample states that have a low overlap $Q$ with the reference configuration. The free energy gained by this exploration is directly given by the Franz-Parisi free energy, $\Delta F_- = V(Q_{\rm glass}) v_d R^d$, where $v_d$ is the volume of the unit sphere in spatial dimension $d$. There is however a free energy cost to explore those states, as the radial overlap profile inside the cavity $Q(r)$ will present an interface between $Q(r=0) \approx 0$ and $Q(r=R) \approx Q_{\rm glass}$. This interface in the profile of the order parameter has a free energy cost, and a simple estimate is given by $\Delta F_+ = Y s_d R^{d-1}$, where $s_d$ is the surface area of the unit sphere in dimension $d$ and $Y$ a surface tension between two distinct glass states. In many disordered systems, the interfacial terms take a more general expression, $\Delta F_+ = \Upsilon R^\theta$, where $\Upsilon$ is a generalized surface tension and the non-trivial exponent $\theta \leq d-1$ accounts for additional fluctuations in directions transverse to the interface. [18, 225] Physically, these fluctuations arise because the system can decrease the interfacial cost by allowing the position of the interface to fluctuate and take advantage of the weakest spots.

The competition between exploring many

states, that decreases the free energy by $\Delta F_-$, and the interfacial cost of an inhomogeneous overlap profile, that increases the free energy by $\Delta F_+$, leads to a well-defined crossover radius for the cavity where the two terms balance each other,

$$\Delta F = \Upsilon R^\theta - V(Q_{\rm glass}) v_d R^d = 0. \qquad (47)$$

This crossover radius defines the point-to-set correlation lengthscale $\xi_{\rm pts}$, given by

$$\xi_{\rm pts} = \left( \frac{\Upsilon}{V(Q_{\rm glass}) v_d} \right)^{1/(d-\theta)}. \qquad (48)$$

This equation directly connects the decrease of the Franz-Parisi free energy to the growth of a spatial correlation lengthscale. It is important to notice that since $V(Q_{\rm glass})$ is unambiguously defined and can be measured in computer simulations, the same is true for the point-to-set correlation lengthscale whose existence and physical interpretation does not require any type of approximation. In particular, there is no need to assume the existence of long-lived free-energy metastable states.

A connection between the point-to-set correlation lengthscale defined in Eq. (48) and the configurational entropy can be established by using Eq. (45) expressing the Franz-Parisi free energy $V(Q_{\rm glass})$ as an estimate of the configurational entropy. We realize that the growth of the point-to-set correlation lengthscale as temperature decreases is equivalent to a decrease of $V(Q_{\rm glass})$, and thus to a decrease of the $S_{\rm conf}$, assuming a modest temperature dependence of $\Upsilon$. [18, 226] Therefore, the growth of the point-to-set correlation lengthscale is a direct real space consequence of the decrease of the configurational entropy. [18, 68] If a Kauzmann transition where $S_{\rm conf} \to 0$ occurs, then it must be accompanied by a divergence of the point-to-set correlation lengthscale, $\xi_{\rm pts} \to \infty$.

The relation between the point-to-set lengthscale and the configurational entropy can be used both ways. [136] First, it provides a useful interpretation of the entropy crisis in terms of a diverging correlation lengthscale, as put forward in the early development of the random first order transition theory. [18] We find it equally convenient to use this connection in the opposite direction and deduce from the growth of the point-to-set correlation length a quantitative determination of the variation of the configurational entropy. [16, 136] Using the above scaling relations, the measurement of $\xi_{\rm pts}$ provides another estimate of the configurational entropy

$$S_{\rm conf} = N \left( \frac{\xi_0}{\xi_{\rm pts}} \right)^{d-\theta}, \qquad (49)$$

where $\xi_0$ is an unknown factor that results from conversion between entropy and lengthscale. At this stage, the value of the exponent $\theta$ is undetermined. It could be measured by comparing measurements of $S_{\rm conf}$ following Eq. (49) to an independent estimate, for example from Eq. (45). The two supported values for the exponent are the simple value $\theta = d-1$, [226, 227, 228] and the renormalized value $\theta = d/2$ [18, 229] stemming from the random interface analogy. They respectively lead to $S_{\rm conf} \sim 1/\xi_{\rm pts}$ and $S_{\rm conf} \sim 1/\xi_{\rm pts}^{d/2}$, which are equivalent in $d = 2$ and not very different in $d = 3$ given the relatively modest variation of the configurational entropy reported in experiments.

## V.2 Computational measurement

To determine the point-to-set correlation length numerically, [135, 230, 231, 232, 233] we essentially follow the theoretical construction described above and illustrated in Fig. 10. First, an equilibrium reference configuration $\mathbf{r}^N_{\rm ref}$ is prepared. We define a cavity of radius $R$, centered on a randomly-chosen position in the reference configuration. We then define a configuration $\mathbf{r}^N$: the particles lying outside the cavity are frozen at the same positions as in the reference configuration, whereas particles inside the cavity can thermalize freely.

The key observable is the overlap profile $Q(r)$ between configurations $\mathbf{r}^N$ and $\mathbf{r}^N_{\rm ref}$ inside the cavity. It is numerically convenient to focus on the value of the overlap at the center of the cavity $Q_{\rm center} \equiv Q(r = 0)$, which depends both

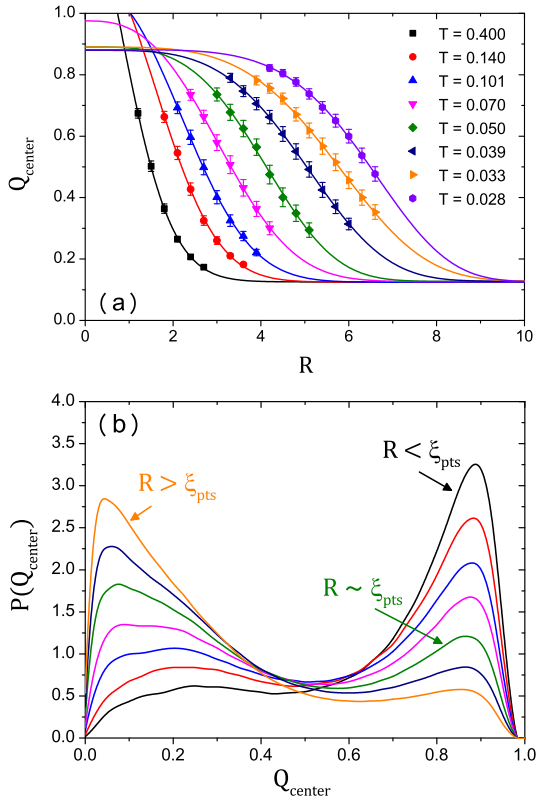


Figure 11: Measurement of the point-to-set lengthscale in a $2d$ systems of polydisperse soft repulsive spheres. [16] (a) Evolution of the overlap at the center of the cavity, $Q_{\rm center}$, with the cavity radius $R$ for different temperatures. (b) Evolution of the probability distribution of the overlap, $P(Q_{\rm center})$, with cavity radius $R$ for a given low temperature $T = 0.035 \approx 0.3T_g$.

on the cavity size $R$, and the temperature $T$. Figure 11(a) shows the evolution of $Q_{\rm center}$ with the cavity size $R$ for polydisperse soft disks in $d = 2$. [16] At small $R$, $Q_{\rm center} \approx Q_{\rm glass}$ meaning that the system is constrained to remain in the same state as the reference configuration. The overlap is not strictly one because thermal fluctuations allow small deviations around the reference configuration $\mathbf{r}^N_{\rm ref}$. At larger $R$, however, $Q_{\rm center}$ decays to a small value, which implies that the system can freely explore states that have different density profiles. The cavity size at which the transition from high to low overlap occurs determines the point-to-set lengthscale $\xi_{\rm pts}$. In practice, one can define $\xi_{\rm pts}$ when $Q_{\rm center}$ reaches a specific value, or from an empirical fitting of the whole function, such as $Q_{\rm center} \approx \exp[-(R/\xi_{\rm pts})^b]$, where $b$ is a fitting parameter. The temperature evolution of $Q_{\rm center}(R)$ is very interesting as it directly reveals that the amorphous boundary condition constrains more strongly the interior of the cavity as the temperature decreases. Physically, it indicates that as temperature decreases, the point-to-set correlation lengthscale grows, or equivalently that the configurational entropy decreases, in virtue of Eq. (49).

An interesting alternative view of the free-energy competition captured by Eq. (47) emerges by considering the evolution of the free-energy gain $\Delta F_-$ of the configuration $\mathbf{r}^N$ inside the cavity, as the cavity size is decreased at constant $T$. For a very large cavity, the particles in $\mathbf{r}^N$ are pinned at the boundaries, but those at the center of the cavity evolve as freely as in the bulk equilibrium system. Since the free-energy gain $\Delta F_-$ scales as $R^d$, it decreases as the cavity size decreases, making it increasingly difficult for the configuration $\mathbf{r}^N$ to explore other states inside cavity. As the cavity size approaches the point-to-set lengthscale, the entropic driving force to explore many states inside the cavity becomes comparable to the free energy cost $\Delta F_+$ of the amorphous boundary. For even smaller cavities, the system is frozen in a single state. The scenario that we have just described for the cavity is nothing but the entropy crisis predicted by the random first transition theory for the bulk system as $T \to T_K$. In other words, decreasing the cavity size for a given $T > T_K$ has an effect similar to approaching the Kauzmann transition in a bulk system. The qualitative difference is that the Kauzmann transition is a sharp thermodynamic transition happening for $N \to \infty$ in the bulk, whereas the entropy crisis in the cavity takes place for a finite system comprising $N \sim \xi^d_{\rm pts}$ particles. The crossover from small to large overlap observed around $R \sim \xi_{\rm pts}(T)$ in the profiles of Fig. 11(a) is conceptually analogous to

a Kauzmann transition rounded by the finite size of the system. [20]

This analogy is even more striking when the fluctuations of the overlap are recorded, [233] and not only its average value. Figure 11(b) shows the probability distribution of $Q_{\text{center}}$, denoted $P(Q_{\text{center}})$, for a fixed temperature as $R$ is varied. For large $R$, the distribution peaks at low values of the overlap, whereas for small $R$ it peaks near $Q_{\text{glass}}$. Interestingly, at the crossover between these two regimes, $P(Q_{\text{center}})$ is clearly bimodal, which is reminiscent of the distribution of the order parameter near a first-order phase transition in a finite system. These observations suggest that it is interesting to monitor the variance of these distributions, which is a measure of the susceptibility $\chi$ associated with this rounded Kauzmann transition. For a given $T$, it is found that $\chi$ has a maximum when $R = \xi_{\text{pts}}$, which provides a fitting-free numerical definition of the point-to-set correlation lengthscale. [233]

Despite the conceptual simplicity of the measurements described above, it is not straightforward to obtain statistically meaningful numerical measurements of the overlap and of its fluctuations inside finite cavities. There are several reasons for this. First, to obtain a value for $\xi_{\text{pts}}$ at a given temperature, one needs to analyze a range of cavity sizes that encompasses the crossover shown in Fig. 11. For each cavity size $R$, a large number of independent cavities need to be studied, and the overlap in each individual cavity needs to be carefully monitored to ensure that its equilibrium fluctuations have been properly recorded. All in all, the number of required simulations is quite substantial.

The second major computational obstacle naturally stems from the physics at play as $R$ is reduced. Because the confined system undergoes a finite-size analog of the Kauzmann transition, a major slowing down arises in the thermalization process. This amounts to studying an 'ideal' glass transition in equilibrium conditions, an obviously daunting task. This is however possible in the present case because only a finite number of particles are contained in the cavity. This allows the use of parallel tempering (or replica exchange) methods, first developed in the context of spin glasses to overcome thermalization issues in systems with complex landscapes. [217] With these techniques, the study of a given set of parameters $(T, R)$ requires simulating a large number of copies of the system interpolating between the original system and a state point at which thermalization is fast. During the course of the simulations, exchanges between neighboring states are performed, so that each copy performs a random walk in parameter space. This method, developed in Ref. [233] has proven sufficiently efficient and versatile to analyze point-to-set correlations in a broad range of model systems down to very low temperetures. [136]

# VI Perspective

We presented a short review of the configurational entropy in supercooled liquids approaching their glass transition. We first described why and how configurational entropy became a central thermodynamic quantity to describe glassy materials, both from experimental and theoretical viewpoints. We then offered our views on several paradoxes surrounding the configurational entropy. In particular, we explained that there is no reason to try to avoid an entropy crisis, that available data neither discard nor disprove its existence, and that there exists no fundamental reason, published proof, or general arguments showing that it must be avoided. In other words, the Kauzmann transition remains a valid and useful hypothesis to interpret glass formation. We also insisted that this is still a hypothesis, but in no way a proven or necessary fact.

The biggest paradox of all, is perhaps that the configurational entropy, which represents the key signature of the entropy crisis occurring in the modern mean-field theory of the glass transition, cannot be rigorously defined in finite dimensions as a complexity that enumerates free energy minima. We have presented several computational schemes which are meant to provide at the same time an estimate of the configurational entropy

in numerical models of glass-forming liquids, and a physical interpretation that is valid in finite dimensions.

We started with the historical method based on inherent structures, which enumerates the number of potential energy minima as well-defined, but incorrect proxies, for free energy minima. It is unclear that the inherent structure configurational entropy can in fact vanish at a Kauzmann transition, and Stillinger provided arguments that it cannot. This method is a computationally cheap method to remove a vibrational contribution to the total entropy, but it cannot be used for simple models such as hard spheres or continuously polydisperse glass-formers.

We then showed that a generalized method elaborating on earlier ideas introduced by Frenkel and Ladd for crystals provides a better estimate of the configurational entropy, as it naturally includes both the glass mixing entropy and finite temperature anharmonicities. Additionally, the method can be applied to all types of models, including hard spheres, at a relatively cheap computational cost.

More recent methods were developed as direct applications of the mean-field theory to computer works, which both bypass the need to mathematically define free energy minima. Free energy measurements, based on the Franz-Parisi free energy, provide an estimate for the configurational entropy that is the closest to the original mean-field definition. This method relies on the definition of a global order parameter for the glass transition, the overlap, which quantifies the similarity between pairs of configurations. Conventional methods employed in the context of equilibrium phase transitions are combined to these measurements.

Finally, we showed that the decrease of the entropy can be given a real space interpretation in terms of a growing correlation lengthscale that is directly related to the configurational entropy.

This brief summary shows that there now exist conceptually solid estimates of the configurational entropy that could truly provide a direct access to the thermodynamic behavior of supercooled liquids. Given the recent progress of computer simulations to efficiently equilibrate model systems down to temperatures that are matching, and in several cases, outperforming experimental work, we feel that this is an exciting moment for glass physics, since a direct demonstration of the relevance and connection to slow dynamics of an entropy crisis and increasingly precise localizations of the putative Kauzmann transition appear possible.

**Acknowledgments** – This perspective is based on two sets of lectures. The first one was given during the 2017 Boulder Summer School on "Disordered and Frustrated systems". The second one was given during the 2018 Bangalore Summer School "Entropy, information and order in soft matter". We thank G. Biroli, P. Charbonneau, D. Coslovich, M. D. Ediger, A. Ikeda, W. Kob, K. Miyazaki, A. Ninarello, G. Parisi, G. Tarjus, and S. Yaida for collaborations and discussions on the topics discussed in this paper. We thank S. Tatsumi and O. Yamamuro for providing us with experimental data and discussions on experimental measurement of the configurational entropy. The research leading to these results has received funding from the Simons Foundation (#454933, Ludovic Berthier).

## Bibliography

[1] Ludovic Berthier and Giulio Biroli. *Rev. Mod. Phys.*, 83:587–645, Jun 2011.

[2] M. D. Ediger, C. A. Angell, and Sidney R. Nagel. *The Journal of Physical Chemistry*, 100(31):13200–13212, 1996.

[3] P. G. Debenedetti and F. H. Stillinger. *Nature*, 410:259, 2001.

[4] Andrea Cavagna. *Physics Reports*, 476(4-6):51–124, 2009.

[5] Jeppe C. Dyre. *Rev. Mod. Phys.*, 78:953–972, Sep 2006.

[6] Kurt Binder and Walter Kob. *Glassy materials and disordered solids: An introduction to their statistical mechanics.* World scientific, 2011.

[7] M. D. Ediger and Peter Harrowell. *The Journal of Chemical Physics*, 137(8): 080901, 2012.

[8] James S Langer. *Reports on Progress in Physics*, 77(4):042501, 2014.

[9] Ludovic Berthier and Mark Ediger. *Physics today*, 69(1):40, 2016.

[10] L. Berthier, G. Biroli, J-P Bouchaud, L. Cipelletti, and W. van Saarloos, editors. *Dynamical Heterogeneities and Glasses*. Oxford University Press, 2011.

[11] M. D. Ediger. *Annual Review of Physical Chemistry*, 51(1):99–128, 2000.

[12] Smarajit Karmakar, Chandan Dasgupta, and Srikanth Sastry. *Annual Review of Condensed Matter Physics*, 5(1):255–284, 2014.

[13] G. Tarjus. An overview of the theories of the glass transition. In L. Berthier, G. Biroli, J-P Bouchaud, L. Cipelletti, and W. van Saarloos, editors, *Dynamical Heterogeneities and Glasses*. Oxford University Press, 2011.

[14] H Eugene Stanley. *Phase transitions and critical phenomena*. Clarendon Press, Oxford, 1971.

[15] P. M. Chaikin and T. C. Lubensky. *Principles of Condensed Matter Physics*. Cambridge University Press, 1995. doi: 10.1017/CBO9780511813467.

[16] Ludovic Berthier, Patrick Charbonneau, Andrea Ninarello, Misaki Ozawa, and Sho Yaida. *arXiv preprint, arXiv:1805.09035*, 2018.

[17] Gerold Adam and Julian H. Gibbs. *J. Chem. Phys.*, 43(1):139–146, 1965.

[18] T. R. Kirkpatrick, D. Thirumalai, and P. G. Wolynes. *Phys. Rev. A*, 40(2):1045–1054, Jul 1989.

[19] Vassiliy Lubchenko and Peter G. Wolynes. *Annual Review of Physical Chemistry*, 58 (1):235–266, 2007.

[20] G. Biroli and J.P. Bouchaud. The Random First-Order Transition Theory of Glasses: a critical assessment. In P.G.Wolynes and V.Lubchenko, editors, *Structural Glasses and Supercooled Liquids: Theory, Experiment and Applications*. Wiley & Sons, 2012.

[21] G Tarjus, S A Kivelson, Z Nussinov, and P Viot. *Journal of Physics: Condensed Matter*, 17(50):R1143–R1182, dec 2005.

[22] CA Angell. *MRS bulletin*, 33(5):544–555, 2008.

[23] John C Mauro, Yuanzheng Yue, Adam J Ellison, Prabhat K Gupta, and Douglas C Allan. *Proceedings of the National Academy of Sciences*, 106(47): 19780–19784, 2009.

[24] David Chandler and Juan P. Garrahan. *Annual Review of Physical Chemistry*, 61 (1):191–217, 2010.

[25] Hajime Tanaka. *The European Physical Journal E*, 35(10):113, 2012.

[26] Frank H Stillinger and Pablo G Debenedetti. *Annu. Rev. Condens. Matter Phys.*, 4(1):263–285, 2013.

[27] Stephen Mirigian and Kenneth S Schweizer. *The Journal of chemical physics*, 140(19):194506, 2014.

[28] T. R. Kirkpatrick and D. Thirumalai. *Rev. Mod. Phys.*, 87:183–209, Mar 2015.

[29] Walter. Kauzmann. *Chemical Reviews*, 43 (2):219–256, 1948.

[30] Julian H. Gibbs. *The Journal of Chemical Physics*, 25(1):185–186, 1956.

[31] Julian H. Gibbs and Edmund A. DiMarzio. *The Journal of Chemical Physics*, 28(3): 373–383, 1958.

[32] R. Richert and C. A. Angell. *The Journal of Chemical Physics*, 108(21):9016–9026, 1998.

[33] Misaki Ozawa, Giorgio Parisi, and Ludovic Berthier. *The Journal of Chemical Physics*, 149(15):154501, 2018.

[34] Soichi Tatsumi, Shintaro Aso, and Osamu Yamamuro. *Phys. Rev. Lett.*, 109:045701, Jul 2012.

[35] M. D. Ediger. *The Journal of Chemical Physics*, 147(21):210901, 2017.

[36] Wolfgang Götze. *Complex dynamics of glass-forming liquids: A mode-coupling theory*, volume 143. Oxford University Press, Oxford, 2008.

[37] Daniel Kivelson and Howard Reiss. *The Journal of Physical Chemistry B*, 103(39): 8337–8343, 1999.

[38] Martin Goldstein. *The Journal of Chemical Physics*, 128(15):154510, 2008.

[39] Prabhat K. Gupta and John Mauro. *Journal of Non-Crystalline Solids*, 355(10-12): 595–599, 5 2009. ISSN 0022-3093.

[40] G. P. Johari and Joseph Khouri. *The Journal of Chemical Physics*, 134(3):034515, 2011.

[41] Jurn W. P. Schmelzer and Timur V. Tropin. *Entropy*, 20(2):103, 2018. ISSN 1099-4300.

[42] Stephen F. Swallen, Kenneth L. Kearns, Marie K. Mapes, Yong Seol Kim, Robert J. McMahon, M. D. Ediger, Tian Wu, Lian Yu, and Sushil Satija. *Science*, 315(5810): 353–356, 2007. ISSN 0036-8075.

[43] Ludovic Berthier, Daniele Coslovich, Andrea Ninarello, and Misaki Ozawa. *Phys. Rev. Lett.*, 116:238002, Jun 2016.

[44] Andrea Ninarello, Ludovic Berthier, and Daniele Coslovich. *Phys. Rev. X*, 7:021039, 2017.

[45] Walter Kob and Hans C. Andersen. *Phys. Rev. E*, 51(5):4626–4641, May 1995.

[46] Frank H. Stillinger. *The Journal of Chemical Physics*, 88(12):7818–7825, 1988.

[47] Pablo G. Debenedetti, Frank H. Stillinger, and M. Scott Shell. *The Journal of Physical Chemistry B*, 107(51):14434–14442, 2003.

[48] M. Wolfgardt, J. Baschnagel, W. Paul, and K. Binder. *Phys. Rev. E*, 54:1535–1543, Aug 1996.

[49] A. J. Moreno, I. Saika-Voivod, E. Zaccarelli, E. La Nave, S. V. Buldyrev, P. Tartaglia, and F. Sciortino. *The Journal of Chemical Physics*, 124(20):204509, 2006.

[50] Aleksandar Donev, Frank H. Stillinger, and Salvatore Torquato. *The Journal of Chemical Physics*, 127(12):124509, 2007.

[51] Frank Smallenburg and Francesco Sciortino. *Nature Physics*, 9(9):554, 2013.

[52] Wen-Sheng Xu, Jack F. Douglas, and Karl F. Freed. *The Journal of Chemical Physics*, 145(23):234509, 2016.

[53] Hajime Tanaka. *Phys. Rev. E*, 68:011505, Jul 2003.

[54] Edgar D Zanotto and John C Mauro. *Journal of Non-Crystalline Solids*, 471:490–495, 2017.

[55] Jürn WP Schmelzer, Alexander S Abyzov, Vladimir M Fokin, and Christoph Schick. *Journal of Non-Crystalline Solids*, 501:21–35, 2018.

[56] Frank H. Stillinger, Pablo G. Debenedetti, and Thomas M. Truskett. *The Journal of Physical Chemistry B*, 105(47):11809–11816, 2001.

[57] M. D. Rintoul and S. Torquato. *The Journal of Chemical Physics*, 105(20):9258–9265, 1996.

[58] Jing Zhao, Sindee L. Simon, and Gregory B. McKenna. *Nature Communications*, 4:1783, 2013.

[59] Dinghai Huang, Sindee L. Simon, and Gregory B. McKenna. *The Journal of Chemical Physics*, 119(7):3590–3593, 2003.

[60] C Patrick Royall, Francesco Turci, Soichi Tatsumi, John Russo, and Joshua Robinson. *Journal of Physics: Condensed Matter*, 30(36):363001, aug 2018.

[61] Melissa R. Feeney, Pablo G. Debenedetti, and Frank H. Stillinger. *The Journal of Chemical Physics*, 119(8):4582–4591, 2003.

[62] Daniel Kivelson and Gilles Tarjus. *The Journal of Chemical Physics*, 109(13): 5481–5486, 1998.

[63] Lev Davidovich Landau, Evgenii M Lifshitz, and LP Pitaevskii. Statistical

physics, part i, 1980.

[64] Matthieu Wyart and Michael E. Cates. *Phys. Rev. Lett.*, 119:195501, Nov 2017.

[65] Ludovic Berthier, Giulio Biroli, Jean-Philippe Bouchaud, and Gilles Tarjus. *The Journal of Chemical Physics*, 150(9): 094501, 2019.

[66] Jeppe C Dyre, Tina Hechsher, and Kristine Niss. *Journal of Non-Crystalline Solids*, 355(10-12):624–627, 2009.

[67] Heedong Yoon and Gregory B. McKenna. *Science Advances*, 4(12), 2018.

[68] Jean-Philippe Bouchaud and Giulio Biroli. *J. Chem. Phys.*, 121(15):7347–7354, 2004.

[69] Aaron S. Keys, Juan P. Garrahan, and David Chandler. *Proceedings of the National Academy of Sciences*, 110(12):4482–4487, 2013.

[70] Giulio Biroli, Jean-Philippe Bouchaud, and Gilles Tarjus. *The Journal of Chemical Physics*, 123(4):044510, 2005.

[71] David Chandler and Juan P. Garrahan. *The Journal of Chemical Physics*, 123(4): 044511, 2005.

[72] P-J_ Flory. *Proc. R. Soc. Lond. A*, 234 (1196):60–73, 1956.

[73] P. D. Gujrati. *Journal of Statistical Physics*, 28(3):441–472, Jul 1982.

[74] Hans-Peter Wittmann. *The Journal of Chemical Physics*, 95(11):8449–8458, 1991.

[75] Jacek Dudowicz, Karl F. Freed, and Jack F. Douglas. *Advances in Chemical Physics*, pages 125–222, 2008.

[76] Wen-Sheng Xu, Jack F. Douglas, and Karl F. Freed. *Advances in Chemical Physics*, pages 443–497, 2016.

[77] G Biroli and R Monasson. *Europhysics Letters (EPL)*, 50(2):155–161, apr 2000.

[78] Marc Mézard and Giorgio Parisi. *Phys. Rev. Lett.*, 82:747–750, Jan 1999.

[79] Giorgio Parisi and Francesco Zamponi. *Rev. Mod. Phys.*, 82(1):789–845, Mar 2010.

[80] Jorge Kurchan, Giorgio Parisi, and Francesco Zamponi. *Journal of Statistical Mechanics: Theory and Experiment*, 2012 (10):P10012, oct 2012.

[81] Jorge Kurchan, Giorgio Parisi, Pierfrancesco Urbani, and Francesco Zamponi. *The Journal of Physical Chemistry B*, 117 (42):12979–12994, 2013.

[82] Patrick Charbonneau, Jorge Kurchan, Giorgio Parisi, Pierfrancesco Urbani, and Francesco Zamponi. *Annual Review of Condensed Matter Physics*, 8(1):265–288, 2017.

[83] Y. Singh, J. P. Stoessel, and P. G. Wolynes. *Phys. Rev. Lett.*, 54:1059–1062, Mar 1985.

[84] T. R. Kirkpatrick and D. Thirumalai. *Phys. Rev. Lett.*, 58:2091–2094, May 1987.

[85] T. R. Kirkpatrick and D. Thirumalai. *Phys. Rev. B*, 36:5388–5397, Oct 1987.

[86] T. R. Kirkpatrick and P. G. Wolynes. *Phys. Rev. A*, 35(7):3072–3080, Apr 1987.

[87] T. R. Kirkpatrick and D. Thirumalai. *Phys. Rev. A*, 37:4439–4448, Jun 1988.

[88] Tommaso Castellani and Andrea Cavagna. *Journal of Statistical Mechanics: Theory and Experiment*, 2005(05):P05012, may 2005.

[89] Bernard Derrida. *Phys. Rev. B*, 24:2613–2626, Sep 1981.

[90] Giulio Biroli and Marc Mézard. *Phys. Rev. Lett.*, 88(2):025501, Dec 2001.

[91] O. Rivoire, G. Biroli, O. C. Martin, and M. Mézard. *The European Physical Journal B - Condensed Matter and Complex Systems*, 37(1):55–78, Jan 2004. ISSN 1434-6036.

[92] Marc Mezard and Andrea Montanari. *Information, Physics, and Computation*. Oxford University Press, Inc., New York, NY, USA, 2009. ISBN 019857083X, 9780198570837.

[93] Silvio Franz and Giorgio Parisi. *J. Phys. I France*, 5(11):1401–1415, 1995.

[94] Silvio Franz and Giorgio Parisi. *Phys. Rev. Lett.*, 79(13):2486–2489, Sep 1997.

[95] Alain Barrat, Silvio Franz, and Giorgio

Parisi. *Journal of Physics A: Mathematical and General*, 30(16):5593–5612, 1997.

[96] Maxim Dzero, Jörg Schmalian, and Peter G. Wolynes. *Phys. Rev. B*, 72:100201, Sep 2005.

[97] Silvio Franz. *Journal of Statistical Mechanics: Theory and Experiment*, 2005(04): P04001, apr 2005.

[98] Maria Chiara Angelini and Giulio Biroli. *Journal of Statistical Physics*, 167(3):476–498, May 2017. ISSN 1572-9613.

[99] C Rulquin, P Urbani, G Biroli, G Tarjus, and M Tarzia. *Journal of Statistical Mechanics: Theory and Experiment*, 2016(2): 023209, feb 2016.

[100] Giulio Biroli, Chiara Cammarota, Gilles Tarjus, and Marco Tarzia. *Phys. Rev. B*, 98:174205, Nov 2018.

[101] Giulio Biroli, Chiara Cammarota, Gilles Tarjus, and Marco Tarzia. *Phys. Rev. B*, 98:174206, Nov 2018.

[102] Martin Goldstein. *J. Chem. Phys.*, 64(11): 4767–4774, 1976.

[103] Osamu Yamamuro, Itaru Tsukushi, Anna Lindqvist, Shuichi Takahara, Mariko Ishikawa, and Takasuke Matsuo. *The Journal of Physical Chemistry B*, 102(9): 1605–1609, 1998.

[104] G. P. Johari. *The Journal of Chemical Physics*, 112(17):7518–7523, 2000.

[105] L-M Martinez and CA Angell. *Nature*, 410 (6829):663, 2001.

[106] CA Angell and S Borick. *J. Non-Cryst. Solids*, 307:393, 2002.

[107] Hillary L Smith, Chen W Li, Andrew Hoff, Glenn R Garrett, Dennis S Kim, Fred C Yang, Matthew S Lucas, Tabitha Swan-Wood, Jiao YY Lin, Matthew B Stone, et al. *Nature Physics*, 13(9):900, 2017.

[108] Daan Frenkel and Anthony J. C. Ladd. *The Journal of Chemical Physics*, 81(7):3188–3193, 1984.

[109] Barbara Coluzzi, Marc Mezard, Giorgio Parisi, and Paolo Verrocchio. *The Journal of Chemical Physics*, 111(19):9039–9052, 1999.

[110] Luca Angelani and Giuseppe Foffi. *J. Phys.:Condens Matter*, 19(25):256207, jun 2007.

[111] Martin Goldstein. *J. Chem. Phys.*, 51(9): 3728–3739, 1969.

[112] Frank H. Stillinger and Thomas A. Weber. *Phys. Rev. A*, 25:978–989, Feb 1982.

[113] Frank H. Stillinger. *Science*, 267(5206): 1935–1939, 1995.

[114] F. Sciortino, W. Kob, and P. Tartaglia. *Phys. Rev. Lett.*, 83:3214–3217, Oct 1999.

[115] Srikanth Sastry. *Nature*, 409(6817):164, 2001.

[116] Misaki Ozawa and Ludovic Berthier. *The Journal of Chemical Physics*, 146(1): 014502, 2017.

[117] Andreas Heuer. *Journal of Physics: Condensed Matter*, 20(37):373101, aug 2008.

[118] Frank H. Stillinger. *Phys. Rev. E*, 59:48–51, Jan 1999.

[119] Aleksandar Donev, Frank H. Stillinger, and Salvatore Torquato. *Phys. Rev. Lett.*, 96 (22):225502, 2006.

[120] Walter Kob. *Journal of Physics: Condensed Matter*, 11(10):R85, 1999.

[121] W. Kob. Supercooled liquids, the glass transition, and computer simulations. In Jean-Louis Barrat, Mikhail Feigelman, Jorge Kurchan, and Jean Dalibard, editors, *Slow Relaxations and nonequilibrium dynamics in condensed matter*, pages 199–269, Berlin, Heidelberg, 2003. Springer Berlin Heidelberg.

[122] J. J. Ullo and Sidney Yip. *Phys. Rev. Lett.*, 54:1509–1512, Apr 1985.

[123] Laurent J. Lewis. *Phys. Rev. B*, 44:4245–4254, Sep 1991.

[124] B. Bernu, J. P. Hansen, Y. Hiwatari, and G. Pastore. *Phys. Rev. A*, 36:4891–4903, Nov 1987.

[125] Jean-Noël Roux, Jean-Louis Barrat, and J-P Hansen. *Journal of Physics: Condensed*

*Matter*, 1(39):7171, 1989.

[126] Göran Wahnström. *Phys. Rev. A*, 44:3752–3764, Sep 1991.

[127] Walter Kob and Jean-Louis Barrat. *Phys. Rev. Lett.*, 78:4581–4584, Jun 1997.

[128] J.-L Barrat and W Kob. *Europhysics Letters (EPL)*, 46(5):637–642, jun 1999.

[129] Ludovic Berthier and Jean-Louis Barrat. *Phys. Rev. Lett.*, 89:095702, Aug 2002.

[130] A Crisanti and F Ritort. *Journal of Physics A: Mathematical and General*, 36 (21):R181–R290, may 2003.

[131] Ryoichi Yamamoto and Akira Onuki. *Phys. Rev. E*, 58:3515–3529, Sep 1998.

[132] Ludovic Berthier and Jean-Louis Barrat. *The Journal of Chemical Physics*, 116(14): 6228–6242, 2002.

[133] Walter Kob, Claudio Donati, Steven J. Plimpton, Peter H. Poole, and Sharon C. Glotzer. *Phys. Rev. Lett.*, 79:2827–2830, Oct 1997.

[134] Asaph Widmer-Cooper, Peter Harrowell, and H. Fynewever. *Phys. Rev. Lett.*, 93: 135701, Sep 2004.

[135] G. Biroli, J.P. Bouchaud, A. Cavagna, TS Grigera, and P. Verrocchio. *Nature Physics*, 4(10):771–775, 2008.

[136] Ludovic Berthier, Patrick Charbonneau, Daniele Coslovich, Andrea Ninarello, Misaki Ozawa, and Sho Yaida. *Proceedings of the National Academy of Sciences*, 114(43): 11356–11361, 2017. ISSN 0027-8424.

[137] B. Doliwa and A. Heuer. *Phys. Rev. E*, 61: 6898–6908, Jun 2000.

[138] Ludovic Berthier and Walter Kob. *Phys. Rev. E*, 85:011102, Jan 2012.

[139] Claudio Donati, Silvio Franz, Sharon C. Glotzer, and Giorgio Parisi. *Journal of Non-Crystalline Solids*, 307-310:215 – 224, 2002. ISSN 0022-3093.

[140] L. Berthier, G. Biroli, J.-P. Bouchaud, L. Cipelletti, D. El Masri, D. L'Hôte, F. Ladieu, and M. Pierno. *Science*, 310 (5755):1797–1800, 2005. ISSN 0036-8075.

[141] Srikanth Sastry, Pablo G Debenedetti, and Frank H Stillinger. *Nature*, 393(6685):554, 1998.

[142] David Wales. *Energy landscapes: Applications to clusters, biomolecules and glasses*. Cambridge University Press, 2003.

[143] Francesco Sciortino. *Journal of Statistical Mechanics: Theory and Experiment*, 2005 (05):P05015, 2005.

[144] Mahdi Zaeifi Yamchi, S. S. Ashwin, and Richard K. Bowles. *Phys. Rev. E*, 91: 022301, Feb 2015.

[145] Shiladitya Sengupta, Smarajit Karmakar, Chandan Dasgupta, and Srikanth Sastry. *Phys. Rev. Lett.*, 109:095705, Aug 2012.

[146] Joel D. Eaves and David R. Reichman. *Proceedings of the National Academy of Sciences*, 106(36):15171–15175, 2009. ISSN 0027-8424.

[147] Patrick Charbonneau, Atsushi Ikeda, Giorgio Parisi, and Francesco Zamponi. *Phys. Rev. Lett.*, 107:185702, Oct 2011.

[148] Francois Sausset, Gilles Tarjus, and Pascal Viot. *Phys. Rev. Lett.*, 101:155701, Oct 2008.

[149] Francesco Turci, Gilles Tarjus, and C. Patrick Royall. *Phys. Rev. Lett.*, 118: 215501, May 2017.

[150] K Kim. *EPL (Europhysics Letters)*, 61(6): 790, 2003.

[151] Walter Kob and Ludovic Berthier. *Physical review letters*, 110(24):245702, 2013.

[152] Walter Kob, Sándalo Roldán-Vargas, and Ludovic Berthier. *Nature Physics*, 8(2): 164, 2012.

[153] Misaki Ozawa, Walter Kob, Atsushi Ikeda, and Kunimasa Miyazaki. *Proceedings of the National Academy of Sciences*, 112(22): 6914–6919, 2015.

[154] Ludovic Berthier, Giulio Biroli, Daniele Coslovich, Walter Kob, and Cristina Toninelli. *Physical Review E*, 86(3):031502, 2012.

[155] Smarajit Karmakar and Itamar Procaccia.

*Physical Review E*, 86(6):061502, 2012.

[156] Ludovic Berthier and Thomas A. Witten. *Phys. Rev. E*, 80(2):021502, Aug 2009.

[157] G. Brambilla, D. El Masri, M. Pierno, L. Berthier, L. Cipelletti, G. Petekidis, and A. B. Schofield. *Phys. Rev. Lett.*, 102(8): 085703, 2009.

[158] Gary L Hunter and Eric R Weeks. *Reports on Progress in Physics*, 75(6):066501, may 2012.

[159] Mingwei Chen. *NPG Asia Materials*, 3(9): 82, 2011.

[160] D Coslovich and G Pastore. *Journal of Physics: Condensed Matter*, 21(28): 285107, jun 2009.

[161] R. Gutiérrez, S. Karmakar, Y. G. Pollack, and I. Procaccia. *EPL (Europhysics Letters)*, 111(5):56009, sep 2015.

[162] Søren Toxvaerd, Ulf R Pedersen, Thomas B Schrøder, and Jeppe C Dyre. *The Journal of Chemical Physics*, 130(22):224501, 2009.

[163] Daniele Coslovich, Misaki Ozawa, and Ludovic Berthier. *Journal of Physics: Condensed Matter*, 30(14):144004, mar 2018.

[164] Daniele Coslovich, Misaki Ozawa, and Walter Kob. *The European Physical Journal E*, 41(5):62, May 2018. ISSN 1292-895X.

[165] S. Mossa, E. La Nave, H. E. Stanley, C. Donati, F. Sciortino, and P. Tartaglia. *Phys. Rev. E*, 65:041205, Apr 2002.

[166] Nicolas Giovambattista, C. Austen Angell, Francesco Sciortino, and H. Eugene Stanley. *Phys. Rev. Lett.*, 93:047801, Jul 2004.

[167] Srikanth Sastry and C Austen Angell. *Nature materials*, 2(11):739, 2003.

[168] Ivan Saika-Voivod, Peter H Poole, and Francesco Sciortino. *Nature*, 412(6846): 514, 2001.

[169] M. P. Allen and D. J. Tildesley. *Computer Simulation of Liquids*. Clarendon Press, New York, NY, USA, 1989. ISBN 0-19-855645-4.

[170] David Landau and Kurt Binder. *A Guide to Monte Carlo Simulations in Statistical Physics*. Cambridge University Press, New York, NY, USA, 2005.

[171] Shuichi Nosé. *The Journal of Chemical Physics*, 81(1):511–519, 1984.

[172] William G. Hoover. *Phys. Rev. A*, 31:1695–1697, Mar 1985.

[173] R. Brand, P. Lunkenheimer, U. Schneider, and A. Loidl. *Phys. Rev. B*, 62:8878–8883, Oct 2000.

[174] U. Schneider, P. Lunkenheimer, R. Brand, and A. Loidl. *Phys. Rev. E*, 59:6924–6936, Jun 1999.

[175] P. Lunkenheimer, R. Wehn, U. Schneider, and A. Loidl. *Phys. Rev. Lett.*, 95:055702, Jul 2005.

[176] Ludovic Berthier, Elijah Flenner, Christopher J Fullerton, Camille Scalliet, and Murari Singh. *arXiv preprint arXiv:1811.12837*, 2018.

[177] C. A. Angell. *Science*, 267(5206):1924–1935, 1995. ISSN 0036-8075.

[178] Yael S. Elmatad, David Chandler, and Juan P. Garrahan. *The Journal of Physical Chemistry B*, 113(16):5563–5567, 2009.

[179] Nicholas P. Bailey, Trond S. Ingebrigtsen, Jesper Schmidt Hansen, Arno A. Veldhorst, Lasse Bøhling, Claire A. Lemarchand, Andreas E. Olsen, Andreas K. Bacher, Lorenzo Costigliola, Ulf R. Pedersen, Heine Larsen, Jeppe C. Dyre, and Thomas B. Schrøder. *SciPost Phys.*, 3:038, 2017.

[180] Jens Glaser, Trung Dac Nguyen, Joshua A Anderson, Pak Lui, Filippo Spiga, Jaime A Millan, David C Morse, and Sharon C Glotzer. *Computer Physics Communications*, 192:97–107, 2015.

[181] Nicholas Metropolis, Arianna W. Rosenbluth, Marshall N. Rosenbluth, Augusta H. Teller, and Edward Teller. *The Journal of Chemical Physics*, 21(6):1087–1092, 1953.

[182] M.?E.?J. Newman and G.?T. Barkema.

*Monte Carlo Methods in Statistical Physics*. Clarendon Press, Oxford, 1999.

[183] L Berthier and W Kob. *Journal of Physics: Condensed Matter*, 19(20):205130, 2007.

[184] Glenn H. Fredrickson and Hans C. Andersen. *Phys. Rev. Lett.*, 53:1244–1247, Sep 1984.

[185] Robert L. Jack, Ludovic Berthier, and Juan P. Garrahan. *Phys. Rev. E*, 72: 016103, Jul 2005.

[186] R.K. Darst, D.R. Reichman, and G. Biroli. *J. Chem. Phys.*, 132:044510, 2010.

[187] Nan-Hsiung Tsai, Farid F Abraham, and GM Pound. *Surface Science*, 77(3):465–492, 1978.

[188] D Gazzillo and G Pastore. *Chem. Phys. Lett.*, 159:388, 1989.

[189] Daan Frenkel and Berend Smit. *Understanding molecular simulation: from algorithms to applications*, volume 1. Academic press, 2001. doi: 10.1063/1.881812.

[190] Tomás S. Grigera and Giorgio Parisi. *Phys. Rev. E*, 63:045102, Mar 2001.

[191] L. A. Fernández, V. Martín-Mayor, and P. Verrocchio. *Phys. Rev. Lett.*, 98:085702, Feb 2007.

[192] J.-P. Hansen and I. R. McDonald. *Theory of simple liquids*. Academic Press, London, 1986.

[193] Daan Frenkel. *Molecular Physics*, 112(17): 2325–2329, 2014.

[194] Srikanth Sastry. *Journal of Physics: Condensed Matter*, 12(29):6515–6523, jul 2000.

[195] Barbara Coluzzi, Giorgio Parisi, and Paolo Verrocchio. *The Journal of Chemical Physics*, 112(6):2933–2944, 2000.

[196] Indaco Biazzo, Francesco Caltagirone, Giorgio Parisi, and Francesco Zamponi. *Phys. Rev. Lett.*, 102(19):195701, 2009.

[197] Harukuni Ikeda, Kunimasa Miyazaki, and Atsushi Ikeda. *The Journal of Chemical Physics*, 145(21):216101, 2016.

[198] Harukuni Ikeda and Francesco Zamponi. *arXiv preprint arXiv:1812.08780*, 2018.

[199] Jorge Nocedal and Stephen Wright. *Numerical optimization*. Springer Science & Business Media, 2006.

[200] Erik Bitzek, Pekka Koskinen, Franz Gähler, Michael Moseler, and Peter Gumbsch. *Phys. Rev. Lett.*, 97:170201, Oct 2006.

[201] E. Flenner and G. Szamel. *Phys. Rev. E*, 73:061505, Jun 2006.

[202] Atreyee Banerjee, Shiladitya Sengupta, Srikanth Sastry, and Sarika Maitra Bhattacharyya. *Phys. Rev. Lett.*, 113:225701, Nov 2014.

[203] Misaki Ozawa, Atsushi Ikeda, Kunimasa Miyazaki, and Walter Kob. *Phys. Rev. Lett.*, 121:205501, Nov 2018.

[204] Luca Angelani, Giuseppe Foffi, Francesco Sciortino, and Piero Tartaglia. *Journal of Physics: Condensed Matter*, 17(12):L113–L119, mar 2005.

[205] Ian Williams, Francesco Turci, James E Hallett, Peter Crowther, Chiara Cammarota, Giulio Biroli, and C Patrick Royall. *Journal of Physics: Condensed Matter*, 30(9):094003, 2018.

[206] Shreyas Gokhale, AK Sood, and Rajesh Ganapathy. *Adv. Phys.*, 65(4):363, 2016.

[207] Atsushi Ikeda and Kunimasa Miyazaki. *Phys. Rev. Lett.*, 106:015701, Jan 2011.

[208] J. J. Salacuse and G. Stell. *The Journal of Chemical Physics*, 77(7):3714–3725, 1982.

[209] Peter Sollich. *Journal of Physics: Condensed Matter*, 14(3):R79–R117, dec 2001.

[210] Vasili Baranau and Ulrich Tallarek. *The Journal of Chemical Physics*, 147(22): 224503, 2017.

[211] Christopher J. Fullerton and Ludovic Berthier. *EPL (Europhysics Letters)*, 119 (3):36003, aug 2017.

[212] Ludovic Berthier and Daniele Coslovich. *Proceedings of the National Academy of Sciences*, 111(32):11668–11672, 2014.

[213] H. B. Callen. *Thermodynamics and an Introduction to Thermostatistics, 2nd Edition*. Wiley, 1985.

[214] Ludovic Berthier. *Phys. Rev. E*, 88:022313, Aug 2013.

[215] Alan M. Ferrenberg and Robert H. Swendsen. *Phys. Rev. Lett.*, 61:2635–2638, Dec 1988.

[216] Ludovic Berthier and Robert L. Jack. *Phys. Rev. Lett.*, 114:205701, May 2015.

[217] Koji Hukushima and Koji Nemoto. *Journal of the Physical Society of Japan*, 65(6): 1604–1608, 1996.

[218] G. Parisi and B. Seoane. *Phys. Rev. E*, 89: 022309, Feb 2014.

[219] Robert L. Jack and Juan P. Garrahan. *Phys. Rev. Lett.*, 116:055702, Feb 2016.

[220] Giulio Biroli, Charlotte Rulquin, Gilles Tarjus, and Marco Tarzia. *SciPost Phys.*, 1:007, 2016.

[221] Misaki Ozawa, Ludovic Berthier, and Daniele Coslovich. *SciPost Physics*, 3(4): 027, 2017.

[222] Giulio Biroli and Jorge Kurchan. *Phys. Rev. E*, 64:016101, Jun 2001.

[223] Andrea Montanari and Guilhem Semerjian. *Journal of statistical physics*, 124(1): 103–189, 2006.

[224] Andrea Montanari and Guilhem Semerjian. *Journal of statistical physics*, 125(1): 23, 2006.

[225] J Villain. *Journal de Physique*, 46(11): 1843–1852, 1985.

[226] C Cammarota, A Cavagna, G Gradenigo, T S Grigera, and P Verrocchio. *Journal of Statistical Mechanics: Theory and Experiment*, 2009(12):L12002, dec 2009.

[227] S Franz and A Montanari. *Journal of Physics A: Mathematical and Theoretical*, 40(11):F251, 2007.

[228] Chiara Cammarota, Andrea Cavagna, Giacomo Gradenigo, Tomas S. Grigera, and Paolo Verrocchio. *The Journal of Chemical Physics*, 131(19):194901, 2009.

[229] Vassiliy Lubchenko. *Advances in Physics*, 64(3):283–443, 2015.

[230] Andrea Cavagna, Tomás S. Grigera, and Paolo Verrocchio. *Phys. Rev. Lett.*, 98(18): 187801, 2007.

[231] A. Cavagna, T. S. Grigera, and P. Verrocchio. *The Journal of Chemical Physics*, 136 (20):204502, 2012.

[232] Glen M. Hocky, Thomas E. Markland, and David R. Reichman. *Phys. Rev. Lett.*, 108: 225506, Jun 2012.

[233] Ludovic Berthier, Patrick Charbonneau, and Sho Yaida. *The Journal of Chemical Physics*, 144(2):024501, 2016.

Article

# Does the Adam-Gibbs relation hold in supercooled liquids?

M. Ozawa, C. Scalliet, A. Ninarello, and L. Berthier, J. Chem. Phys. 151, 084504 (2019).

**We perform stringent tests of thermodynamic theories of the glass transition over the experimentally relevant temperature regime for several simulated glass-formers. The swap Monte Carlo algorithm is used to estimate the configurational entropy and static point-to-set lengthscale, and careful extrapolations are used for the relaxation times. We first quantify the relation between configurational entropy and the point-to-set lengthscale in two and three dimensions. We then show that the Adam-Gibbs relation is generally violated in simulated models for the experimentally relevant time window. Collecting experimental data for several supercooled molecular liquids, we show that the same trends are observed experimentally. Deviations from the Adam-Gibbs relation remain compatible with random first order transition theory, and may account for the reported discrepancies between Kauzmann and Vogel-Fulcher-Tammann temperatures. Alternatively, they may also indicate that even near $T_g$ thermodynamics is not the only driving force for slow dynamics.**

## I Introduction

Since its first derivation in 1965 [1], the Adam-Gibbs relation has played a central role in glass transition studies [2], since it is at the core of thermodynamic approaches to the glass problem [1, 2, 3, 4, 5, 6, 7, 8, 9]. The Adam-Gibbs relation captures in a simple mathematical form the physical idea that the decrease of the configurational entropy $S_{\rm conf}$ controls the growth of the relaxation time $\tau_\alpha$ as the experimental glass transition temperature $T_g$ is approached:

$$\log(\tau_\alpha/\tau_0) \propto \frac{1}{TS_{\rm conf}}, \tag{1}$$

where $\tau_0$ is a microscopic timescale. Testing the Adam-Gibbs relation has almost become synonymous to testing the thermodynamic nature of glass formation [10, 11, 12, 13].

Since computational methods have become available in the early 2000's to measure the configurational entropy in numerical simulations [14, 15, 16], the Adam-Gibbs relation has been tested in a large number of studies using many different models of glass-forming materials [12, 17, 18, 19, 20, 21, 22, 23, 24]. Importantly, these simulations are all restricted to a high temperature regime (typically above the mode-coupling crossover temperature $T_{\rm mct}$ [25]) that barely overlaps with the corresponding experimental studies. In addition simulations typically cover a dynamic window of at most 3-4 decades, much narrower than in experimental studies. Despite these caveats, the general consensus is that the Adam-Gibbs relation is generally valid in the regime accessed by the simulations. In experiments, which typically analyse temperatures close to $T_g$, the Adam-Gibbs relation seems again to be well obeyed for a range of materials [10, 11, 26, 27, 28, 29, 30, 31, 32]. Yet, experiments indicate as well that the Adam-Gibbs relation does not hold anymore above a temperature scale close to $T_{\rm mct}$ [11, 28], in stark contrast with the numerical results. Systematic deviations from the Adam-Gibbs relation were also reported below $T_{\rm mct}$ for some systems [28, 30], but imprecise entropy measurements or inappropriate timescale determinations have been invoked to rationalise them.

In the last three decades, the random first order transition (RFOT) theory of the glass transition [3, 5] has revisited the Adam-Gibbs relation in greater depth [4, 5, 6, 7] to provide an increasingly precise description of the connection between thermodynamics and dynamics in supercooled liquids. This connection can be decomposed in two steps. First, the decrease of the configurational entropy is shown, by a purely thermodynamic reasoning [4], to give rise to a growing 'point-to-set' static correlation lengthscale:

$$\xi_{\rm pts} \propto S_{\rm conf}^{-1/(d-\theta)}, \tag{2}$$

where an interface exponent $\theta$ is introduced. In the simplest approximation, one has $\theta = d-1$ which corresponds to a (hyper-)surface in a space of dimension $d$. The value $\theta = d/2$ was also proposed [3, 7], to take into account finite dimensional surface fluctuations due to the disordered nature of the amorphous phase. More generally, the inequality $\theta \leq d-1$ is expected to hold. Second, the connection to dynamics is made via the assumption that relaxation in the liquid for $T < T_{\rm mct}$ proceeds via thermally activated events correlated over a lengthscale $\xi_{\rm pts}$, resulting in the general relation [3, 4],

$$\log(\tau_\alpha/\tau_0) \propto \xi_{\rm pts}^{\psi}/T, \tag{3}$$

where $\psi$ is a dynamical exponent. Various theoretical and numerical estimates of $\psi$ have been proposed [4, 33, 34, 35, 36]. In the original paper by Kirkpatrick *et al.* [3], $\psi = \theta = d/2$ was assumed and so only one exponent had been introduced.

Using Eqs. (2, 3), one finds a generalised version of the Adam-Gibbs relation,

$$\log(\tau_\alpha/\tau_0) \propto \frac{1}{TS_{\rm conf}^{\alpha}}, \tag{4}$$

with a non-trivial exponent

$$\alpha = \frac{\psi}{d-\theta}. \tag{5}$$

This shows that $\alpha$ may or may not be equal to unity, depending on the relative values of the two independent exponents $\psi$ and $\theta$. As a consequence, Eq. (4) may or may not be equivalent to Eq. (1).

To our knowledge, a direct test of Eqs. (3, 4, 5) in the theoretically-motivated temperature regime, employing appropriate observables, has never been performed. Most previous simulations have considered a temperature regime $T \gtrsim T_{\rm mct}$ [12, 17, 21, 37] where the physics is expected to

be non-activated and the configurational entropy and point-to-set lengthscales are not well-defined. This is of course valuable work, but theory itself suggests that the tested scaling relations have no reason to hold in this temperature regime. Experiments instead access the correct temperature regime, but cannot easily measure the point-to-set correlation lengthscale. As a proxy, Refs. [38, 39] replaced $\xi_{\rm pts}$ by the lengthscale of dynamic heterogeneities that can be more easily estimated experimentally [40]. Many other experimental studies study Eq. (1) directly near $T_g$ [11, 30].

In this work, we take advantage of the progress allowed by the swap Monte Carlo algorithm [41, 42] to measure directly in several numerical models the temperature dependence of the configurational entropy and point-to-set lengthscale down to $T_g$. For the dynamics, we build on previous work [42] and provide additional experimental support showing that one can safely estimate the temperature dependence of the relaxation time also down to $T_g$, using a careful fitting procedure. We collect data from earlier works [43, 44, 45] that we extend where needed, and perform new simulations for one additional model.

As a result, we are in a position to provide for the first time stringent tests of the Adam-Gibbs relation and of RFOT theory for computer models simulated in the same regime as in experiments. Our results suggest that the Adam-Gibbs relation is generally not valid in computer models in the experimental regime $T_g < T < T_{\rm mct}$. To test our findings against experiments, we collect high-quality thermodynamic and dynamic data for several supercooled liquids (most of which are obtained by state-of-the-art thermodynamic measurements [46]), and reach similar conclusions. Overall, we find that Eq. (1) is not obeyed for most systems, while Eq. (4) is obeyed with an exponent $\alpha$ that fluctuates weakly from system to system, with typically $\alpha < 1$. Our findings can be taken either as a confirmation that RFOT theory works well, with a non-trivial set of critical exponents, or that a small $\alpha < 1$ exponent indicates that thermodynamics is not the only driving force for the dynamic slowdown near $T_g$.

This paper is organised as follows. In Sec. II we present the numerical methods used to obtain the configurational entropy, the point-to-set lengthscale, and the relaxation time. We also describe our choice of experimental data to reliably test the Adam-Gibbs relation over a broad range of temperatures. In Sec. III we present the results of our analysis of the exponents $\theta$ and $\alpha$ in simulations, then in experiments. We discuss the physical meaning of our results in Sec. IV.

# II Description of the data

In order to analyse quantitatively the connection between dynamic and thermodynamic properties, we collect and extend data from previous numerical works. We also collect data from selected published experimental works, and motivate our selection.

## II.1 Numerical models

The recent development of the swap Monte Carlo algorithm allows us to access very low-temperature equilibrium configurations in computer simulations. In particular, the temperature regime $T_g < T < T_{\rm mct}$ can be comfortably accessed. This temperature regime is the correct one to test thermodynamic theories, as it is precisely where they should apply, and it corresponds to the regime explored experimentally.

We gather simulation data for polydisperse systems using a continuous size distribution [42]. The particle diameters $\sigma$ are distributed between $\sigma_{\rm min}$ and $\sigma_{\rm max}$ from $f(\sigma) = c\sigma^{-3}$, where $c$ is a normalization constant and $\sigma_{\rm min}/\sigma_{\rm max} = 0.45$. We use the average diameter $\overline{\sigma}$ as the unit length.

We study four numerical models: three-dimensional additive hard spheres (HS3D) [41], two and three dimensional non-additive soft disks (SSV2D) [43] and spheres (SSV3D) [42] under an isochoric path. We also perform new simulations of three-dimensional non-additive soft spheres (SSP3D), under an isobaric path. To thermalize the last model, we use an hybrid molecular dynamics/swap Monte Carlo scheme [47].

We use the following pairwise potential for the polydisperse soft sphere/disk models [42],

$$v_{ij}(r) = v_0 \left(\frac{\sigma_{ij}}{r}\right)^{12} + c_0 + c_1 \left(\frac{r}{\sigma_{ij}}\right)^2 + c_2 \left(\frac{r}{\sigma_{ij}}\right)^4, \quad (6)$$

$$\sigma_{ij} = \frac{(\sigma_i + \sigma_j)}{2}(1 - \epsilon|\sigma_i - \sigma_j|), \quad (7)$$

where $v_0$ is the energy unit, and $\epsilon$ quantifies the degree of non-additivity of the system. We set $\epsilon = 0.2$ for SSV3D and SSV2D, and $\epsilon = 0.1$ for SSP3D. The constants, $c_0$, $c_1$ and $c_2$, are chosen to smooth $v_{ij}(r)$ up to its second derivative at the cut-off distance $r_{\rm cut} = 1.25\sigma_{ij}$. We set the number density $\rho = N/L^3 = 1.02$ with $N = 1500$ for SSV3D, and $\rho = N/L^2 = 1.01$ with $N = 1000$ for SSV2D. For SSP3D, the pressure on the isobaric path is $P = 30.0$. For HS3D [41], the pair interaction is zero for non-overlapping particles and infinite otherwise. The relevant control parameter for hard spheres is the reduced pressure $p = P/(\rho T)$. For hard spheres, $1/p$ plays precisely the same role as temperature $T$ for a dense liquid [48], and there is no distinction between isochoric and isobaric paths.

Relaxation times for HS3D, SSV3D, and SSV2D are measured in units of MC sweeps, which comprise $N$ Monte Carlo trial moves. For SSP3D, the relaxation time is expressed in units of $\sqrt{v_0/m\overline{\sigma}^2}$, where $m$ is the mass of the particles.

## II.2 Configurational entropy and point-to-set length

The configurational entropy $S_{\rm conf}$ is measured from configurations generated with swap Monte Carlo simulations. It is defined as $S_{\rm conf} = S_{\rm tot} - S_{\rm glass}$, where $S_{\rm tot}$ and $S_{\rm glass}$ are the total and glass entropies, respectively [16]. $S_{\rm tot}$ and $S_{\rm glass}$ are computed using thermodynamic integration schemes, as explained in Ref. [45]. In Appendix IV we describe how to measure $S_{\rm conf}$ along an isobaric path using constant pressure simulations for SSP3D, as this was not documented before.

Figure 1 shows the configurational entropy that we use for latter analysis. The data for $S_{\rm conf}(T)$ are normalized by the values at the mode coupling crossover $T_{\rm mct}$, whose value is determined by a power law fit to the dynamic relaxation time data [25]. The actual values are $T_{\rm mct} = 0.0426$, 0.104, 0.556, and 0.123 for HS3D, SSV3D, SSP3D, and SSV2D, respectively.

In order to increase the accuracy of the analysis, we employ empirical fitting functions. For the three-dimensional models, we use a conventional fitting function $TS_{\rm conf} = A(T - T_{\rm K}) + B(T - T_{\rm K})^2$ [11, 49]. For the two-dimensional model, we use $1/S_{\rm conf} = A/T + B$ [43]. The fitting parameters are presented in Table 1.

We also collect the point-to-set lengthscale $\xi_{\rm pts}$ data for SSV2D [43] and HS3D [44], obtained from recently developed computational methods [50, 51]. Together with $S_{\rm conf}$, the data for $\xi_{\rm pts}$ will allow us to estimate the exponent $\theta$ using Eq. (2).

## II.3 Relaxation times

Dynamical information is obtained using either standard Monte Carlo (for HS3D, SSV3D, SSV2D) or molecular dynamics (for SSP3D). The equivalence between the two types of dynamics is well

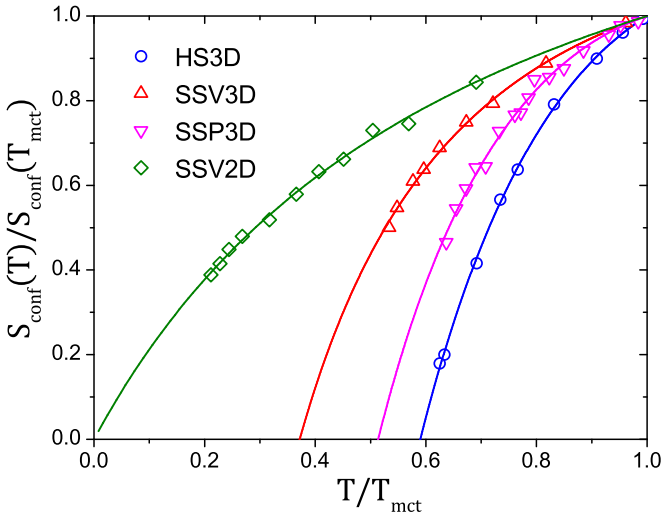


Figure 1: Configurational entropy data for the four simulated models. The data are normalized by the values at the mode coupling crossover $T_{\rm mct}$. The solid curves represent the fitting functions defined in the text and Table 1.

documented [52]. Both Monte Carlo and molecular dynamics simulations are run starting from initial configurations that are obtained using the swap Monte Carlo algorithm. This procedure allows us to cover about 5 orders of magnitude of relevant slow dynamics.

The relaxation time $\tau_\alpha$ is measured by the self-intermediate scattering function in three dimensional models. For the two-dimensional model, we use the autocorrelation function of the bond-orientational order parameter, which is insensitive to the long-range Mermin-Wagner fluctuations that are specific to $d = 2$ [53].

The relaxation time $\tau_\alpha$ for HS3D [44], SSV3D [42], SSP3D (new to this work), and SSV2D [43] is shown in Figure 2. The data are normalized using an onset temperature $T_o$ for the emergence of slow dynamics, determined from the fitting procedure described below, and define $\tau_o = \tau_\alpha(T = T_o)$. Clearly, all simulation data show a non-Arrhenius temperature dependence of the relaxation time, which demonstrates that our models describe fragile glass-formers.

The swap numerical schemes allow us to prepare equilibrated configurations at very low temperatures. Because they involve non-physical particle dynamics, one cannot use them to measure

| Model | $A$ | $B$ | $T_{\rm K}$ | $\log_{10}\tau_o$ | $T_o$ | $C$ | $m$ |
|---|---|---|---|---|---|---|---|
| HS3D | 3.208 | -37.33 | 0.0251 | 3.88 | 0.063 | 22.72 | 45.5 |
| SSV3D | 1.495 | -1.92 | 0.0386 | 3.02 | 0.266 | 3.15 | 32.0 |
| SSP3D | 2.082 | -1.74 | 0.2902 | 0.41 | 0.961 | 16.77 | 42.4 |
| SSV2D | 0.453 | 1.89 | - | 2.40 | 1.006 | 0.25 | 31.2 |

Table 1: Fitting parameters for the configurational entropy ($A$, $B$, and $T_{\rm K}$), for the relaxation time ($\tau_o$, $T_o$, and $C$) and kinetic fragility index $m$ for the simulated models. Note that Monte Carlo dynamics (HS3D, SSV3D, SSV2D) and molecular dynamics (SSP3D) have different time units.

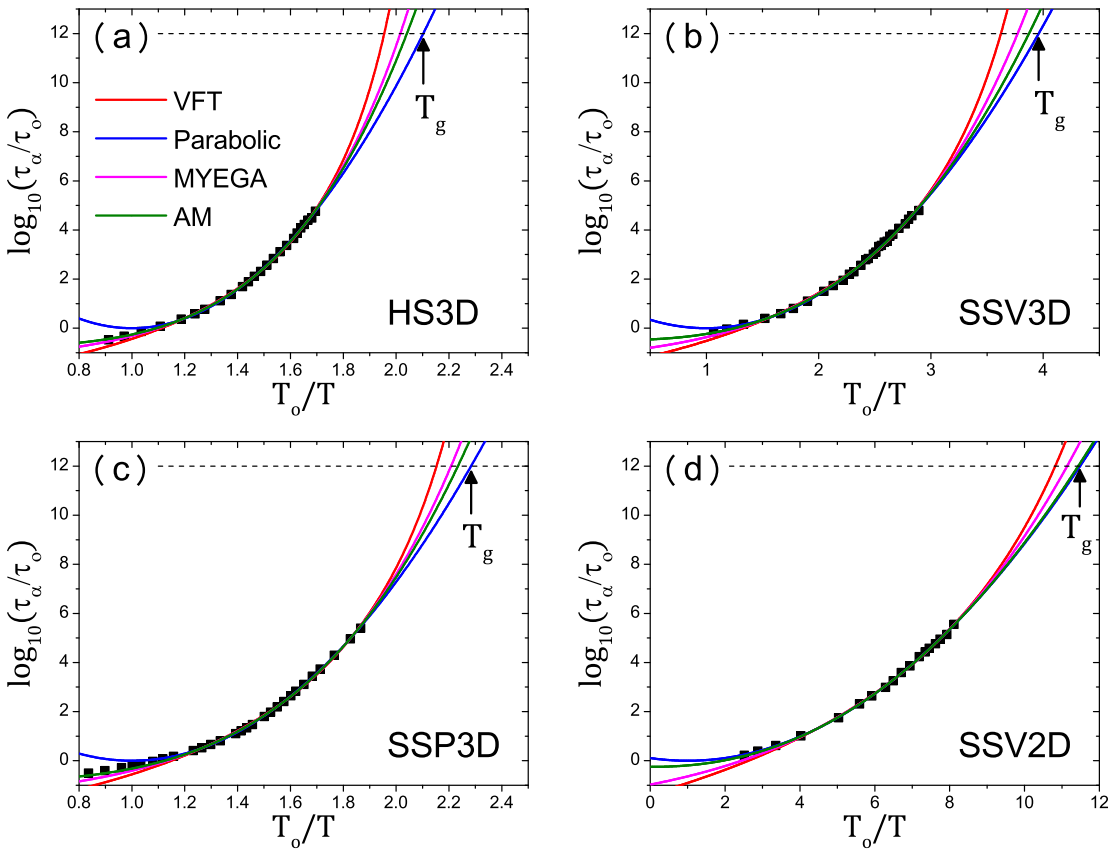


Figure 2: Relaxation time as a function of inverse temperature for the four simulated models: HS3D (a), SSV3D (b), SSP3D (c), and SSV2D (d). The data are normalized by $\tau_o$ and $T_o$, determined from a parabolic-law fitting. The horizontal dashed line indicates the timescale of the experimental glass transition, $\tau_\alpha/\tau_o = 10^{12}$. The vertical arrow indicates the experimental glass transition temperature $T_\mathrm{g}$ using the parabolic-raw fitting. Three additional fitting functions are shown.

the relaxation time of the physical dynamics in this low-temperature regime. Therefore, we need to extrapolate the relaxation time from the regime where $\tau_\alpha$ can be measured to the experimental regime, where this is unachievable.

We start by employing the Vogel-Fulcher-Tammann (VFT) law:

$$\log(\tau_\alpha/\tau_0) \propto (T - T_\mathrm{VFT})^{-1}. \tag{8}$$

where $\tau_0$ and $T_\mathrm{VFT}$ are fitting parameters. We fitted this function on our numerical data over the accessible time window and we concluded that it performs very badly when extrapolated at lower temperatures. We found for instance that the swap Monte Carlo algorithm easily thermalises at temperatures below the extrapolated VFT critical temperature $T_\mathrm{VFT}$, which invalidates directly its use to describe numerical data [42]. The inability of the VFT law to describe experimental data over a wide range of temperature was discussed in detail in Refs. [54, 55].

It has been found in previous experimental studies that the parabolic law

$$\tau_\alpha^\mathrm{para} = \tau_o \exp[C(T_o/T - 1)^2] \tag{9}$$

fits accurately the data over a very large temperature range [56, 57]. Its fitting parameters are $\tau_o$, $C$, and $T_o$.

In addition to the VFT and parabolic laws, we consider two other functional forms, shown in Fig. 2. One is a double exponential equation (MEYGEA) discussed in Refs. [56, 57]:

$$\tau_\alpha = \tau_0 \exp\left[\frac{K}{T}\exp[C/T]\right], \tag{10}$$

where $\tau_0$, $K$, and $C$ are the fitting parameters. The other one is the Avramov and Milchev (AM) equation [58] given by

$$\tau_\alpha = \tau_0 \exp[A/T^n], \tag{11}$$

where $\tau_0$, $A$, and $n$ (real exponent) are the fitting parameters. All the fitting functions considered in this paper have three free-fitting parameters which is the minimal number to mathematically characterize non-Arrhenius behavior. Given the small variation of the apparent activation energy over the dynamic range studied experimentally, it is not surprising that several smooth functions of temperature can describe the evolution of $\log(\tau_\alpha)$. Figure 2 shows that different fitting functions produce slight variations in the extrapolated value for $T_g$. The key issue is therefore to choose the best fitting function, *i.e.*, the one from which the low temperature data can be inferred accurately from the high temperature one.

To find the best fitting procedure, we train on experimental data with kinetic fragility indexes similar to our numerical models (see Appendix III). We fit the above four equations to the data, restricting ourselves to a modest dynamic range, comparable to numerical timescales. We then extrapolate to temperatures close to $T_g$, and compare the extrapolation to the actual data. We find excellent agreement when using the parabolic law, which validates further our procedure. Thus, we empirically find that fitting the parabolic law to the numerical time window provides an excellent description of the data close to $T_g$, as reported previously [56, 57]. This is a purely practical choice, and we make no assumption about the physical mechanism which could lead to such a law.

By using the fitting parameter $\tau_o$ obtained from the parabolic law, we define two time windows. First we define the *simulation window* by $\tau_\alpha/\tau_o \in [10^0, 10^5]$. The upper bound of this timescale corresponds to recent simulation studies with very long timescales [44, 59]. The *experimental window* is defined by $\tau_\alpha/\tau_o \in [10^3, 10^{12}]$. The lower bound corresponds to a timescale around the mode-coupling crossover $T_{\rm mct}$ ($\tau_\alpha \simeq 10^{-7}$ s [60]), and the upper bound corresponds to the timescale at the experimental glass transition $T_{\rm g}$ ($\tau_\alpha \simeq 100$ s). The experimental window is therefore the appropriate regime to test the predictions made by the RFOT theory. Notice that in this paper, we neither try to go below $T_g$, nor to examine the fate of supercooled liquids at even lower temperature [61].

For numerical models, we determine the experimental glass transition temperature $T_{\rm g}$ as $\tau_\alpha^{\rm para}(T_{\rm g})/\tau_o = 10^{12}$. The kinetic fragility index $m$ is determined by $m = \partial \log_{10} \tau_\alpha^{\rm para}/\partial(T_{\rm g}/T)|_{T=T_{\rm g}}$. The fitting parameters and fragility indexes are given in Table 1.

## II.4 Experimental data

We select materials for which high-quality data for the configurational entropy and relaxation time over a broad temperature range is available in the literature. This allows for a comparison with computer simulations and an accurate determination of the exponent $\alpha$ in Eq. (4).

We select 2-methyl tetrahydrofuran (2MTHF), ethylbenzene (ETB), ethanol, glycerol, *o*-terphenyl (OTP), 1-propanol, propylene carbonate (PC), salol, and toluene. The configurational entropy data for 2MTHF, ETB, OTP, PC, salol, and toluene were recently obtained from accurate experiments

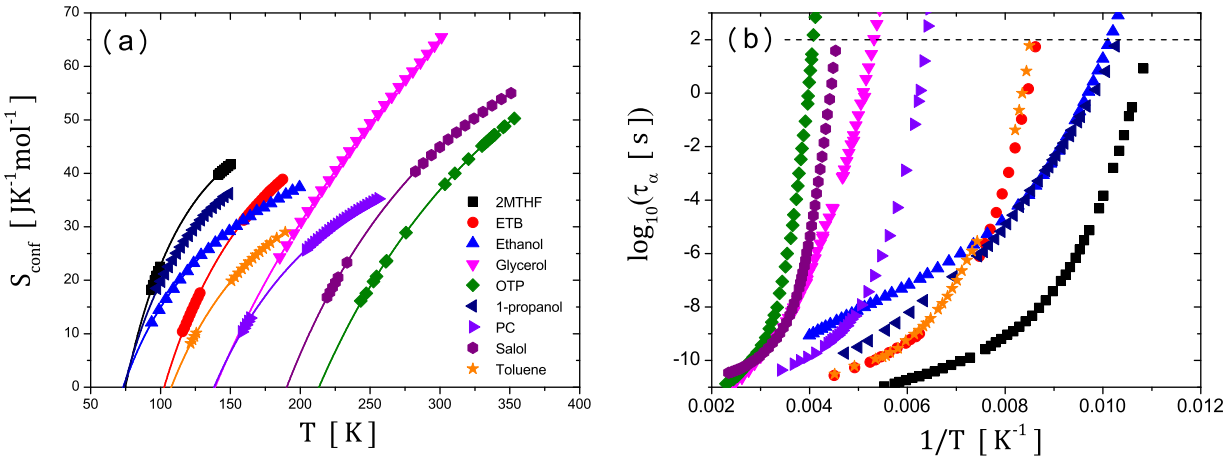


Figure 3: (a) Configurational entropy data for 2MTHF [46], ETB [46], ethanol [66], glycerol [67], OTP [78], 1-propanol [62], PC [46], salol [78], and toluene [46]. The solid curves are quadratic fitting functions, as used for the $d = 3$ numerical models. (b) Relaxation time data for 2MTHF [11], ETB [68, 69, 70], Ethanol [79], glycerol [71, 72, 73], OTP [74], 1-propanol [11, 75], PC [72, 73, 76], salol [77], and toluene [74]. The horizontal dashed line indicates the timescale of the experimental glass transition, $\tau_\alpha = 100$ s.

by Tatsumi, Aso and Yamamuro. Some of the data is presented in Ref. [46]. The data for 1-propanol is taken from Ref. [62]. In these data for all the above materials, $S_{\rm conf}$ is measured by thermodynamic integration of the heat capacity difference between supercooled liquids and non-equilibrium glasses. This treatment should be conceptually better than using the crystal entropy [11], but this is still a rather crude approximation [63], whose accuracy is expected to be material-dependent [64]. For ethanol [65, 66] and glycerol [65, 67], $S_{\rm conf}$ is obtained using the crystal entropy $S_{\rm cry}$, *i.e.*, $S_{\rm conf} = S_{\rm liq} - S_{\rm cry}$.

The relaxation time data are mainly obtained from dielectric measurements, but some data are combined with other methods, such as viscosity measurements. The corresponding references are: 2MTHF [11], ETB [68, 69, 70], ethanol [46], glycerol [71, 72, 73], OTP [74], 1-propanol [11, 75], PC [72, 73, 76], salol [77], and toluene [74].

For the experimental data, we set $\tau_o = 10^{-10}$ s. Therefore the simulation and experimental time windows correspond to $\tau_\alpha \in [10^{-10}\ {\rm s}, 10^{-5}\ {\rm s}]$ and $\tau_\alpha \in [10^{-7}\ {\rm s}, 10^{2}\ {\rm s}]$, respectively. In particular, $T_g$ corresponds to the standard relaxation time $\tau_\alpha = 100$ s.

The configurational entropy and relaxation time data for the materials presented above are gathered in Fig. 3, together with empirical quadratic fits to the configurational entropy.

## III Results

In this section, we perform a test of Eqs. (1, 2, 3, 4, 5) using the experimental and numerical data presented in Sec. II. We first study Eq. (2) using numerical data for $\xi_{\rm pts}$ and $S_{\rm conf}$ to estimate $\theta$. Then, we estimate $\alpha$ in Eq. (4) by comparing $\tau_\alpha$ and $S_{\rm conf}$ using both computer simulations and experiments to investigate the validity of the Adam-Gibbs relation in Eq. (1). Finally, the values of

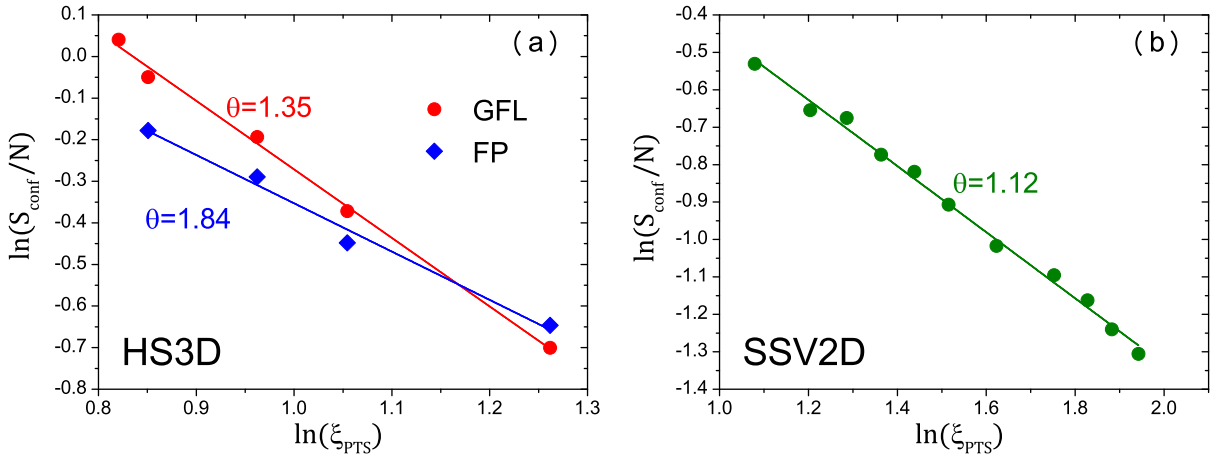


Figure 4: $S_{\rm conf}$ vs. $\xi_{\rm pts}$ plot in $d = 3$ hard spheres (HS3D) (a) and $d = 2$ soft disks (SSV2D) (b). The straight lines are power law fits. For HS3D, we show two independent estimates of $S_{\rm conf}$ obtained from: the generalized Frenkel-Ladd (GFL) method and the Franz-Parisi (FP) free energy approach.

$\theta$ and $\alpha$ allow us to discuss that taken by $\psi = (d - \theta)\alpha$, deduced from Eq. (5).

### III.1 The static exponent $\theta$

First we estimate the exponent $\theta$ in Eq. (2) combining independent data obtained for $S_{\rm conf}$ and $\xi_{\rm pts}$.

Figure 4 shows a log-log plot of $S_{\rm conf}$ versus $\xi_{\rm pts}$ for three dimensional polydisperse hard spheres (HS3D) (a) and two dimensional soft disks (SSV2D) (b). We emphasize that while temperature is a running parameter in this plot, the data point in Fig. 4 correspond to the regime of interest $T < T_{\rm mct}$. Such results have never been achieved, as earlier numerical work were all performed for $T > T_{\rm mct}$, or only slightly below $T_{\rm mct}$ [33].

For HS3D, we report two estimates for $S_{\rm conf}$, obtained from different schemes. One is a generalized Frenkel-Ladd (GFL) method [45, 80], and the other is the Franz-Parisi (FP) free energy method proposed earlier [44, 81, 82]. The exponent $\theta$ is extracted by fits to straight lines, whose slope gives $\theta - d$, see Eq. (2). We obtain $\theta \simeq 1.35$ for GFL and $\theta \simeq 1.84$ for FP. These values are compatible with either the theoretical prediction $\theta = d/2$ by Kirkpatrick *et al.* [3], or with that of Franz $\theta = d - 1$ [83].

We obtain $\theta = 1.12$ for SSV2D. This value is close to both theoretical predictions, $\theta = d/2$ and $\theta = d - 1$, which coincide in $d = 2$, giving $\theta = 1$ . Obviously, one cannot discriminate between the two predictions.

Overall, we find that for $d = 3$ the value measured for $\theta$ conforms with the two available predictions, which is an encouraging result from the viewpoint of RFOT theory. Unfortunately, the obtained values fall in-between the two predictions, which are too close to be discriminated. We suggest that performing point-to-set and configurational entropy measurements in $d = 4$, combining recently developed tools [45, 51, 84], would be very useful to conclude on this point. Indeed, when $d = 4$, the two predictions yield $\theta = d/2 = 2$ and $\theta = d - 1 = 3$, which are further appart than in $d = 3$.

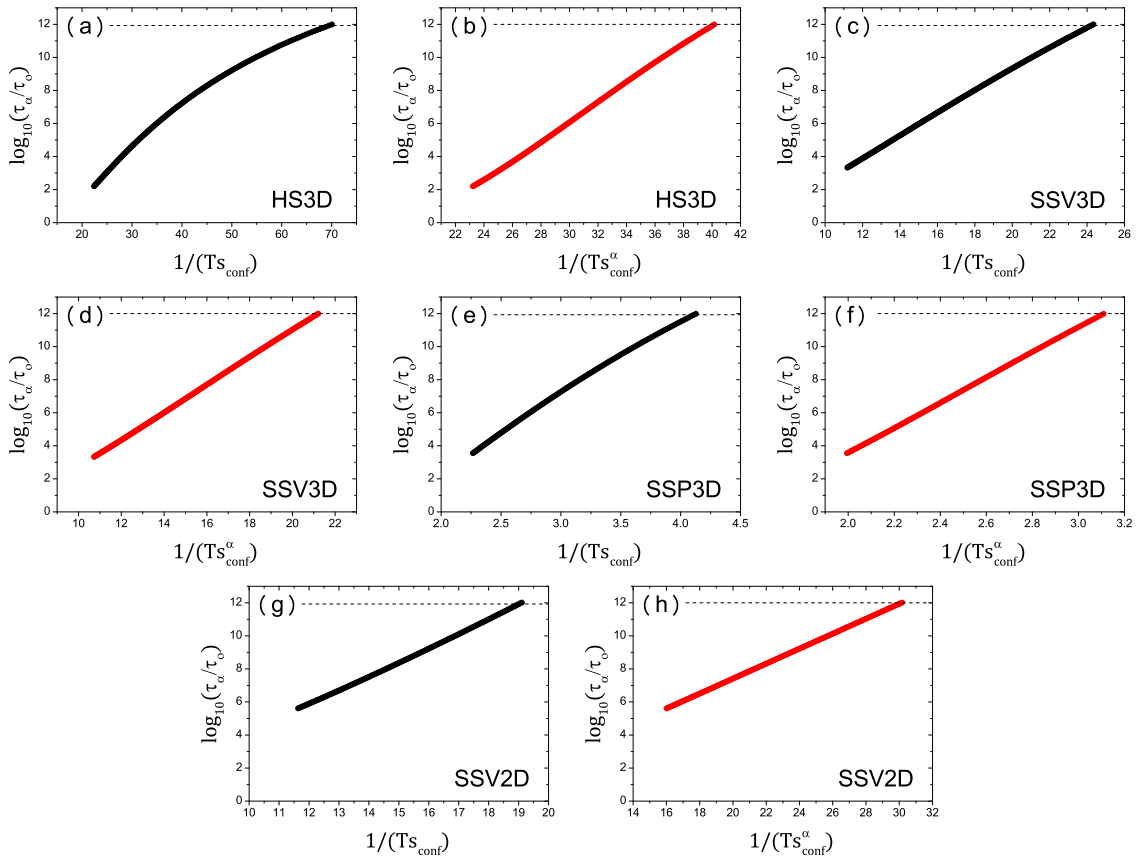


Figure 5: Left panels: Standard Adam-Gibbs plot for the $d = 3$ hard spheres (HS3D) (a), $d = 3$ soft spheres along the isochoric path (SSV3D) (b), the isobaric path (SSP3D) (c), and $d = 2$ soft disks (SSV2D) (d). Right panels: Generalized Adam Gibbs plots with the fitted $\alpha$ value for each model. The horizontal dashed lines correspond to the timescale for the experimental glass transition $T_g$.

### III.2 Breakdown of the Adam-Gibbs relation and numerical estimation of $\alpha$

We next examine the validity of Eq. (4) by connecting $\tau_\alpha$ and $S_{\rm conf}$, and estimating the exponent $\alpha$. When $\alpha = 1$, the Adam-Gibbs relation in Eq. (1) is recovered.

In Fig. 5(a,c,e,g) we show conventional Adam-Gibbs plots where the evolution of $\log_{10}(\tau_\alpha/\tau_o)$ is represented as a function of $1/(Ts_{\rm conf})$, where $s_{\rm conf} = S_{\rm conf}/N$, for hard spheres (HS3D) (a), soft spheres along the isochoric path (SSV3D) (c), along the isobaric path (SSP3D) (e), and the soft disks (SSV2D) (g). We combine the dynamic and thermodynamic data described in Sec. II, restricted to the experimental time window ($\tau_\alpha/\tau_o \in [10^3 - 10^{12}]$). To our knowledge, this is the first time that the Adam-Gibbs relation is tested for computer models over the time window where it is actually supposed to apply.

For all three-dimensional models, we find that $\log_{10}(\tau_\alpha/\tau_o)$ is a concave function of $1/Ts_{\rm conf}$, whereas it is convex for the two-dimensional model. If tested over a narrow time window close to $T_{\rm mct}$, an acceptable linear behaviour could possibly be observed, that would suggest the validity of the Adam-Gibbs relation, in agreement with many earlier findings [12, 17, 18, 19, 20, 21, 22, 23, 24].

The trend that we report here appears to contrast with recent results obtained in the Kob-Andersen model, where slight convexity and concavity are respectively observed in $d = 3$ [23] and $d = 2$ [21]. These results were however obtained in the numerical time window, above $T_{\rm mct}$. Our results demonstrate that when observed over a much broader range, and closer to $T_g$, the Adam-Gibbs relation is actually not obeyed for any of the numerical models studied here.

The clear violations of the standard Adam-Gibbs relation that we find over the experimental time window imply that the exponent $\alpha$ must deviate from the value $\alpha = 1$. We varied its value around unity and used it as a free parameter to obtain generalised Adam-Gibbs plots, which are shown in Fig. 5(b,d,f,h) for the same numerical models. All plots now show a perfect straight line, suggesting that the introduction of the parameter $\alpha$ is sufficient to describe the data. We obtain $\alpha = 0.24$, 0.49, 0.72, and 1.89, for HS3D, SSP3D, SSV3D, and SSV2D, respectively, so that $\alpha < 1$ for the three dimensional models, whereas $\alpha > 1$ for the two dimensional model.

Since the four models we have simulated all display violations of the Adam-Gibbs relation, we conclude that Eq. (1) does not describe well the physics of simulated supercooled liquids when analysed over the experimental time window. Additional models should be studied and analysed before concluding about the possible universality of the exponent $\alpha$, but our initial results do not point towards a constant value. Once more, it would be very valuable to obtain data in $d = 4$ to see if a different value for $\alpha$ is found in larger spatial dimensions.

### III.3 Breakdown of the Adam-Gibbs relation and experimental estimation of $\alpha$

Before starting this study, we felt that there was a general consensus in the community that the Adam-Gibbs relation is well-obeyed in real materials analysed near the experimental glass transition $T_g$. Thus, the outcome of the computer simulations showing deviations from Eq. (1) appeared as a worrying disagreement between simulations and experiments.

Therefore, we decided to collect data sets for several molecular liquids, where high-precision dynamic and thermodynamic data would be available over both simulation and experimental time windows, in order to perform a direct comparison with computer models.

We present the results of our data collection in Fig. 6 using again the representation where the standard Adam-Gibbs relation would yield a straight line. When analysed over the entire experimental time window, defined above, we again observe a clear concavity for most materials. The Adam-Gibbs relation in Eq. (1) is violated over this regime, although of course it holds if observed over a restricted time window close to $T_g$ [11] (almost by definition–the data is continuous!).

As for the simulations, we fit the experimental data using the exponent $\alpha$ as an additional free parameter. From the experimental data, we determine two distinct values for $\alpha$, obtained by fitting either over the simulation or the experimental time window. The typical trend that we observe is that $\alpha > 1$ over the simulation time window, but $\alpha < 1$ over the experimental time window. The latter fits are included in Fig. 6, and they describe well the data over the entire experimental time window.

We notice that the concavity in the Adam-Gibbs plot in the experimental time window was already reported [28, 30]. However, the concavity would be overlooked as it is less pronounced than the convexity found at much higher temperature, close to $T_{\rm mct}$ and above [28]. Moreover, Ref. [30] concluded that the observed concavity was attributed to an imprecise estimate of the configurational entropy. Our results obtained from simulation data with accurate configurational entropy measurements and recent high-quality experimental data suggest instead that the observed concavity is a generic physical phenomenon reflecting the nature of glassy dynamics over the experimental time

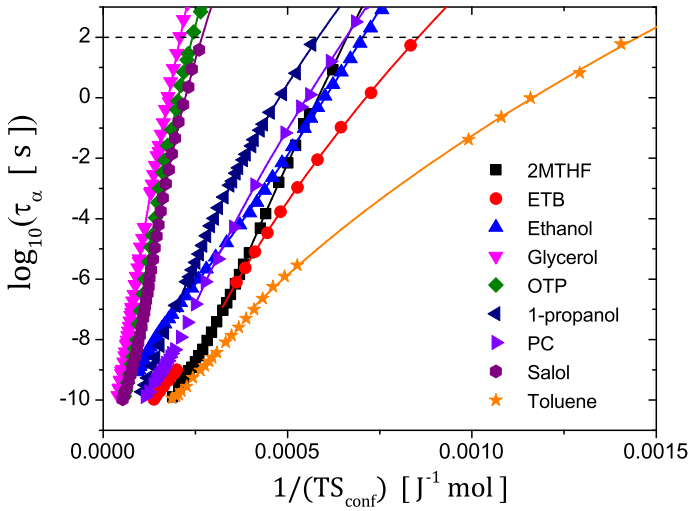


Figure 6: Standard Adam-Gibbs plot constructed from experimental data all except ethanol display a concave behaviour. The solid curves correspond to fits using Eq. (4) using a varying $\alpha$ exponent, over the experimental time window.

window.

## IV Discussion

Our central conclusion from both simulations and experiments considered over a broad time regime $\tau_\alpha/\tau_o \in [10^3, 10^{12}]$ (defined to be both experimentally accessible and theoretically relevant) is that the conventional Adam-Gibbs relation in Eq. (1) is not obeyed. Instead, the general form predicted by RFOT theory in Eq. (4) describes numerical and experimental data well. This is maybe not so surprising, from an empirical viewpoint, given that the generalised relation has one more free fitting parameter.

We compile all our results for the values of $\alpha$ from simulations (empty points) and experiments (filled points) in Fig. 7. To organise the data, we use the kinetic fragility index $m$ as the horizontal axis. This is simply a matter of convenience (as a matter of fact, no strong trend is observed). Note that, somewhat paradoxically, we do not have values for $\alpha$ in the computer models over the simulation time window because our computational schemes to measure $S_{\rm conf}$ only become applicable for low enough temperatures, typically $T \lesssim T_{\rm mct}$ [45, 82].

The experimental data in Fig. 7 obtained by considering the simulation time window are dispersed, $\alpha = 0.61 - 2.34$, and tend to be characterised by rather large values $\alpha > 1$. By contrast, considering a broader and physically better justified experimental time window, data for both simulations and experiments are much less scattered, $\alpha \simeq 0.25 - 1.28$, with a preferred average value $\alpha \simeq 0.5 - 0.6$, except for ethanol. We notice that the deviation for ethanol might be due to a poor estimation of $S_{\rm conf}$. The data was measured using the crystal entropy, and the approximation $S_{\rm glass} \simeq S_{\rm cry}$ may not be good for this material.

Before concluding, we make a further caveat regarding the above analysis of the RFOT theory predictions. In principle, we could have introduced additional subdominant physical prefactors

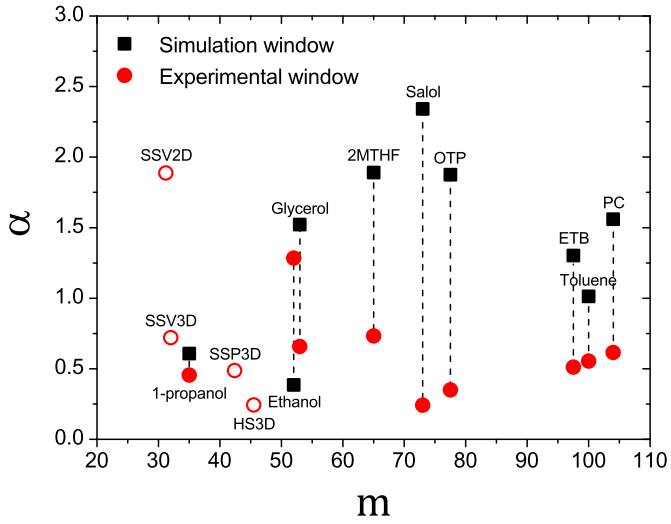


Figure 7: The measured values of $\alpha$ presented, for convenience, as a function of the kinetic fragility index $m$ for the simulation (black squares) and experimental (red circles) time windows for various materials. The vertical dashed lines connects the two values for each material. Empty circles correspond to simulation models where $\alpha$ is measured over the experimental time window only.

into the scaling relations in Eqs. (2, 3) that could also be temperature dependent quantities. In particular, a surface tension could enter the relation between $S_{\rm conf}$ and $\xi_{\rm pts}$ [6, 85], and an energy scale could enter the activated scaling relation in Eq. (3). In the absence of strong theoretical insights into these quantities, we decided to ignore them. They could of course very well affect the measured values of the reported exponents. Thus, a better determination of these quantities is an important research goal [33, 86, 87], in particular in the experimental time window.

To summarize our results in terms of numerical values for the critical exponents introduced within RFOT theory, we observe in $d = 3$ that the combination $\theta \simeq 3/2$ and $\alpha \simeq 0.5 - 0.6$ works well, which would then result in $\psi$ falling in the range $\psi \simeq 0.75 - 0.90$. If we use instead the value $\theta = 2$, we would obtain a somewhat larger value for the dynamic exponent $\psi \simeq 1.0 - 1.2$, which agrees well with earlier indirect analysis [38, 39]. Both values violate the general bound $\psi \geq \theta$ discussed in the context of spin glasses [88], the equality $\psi = \theta$ found for the random field Ising model [89], and the prediction $\psi = \theta = d/2$ in Ref. [3]. In the absence of stronger theoretical constraints, we tentatively conclude that the measured $\psi$ value that we observe appears somewhat small, *i.e.*, smaller than all known theoretical predictions. In $d = 2$, we get $\theta \simeq 1.1$ and $\alpha \simeq 1.9$, which in turns implies that $\psi \simeq 1.7$, which appears somewhat large, by contrast with $d = 3$.

Our conclusion that $\alpha < 1$ is favored by the data over the experimental time window sheds some new light on an old debate in the glass literature [5, 56, 90, 91]. Assuming the existence of an ideal glass transition at equilibrium where $S_{\rm conf} \to 0$ and $\tau_\alpha \to \infty$, one is naturally led to the determination of two critical temperatures: the Kauzmann temperature $T_K$ where $S_{\rm conf}$ vanishes, and the critical temperature $T_0$ where the relaxation time diverges (not to be confused with onset temperature $T_o$ used above). Typically, the latter is obtained from a Vogel-Fulcher-Tammann fit ($T_0 = T_{\rm VFT}$ in Eq. (8)) to the relaxation time. The possible equality $T_0 = T_K$ would provide a strong empirical sign for the existence of an ideal glass transition underlying

glass formation [5]. A large data set collected by Tanaka suggests the existence of systematic differences between the two temperatures [90], with the tendency that $T_K > T_0$, and an apparent correlation with kinetic fragility. In our analysis using Eq. (4) to describe the data, the connection between thermodynamics and dynamics becomes automatically satisfied, and thus by construction thermodynamic and dynamic singularities necessarily coincide. Assuming that the determination of $T_K$ is the most robust one, we conclude that it is the experimental determination of $T_0$ which should be questioned. In particular, using $\alpha < 1$ in Eqs. (4) and assuming an asymptotically linear vanishing of $S_{\rm conf}$, one would predict that $\log(\tau_\alpha/\tau_0) \propto (T - T_0)^{-\alpha}$, which is distinct from the standard Vogel-Fulcher-Tamman fit and would automatically produce the equality $T_K = T_0$.

From a broader perspective, we conclude that the Adam-Gibbs relation, which is an important milestone in the field of glass transition studies, is generally violated in both computer models and real materials when tested over a broad, experimentally-relevant temperature range. We nevertheless argued that the failure of Eq. (1) cannot be taken as evidence that thermodynamic theories of the glass transition are incorrect. The RFOT theory prediction of a connexion between statics and dynamics in Eq. (4) is obeyed by all materials, with exponent values that are reasonable, but remain to be predicted from first principles. A larger concern, perhaps, is the apparent lack of universality in the data shown in Fig. 7 which clearly display variations from one system to another. This may still be rationalised by invoking the fact that $\alpha$ is obtained from the analysis of a finite time window where additional preasymptotic effects and temperature dependent prefactors may influence the reported results.

Taking an orthogonal perspective, we finally ask: Do our results validate or invalidate some theories of the glass transition? After all, we just established that a slightly generalised version of the Adam-Gibbs relation with $\alpha \simeq 0.5 - 0.6$ describes simulations and experiments over 9 orders of magnitude in the experimentally relevant regime. This is not a small accomplishment. One can take the alternative view that the deviations from the canonical exponent values should be taken as an indirect sign that thermodynamics only contributes some part of the slowing down, in addition to other physical factors [92, 93, 94, 95, 96, 97]. This view is sometimes also invoked to rationalise the "modest" growth of static correlation lengthscale observed numerically and experimentally [98, 99]. Our finding that $\alpha < 1$ suggests instead that it is the growth of the relaxation time that is actually too modest! It is therefore difficult to rationalise how another physical factor working in addition to the entropy could be invoked to explain our findings. The most radical view is in fact that thermodynamics is just a spectator to the glassy dynamics [100], in which case our findings should be interpreted as purely coincidental since entropy plays in fact no role. We have no strong argument to oppose to this view, which remains perfectly admissible.

**Acknowledgments** We thank D. Coslovich and F. Zamponi for insightful discussions. We also thank S. Tatsumi and O. Yamamuro for sharing their high-quality experimental data for the configurational entropy. The research leading to these results has received funding from the Simons Foundation (#454933, Ludovic Berthier).

## Bibliography

[1] Gerold Adam and Julian H Gibbs. *J. Chem. Phys.*, 43(1):139, 1965.

[2] Ludovic Berthier and Giulio Biroli. *Rev. Mod. Phys.*, 83(2):587, 2011.

[3] T. R. Kirkpatrick, D. Thirumalai, and P. G. Wolynes. *Phys. Rev. A*, 40(2):1045–1054, Jul 1989.

[4] Jean-Philippe Bouchaud and Giulio Biroli. *J. Chem. Phys.*, 121(15):7347–7354, 2004.

[5] Vassiliy Lubchenko and Peter G. Wolynes. *Annual Review of Physical Chemistry*, 58(1): 235–266, 2007.

[6] G. Biroli and J.P. Bouchaud. The Random First-Order Transition Theory of Glasses: a critical assessment. In P.G.Wolynes and V.Lubchenko, editors, *Structural Glasses and Supercooled Liquids: Theory, Experiment and Applications*. Wiley & Sons, 2012.

[7] Vassiliy Lubchenko. *Advances in Physics*, 64(3):283–443, 2015.

[8] Patrick Charbonneau, Jorge Kurchan, Giorgio Parisi, Pierfrancesco Urbani, and Francesco Zamponi. *Annual Review of Condensed Matter Physics*, 8(1):265–288, 2017.

[9] Jacek Dudowicz, Karl F. Freed, and Jack F. Douglas. *Advances in Chemical Physics*, pages 125–222, 2008.

[10] CA Angell. *Journal of research of the National Institute of Standards and Technology*, 102(2): 171, 1997.

[11] R. Richert and C. A. Angell. *The Journal of Chemical Physics*, 108(21):9016–9026, 1998.

[12] Srikanth Sastry. *Nature*, 409(6817):164, 2001.

[13] Jeppe C Dyre, Tina Hechsher, and Kristine Niss. *Journal of Non-Crystalline Solids*, 355 (10-12):624–627, 2009.

[14] F. Sciortino, W. Kob, and P. Tartaglia. *Phys. Rev. Lett.*, 83:3214–3217, Oct 1999.

[15] Srikanth Sastry. *Journal of Physics: Condensed Matter*, 12(29):6515–6523, jul 2000.

[16] Ludovic Berthier, Misaki Ozawa, and Camille Scalliet. *The Journal of Chemical Physics*, 150 (16):160902, 2019.

[17] S. Mossa, E. La Nave, H. E. Stanley, C. Donati, F. Sciortino, and P. Tartaglia. *Phys. Rev. E*, 65:041205, Apr 2002.

[18] Francesco Sciortino. *Journal of Statistical Mechanics: Theory and Experiment*, 2005(05): P05015, 2005.

[19] Ivan Saika-Voivod, Peter H Poole, and Francesco Sciortino. *Nature*, 412(6846):514, 2001.

[20] Luca Angelani, Giuseppe Foffi, Francesco Sciortino, and Piero Tartaglia. *Journal of Physics: Condensed Matter*, 17(12):L113–L119, mar 2005.

[21] Shiladitya Sengupta, Smarajit Karmakar, Chandan Dasgupta, and Srikanth Sastry. *Phys. Rev. Lett.*, 109:095705, Aug 2012.

[22] Francis W Starr, Jack F Douglas, and Srikanth Sastry. *The Journal of chemical physics*, 138 (12):12A541, 2013.

[23] Anshul DS Parmar, Shiladitya Sengupta, and Srikanth Sastry. *Physical review letters*, 119(5): 056001, 2017.

[24] Philip H Handle and Francesco Sciortino. *Molecular physics*, 116(21-22):3366–3371, 2018.

[25] Wolfgang Götze. *Complex dynamics of glass-forming liquids: A mode-coupling theory*, volume 143. Oxford University Press, Oxford, 2008.

[26] JH Magill. *The Journal of chemical physics*, 47(8):2802–2807, 1967.

[27] Shuichi Takahara, Osamu Yamamuro, and Takasuke Matsuo. *The Journal of Physical Chemistry*, 99(23):9589–9592, 1995.

[28] KL Ngai. *The Journal of Physical Chemistry B*, 103(28):5895–5902, 1999.

[29] C Alba-Simionesco. *Comptes Rendus de l'Académie des Sciences-Series IV-Physics-Astrophysics*, 2(2):203–216, 2001.

[30] CM Roland, Simone Capaccioli, Mauro Lucchesi, and R Casalini. *The Journal of chemical physics*, 120(22):10640–10646, 2004.

[31] D Cangialosi, A Alegria, and J Colmenero. *EPL (Europhysics Letters)*, 70(5):614, 2005.

[32] Elżbieta Masiewicz, Andrzej Grzybowski, Katarzyna Grzybowska, Sebastian Pawlus, Jürgen Pionteck, and Marian Paluch. *Scientific reports*, 5:13998, 2015.

[33] Chiara Cammarota, Andrea Cavagna, Giacomo Gradenigo, Tomas Grigera, and Paolo Verrocchio. *The Journal of Chemical Physics*, 131(19):194901, 2009.

[34] Smarajit Karmakar, Chandan Dasgupta, and Srikanth Sastry. *Proceedings of the National Academy of Sciences*, 106(10):3675–3679, 2009.

[35] Glen M. Hocky, Thomas E. Markland, and David R. Reichman. *Phys. Rev. Lett.*, 108:225506, Jun 2012.

[36] R. Gutiérrez, S. Karmakar, Y. G. Pollack, and I. Procaccia. *EPL (Europhysics Letters)*, 111 (5):56009, sep 2015.

[37] Andrea Cavagna, Tomas S. Grigera, and Paolo Verrocchio. *The Journal of Chemical Physics*, 136(20):204502, 2012.

[38] Simone Capaccioli, Giancarlo Ruocco, and Francesco Zamponi. *The Journal of Physical Chemistry B*, 112(34):10652–10658, 2008.

[39] C Brun, F Ladieu, D L'Hôte, G Biroli, and JP Bouchaud. *Physical review letters*, 109(17): 175702, 2012.

[40] L. Berthier, G. Biroli, J.-P. Bouchaud, L. Cipelletti, D. El Masri, D. L'Hôte, F. Ladieu, and M. Pierno. *Science*, 310(5755):1797–1800, 2005. ISSN 0036-8075.

[41] Ludovic Berthier, Daniele Coslovich, Andrea Ninarello, and Misaki Ozawa. *Phys. Rev. Lett.*, 116:238002, Jun 2016.

[42] Andrea Ninarello, Ludovic Berthier, and Daniele Coslovich. *Phys. Rev. X*, 7:021039, 2017.

[43] Ludovic Berthier, Patrick Charbonneau, Andrea Ninarello, Misaki Ozawa, and Sho Yaida. *Nature Communications*, 10(1):1508, 2019.

[44] Ludovic Berthier, Patrick Charbonneau, Daniele Coslovich, Andrea Ninarello, Misaki Ozawa, and Sho Yaida. *Proceedings of the National Academy of Sciences*, 114(43):11356–11361, 2017. ISSN 0027-8424.

[45] Misaki Ozawa, Giorgio Parisi, and Ludovic Berthier. *The Journal of Chemical Physics*, 149 (15):154501, 2018.

[46] Soichi Tatsumi, Shintaro Aso, and Osamu Yamamuro. *Phys. Rev. Lett.*, 109:045701, Jul 2012.

[47] Ludovic Berthier, Elijah Flenner, Christopher J Fullerton, Camille Scalliet, and Murari Singh. *arXiv preprint arXiv:1811.12837*, 2018.

[48] Ludovic Berthier and Thomas A. Witten. *Phys. Rev. E*, 80(2):021502, Aug 2009.

[49] Atreyee Banerjee, Shiladitya Sengupta, Srikanth Sastry, and Sarika Maitra Bhattacharyya. *Phys. Rev. Lett.*, 113:225701, Nov 2014.

[50] G. Biroli, J.P. Bouchaud, A. Cavagna, TS Grigera, and P. Verrocchio. *Nature Physics*, 4(10): 771–775, 2008.

[51] Ludovic Berthier, Patrick Charbonneau, and Sho Yaida. *The Journal of Chemical Physics*,

144(2):024501, 2016.

[52] Ludovic Berthier and Walter Kob. *J. Phys.: Condens. Matter*, 19(20):205130, 2007.

[53] Elijah Flenner and Grzegorz Szamel. *Nature communications*, 6:7392, 2015.

[54] F. Stickel, E. W. Fischer, and R. Richert. *J. Chem. Phys.*, 102(15):6251–6257, 1995.

[55] ME Blodgett, Takeshi Egami, Z Nussinov, and KF Kelton. *Scientific reports*, 5:13837, 2015.

[56] Yael S. Elmatad, David Chandler, and Juan P. Garrahan. *The Journal of Physical Chemistry B*, 114(51):17113–17119, 2010.

[57] John C. Mauro, Yuanzheng Yue, Adam J. Ellison, Prabhat K. Gupta, and Douglas C. Allan. *Proceedings of the National Academy of Sciences*, 106(47):19780–19784, 2009. ISSN 0027-8424.

[58] I Avramov and A Milchev. *Journal of non-crystalline solids*, 104(2-3):253–260, 1988.

[59] Daniele Coslovich, Misaki Ozawa, and Walter Kob. *The European Physical Journal E*, 41(5): 62, May 2018. ISSN 1292-895X.

[60] V. N. Novikov and A. P. Sokolov. *Phys. Rev. E*, 67(3):031507, 2003.

[61] C Patrick Royall, Francesco Turci, Soichi Tatsumi, John Russo, and Joshua Robinson. *Journal of Physics: Condensed Matter*, 30(36):363001, aug 2018.

[62] Shuichi Takahara, Osamu Yamamuro, and Hiroshi Suga. *Journal of non-crystalline solids*, 171(3):259–270, 1994.

[63] Akira Yoshimori and Takashi Odagaki. *Journal of the Physical Society of Japan*, 80(6):064601, 2011.

[64] Hillary L Smith, Chen W Li, Andrew Hoff, Glenn R Garrett, Dennis S Kim, Fred C Yang, Matthew S Lucas, Tabitha Swan-Wood, Jiao YY Lin, Matthew B Stone, et al. *Nature Physics*, 13(9):900, 2017.

[65] Kiyoshi Takeda, Osamu Yamamuro, Itaru Tsukushi, Takasuke Matsuo, and Hiroshi Suga. *Journal of molecular structure*, 479(2-3):227–235, 1999.

[66] Osamu Haida, Hiroshi Suga, and Syûzô Seki. *The Journal of Chemical Thermodynamics*, 9 (12):1133–1148, 1977.

[67] G. E. Gibson and W. F. Giauque. *Journal of the American Chemical Society*, 45(1):93–104, 1923.

[68] Zhen Chen and Ranko Richert. *The Journal of chemical physics*, 135(12):124515, 2011.

[69] AJ Barlow, J Lamb, and AJ Matheson. *Proceedings of the Royal Society of London. Series A. Mathematical and Physical Sciences*, 292(1430):322–342, 1966.

[70] Frederick Dominic Rossini. *Selected values of physical and thermodynamic properties of hydrocarbons and related compounds: comprising the tables of the American Petroleum Institute Research Project 44 extant as of December 31, 1952*, volume 44. American Petroleum Institute, 1953.

[71] Ulrich Schneider, P Lunkenheimer, R Brand, and A Loidl. *Journal of non-crystalline solids*, 235:173–179, 1998.

[72] P. Lunkenheimer, U. Schneider, R. Brand, and A. Loid. *Contemporary Physics*, 41(1):15–36, 2000.

[73] P. Lunkenheimer, R. Wehn, U. Schneider, and A. Loidl. *Phys. Rev. Lett.*, 95:055702, Jul 2005.

[74] B Schmidtke, N Petzold, R Kahlau, M Hofmann, and EA Rössler. *Physical Review E*, 86(4): 041507, 2012.

[75] Per Sillrén, Aleksandar Matic, Maths Karlsson, M Koza, M Maccarini, P Fouquet, M Götz, Th Bauer, R Gulich, P Lunkenheimer, et al. *The Journal of chemical physics*, 140(12):124501, 2014.

[76] U. Schneider, P. Lunkenheimer, R. Brand, and A. Loidl. *Phys. Rev. E*, 59:6924–6936, Jun 1999.

[77] F Stickel, Erhard W Fischer, and Ranko Richert. *The Journal of chemical physics*, 104(5): 2043–2055, 1996.

[78] Soichi Tatsumi and Osamu Yamamuro.

[79] R. Brand, P. Lunkenheimer, U. Schneider, and A. Loidl. *Phys. Rev. B*, 62:8878–8883, Oct 2000.

[80] Daan Frenkel and Berend Smit, editors. *Understanding Molecular Simulation (Second Edition)*. Academic Press, San Diego, second edition edition, 2002.

[81] Silvio Franz and Giorgio Parisi. *Phys. Rev. Lett.*, 79(13):2486–2489, Sep 1997.

[82] Ludovic Berthier and Daniele Coslovich. *Proceedings of the National Academy of Sciences*, 111(32):11668–11672, 2014.

[83] Silvio Franz. *Journal of Statistical Mechanics: Theory and Experiment*, 2005(04):P04001, apr 2005.

[84] Ludovic Berthier, Patrick Charbonneau, and Joyjit Kundu. *Phys. Rev. E*, 99:031301, Mar 2019.

[85] Vassiliy Lubchenko and Pyotr Rabochiy. *The Journal of Physical Chemistry B*, 118(47): 13744–13759, 2014.

[86] C Cammarota, A Cavagna, G Gradenigo, T S Grigera, and P Verrocchio. *Journal of Statistical Mechanics: Theory and Experiment*, 2009(12):L12002, dec 2009.

[87] Divya Ganapathi, K Hima Nagamanasa, AK Sood, and Rajesh Ganapathy. *Nature communications*, 9(1):397, 2018.

[88] Daniel S Fisher and David A Huse. *Physical Review B*, 38(1):373, 1988.

[89] Ivan Balog and Gilles Tarjus. *Phys. Rev. B*, 91:214201, Jun 2015.

[90] Hajime Tanaka. *Physical review letters*, 90(5):055701, 2003.

[91] Tina Hecksher, Albena I Nielsen, Niels Boye Olsen, and Jeppe C Dyre. *Nature Physics*, 4(9): 737, 2008.

[92] G Tarjus, S A Kivelson, Z Nussinov, and P Viot. *Journal of Physics: Condensed Matter*, 17 (50):R1143–R1182, dec 2005.

[93] Pyotr Rabochiy, Peter G. Wolynes, and Vassiliy Lubchenko. *The Journal of Physical Chemistry B*, 117(48):15204–15219, 2013.

[94] Matthieu Wyart and Michael E. Cates. *Phys. Rev. Lett.*, 119:195501, Nov 2017.

[95] Jeppe C. Dyre. *Rev. Mod. Phys.*, 78:953–972, Sep 2006.

[96] Hajime Tanaka. *The European Physical Journal E*, 35(10):113, 2012.

[97] Harukuni Ikeda, Francesco Zamponi, and Atsushi Ikeda. *J. Chem. Phys.*, 147(23):234506, 2017.

[98] G. Tarjus. An overview of the theories of the glass transition. In L. Berthier, G. Biroli, J-P Bouchaud, L. Cipelletti, and W. van Saarloos, editors, *Dynamical Heterogeneities and Glasses*. Oxford University Press, 2011.

[99] Sho Yaida, Ludovic Berthier, Patrick Charbonneau, and Gilles Tarjus. *Phys. Rev. E*, 94: 032605, Sep 2016.

[100] David Chandler and Juan P. Garrahan. *Annual Review of Physical Chemistry*, 61(1):191–217, 2010.

[101] J. L. Lebowitz, J. K. Percus, and L. Verlet. *Phys. Rev.*, 153:250–254, Jan 1967.

[102] Bingqing Cheng and Michele Ceriotti. *Physical Review B*, 97(5):054102, 2018.

## Appendix 1: Configurational entropy along an isobaric path

We wish to measure the configurational entropy $S_{\rm conf}(T,P)$ along an isobaric (constant pressure) path. It is computed as $S_{\rm conf}(T,P) = S_{\rm tot}(T,P) - S_{\rm glass}(T,P)$, where $S_{\rm tot}(T,P)$ and $S_{\rm glass}(T,P)$ are the total and glass entropies at the temperature $T$ and pressure $P$. We explain how to get $S_{\rm conf}(T,P)$ from $NPT$ simulation trajectories.

### Notations

We consider the Helmholtz free energy $-\beta F(T,V) = \ln Z(T,V)$, where $\beta = 1/T$ and $Z(T,V)$ is the partition function of the $NVT$ ensemble. We also consider the Gibbs free energy $-\beta G(T,P) = \ln Y(T,P)$, where $Y(T,P)$ is the partition function of the $NPT$ ensemble, given by

$$Y(T,P) = \int_0^\infty {\rm d}V e^{-\beta(PV+F(T,V))}. \tag{12}$$

We introduce the probability distribution of the volume $V$ for a given $T$ and $P$,

$$\rho(V|T,P) = \frac{e^{-\beta(PV+F(T,V))}}{Y(T,P)}. \tag{13}$$

In equilibrium, $\rho(V|T,P)$ is given by Gaussian distribution,

$$\rho(V|T,P) = \frac{1}{\sqrt{2\pi\sigma_V^2}} \exp\left[-\frac{(V-V_*)^2}{2\sigma_V^2}\right], \tag{14}$$

where $V_*$ and $\sigma_V^2$ are the mean and variance of the volume, respectively. We define $\langle(\cdots)\rangle_{T,P} = \int_0^\infty {\rm d}V \rho(V|T,P)(\cdots)$. Using this average, we can write $V_* = \langle V\rangle_{T,P}$ and $\sigma_V^2 = \langle (V-V_*)^2\rangle_{T,P}$.

### Total entropy

The total entropy $S_{\rm tot}(T,P)$ is obtained by a thermodynamic integration of the isobaric heat capacity from a reference temperature $T_{\rm ref} = 1/\beta_{\rm ref}$, to the target temperature $T = 1/\beta$,

$$\begin{aligned} S_{\rm tot}(T,P) &= S_{\rm tot}(T_{\rm ref},P) - \frac{Nd}{2}\left(\ln\beta - \ln\beta_{\rm ref}\right) \\ &\quad +\beta U_*(T,P) - \beta_{\rm ref} U_*(T_{\rm ref},P) \\ &\quad -\int_{\beta_{\rm ref}}^{\beta} {\rm d}\beta' U_*(T',P) \\ &\quad +P\left(\beta V_*(T,P) - \beta_{\rm ref} V_*(T_{\rm ref},P)\right) \\ &\quad -P\int_{\beta_{\rm ref}}^{\beta} {\rm d}\beta' V_*(T',P), \end{aligned} \tag{15}$$

where $U_*(T,P)$ is the mean potential energy, and $V_*(T,P)$ is the mean volume; $U_*(T,P)$ and $V_*(T,P)$ are measured by constant pressure simulations. The entropy at the reference state is obtained by $S_{\rm tot}(T_{\rm ref},P) = \langle S_{\rm tot}(T_{\rm ref},V)\rangle_{T,P}$ using the $NVT$ ensemble scheme [44]. This treatment for the reference state will be justified below.

### Glass entropy

To get the glass entropy, we use the generalised Frenkel-Ladd method which relies on the $NVT$ ensemble [45]. In general, one can smoothly connect $NVT$ and $NPT$ ensembles in terms of mean values. For example, thermodynamics guarantees that $S(T,P) = S(T, \langle V \rangle_{T,P})$. However, special attention should be paid if one uses the $NVT$ ensemble scheme with trajectories generated by the $NPT$ ensemble for finite system size [101]. A related issue is discussed in Ref. [102]. Indeed, what we can compute is $\langle S(T,V) \rangle_{T,P}$. In general,

$$S(T,P) = \langle S(T,V) \rangle_{T,P} - \langle \ln \rho(V|T,P) \rangle_{T,P}. \tag{16}$$

Therefore, we need to consider the second term in Eq. (16) as a correction term. We can evaluate this term with Eq. (14):

$$-\frac{1}{N} \langle \ln \rho(V|T,P) \rangle_{T,P} = \frac{1}{N} \ln \sqrt{2\pi e \sigma_V^2}. \tag{17}$$

Since $\sigma_V^2 \sim N$, this term vanishes in the thermodynamic limit, as expected. Indeed, for $N = 1500$ systems, we get negligible values, $\frac{1}{N} \ln \sqrt{2\pi e \sigma_V^2} \simeq 0.0026$ and $0.0013$ at $T_{\rm ref} = 7.0$ and $T = 0.37$, respectively. These values are small compared to the absolute value of $S_{\rm conf}/N \simeq 0.36 - 0.80$. Thus we can safely use $S(T,P) = \langle S(T,V) \rangle_{T,P}$. Especially we use the following equation, $S_{\rm glass}(T,P) = \langle S_{\rm glass}(T,V) \rangle_{T,P}$.

## Appendix 2: Extrapolation of relaxation times towards $T_g$

Here we test the validity of the extrapolation of relaxation time from the numerical to the experimental timescale using various fitting functions. The experimental data on which this is done have kinetic fragility indexes similar to the simulation models.

Figure 8 shows various fits of the data performed over the simulation time window, $\tau_\alpha \leq 10^{-5}$ s, and then extrapolated to lower temperatures down to $T_g$ where $\tau_\alpha = 100$ s. In all three cases shown in Fig. 8, the parabolic law is the best functional form that correctly predicts the actual data over the experimental time window. All other functional forms, when fitted over the simulation time window, tend to deviate from the actual data at low temperatures. Notice that the uncertainty on the determination of $T_g$ using the numerical time window and a parabolic fit is very small. This is the strategy we have used in previous numerical studies [42, 43, 44].

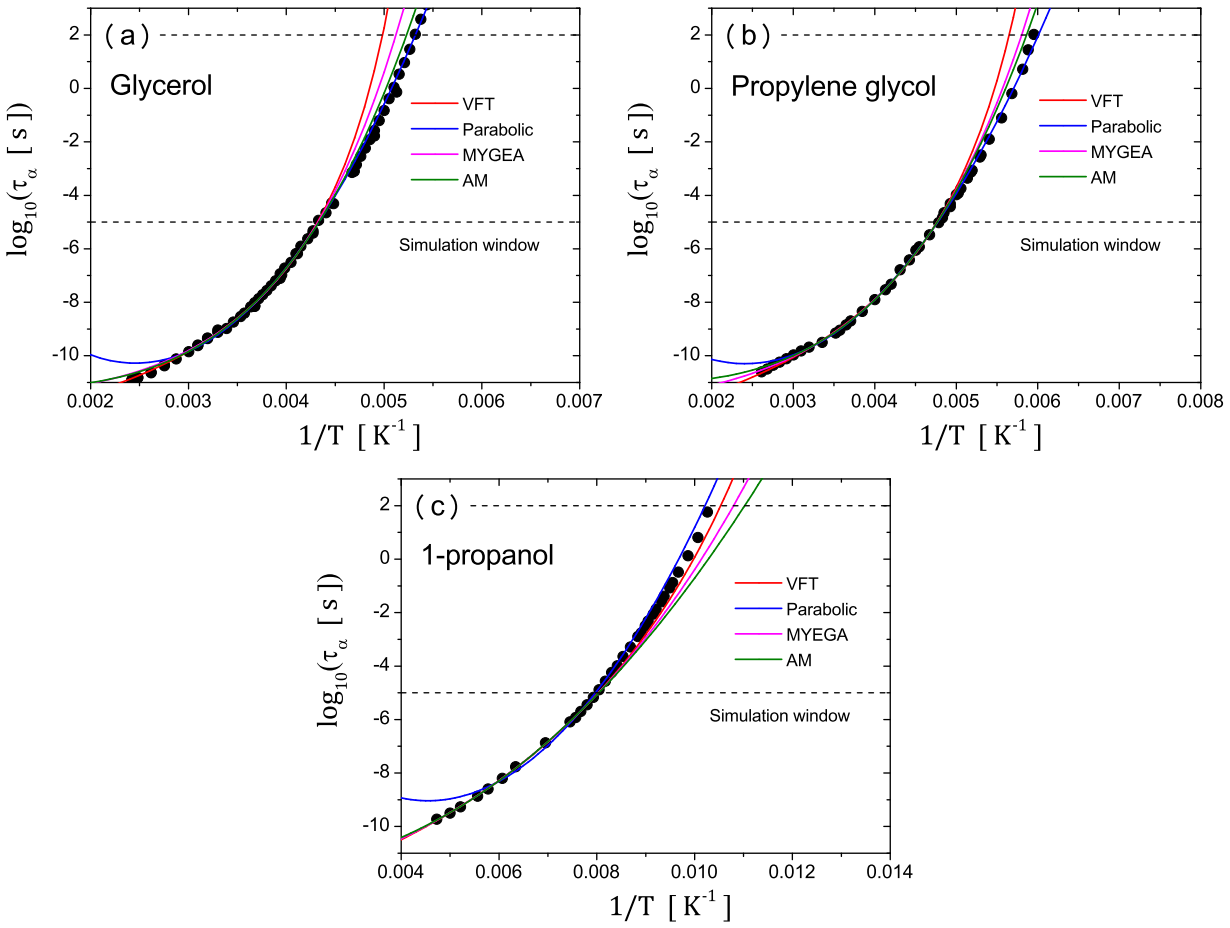


Figure 8: Extrapolation from simulation timescale ($\tau_\alpha \leq 10^{-5}$ sec.) to experimental timescale for glycerol, propylene glycol, and 1-propanol, whose kinetic fragility index, $m$, takes comparable to the simulation models employed in this paper. $m = 53$, 48, 35 for glycerol, propylene glycol, and 1-propanol, respectively.

Chapter 6

# Conclusions and Perspectives

This manuscript presents a series of works addressing fundamental questions about the formation and properties of amorphous solids. We provide the reader with general conclusions of these studies, emphasizing the advances made in our understanding of the nature of glasses and the glass transition. We also discuss some perspectives which emerge naturally from this work.

A large part of this work is devoted to improving our theoretical understanding of the nature and properties of glassy solids. In particular, we explore the novel hypothesis that the properties of amorphous solids are naturally explained by the existence of a new amorphous phase of matter. Chapters 2 and 3 present original results in this direction.

**Chapter 2** presents the mean field theory for dense assemblies of particles interacting via a generic pair-potential, embedded in a space of large dimensions. The model analyzed is the Weeks-Chandler-Andersen (WCA) model. Varying the external parameters of the model (packing fraction, temperature), we continuously explore physical regimes relevant to describe dense liquids, soft or hard colloidal suspensions, emulsions, and granular materials. We compute the free energy of glasses prepared in equilibrium, then brought adiabatically to another state point. In the stable glass phase, a replica symmetric solution is employed. Upon some temperature or density change, the replica symmetric solution destabilizes and a full replica symmetry breaking should be employed to compute the free energy of the glass. In this case, the glass becomes marginally stable, and is characterized by a hierarchical free energy landscape. We explore the physical regimes relevant to granular matter, foams, emulsions, hard and soft colloids, and atomic glasses, showing that marginal stability may be found in all these materials. We provide for the first time the exact mean field phase diagram for amorphous solids, locating the simple glass and marginally stable glass phases, as well as the location of the jamming transition. The phase diagrams presented in Chapter 2 provide a solid basis for computer simulations and experiments aimed at detecting marginal stability in structural glasses.

**Chapter 3** presents an extensive study of the energy landscape of glasses by means of numerical simulations in three dimensions. In the first work entitled 'Absence of marginal stability in a structural glass', we study marginal stability in a model for atomic glasses. The main conclusion is that the marginally stable phase, predicted by mean field theory, is not observed in three dimensional

simulations of a model atomic glass. We however detect ergodicity breaking at low temperature, which is attributed to the presence of localized defects. The conclusion of this work contrasts with previous numerical studies of three-dimensional hard spheres, in which strong evidence was put forward for a marginally stable glass phase.

The apparent contradiction of the above results is clarified in the work 'Nature of excitations and defects in structural glasses'. This work parallels the mean field study of WCA glasses, and provides the phase diagram of the WCA model obtained by three dimensional simulations. The main outcome is that the structure of the energy landscape of glasses changes dramatically with the physical regime, from atomic liquid, to soft and hard colloids. At finite temperature, and density close to the jamming transition, the energy landscape is extremely complex, with a large number of local minima, energy barriers of all sizes, corresponding to both localized and delocalized motion of particles. We give evidence for a hierarchical structure of energy minima. These results echo those found for hard spheres, in a regime close to the jamming transition. At high densities, relevant to describe atomic glasses modeled by smooth long-ranged interactions, the energy landscape is relatively much simpler. Less energy minima are identified, and the energy barriers separating two distinct minima correspond to localized motion of particles, confirming the results of the above work. We investigate the crossover between the two distinct regimes, showing that both localized and delocalized excitations coexist at intermediate densities and temperatures. This work reconciles a number of apparently contradictory results, providing a complete and coherent picture of the energy landscape of glasses in a wide variety of physical regimes.

The work 'Rejuvenation and memory effects in a structural glass', builds on the previous study and explores the consequences of marginal stability on the properties of glasses. Having identified the region of the phase diagram in which the glass is marginally stable, we investigate the out-of-equilibrium dynamics of glasses subject to temperature cycles. This type of protocol was used more than 20 years ago on disordered magnets, which are known to have a hierarchical landscape. We show that rejuvenation and memory effects, originally detected in disordered magnets, are also observed in dense disordered assemblies of particles. Such effects were unsuccessfully searched in experiments on molecular glasses. Our work rationalizes this failure: molecular and atomic glasses are characterized by relatively simple landscapes. Rejuvenation and memory effects can only be observed in systems which have a hierarchical landscape.

The last work of Chapter 3, 'Depletion of two-level systems in ultrastable computer-generated glasses' was motivated by the findings of the first study 'Absence of marginal stability in a structural glass'. While this first work established the absence of marginal stability in atomic glasses, it evidenced the existence of localized defects in computer glasses. Indirect signs that the nature of these defects change with the stability of the glasses was also provided. Building on these preliminary results, and motivated by recent measurements of the density of TLS in ultrastable vapor-deposited glasses, we analyze the classical and quantum nature of these defects in glasses. We investigate computer samples which are prepared in hyperquenched, experimental, and ultrastable conditions. We show that the density of TLS decreases by two orders of magnitude from the hyperquenched to ultrastable glasses. We unambiguously prove that the density of TLS, and therefore the low-temperature transport properties of glasses are not intrinsic to their disordered nature, and can be tuned with the preparation protocol.

The results presented in Chapter 2 and 3 shed new light on our understanding of the energy landscape of glasses. These results also motivate future work addressing the nature of the Gardner transition, and two-level systems in glasses.

**Perspectives on the Gardner transition.** The discrepancy between the mean field prediction of a Gardner transition towards a marginally stable phase in model atomic glasses, and its absence in the three-dimensional counterpart raises new questions. In this work, we studied numerically how marginal stability is recovered in $3d$ glasses by moving continuously from physical regimes relevant to atomic glasses to that of colloidal glasses. It would be interesting to study how marginal stability is recovered from $3d$ to the mean field theory in $d = \infty$ in model atomic glasses. Several strategies could be employed to achieve this. A first strategy would be to investigate the Gardner transition in the same model in spatial dimensions from $d = 4$ to above. From a practical point of view, the algorithms needed to prepare stable glasses in spatial dimensions higher than three are at hand [237]. A more elegant, alternative strategy would be to study the Mari-Kurchan (MK) version of the atomic pair-potential in three dimensions [238]. In the MK model, the interparticle distance used in the interaction potential is shifted by a random parameter which is tunable. Varying this interaction parameter from zero to values comparable to the system size allows to interpolate continuously from the original model to a three-dimensional version of it.

The absence of marginal stability evidenced in atomic glass-forming models is also in contrast with a recent work, in which the marginal behavior of glasses is revealed by elastic avalanches [239]. In this article, the authors address this apparent conflict and suggest that the system sizes needed to observe large scale avalanches at small strains could be prohibitively large, so that observed excitations are limited to localised defects. It would be interesting to analyze the role of the localized defects identified in our work in elastic avalanches under small strains.

Our work clearly identifies physical regimes in which the energy landscape of glasses is characterized by a complex, hierarchical organization, reminiscent of the mean field description of a Gardner phase. The nature of the Gardner transition in finite-dimensional glasses is however not settled. Addressing this question theoretically is challenging. While this problem is relatively new to the field of structural glasses, it bears a twin in the field of spin-glasses in a field, and therefore inherits more than 30 years of intense research. The existence of a thermodynamic spin-glass phase transition is still debated, despite the construction of efficient supercomputer [240].

Finally, this work lays the ground for future experiments searching marginal stability and its consequences. Existing results on granular and colloidal experiments bring evidence for marginal stability in glasses, in line with the conclusions presented above. On the other hand, experiments on molecular glasses are harder to interpret. Unpublished results on the non-linear susceptibility of glycerol down to very low temperature also confirm the absence of marginal stability in this physical regime.

**Perspectives on low-temperature properties of glasses** – We presented above the first computer work successful at obtaining a direct sampling of active tunneling two-level systems with sufficient statistics to avoid any kind of extrapolation. This achievement opens exciting directions to study the low-temperature properties of glasses. More specifically, it would be interesting to investigate the properties and density of TLS in the marginally stable glassy phase. Given the extremely large number of energy minima and energy barriers identified above in this regime, we

expect a much higher density of TLS.

A natural continuation of the work presented above on TLS in computer glasses would be to refine and confirm the results. As a matter of fact, the tunnel splitting of the double-well potentials is computed by solving the $1d$ Schrödinger equation for an effective particle. This is an approximation, given the collective nature of the transitions, and it needs to be verified. Path-integral molecular dynamics have been successfully used to compute tunnel splittings of symmetric double-wells in small molecules. Applying this method to larger systems in order to compute exactly the tunnel splitting is technically sophisticated by seems within reach.

**Chapter 4** presents an important technical aspect of the present work, which requires the synthesis of stable computer glasses. Building on recent computational developments, we developed a hybrid Molecular Dynamics/Monte Carlo algorithm. We implemented this algorithm in the simulation package LAMMPS, making it accessible to a large community. The equilibrium configurations produced allow to investigate a wide diversity of questions around the glass transition and the properties of glassy solids. We presented in Chapter 3 some original works on the energy landscape of glasses, which were made possible with this computational breakthrough.

**Chapter 5** uses the computational advances presented in Chapter 4 to address recent thermodynamic theories of glass formation. We describe state-of-the-art methods to estimate numerically the configurational entropy of supercooled liquids. We assessed numerically the relation between the dynamics of supercooled liquids, static lengthscales, and thermodynamic quantities, in particular the configurational entropy. Our main result is that the standard Adam-Gibbs relation is generally not obeyed. A generalized relation, predicted by the most advanced theory, however describes well the most accurate numerical and experimental data currently available.

**Perspectives on ultrastable computer glasses** – Recent computational and experimental studies have shown that the most stable computer glasses created with the particle-swap algorithm possess dynamic and thermodynamic properties similar to vapor-deposited glasses. Some of these studies focus on the melting mechanism of ultrastable glasses. Experiments indirectly suggest that two mechanisms compete: bulk melting and surface-initiated melting. This gives rise to a 'giant' crossover thickness of film, below which melting is dominated by surface-initiated fronts, and above which bulk melting dominates the overall process [241]. The constant-velocity propagation of melting front was confirmed by computational studies [242]. Little is known, both experimentally and numerically, about the bulk melting mechanism in stable glasses. We are currently investigating the bulk melting of stable glasses in two dimensions. Preliminary results indicate that this is a two-step process. The first step corresponds to the nucleation of liquid droplets in the glassy solid, which then grow at a pressure higher than the external pressure. In the second step, these droplets percolate, and the pressure of the liquid drops to the external pressure.

Chapter 7

# Résumé

## 7.1 Motivations

Dans le chapitre d'introduction, nous présentons le contexte de recherche de cette thèse. Nous introduisons certains aspects liés à la formation des solides amorphes, ainsi qu'à leurs propriétés physiques. Dans cette section, nous nous concentrons brièvement sur certaines d'entre elles qui ont été la principale source de motivation de ce travail.

Nous présentons dans la section 1.1 la phénoménologie associée à la transition vitreuse expérimentale. La transition vitreuse est définie en tant que transition dynamique, par contraste avec les transitions de phase usuelles, d'origine thermodynamique. Nous nous intéressons à deux observables, une dynamique et une autre thermodynamique, mesurées dans les liquides surfondus à l'approche de la transition vitreuse. L'une est le temps de relaxation du liquide, qui indique un ralentissement dramatique de la dynamique de ce dernier, ainsi que l'entropie configurationnelle. Cette dernière joue un rôle important dans les théories thermodynamiques de la transition vitreuse, explorées dans notre travail.

Nous abordons ensuite les propriétés des verres sous la température de transition vitreuse. Les verres sont des solides hors équilibre dont les propriétés évoluent au cours du temps, un comportement appelé vieillissement. Dans certains systèmes vitreux, tels les verres de spin, la dynamique hors d'équilibre peut être encore plus spectaculaire, avec des effets de rajeunissement et de mémoire. Dans ce travail, nous démontrons pour la première fois que de tels effets peuvent être observés dans certains verres structuraux, tels que les verres colloïdaux. Nous discutons également les propriétés des verres moléculaires ou atomiques à très basse temperature, aux alentours de 1 Kelvin. A ces températures, les propriétés thermodynamiques et de transport des verres ont un comportement différent de celui des solides cristallins, et violent en particulier la loi de Debye. Depuis leur découverte dans les années 1970, ces anomalies sont expliquées dans un modele phénoménologique par la présence de défauts dans les verres, appelés "systèmes à deux niveaux". A très basse temperature, les défauts peuvent être excités par effet tunnel, ce qui pourrait expliquer le comportement des verres dans ce régime. Une compréhension théorique de ces défauts, en particulier de leur nature microscopique, reste à obtenir.

Nous présentons par la suite une technique expérimentale récente, basée sur le dépôt physique par phase vapeur, utilisée pour créer des verres "ultrastables". Ces verres ont des propriétés

physiques différentes des verres ordinaires crées par refroidissement du liquide. Ils ne présentent en particulier pas les anomalies vitreuses à basse température, ont une entropie configurationnelle bien plus faible que celle des liquides surfondus, et fondent par un mécanisme de nucléation et croissance. L'étude expérimentale de ces échantillons ouvre de nouvelles perspectives sur l'étude de la transition vitreuse, et sur les propriétés des verres.

Nous introduisons ensuite la transition de blocage, qui conduit à la formation de solides amorphes dans assemblées de particules insensibles aux fluctuations thermiques. La transition de blocage est conceptuellement distincte de la transition vitreuse. C'est une transition critique d'origine géométrique. Les systèmes de sphères molles thermiques permet l'étude simultanée des deux types de transitions, et l'élaboration d'un diagramme de phase en température et densité pour les solides amorphes. Un tel diagramme de phase est présenté, et montre que la phase bloquée se situe au sein de la phase vitreuse.

La théorie de champ moyen pour les liquides et les verres, obtenue dans la limite de grande dimension est introduite. Cette théorie permet un traitement de la thermodynamique du liquide et du verre. Dans le limite de champ moyen, il existe deux transitions qui ont lieu à des températures distinctes. La transition dynamique est celle ayant lieu à plus haute température. Elle correspond à l'apparition d'états métastables, qui se traduit par une divergence du temps de relaxation du liquide. Une transition thermodynamique, dite de Kauzmann, a lieu à plus basse temperature. Elle correspond à la disparition d'un nombre exponentiel d'états métastables, c'est-à-dire à une entropie configurationnelle nulle. La théorie de champ moyen permet d'expliquer le ralentissement dynamique par une raréfaction des états métastables. Une prédiction majeure de la théorie de champ moyen est l'existence de deux phases vitreuses aux propriétés physiques distinctes. Le verre peut se trouver dans la phase thermodynamiquement stable, ou dans une phase marginalement stable. Dans cette dernière, une perturbation locale et infinitésimale induit des réarrangements du système entier. Les deux phases sont séparées par une transition de Gardner. La phase marginalement stable, dite de Gardner, a été découverte en 2014, peu avant le début de cette thèse. Ce travail s'attache à déterminer dans quelles conditions physiques les verres sont marginalement stable, et quelles en sont les conséquences pour leurs propriétés physiques.

La théorie de champ moyen pour les liquides et les verres structuraux est désormais bien établie, et constitue un premier pas important vers une théorie microscopique des solides amorphes à trois dimensions. Elle permet de décrire la transition vitreuse, qui correspond à un phénomène dynamique, avec des observables purement statiques, en tant que transition thermodynamique "cachée". La principale difficulté consiste à transposer les concepts et outils de la théorie de champ moyen à la description de liquides et verres évoluant en dimension finie. Dans les liquides surfondus, il n'est pas évident d'établir une relation entre la thermodynamique et la dynamique, c'est-à-dire entre les temps de relaxation et l'entropie configurationnelle. La théorie de champ moyen, aussi appelée théorie RFOT, soutient une relation directe entre ces deux quantités. Nous employons des résultats de simulations obtenus à des température extrêmement basses pour tester ces théories et mesurer les exposants critiques introduits dans la théorie RFOT.

Nous avons discuté qu'un problème fondamental dans les études numériques des liquides surfondus provient du fait que seulement quatre ou cinq ordres de ralentissement dynamique sont accessibles à équilibre, par rapport aux 13 ordres de grandeur accessibles expérimentalement à

l'équilibre. L'algorithme de SWAP a récemment été introduit afin de combler cet écart entre simulations et expériences. Cette méthode permet d'accélérer la thermalisation et étendre le régime de simulation à des échelles de temps comparables a‘ celles accessibles expérimentalement. Nous utilisons cette découverte afin de proposer un nouvel algorithme, alliant simulations Monte Carlo et dynamique moléculaire. Cet algorithme est flexible, et implémenté dans LAMMPS, un programme de dynamique moléculaire extrêmement répandu. Cet outil, développé au cours de cette thèse, permet l'étude des liquides surfondus et des verres dans des régimes inexplorés, et l'obtention de résultats originaux.

## 7.2 Résultats

Cette thèse a donné lieu à huit publications [175, 213, 214, 222, 226–228, 243]. Cinq d'entre elles sont une production directe de cette thèse [214, 222, 226–228]. Les trois autres résultent d'une plus large collaboration et incluent des résultats et des analyses développés dans cette thèse [175, 213, 243]. Une autre publication est en cours de préparation. Il s'agit d'une étude numérique du mécanisme de fusion des verres ultrastables. Cette étude est réalisée sur des verres bidimensionnels relaxés par la méthode SWAP à des temperatures sous la transition vitreuse expérimentale. Nous résumons dans cette section les résultats principaux de cette thèse.

Le chapitre 2 présente l'étude du diagramme de phase des solides amorphes, dans la limite de dimension infinie. Nous résolvons la thermodynamique de verres formés sous la température de transition dynamique. En utilisant un formalisme de "suivi d'état", nous calculons les propriétés thermodynamiques de ces verres lorsqu'ils sont amenés à un temperature et une densité différentes de celles auxquelles le verre a été formé. Ces calculs sont fait dans l'hypothèse de symétrie des répliques, autrement dit en en supposant que le verre est dans la phase stable. Nous étudions la limite de stabilité du verre, qui permet de déterminer la transition de Gardner vers une phase vitreuse marginalement stable. Nous calculons le diagramme de phase de sphères molles thermiques, qui interagissent via la potentiel de Weeks-Chandler-Andersen (WCA). En fonction des conditions de température et de densité, ce modèle est pertinent pour décrire la physique de solides amorphes aussi variés que les granulaires denses, les mousses, les émulsions, les suspensions de colloïdes mous ou durs, ainsi que les verres moléculaires ou atomiques. Pour chaque régime physique, nous identifions la limite de stabilité du verre simple. La théorie prédit notamment que les verres caractérisés par des interactions à longue portée, qui modélisent des verres atomiques, sont marginalement stables à basse température. L'excès d'excitations basses associées à une phase de Gardner pourrait fournir une nouvelle explication, basée sur les principes microscopique, de la violation de la théorie de Debye dans les verres à basse température.

Nous montrons que dans la limite de champ moyen, la nouvelle phase vitreuse, celle marginalement stable, est pertinente pour décrire tous les types de solides amorphes dans une région étendue du diagramme de phase. Cela ouvre la possibilité d'une étude unifiée des anomalies vitreuses à basse température.

Les résultats de ce chapitre ont conduit à la publication d'un article, Ref. [214].

Le chapitre 3 présente des résultats numériques qui portent sur l'analyse des propriétés des verres en trois dimensions.

Dans un premier travail, intitulé “Absence de stabilité marginale dans un verre structurel”, nous comparons les résultats numériques et de champ moyen pour un modèle formateur de verre caractérisé par des interactions répulsives à longue portée $V(r) \propto 1/r^{12}$. Cette étude est la première étude numérique d'une transition de Gardner induite par refroidissement dans un modèle ne possédant pas de transition de blocage. L'objectif était de déterminer si une transition Gardner pouvait être induite loin de la transition de blocage dans des verres tridimensionnels. Afin de répondre à cette question, nous avons étudié des verres numériques très stables, synthétisés par la méthode SWAP décrite plus bas. Nous sondons le paysage d'énergie libre du verre en créant des clones de celui-ci (mêmes positions des particules, mais vitesses initiales aléatoires). Nous nous intéressons à la dynamique des clones après une trempe thermique. Nous mesurons en particulier le déplacement quadratique moyen des clones, ainsi que la distance moyenne entre les clones. Nous définissons une susceptibilité de type verre de spin qui quantifie le nombre de particules corrélées dans la dynamique vibrationnelle. Ces observables nous permettent de détecter une perte d'ergodicité au sein du verre à basse température: les clones tombent dans des minima dynamiquement inaccessibles à $T < T^\star$. Cette perte d'ergodicité à l'intérieur d'un verre correspond à l'image du champ moyen d'une transition de Gardner.

Nous montrons cependant que la perte d'ergodicité n'est pas accompagnée par d'autres signes attendus à une transition de Gardner. Aucun ralentissement de la dynamique vibrationnelle n'est détecté à l'approche de $T^\star$. La susceptibilité verre de spin est d'ordre un à tout temps et à toute température, signalant une dynamique non corrélée. L'absence d'échelle de temps et de longueur autour de $T^\star$ est observée pour tous les verres étudiés, indépendamment de leur stabilité initiale. Nous démontrons que la perte d'ergodicité est due à des défauts localisés, qui correspondent à quelques particules qui peuvent prendre au moins deux positions proches. A haute température, les particules peuvent sauter d'un minimum à l'autre. Cette transition devient bloquée aux alentours de $T^\star$, induisant une perte d'ergodicité.

La conclusion principale de ce travail est que les verres tridimensionnels de type Lennard-Jones, qui modélisent bien les verres atomiques, ne subissent pas de transition Gardner vers une phase marginalement stable à basse température. Ce résultat contraste fortement avec ceux obtenus pour des verres de type sphère dure, pour lesquels une transition de Gardner est prédite en trois dimensions. Ce travail souligne la nécessité d'une exploration systématique de la phase vitreuse en trois dimensions, afin de concilier l'existence et l'absence de stabilité marginale dans des verres à interactions dures ou de type Lennard-Jones.

Ces résultats ont conduit à la publication d'un article, Ref. [222].

Les résultats d'une telle exploration systématique sont présentés dans un article “Nature des défauts et des excitations dans les verres structuraux”. Nous explorons la phase vitreuse du modèle WCA tridimensionnel. Le modèle WCA permet d'interpoler de manière continue entre le régime sphère dure, retrouvé dans la limite de température nulle, et le régime du liquide dense, obtenu à haute densité. Nous étudions les propriétés de verres préparés dans différents régimes physiques.

Une perte d'ergodicité est détectée dans tous les types de verres à basse température. Cela suggère que tous les verres sont caractérisés par un paysage d'énergie libre rugueux, composé de nombreux minima. Cette perte d'ergodicité peut être accompagnée ou non d'une augmentation de l'échelle de longueur, de l'hétérogénéité dynamique et des effets de vieillissement, en fonction du régime physique étudié. Notre principale constatation est que la nature du paysage énergé-

tique dépend fortement du régime de densité et évolue continuellement en allant de la transition de blocage (comportement de type sphère dure) à des densités et des températures plus élevées (comportement de type Lennard-Jones).

A des densités élevées, dans le régime pertinent pour les verres moléculaires et atomiques, le paysage est simple et caractérisé par peu de minima. La physique du verre est dictée par des défauts très localisés. En revanche, aux plus faibles densités correspondant au voisinage de la transition de blocage, ce qui est pertinent pour les matériaux granulaires, le paysage d'énergie à une structure très complexe, voire hiérarchique. Nous trouvons des barrières avec une large gamme d'échelles d'énergie et un degré de localisation allant de très localisés à très étendus, en accord avec les études numériques antérieures.

Plus intéressant encore, dans le régime de densités intermédiaire pertinent pour les suspensions de colloïdes mous et les émulsions, le paysage d'énergie possède tous les types de barrières (localisées, délocalisées, grande et faible énergie). Nous trouvons des défauts localisés associés à des barrières de haute énergie, responsables de la perte d'ergodicité du verre. A plus basse énergie, on trouve une organisation complexe d'un grand nombre de minima. Les barrières entre ces minima sont de faible énergie, et correspondent à un mouvement collectif d'un grand nombre de particules.

Nous fournissons la première preuve numérique de la transition de Gardner dans les sphères molles thermiques en $3d$. Lorsqu'elle est présente, la phase de Gardner forme un "dôme" en termes de température et de densité autour de la transition de blocage. La phase de Gardner et le régime critique de la transition de blocage ont une forme similaire, mais la région marginalement stable est beaucoup plus étendue que celle de la criticalité de la transition de blocage.

Nous avons réussi à trouver dans quelles conditions physiques les verres tridimensionnels sont marginalement stables, caractérisés par un paysage d'énergie hiérarchique. Cela ouvre la possibilité d'explorer la physique et la dynamique à basse température de verres de structuraux caractérisés par des paysages d'énergie complexes.

Ces résultats ont conduit à la publication d'un article, Ref. [226].

Dans le troisième travail de ce chapitre, intitulé "Effets de rajeunissement et de mémoire dans un verre structurel", nous tirons profit des résultats ci-dessus afin d'étudier la dynamique hors d'équilibre des verres évoluant dans un paysage hiérarchique. Nous étudions l'influence de variations cycliques de la température sur la dynamique des verres. Nous étudions des verres WCA préparés à densité intermédiaire, pour lesquels une phase de Gardner a été trouvée à basse température. Le fluide à haute température est soudainement refroidi à $T_1$ dans la phase vitreuse, où il vieillit pendant un temps $t_1$. Le verre est ensuite refroidi à une température $T_2 < T_1$. Pour $T_2$ suffisamment bas, la dynamique du vieillissement redémarre. Cet effet non trivial de "rajeunissement" est dû à la structure hiérarchique du paysage d'énergie du verre. Le verre reste durant $t_2 = t_1$ à la température $T_2$, avant d'être réchauffé à $T_1$. à $T_1$, le verre a gardé une "mémoire" de son état, et la dynamique de vieillissement reprend comme si rien ne s'était passé à $T_2$.

Les effets de rajeunissement et de mémoire ont été utilisés dans le passé pour comparer et classer différents types de verres. Nous démontrons que dans certaines conditions, les verres structurels tels que les verres colloïdaux et granulaires se comportent comme des verres de spin plutôt que des verres moléculaires. Nos trois études numériques rationalisent l'absence d'effets de mémoire et de rajeunissement dans les verres atomiques et moléculaires. Leur comportement est dominé par la présence de quelques défauts localisés et non par une distribution hiérarchique des barrières d'énergie correspondant à des défauts étendus.

Ces résultats ont conduit à la publication d'un article, Ref. [227].

Dans le quatrième travail de ce Chapitre, "Dépletion des systèmes à deux niveaux dans des verres ultrastables numériques", nous étudions les propriétés classiques et quantiques d'effet tunnel des défauts localisés identifiés dans le travail "Absence de stabilité marginale dans un verre structurel".

Pendant les années 70, des experiences ont eu lieu afin de d'observer les propriétés de transport des verres de température ambiante jusqu'à basse température, vers environ 1 $K$. Alors que la théorie de Debye pour les solides cristallins prédit que la chaleur spécifique varie comme $T^3$ à basse température, les mesures montrent qu'elle varie comme $T$ de façon quasi universelle dans les verres [48]. Cela implique qu'il existe des excitations autres que les phonons dans les verres à très basse température. Peu après la publication de ces résultats expérimentaux, un modèle phénoménologique a été proposé pour les rationaliser [51]. Depuis, l'idée selon laquelle le désordre inhérent aux verres donne lieu a des défauts supplémentaires, appelés systèmes à deux niveaux (TLS), est largement répandue et acceptée. Ces défauts correspondent à un ensemble de particules qui peuvent prendre deux configurations proches en énergie, qui peuvent être excitées par effet tunnel à basse température. Ces défauts ne sont pas observables directement dans les expériences, ce qui limite notre compréhension. Notre étude numérique est motivée par le fait que les verres préparés par dépôt physique en phase vapeur à une température de 0.85 $T_g$, ne présentent pas ces anomalies soit-disant "universelles" [69]. Par ailleurs, il semblerait que ces verres déposés en phase vapeur (VD) se trouvent profond dans le paysage d'énergie [229]. D'autres mesures indiquent que les verres ultrastables sont anisotropes. La question actuelle est de savoir si la suppression des TLS est due à l'anisotropie des verres, ou à leur faible enthalpie.

Nous apportons un nouvel éclairage sur ces questions à la fois anciennes et récentes. Nous utilisons la méthode présentée dans le chapitre 4 pour préparer des verres numériques dans une gamme de stabilités sans précédent. Cela revient à ajuster le taux de trempe utilisé lors de la préparation du verre. Nous nous concentrons en particulier sur trois stabilités du verre, appelées hyper-trempé, liquide refroidi, et ultrastable.

Nous développons une méthode permettant d'identifier les minima proches dans le paysage d'énergie potentielle, ou "double puits" (DWP). Nous étudions les paramètres classiques des DWPs, en particulier la barrière énergétique, l'asymétrie, le nombre de particules impliquées dans le franchissement de la barrière. Nous analysons ensuite les propriétés quantiques des DWP, en résolvant l'équation de Schrödinger unidimensionnelle pour le chemin d'énergie minimum reliant les deux minima. Nous calculons la levée de dégénérescence $\delta E$ des DWPs, sa distribution de probabilité, et identifions ceux qui sont actifs en dessous de 1 K et qui correspondent à des systèmes à deux niveaux (TLS). Nous montrons que la densité des TLS diminue avec la stabilité du verre, confirmant les résultats expérimentaux récents. Les verres numériques étant isotropes, nous concluons que la densité des TLS est directement reliée à la stabilité du verre. L'universalité des anomalies vitreuses proviendrait de la similarité des protocoles utilisés (trempe d'un liquide), et ne serait donc pas une caractéristique universelle des solides désordonnés.

Ces résultats ont conduit à la publication d'un article, Ref. [228].

Le chapitre 4 présente l'élaboration d'un nouvel algorithme numérique capable d'équilibrer des liquides surfondus sous la température de transition vitreuse expérimentale.

Le développement de l'algorithme SWAP Monte Carlo a ouvert la voie à des études numériques de liquides surfondus dans un régime de température auparavant inaccessible. La plupart des travaux numériques présentés dans cette thèse ont été rendus possibles par cette avancée récente. Dans ce travail, nous développons un algorithme alliant simulations par dynamique moléculaire et Monte Carlo. L'algorithme consiste en une succession de courts blocs de simulations par dynamique moléculaires, dans lesquelles les diamètres des particules sont constants, et de courts blocs de simulations swap Monte Carlo, pendant lesquels les diamètres des particules sont échangés selon un critère de Metropolis. Cet algorithme est implémenté dans le logiciel de simulations numériques LAMMPS, largement utilisé en simulations numériques. L'objectif de mettre au point un algorithme flexible, accessible et efficace a été atteint. La dynamique moléculaire peut être parallelisée, c'est-à-dire exécutée sur plusieurs processeurs à la fois, ce qui permet une réduction du temps de calcul. Nous optimisons l'algorithme et ses paramètres pour obtenir la meilleure efficacité, que nous comparons à la méthode SWAP Monte Carlo. Nous trouvons que cette méthode est aussi efficace que SWAP MC lorsqu'elle est exécutée en série (un processeur). Notre implémentation dans le package LAMMPS rend l'algorithme accessible à une large communauté d'utilisateurs. Cependant, lorsqu'elle est exécutée en parallèle, la version actuelle de l'algorithme ne permet pas de gagner en efficacité. L'accélération du temps de calcul obtenue dans la dynamique moléculaire de l'algorithme est contrebalancée par un coût plus élevé de la parallélisation du code Monte Carlo. Cette méthode hybride est utilisée pour préparer les configurations de verres étudiées dans le chapitre 3. Cette méthode permet de faire facilement des simulations à pression constante, dont les résultats sont présentés dans le chapitre 5.

Ces résultats ont conduit à la publication d'un article, Ref. [213].

Dans le chapitre 5, nous employons la capacité développée pour équilibrer des liquides à des températures avoisinant la transition vitreuse expérimentale pour examiner les théories thermodynamique pour la formation du verre.

Dans le travail "La relation Adam-Gibbs est-elle valable dans des liquides surfondus simulés?", nous traitons de la validité de la relation Adam-Gibbs (AG) qui relie l'entropie configurationnelle et le temps de relaxation du liquide surfondu. Nous abordons également la relation généralisée Adam-Gibbs (gAG), obtenue au sein de la théorie Random First Order Transition (RFOT). Cette dernière fait intervenir des exposants non triviaux $\theta$ et $\psi$ qui correspondent respectivement à un terme d'interface et un exposant dynamique. En utilisant l'accélération de la thermalisation, nous revisitons les tests numériques des relations d'AG. Plus important encore, nous abordons leur validité dans un vaste régime de température, pertinent pour tester les prévisions théoriques. Nous employons des mesures d'entropie configurationnelle, de longueur point-to-set et de temps de relaxation pour mettre à l'épreuve les prédictions théoriques. Nous montrons que pour quatre modèles formateurs de verre, étudiés en deux ou trois dimensions, la prédiction Adam-Gibbs est erronée. L'introduction de deux exposants, l'un reliant l'entropie configurationnelle à la taille typique des régions amorphes corrélées, et l'autre reliant la longueur des régions amorphes corrélées au temps de relaxation du liquide. Ces deux exposants sont mesurés numériquement, et nous obtenons des valeurs en accord avec les prédictions théoriques. Nous constatons que l'introduction d'un terme

de surface qui reflète l'existence d'un ordre amorphe est un ingrédient nécessaire à une description correcte du ralentissement dynamique. Enfin, nous utilisons des données expérimentales pour fournir une base solide à notre résultat. Nous trouvons qu'une étude fine des résultats expérimentaux valide notre conclusion, à savoir que la relation d'Adam-Gibbs n'est pas vérifiée lorsqu'elle est considérée sur une large gamme de températures.

Ces résultats ont conduit à la publication d'un article, Ref. [243].

# References


[1] Ludovic Berthier and Giulio Biroli. Theoretical perspective on the glass transition and amorphous materials. *Rev. Mod. Phys.*, 83:587–645, Jun 2011.

[2] Andrea Cavagna. Supercooled liquids for pedestrians. *Physics Reports*, 476(4-6):51–124, 2009.

[3] Vassiliy Lubchenko and Peter G Wolynes. Theory of structural glasses and supercooled liquids. *Annu. Rev. Phys. Chem.*, 58:235–266, 2007.

[4] A Peter Young. *Spin glasses and random fields*, volume 12. World Scientific, 1998.

[5] Jean-Pierre Hansen and Ian Ranald McDonald. *Theory of simple liquids: with applications to soft matter*. Academic Press, 2013.

[6] Ludovic Berthier and Mark D Ediger. Facets of glass physics. *Physics Today*, 69(1), 2016.

[7] Herbert B Callen. Thermodynamics and an introduction to thermostatistics, 1998.

[8] C. A. Angell. Formation of glasses from liquids and biopolymers. *Science*, 267(5206):1924–1935, 1995.

[9] F Sausset, G Biroli, and J Kurchan. Do solids flow? *Journal of Statistical Physics*, 140(4):718–727, 2010.

[10] Shiro Matsuoka. *Relaxation phenomena in polymers*. Hanser Munich etc., 1992.

[11] James A Forrest and Kari Dalnoki-Veress. The glass transition in thin polymer films. *Advances in Colloid and Interface Science*, 94(1-3):167–195, 2001.

[12] W Klement Jun, RH Willens, and POL Duwez. Non-crystalline structure in solidified gold–silicon alloys. *Nature*, 187(4740):869, 1960.

[13] Akihisa Inoue. Stabilization of metallic supercooled liquid and bulk amorphous alloys. *Acta materialia*, 48(1):279–306, 2000.

[14] Peter N Pusey and W Van Megen. Phase behaviour of concentrated suspensions of nearly hard colloidal spheres. *Nature*, 320(6060):340, 1986.

[15] Giovanni Brambilla, Djamel El Masri, Matteo Pierno, Ludovic Berthier, Luca Cipelletti, George Petekidis, and Andrew B Schofield. Probing the equilibrium dynamics of colloidal hard spheres above the mode-coupling glass transition. *Physical review letters*, 102(8):085703, 2009.

[16] Gary L Hunter and Eric R Weeks. The physics of the colloidal glass transition. *Reports on Progress in Physics*, 75(6):066501, may 2012.

[17] Gianfranco D'Anna and Gerard Grémaud. The jamming route to the glass state in weakly perturbed granular media. *Nature*, 413(6854):407, 2001.

[18] Olivier Dauchot, Guillaume Marty, and Giulio Biroli. Dynamical heterogeneity close to the jamming transition in a sheared granular material. *Physical review letters*, 95(26):265701, 2005.

[19] Aaron S Keys, Adam R Abate, Sharon C Glotzer, and Douglas J Durian. Measurement of growing dynamical length scales and prediction of the jamming transition in a granular material. *Nature physics*, 3(4):260, 2007.

[20] Raphael Candelier, Olivier Dauchot, and Giulio Biroli. Building blocks of dynamical heterogeneities in dense granular media. *Physical review letters*, 102(8):088001, 2009.

[21] M. E. Cates. Course 3: Structural Relaxation and Rheology of Soft Condensed Matter. In J.-L. Barrat, M. Feigelman, J. Kurchan, and et al., editors, *Slow Relaxations and Nonequilibrium Dynamics in Condensed Matter*, pages 75–129, 2004.

[22] Walter. Kauzmann. The nature of the glassy state and the behavior of liquids at low temperatures. *Chemical Reviews*, 43(2):219–256, 1948.

[23] M. D. Ediger, C. A. Angell, and Sidney R. Nagel. Supercooled liquids and glasses. *The Journal of Physical Chemistry*, 100(31):13200–13212, 1996.

[24] C Patrick Royall, Francesco Turci, Soichi Tatsumi, John Russo, and Joshua Robinson. The race to the bottom: approaching the ideal glass? *Journal of Physics: Condensed Matter*, 30(36):363001, 2018.

[25] Jean-Louis Barrat, Mikhail Feigelman, Jorge Kurchan, et al. Slow relaxations and nonequilibrium dynamics in condensed matter. In *Slow Relaxations and Nonequilibrium Dynamics in Condensed Matter*, 2004.

[26] Jean-Philippe Bouchaud, Leticia F Cugliandolo, Jorge Kurchan, and Marc Mezard. Out of equilibrium dynamics in spin-glasses and other glassy systems. *Spin glasses and random fields*, pages 161–223, 1998.

[27] LGE Struik. Physical aging in amorphous polymers and other materials elsevier sci. *Publ. Comp., Amsterdam-Oxford-New York*, 1978.

[28] J-Ph Bouchaud. Aging in glassy systems: new experiments, simple models, and open questions. *Soft and Fragile Matter: Nonequilibrium Dynamics, Metastability and Flow*, pages 285–304, 2000.

[29] Eric Vincent, Jacques Hammann, Miguel Ocio, Jean-Philippe Bouchaud, and Leticia F Cugliandolo. Slow dynamics and aging in spin glasses. In *Complex Behaviour of Glassy Systems*, pages 184–219. Springer, 1997.

[30] Hajime Yoshino. Aging effects of an elastic string diffusing in a disordered media. *Physical review letters*, 81(7):1493, 1998.

[31] Luca Cipelletti, Suliana Manley, RC Ball, and DA Weitz. Universal aging features in the restructuring of fractal colloidal gels. *Physical review letters*, 84(10):2275, 2000.

[32] Walter Kob and Jean-Louis Barrat. Aging effects in a lennard-jones glass. *Physical review letters*, 78(24):4581, 1997.

[33] Mark Kroon, Gerard H Wegdam, and Rudolf Sprik. Dynamic light scattering studies on the sol-gel transition of a suspension of anisotropic colloidal particles. *Physical Review E*, 54(6):6541, 1996.

[34] Jennifer M. Lynch, Gianguido C. Cianci, and Eric R. Weeks. Dynamics and structure of an aging binary colloidal glass. *Phys. Rev. E*, 78:031410, Sep 2008.

[35] F Lefloch, J Hammann, M Ocio, and E Vincent. Can aging phenomena discriminate between the droplet model and a hierarchical description in spin glasses? *EPL (Europhysics Letters)*, 18(7):647, 1992.

[36] J. P. Bouchaud. Weak ergodicity breaking and aging in disordered systems. *J. Phys. I France*, 2(9):1705–1713, 1992.

[37] Ludovic Berthier, Virgile Viasnoff, Olivia White, Vladimir Orlyanchik, and Florent Krzakala. Hiking through glassy phases: physics beyond aging. *arXiv preprint cond-mat/0211106*, 2002.

[38] J. O. Andersson, J. Mattsson, and P. Nordblad. Overlap length in a cu-mn spin glass probed by ac susceptibility. *Phys. Rev. B*, 48:13977–13980, Nov 1993.

[39] V. Dupuis, E. Vincent, J.-P. Bouchaud, J. Hammann, A. Ito, and H. Aruga Katori. Aging, rejuvenation, and memory effects in ising and heisenberg spin glasses. *Phys. Rev. B*, 64:174204, Oct 2001.

[40] P. E. Jönsson, H. Yoshino, and P. Nordblad. Symmetrical temperature-chaos effect with positive and negative temperature shifts in a spin glass. *Phys. Rev. Lett.*, 89:097201, Aug 2002.

[41] P. E. Jönsson, R. Mathieu, P. Nordblad, H. Yoshino, H. Aruga Katori, and A. Ito. Nonequilibrium dynamics of spin glasses: Examination of the ghost domain scenario. *Phys. Rev. B*, 70:174402, Nov 2004.

[42] F. Bert, V. Dupuis, E. Vincent, J. Hammann, and J.-P. Bouchaud. Spin anisotropy and slow dynamics in spin glasses. *Phys. Rev. Lett.*, 92:167203, Apr 2004.

[43] Robert L. Leheny and Sidney R. Nagel. Frequency-domain study of physical aging in a simple liquid. *Phys. Rev. B*, 57:5154–5162, Mar 1998.

[44] H Yardimci and R. L Leheny. Memory in an aging molecular glass. *Europhysics Letters (EPL)*, 62(2):203–209, apr 2003.

[45] L Bellon, S Ciliberto, and C Laroche. Memory in the aging of a polymer glass. *Europhysics Letters (EPL)*, 51(5):551–556, sep 2000.

[46] Ludovic Bellon, Sergio Ciliberto, and Claude Laroche. Advanced memory effects in the aging of a polymer glass. *The European Physical Journal B-Condensed Matter and Complex Systems*, 25(2):223–231, 2002.

[47] Alan Parker and Valéry Normand. Glassy dynamics of gelatin gels. *Soft Matter*, 6:4916–4919, 2010.

[48] R. C. Zeller and R. O. Pohl. Thermal conductivity and specific heat of noncrystalline solids. *Phys. Rev. B*, 4:2029–2041, Sep 1971.

[49] P. Debye. Zur theorie der spezifischen wärmen. *Annalen der Physik*, 344(14):789–839, 1912.

[50] W A Phillips. Two-level states in glasses. *Reports on Progress in Physics*, 50(12):1657–1708, dec 1987.

[51] P. W. Anderson, B. I. Halperin, and C. M. Varma. Anomalous low-temperature thermal properties of glasses and spin glasses. *Philosophical Magazine*, 25(1):1–9, 1972.

[52] Vassiliy Lubchenko§, Robert J. Silbey, and Peter G. Wolynes. Electrodynamics of amorphous media at low temperatures. *Molecular Physics*, 104(8):1325–1335, 2006.

[53] A-M Boiron, Ph Tamarat, B Lounis, R Brown, and M Orrit. Are the spectral trails of single molecules consistent with the standard two-level system model of glasses at low temperatures? *Chemical physics*, 247(1):119–132, 1999.

[54] Douglas Natelson, Danna Rosenberg, and D. D. Osheroff. Evidence for growth of collective excitations in glasses at low temperatures. *Phys. Rev. Lett.*, 80:4689–4692, May 1998.

[55] Osamu Haida, Hiroshi Suga, and Syûzô Seki. New finding of three kinds of glassy state por cyclohexene as a single compound. *Chemistry Letters*, 2(1):79–82, 1973.

[56] Hideaki Hikawa, Masaharu Oguni, and Hiroshi Suga. Construction of an adiabatic calorimeter for a vapor-deposited sample and thermal characterization of amorphous butyronitrile. *Journal of non-crystalline solids*, 101(1):90–100, 1988.

[57] Stephen F Swallen, Kenneth L Kearns, Marie K Mapes, Yong Seol Kim, Robert J McMahon, Mark D Ediger, Tian Wu, Lian Yu, and Sushil Satija. Organic glasses with exceptional thermodynamic and kinetic stability. *Science*, 315(5810):353–356, 2007.

[58] Kenneth L Kearns, Stephen F Swallen, Mark D Ediger, Tian Wu, Ye Sun, and Lian Yu. Hiking down the energy landscape: Progress toward the kauzmann temperature via vapor deposition. *The Journal of Physical Chemistry B*, 112(16):4934–4942, 2008.

[59] Jacob D Stevenson and Peter G Wolynes. On the surface of glasses. *The Journal of chemical physics*, 129(23):234514, 2008.

[60] L Zhu, CW Brian, SF Swallen, PT Straus, MD Ediger, and L Yu. Surface self-diffusion of an organic glass. *Physical Review Letters*, 106(25):256103, 2011.

[61] Pyotr Rabochiy, Peter G Wolynes, and Vassiliy Lubchenko. Microscopically based calculations of the free energy barrier and dynamic length scale in supercooled liquids: The comparative role of configurational entropy and elasticity. *The Journal of Physical Chemistry B*, 117(48):15204–15219, 2013.

[62] Lian Yu. Surface mobility of molecular glasses and its importance in physical stability. *Advanced drug delivery reviews*, 100:3–9, 2016.

[63] Ivan Lyubimov, Mark D Ediger, and Juan J de Pablo. Model vapor-deposited glasses: Growth front and composition effects. *The Journal of chemical physics*, 139(14):144505, 2013.

[64] Daniel R Reid, Ivan Lyubimov, MD Ediger, and Juan J De Pablo. Age and structure of a model vapour-deposited glass. *Nature communications*, 7:13062, 2016.

[65] Ludovic Berthier, Patrick Charbonneau, Elijah Flenner, and Francesco Zamponi. Origin of ultrastability in vapor-deposited glasses. *Physical review letters*, 119(18):188002, 2017.

[66] Jing Zhao, Sindee L Simon, and Gregory B McKenna. Using 20-million-year-old amber to test the super-arrhenius behaviour of glass-forming systems. *Nature communications*, 4:1783, 2013.

[67] M. D. Ediger. Perspective: Highly stable vapor-deposited glasses. *The Journal of Chemical Physics*, 147(21):210901, 2017.

[68] Shakeel S. Dalal and M. D. Ediger. Molecular orientation in stable glasses of indomethacin. *The Journal of Physical Chemistry Letters*, 3(10):1229–1233, 2012. PMID: 26286762.

[69] Tomás Pérez-Castañeda, Cristian Rodríguez-Tinoco, Javier Rodríguez-Viejo, and Miguel A. Ramos. Suppression of tunneling two-level systems in ultrastable glasses of indomethacin. *Proceedings of the National Academy of Sciences*, 111(31):11275–11280, 2014.

[70] M Tylinski, YZ Chua, MS Beasley, C Schick, and MD Ediger. Vapor-deposited alcohol glasses reveal a wide range of kinetic stability. *The Journal of chemical physics*, 145(17):174506, 2016.

[71] A Sepúlveda, M Tylinski, Anthony Guiseppi-Elie, Ranko Richert, and MD Ediger. Role of fragility in the formation of highly stable organic glasses. *Physical review letters*, 113(4):045901, 2014.

[72] Katherine R Whitaker, M Tylinski, Mathias Ahrenberg, Christoph Schick, and MD Ediger. Kinetic stability and heat capacity of vapor-deposited glasses of o-terphenyl. *The Journal of chemical physics*, 143(8):084511, 2015.

[73] Christopher J Fullerton and Ludovic Berthier. Density controls the kinetic stability of ultrastable glasses. *EPL (Europhysics Letters)*, 119(3):36003, 2017.

[74] Stephen F Swallen, Katherine Traynor, Robert J McMahon, MD Ediger, and Thomas E Mates. Stable glass transformation to supercooled liquid via surface-initiated growth front. *Physical review letters*, 102(6):065503, 2009.

[75] Kenneth L Kearns, MD Ediger, Heiko Huth, and Christoph Schick. One micrometer length scale controls kinetic stability of low-energy glasses. *The Journal of Physical Chemistry Letters*, 1(1):388–392, 2009.

[76] Yi Peng, Ziren Wang, Ahmed M Alsayed, Arjun G Yodh, and Yilong Han. Melting of colloidal crystal films. *Physical review letters*, 104(20):205703, 2010.

[77] Peter G Wolynes. Spatiotemporal structures in aging and rejuvenating glasses. *Proceedings of the National Academy of Sciences*, pages pnas–0812418106, 2009.

[78] Robert L Jack and Ludovic Berthier. The melting of stable glasses is governed by nucleation-and-growth dynamics. *The Journal of chemical physics*, 144(24):244506, 2016.

[79] Glen M Hocky, Ludovic Berthier, and David R Reichman. Equilibrium ultrastable glasses produced by random pinning. *The Journal of chemical physics*, 141(22):224503, 2014.

[80] MD Ediger. Vapor-deposited glasses provide clearer view of two-level systems. *Proceedings of the National Academy of Sciences*, 111(31):11232–11233, 2014.

[81] DR Queen, X Liu, J Karel, TH Metcalf, and F Hellman. Excess specific heat in evaporated amorphous silicon. *Physical review letters*, 110(13):135901, 2013.

[82] Shakeel S Dalal, Zahra Fakhraai, and Mark D Ediger. High-throughput ellipsometric characterization of vapor-deposited indomethacin glasses. *The Journal of Physical Chemistry B*, 117(49):15415–15425, 2013.

[83] Kenneth L Kearns, Katherine R Whitaker, MD Ediger, Heiko Huth, and Christoph Schick. Observation of low heat capacities for vapor-deposited glasses of indomethacin as determined by ac nanocalorimetry. *The Journal of chemical physics*, 133(1):014702, 2010.

[84] Tomás Pérez-Castañeda, Rafael J Jiménez-Riobóo, and Miguel A Ramos. Two-level systems and boson peak remain stable in 110-million-year-old amber glass. *Physical review letters*, 112(16):165901, 2014.

[85] Frank Arute, Kunal Arya, Ryan Babbush, Dave Bacon, Joseph C Bardin, Rami Barends, Rupak Biswas, Sergio Boixo, Fernando GSL Brandao, David A Buell, et al. Quantum supremacy using a programmable superconducting processor. *Nature*, 574(7779):505–510, 2019.

[86] M. Beasley, C. Bishop, B. Kasting, and MD Ediger, (To appear).

[87] Andrea J Liu and Sidney R Nagel. Nonlinear dynamics: Jamming is not just cool any more. *Nature*, 396(6706):21, 1998.

[88] Andrea J. Liu and Sidney R. Nagel. The jamming transition and the marginally jammed solid. *Annual Review of Condensed Matter Physics*, 1(1):347–369, 2010.

[89] TS Majmudar, M Sperl, Stefan Luding, and Robert P Behringer. Jamming transition in granular systems. *Physical review letters*, 98(5):058001, 2007.

[90] John D Bernal. A geometrical approach to the structure of liquids. *Nature*, 183(4655):141, 1959.

[91] Shlomo Alexander. Amorphous solids: their structure, lattice dynamics and elasticity. *Physics reports*, 296(2-4):65–236, 1998.

[92] Corey S O?hern, Leonardo E Silbert, Andrea J Liu, and Sidney R Nagel. Jamming at zero temperature and zero applied stress: The epitome of disorder. *Physical Review E*, 68(1):011306, 2003.

[93] Douglas J Durian. Foam mechanics at the bubble scale. *Physical review letters*, 75(26):4780, 1995.

[94] Douglas J Durian. Bubble-scale model of foam mechanics: mmelting, nonlinear behavior, and avalanches. *Physical Review E*, 55(2):1739, 1997.

[95] Boris D Lubachevsky and Frank H Stillinger. Geometric properties of random disk packings. *Journal of statistical Physics*, 60(5-6):561–583, 1990.

[96] William H Press, Saul A Teukolsky, William T Vetterling, Brian P Flannery, and M Metcalf. Numerical recipes in fortran 90. *The art of scientific computing,(Cambridge, 1996)*, 1992.

[97] Aleksandar Donev, Salvatore Torquato, and Frank H Stillinger. Pair correlation function characteristics of nearly jammed disordered and ordered hard-sphere packings. *Physical Review E*, 71(1):011105, 2005.

[98] Giorgio Parisi and Francesco Zamponi. Mean-field theory of hard sphere glasses and jamming. *Reviews of Modern Physics*, 82(1):789, 2010.

[99] Pinaki Chaudhuri, Ludovic Berthier, and Srikanth Sastry. Jamming transitions in amorphous packings of frictionless spheres occur over a continuous range of volume fractions. *Physical review letters*, 104(16):165701, 2010.

[100] Misaki Ozawa, Ludovic Berthier, and Daniele Coslovich. Exploring the jamming transition over a wide range of critical densities. *SciPost Phys.*, 3:027, 2017.

[101] Cristian F Moukarzel. Isostatic phase transition and instability in stiff granular materials. *Physical review letters*, 81(8):1634, 1998.

[102] Jean-Noël Roux. Geometric origin of mechanical properties of granular materials. *Physical Review E*, 61(6):6802, 2000.

[103] J Clerk Maxwell. L. on the calculation of the equilibrium and stiffness of frames. *The London, Edinburgh, and Dublin Philosophical Magazine and Journal of Science*, 27(182):294–299, 1864.

[104] Matthieu Wyart, Sidney R Nagel, and Thomas A Witten. Geometric origin of excess low-frequency vibrational modes in weakly connected amorphous solids. *EPL (Europhysics Letters)*, 72(3):486, 2005.

[105] Matthieu Wyart. Marginal stability constrains force and pair distributions at random close packing. *Physical review letters*, 109(12):125502, 2012.

[106] Ludovic Berthier and Thomas A. Witten. Glass transition of dense fluids of hard and compressible spheres. *Phys. Rev. E*, 80:021502, Aug 2009.

[107] Patrick Charbonneau, Jorge Kurchan, Giorgio Parisi, Pierfrancesco Urbani, and Francesco Zamponi. Fractal free energy landscapes in structural glasses. *Nature communications*, 5:3725, 2014.

[108] Patrick Charbonneau, Eric I Corwin, Giorgio Parisi, and Francesco Zamponi. Universal microstructure and mechanical stability of jammed packings. *Physical review letters*, 109(20):205501, 2012.

[109] Patrick Charbonneau, Eric I Corwin, Giorgio Parisi, and Francesco Zamponi. Jamming criticality revealed by removing localized buckling excitations. *Physical review letters*, 114(12):125504, 2015.

[110] Carl P Goodrich, Andrea J Liu, and Sidney R Nagel. Finite-size scaling at the jamming transition. *Physical review letters*, 109(9):095704, 2012.

[111] Markus Müller and Matthieu Wyart. Marginal stability in structural, spin, and electron glasses. 2015.

[112] Edan Lerner, Gustavo Düring, and Matthieu Wyart. Low-energy non-linear excitations in sphere packings. *Soft Matter*, 9(34):8252–8263, 2013.

[113] Carolina Brito and Matthieu Wyart. Geometric interpretation of previtrification in hard sphere liquids. *The Journal of chemical physics*, 131(2):149, 2009.

[114] Atsushi Ikeda, Ludovic Berthier, and Peter Sollich. Unified study of glass and jamming rheology in soft particle systems. *Physical review letters*, 109(1):018301, 2012.

[115] Atsushi Ikeda, Ludovic Berthier, and Peter Sollich. Disentangling glass and jamming physics in the rheology of soft materials. *Soft Matter*, 9(32):7669–7683, 2013.

[116] Patrick Charbonneau, Jorge Kurchan, Giorgio Parisi, Pierfrancesco Urbani, and Francesco Zamponi. Glass and jamming transitions: From exact results to finite-dimensional descriptions. *Annual Review of Condensed Matter Physics*, 8:265–288, 2017.

[117] Wolfgang Götze. *Complex dynamics of glass-forming liquids: A mode-coupling theory*, volume 143. OUP Oxford, 2008.

[118] John D Weeks, David Chandler, and Hans C Andersen. Role of repulsive forces in determining the equilibrium structure of simple liquids. *The Journal of chemical physics*, 54(12):5237–5247, 1971.

[119] Ludovic Berthier and Gilles Tarjus. Nonperturbative effect of attractive forces in viscous liquids. *Physical review letters*, 103(17):170601, 2009.

[120] Misaki Ozawa, Takeshi Kuroiwa, Atsushi Ikeda, and Kunimasa Miyazaki. Jamming transition and inherent structures of hard spheres and disks. *Physical review letters*, 109(20):205701, 2012.

[121] Jorge Kurchan, Giorgio Parisi, and Francesco Zamponi. Exact theory of dense amorphous hard spheres in high dimension i. the free energy. *Journal of Statistical Mechanics: Theory and Experiment*, 2012(10):P10012, 2012.

[122] Jorge Kurchan, Giorgio Parisi, Pierfrancesco Urbani, and Francesco Zamponi. Exact theory of dense amorphous hard spheres in high dimension. ii. the high density regime and the gardner transition. *The Journal of Physical Chemistry B*, 117(42):12979–12994, 2013.

[123] Patrick Charbonneau, Jorge Kurchan, Giorgio Parisi, Pierfrancesco Urbani, and Francesco Zamponi. Exact theory of dense amorphous hard spheres in high dimension. iii. the full replica symmetry breaking solution. *Journal of Statistical Mechanics: Theory and Experiment*, 2014(10):P10009, 2014.

[124] Ludovic Berthier, Hugo Jacquin, and Francesco Zamponi. Microscopic theory of the jamming transition of harmonic spheres. *Physical Review E*, 84(5):051103, 2011.

[125] Eric Degiuli, E Lerner, and M Wyart. Theory of the jamming transition at finite temperature. *The Journal of chemical physics*, 142(16):164503, 2015.

[126] Atsushi Ikeda, Ludovic Berthier, and Giulio Biroli. Dynamic criticality at the jamming transition. *J. Chem. Phys.*, 138:12A507, 2013.

[127] Antina Ghosh, Vijayakumar K Chikkadi, Peter Schall, Jorge Kurchan, and Daniel Bonn. Density of states of colloidal glasses. *Physical review letters*, 104(24):248305, 2010.

[128] Ke Chen, Wouter G Ellenbroek, Zexin Zhang, Daniel TN Chen, Peter J Yunker, Silke Henkes, Carolina Brito, Olivier Dauchot, Wim Van Saarloos, Andrea J Liu, et al. Low-frequency vibrations of soft colloidal glasses. *Physical review letters*, 105(2):025501, 2010.

[129] Thomas A Caswell, Zexin Zhang, Margaret L Gardel, and Sidney R Nagel. Observation and characterization of the vestige of the jamming transition in a thermal three-dimensional system. *Physical Review E*, 87(1):012303, 2013.

[130] JS Rowlinson. The equation of state of dense systems. *Reports on Progress in Physics*, 28(1):169, 1965.

[131] Jerome K Percus and George J Yevick. Analysis of classical statistical mechanics by means of collective coordinates. *Physical Review*, 110(1):1, 1958.

[132] Michael P Allen and Dominic J Tildesley. *Computer simulation of liquids*. Oxford university press, 2017.

[133] Neil W Ashcroft and N David Mermin. Solid state physics. 1976.

[134] Antoine Georges, Gabriel Kotliar, Werner Krauth, and Marcelo J Rozenberg. Dynamical mean-field theory of strongly correlated fermion systems and the limit of infinite dimensions. *Reviews of Modern Physics*, 68(1):13, 1996.

[135] Anatoly Svidzinsky, Marlan Scully, and Dudley Herschbach. Bohrs molecular model, a century later. *Physics Today*, 67(1):33, 2014.

[136] J-M Drouffe, G Parisi, and N Sourlas. Strong coupling phase in lattice gauge theories at large dimension. *Nuclear Physics B*, 161(2-3):397–416, 1979.

[137] HL Frisch, N Rivier, and D Wyler. Classical hard-sphere fluid in infinitely many dimensions. *Physical review letters*, 54(19):2061, 1985.

[138] HL Frisch, N Rivier, and D Wyler. Frisch, rivier, and wyler respond. *Physical review letters*, 57(9):1192, 1986.

[139] Marshall Luban. Comment on" classical hard-sphere fluid in infinitely many dimensions". *Physical review letters*, 56(21):2330, 1986.

[140] D Wyler, N Rivier, and HL Frisch. Hard-sphere fluid in infinite dimensions. *Physical Review A*, 36(5):2422, 1987.

[141] HL Frisch and JK Percus. Nonuniform classical fluid at high dimensionality. *Physical Review A*, 35(11):4696, 1987.

[142] HL Frisch and JK Percus. High dimensionality as an organizing device for classical fluids. *Physical Review E*, 60(3):2942, 1999.

[143] TR Kirkpatrick and PG Wolynes. Connections between some kinetic and equilibrium theories of the glass transition. *Physical Review A*, 35(7):3072, 1987.

[144] Marc Mézard and Giorgio Parisi. A tentative replica study of the glass transition. *Journal of Physics A: Mathematical and General*, 29(20):6515, 1996.

[145] Marc Mézard. How to compute the thermodynamics of a glass using a cloned liquid. *Physica A: Statistical Mechanics and its Applications*, 265(3-4):352–369, 1999.

[146] Marc Mézard and Giorgio Parisi. A first-principle computation of the thermodynamics of glasses. *The Journal of chemical physics*, 111(3):1076–1095, 1999.

[147] Marc Mézard and Giorgio Parisi. Thermodynamics of glasses: A first principles computation. *Journal of Physics: Condensed Matter*, 11(10A):A157, 1999.

[148] Silvio Franz and Giorgio Parisi. Recipes for metastable states in spin glasses. *Journal de Physique I*, 5(11):1401–1415, 1995.

[149] Marc Mézard and Giorgio Parisi. Statistical physics of structural glasses. *Journal of Physics: Condensed Matter*, 12(29):6655, 2000.

[150] Marc Mézard and Giorgio Parisi. Glasses and replicas. *Structural Glasses and Supercooled Liquids: Theory, Experiment, and Applications*, pages 151–191, 2012.

[151] Corrado Rainone, Pierfrancesco Urbani, Hajime Yoshino, and Francesco Zamponi. Following the evolution of hard sphere glasses in infinite dimensions under external perturbations: Compression and shear strain. *Physical review letters*, 114(1):015701, 2015.

[152] Corrado Rainone and Pierfrancesco Urbani. Following the evolution of glassy states under external perturbations: the full replica symmetry breaking solution. *Journal of Statistical Mechanics: Theory and Experiment*, 2016(5):053302, 2016.

[153] Marc Mézard, Giorgio Parisi, and Miguel Virasoro. *Spin glass theory and beyond: An Introduction to the Replica Method and Its Applications*, volume 9. World Scientific Publishing Company, 1987.

[154] Giulio Biroli and Jean-Philippe Bouchaud. The random first-order transition theory of glasses: a critical assessment. *Structural Glasses and Supercooled Liquids: Theory, Experiment, and Applications*, pages 31–113, 2012.

[155] Alain Barrat, Silvio Franz, and Giorgio Parisi. Temperature evolution and bifurcations of metastable states in mean-field spin glasses, with connections with structural glasses. *Journal of Physics A: Mathematical and General*, 30(16):5593, 1997.

[156] Florent Krzakala and Lenka Zdeborová. Following gibbs states adiabatically?the energy landscape of mean-field glassy systems. *EPL (Europhysics Letters)*, 90(6):66002, 2010.

[157] Lenka Zdeborová and Florent Krzakala. Generalization of the cavity method for adiabatic evolution of gibbs states. *Physical Review B*, 81(22):224205, 2010.

[158] Florent Krzakala and Lenka Zdeborová. Performance of simulated annealing in p-spin glasses. In *Journal of Physics: Conference Series*, volume 473, page 012022. IOP Publishing, 2013.

[159] Flaviano Morone, Francesco Caltagirone, Elizabeth Harrison, and Giorgio Parisi. Replica theory and spin glasses. *arXiv preprint arXiv:1409.2722*, 2014.

[160] Giorgio Parisi. The order parameter for spin glasses: a function on the interval 0-1. *Journal of Physics A: Mathematical and General*, 13(3):1101, 1980.

[161] AJ Bray and MA Moore. Evidence for massless modes in the'solvable model'of a spin glass. *Journal of Physics C: Solid State Physics*, 12(11):L441, 1979.

[162] David J Gross, Ido Kanter, and Haim Sompolinsky. Mean-field theory of the potts glass. *Physical review letters*, 55(3):304, 1985.

[163] Elisabeth Gardner. Spin glasses with p-spin interactions. *Nuclear Physics B*, 257:747–765, 1985.

[164] David Sherrington and Scott Kirkpatrick. Solvable model of a spin-glass. *Physical review letters*, 35(26):1792, 1975.

[165] Hajime Yoshino and Francesco Zamponi. Shear modulus of glasses: Results from the full replica-symmetry-breaking solution. *Physical Review E*, 90(2):022302, 2014.

[166] Daijyu Nakayama, Hajime Yoshino, and Francesco Zamponi. Protocol-dependent shear modulus of amorphous solids. *Journal of Statistical Mechanics: Theory and Experiment*, 2016(10):104001, 2016.

[167] Hajime Yoshino. Replica theory of the rigidity of structural glasses. *The Journal of Chemical Physics*, 136(21):214108, 2012.

[168] Kenneth G. Wilson and J. B. Kogut. The renormalization group and the $\epsilon$ expansion. 1973.

[169] Silvio Franz and Andrea Montanari. Analytic determination of dynamical and mosaic length scales in a kac glass model. *Journal of Physics A: Mathematical and Theoretical*, 40(11):F251, 2007.

[170] Silvio Franz. First steps of a nucleation theory in disordered systems. *Journal of Statistical Mechanics: Theory and Experiment*, 2005(04):P04001, 2005.

[171] Silvio Franz. Metastable states, relaxation times and free-energy barriers in finite-dimensional glassy systems. *EPL (Europhysics Letters)*, 73(4):492, 2006.

[172] TR Kirkpatrick and PG Wolynes. Stable and metastable states in mean-field potts and structural glasses. *Physical Review B*, 36(16):8552, 1987.

[173] Theodore R Kirkpatrick, Devarajan Thirumalai, and Peter G Wolynes. Scaling concepts for the dynamics of viscous liquids near an ideal glassy state. *Physical Review A*, 40(2):1045, 1989.

[174] G Biroli and JP Bouchaud. Structural glasses and supercooled liquids: Theory, experiment, and applications, 2012.

[175] Ludovic Berthier, Misaki Ozawa, and Camille Scalliet. Configurational entropy of glass-forming liquids. *The Journal of chemical physics*, 150(16):160902, 2019.

[176] Jean-Philippe Bouchaud and Giulio Biroli. On the adam-gibbs-kirkpatrick-thirumalai-wolynes scenario for the viscosity increase in glasses. *The Journal of chemical physics*, 121(15):7347–7354, 2004.

[177] Andrea Cavagna, Tomás S Grigera, and Paolo Verrocchio. Mosaic multistate scenario versus one-state description of supercooled liquids. *Physical review letters*, 98(18):187801, 2007.

[178] GBJP Biroli, J-P Bouchaud, Andrea Cavagna, Tomás S Grigera, and Paolo Verrocchio. Thermodynamic signature of growing amorphous order in glass-forming liquids. *Nature Physics*, 4(10):771, 2008.

[179] C Cammarota, A Cavagna, G Gradenigo, TS Grigera, and P Verrocchio. Evidence for a spinodal limit of amorphous excitations in glassy systems. *Journal of Statistical Mechanics: Theory and Experiment*, 2009(12):L12002, 2009.

[180] Ludovic Berthier and Walter Kob. Static point-to-set correlations in glass-forming liquids. *Physical Review E*, 85(1):011102, 2012.

[181] J Villain. Equilibrium critical properties of random field systems: new conjectures. *Journal de Physique*, 46(11):1843–1852, 1985.

[182] Andrea Montanari and Guilhem Semerjian. Rigorous inequalities between length and time scales in glassy systems. *Journal of statistical physics*, 125(1):23, 2006.

[183] Silvio Franz, Guilhem Semerjian, et al. Analytical approaches to time-and length scales in models of glasses. *Dynamical Heterogeneities in Glasses, Colloids, and Granular Media*, 407, 2011.

[184] Gerold Adam and Julian H Gibbs. On the temperature dependence of cooperative relaxation properties in glass-forming liquids. *The journal of chemical physics*, 43(1):139–146, 1965.

[185] Patrick Charbonneau and Sho Yaida. Nontrivial critical fixed point for replica-symmetry-breaking transitions. *Physical review letters*, 118(21):215701, 2017.

[186] JRL De Almeida and David J Thouless. Stability of the sherrington-kirkpatrick solution of a spin glass model. *Journal of Physics A: Mathematical and General*, 11(5):983, 1978.

[187] MA Moore and Allan J Bray. Disappearance of the de almeida-thouless line in six dimensions. *Physical Review B*, 83(22):224408, 2011.

[188] AJ Bray and SA Roberts. Renormalisation-group approach to the spin glass transition in finite magnetic fields. *Journal of Physics C: Solid State Physics*, 13(29):5405, 1980.

[189] Patrick Charbonneau, Yi Hu, Archishman Raju, James P Sethna, and Sho Yaida. Morphology of renormalization-group flow for the de almeida–thouless–gardner universality class. *Physical Review E*, 99(2):022132, 2019.

[190] Maria Chiara Angelini and Giulio Biroli. Spin glass in a field: A new zero-temperature fixed point in finite dimensions. *Physical review letters*, 114(9):095701, 2015.

[191] MA Moore and Barbara Drossel. p-spin model in finite dimensions and its relation to structural glasses. *Physical review letters*, 89(21):217202, 2002.

[192] Joonhyun Yeo and MA Moore. Origin of the growing length scale in m-p-spin glass models. *Physical Review E*, 86(5):052501, 2012.

[193] Ludovic Berthier, Patrick Charbonneau, Yuliang Jin, Giorgio Parisi, Beatriz Seoane, and Francesco Zamponi. Growing timescales and lengthscales characterizing vibrations of amorphous solids. *Proceedings of the National Academy of Sciences*, 113(30):8397–8401, 2016.

[194] Patrick Charbonneau, Yuliang Jin, Giorgio Parisi, Corrado Rainone, Beatriz Seoane, and Francesco Zamponi. Numerical detection of the gardner transition in a mean-field glass former. *Physical Review E*, 92(1):012316, 2015.

[195] Daan Frenkel and Berend Smit. *Understanding molecular simulation: from algorithms to applications*, volume 1. Elsevier, 2001.

[196] Hans C Andersen. Molecular dynamics studies of heterogeneous dynamics and dynamic crossover in supercooled atomic liquids. *Proceedings of the National Academy of Sciences*, 102(19):6686–6691, 2005.

[197] Walter Kob. Computer simulations of supercooled liquids and glasses. *Journal of Physics: Condensed Matter*, 11(10):R85, 1999.

[198] William G Hoover. Canonical dynamics: Equilibrium phase-space distributions. *Physical review A*, 31(3):1695, 1985.

[199] Nicholas Metropolis, Arianna W Rosenbluth, Marshall N Rosenbluth, Augusta H Teller, and Edward Teller. Equation of state calculations by fast computing machines. *The journal of chemical physics*, 21(6):1087–1092, 1953.

[200] Ludovic Berthier, Giulio Biroli, Daniele Coslovich, Walter Kob, and Cristina Toninelli. Finite-size effects in the dynamics of glass-forming liquids. *Physical Review E*, 86(3):031502, 2012.

[201] Francesco Sciortino. Potential energy landscape description of supercooled liquids and glasses. *Journal of Statistical Mechanics: Theory and Experiment*, 2005(05):P05015, 2005.

[202] Hannes Jónsson, Greg Mills, and Karsten W Jacobsen. Nudged elastic band method for finding minimum energy paths of transitions. 1998.

[203] Nicholas Bailey, Trond Ingebrigtsen, Jesper Schmidt Hansen, Arno Veldhorst, Lasse Bøhling, Claire Lemarchand, Andreas Olsen, Andreas Bacher, Lorenzo Costigliola, Ulf Pedersen, et al. Rumd: A general purpose molecular dynamics package optimized to utilize gpu hardware down to a few thousand particles. *SciPost Physics*, 3(6):038, 2017.

[204] Andrea Ninarello, Ludovic Berthier, and Daniele Coslovich. Models and algorithms for the next generation of glass transition studies. *Physical Review X*, 7(2):021039, 2017.

[205] Werner Krauth. *Statistical mechanics: algorithms and computations*, volume 13. OUP Oxford, 2006.

[206] Ludger Santen and Werner Krauth. Absence of thermodynamic phase transition in a model glass former. *Nature*, 405(6786):550, 2000.

[207] Ryoichi Yamamoto and Walter Kob. Replica-exchange molecular dynamics simulation for supercooled liquids. *Physical Review E*, 61(5):5473, 2000.

[208] D Gazzillo and G Pastore. Equation of state for symmetric non-additive hard-sphere fluids: An approximate analytic expression and new monte carlo results. *Chemical Physics Letters*, 159(4):388–392, 1989.

[209] Tomás S Grigera and Giorgio Parisi. Fast monte carlo algorithm for supercooled soft spheres. *Physical Review E*, 63(4):045102, 2001.

[210] Ludger Santen and Werner Krauth. Liquid, glass and crystal in two-dimensional hard disks. *arXiv preprint cond-mat/0107459*, 2001.

[211] Ludovic Berthier, Daniele Coslovich, Andrea Ninarello, and Misaki Ozawa. Equilibrium sampling of hard spheres up to the jamming density and beyond. *Physical review letters*, 116(23):238002, 2016.

[212] Yisroel Brumer and David R Reichman. Numerical investigation of the entropy crisis in model glass formers. *The Journal of Physical Chemistry B*, 108(21):6832–6837, 2004.

[213] Ludovic Berthier, Elijah Flenner, Christopher J Fullerton, Camille Scalliet, and Murari Singh. Efficient swap algorithms for molecular dynamics simulations of equilibrium supercooled liquids. *Journal of Statistical Mechanics: Theory and Experiment*, 2019(6):064004, jun 2019.

[214] Camille Scalliet, Ludovic Berthier, and Francesco Zamponi. Marginally stable phases in mean-field structural glasses. *Physical Review E*, 99(1):012107, 2019.

[215] Y Singh, JP Stoessel, and PG Wolynes. Hard-sphere glass and the density-functional theory of aperiodic crystals. *Physical review letters*, 54(10):1059, 1985.

[216] TR Kirkpatrick and D Thirumalai. Comparison between dynamical theories and metastable states in regular and glassy mean-field spin models with underlying first-order-like phase transitions. *Physical Review A*, 37(11):4439, 1988.

[217] TR Kirkpatrick and D Thirumalai. Random solutions from a regular density functional hamiltonian: a static and dynamical theory for the structural glass transition. *Journal of Physics A: Mathematical and General*, 22(5):L149, 1989.

[218] Giulio Biroli and Pierfrancesco Urbani. Liu-nagel phase diagrams in infinite dimension. *SciPost Physics*, 4(4):020, 2018.

[219] David Ruelle. *Statistical mechanics: Rigorous results*. World Scientific, 1999.

[220] Giovanni Gallavotti. *Statistical mechanics: A short treatise*. Springer Science & Business Media, 2013.

[221] Giulio Biroli and Pierfrancesco Urbani. Breakdown of elasticity in amorphous solids. *Nature Physics*, 12(12):1130, 2016.

[222] Camille Scalliet, Ludovic Berthier, and Francesco Zamponi. Absence of marginal stability in a structural glass. *Physical review letters*, 119(20):205501, 2017.

[223] Beatriz Seoane and Francesco Zamponi. Spin-glass-like aging in colloidal and granular glasses. *Soft matter*, 14(25):5222–5234, 2018.

[224] Qinyi Liao and Ludovic Berthier. Hierarchical landscape of hard disk glasses. *Physical Review X*, 9(1):011049, 2019.

[225] Beatriz Seoane, Daniel R Reid, Juan J de Pablo, and Francesco Zamponi. Low-temperature anomalies of a vapor deposited glass. *Physical Review Materials*, 2(1):015602, 2018.

[226] Camille Scalliet, Ludovic Berthier, and Francesco Zamponi. Nature of excitations and defects in structural glasses. *Nature communications*, 10:5102, 2019.

[227] Camille Scalliet and Ludovic Berthier. Rejuvenation and memory effects in a structural glass. *Phys. Rev. Lett.*, 122:255502, Jun 2019.

[228] Dmytro Khomenko, Camille Scalliet, Ludovic Berthier, David R Reichman, and Francesco Zamponi. Depletion of two-level systems in ultrastable computer-generated glasses. *arXiv preprint arXiv:1910.11168*, 2019.

[229] Madeleine S Beasley, Camille Bishop, Benjamin J Kasting, and Mark D Ediger. Vapor-deposited ethylbenzene glasses approach "ideal glass" density. *The journal of physical chemistry letters*, 10(14):4069–4075, 2019.

[230] Matthieu Wyart and Michael E Cates. Does a growing static length scale control the glass transition? *Physical review letters*, 119(19):195501, 2017.

[231] Ludovic Berthier, Giulio Biroli, Jean-Philippe Bouchaud, and Gilles Tarjus. Can the glass transition be explained without a growing static length scale? *The Journal of chemical physics*, 150(9):094501, 2019.

[232] Ludovic Berthier, Patrick Charbonneau, Daniele Coslovich, Andrea Ninarello, Misaki Ozawa, and Sho Yaida. Configurational entropy measurements in extremely supercooled liquids that break the glass ceiling. *Proceedings of the National Academy of Sciences*, 114(43):11356–11361, 2017.

[233] Ludovic Berthier, Patrick Charbonneau, Andrea Ninarello, Misaki Ozawa, and Sho Yaida. Zero-temperature glass transition in two dimensions. *arXiv preprint arXiv:1805.09035*, 2018.

[234] Elijah Flenner, Ludovic Berthier, Patrick Charbonneau, and Christopher J Fullerton. Front-mediated melting of ultrastable glasses. *arXiv preprint arXiv:1903.09108*, 2019.

[235] Misaki Ozawa, Ludovic Berthier, Giulio Biroli, Alberto Rosso, and Gilles Tarjus. Random critical point separates brittle and ductile yielding transitions in amorphous materials. *Proceedings of the National Academy of Sciences*, 115(26):6656–6661, 2018.

[236] Lijin Wang, Andrea Ninarello, Pengfei Guan, Ludovic Berthier, Grzegorz Szamel, and Elijah Flenner. Low-frequency vibrational modes of stable glasses. *Nature communications*, 10(1):26, 2019.

[237] Ludovic Berthier, Patrick Charbonneau, and Joyjit Kundu. Bypassing sluggishness: Swap algorithm and glassiness in high dimensions. *Phys. Rev. E*, 99:031301, Mar 2019.

[238] Romain Mari and Jorge Kurchan. Dynamical transition of glasses: From exact to approximate. *The Journal of Chemical Physics*, 135(12):124504, 2011.

[239] Baoshuang Shang, Pengfei Guan, and Jean-Louis Barrat. Elastic avalanches reveal marginal behaviour in amorphous solids. *arXiv preprint arXiv:1908.08820*, 2019.

[240] M. Baity-Jesi, R.A. Baños, A. Cruz, L.A. Fernandez, J.M. Gil-Narvion, A. Gordillo-Guerrero, D. Iñiguez, A. Maiorano, F. Mantovani, E. Marinari, V. Martin-Mayor, J. Monforte-Garcia, A. Muñoz Sudupe, D. Navarro, G. Parisi, S. Perez-Gaviro, M. Pivanti, F. Ricci-Tersenghi, J.J. Ruiz-Lorenzo, S.F. Schifano, B. Seoane, A. Tarancon, R. Tripiccione, and D. Yllanes. Janus ii: A new generation application-driven computer for spin-system simulations. *Computer Physics Communications*, 185(2):550 – 559, 2014.

[241] Kenneth L. Kearns, M. D. Ediger, Heiko Huth, and Christoph Schick. One micrometer length scale controls kinetic stability of low-energy glasses. *The Journal of Physical Chemistry Letters*, 1(1):388–392, 2010.

[242] Elijah Flenner, Ludovic Berthier, Patrick Charbonneau, and Christopher J. Fullerton. Front-mediated melting of isotropic ultrastable glasses. *Phys. Rev. Lett.*, 123:175501, Oct 2019.

[243] Misaki Ozawa, Camille Scalliet, Andrea Ninarello, and Ludovic Berthier. Does the adam-gibbs relation hold in simulated supercooled liquids? *The Journal of Chemical Physics*, 151(8):084504, 2019.